



Large Scale Integration of Carbon Nanotubes in Microsystems

Gjerde, Kjetil; Bøggild, Peter; Nielsen, Michael Brorson

Publication date:
2007

Document Version
Early version, also known as pre-print

[Link back to DTU Orbit](#)

Citation (APA):
Gjerde, K., Bøggild, P., & Nielsen, M. B. (2007). Large Scale Integration of Carbon Nanotubes in Microsystems.

DTU Library

Technical Information Center of Denmark

General rights

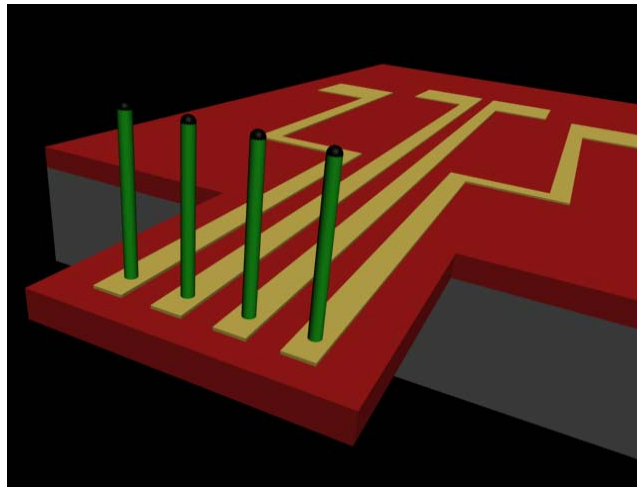
Copyright and moral rights for the publications made accessible in the public portal are retained by the authors and/or other copyright owners and it is a condition of accessing publications that users recognise and abide by the legal requirements associated with these rights.

- Users may download and print one copy of any publication from the public portal for the purpose of private study or research.
- You may not further distribute the material or use it for any profit-making activity or commercial gain
- You may freely distribute the URL identifying the publication in the public portal

If you believe that this document breaches copyright please contact us providing details, and we will remove access to the work immediately and investigate your claim.

Large Scale Integration of Carbon Nanotubes in Microsystems

Kjetil Gjerde



PhD. Thesis
June 2006

Department of Micro and Nanotechnology
Technical University of Denmark

Preface

This thesis has been written as a partial fulfillment of the requirements for obtaining the PhD degree at the Technical University of Denmark (DTU). The present work has mainly been carried out at the Department of Micro and Nanotechnology at DTU. Smaller parts have been conducted at Cambridge University, Department of Engineering, and at Lund University, Division of Materials Engineering group.

The project has been financed by a scholarship granted by the Technical University of Denmark. It has been supervised by Peter Bøggild, project leader of Nanointegration in the Nano Systems Engineering group.

Acknowledgements

Many people have been very helpful during the course of this work. I will here mention those who have been particular helpful. Thus my deepest thanks go to my colleagues Lauge Gammelgaard and Jakob Kjelstrup-Hansen, for invaluable help and support throughout the project. They were not only colleagues, but also humans. In the same category comes Tommy Schurmann, the first master student I supervised. We shared many challenges and problems in the start of this project. Many thanks also go to Kristian Mølhav for his willingness to share ideas and knowledge which often were quite useful. The collaboration with master student Marc Fornes Mora was also very rewarding. A deep thanks also goes to my supervisor Peter Bøggild, for valuable contributions, and especially proofreading of papers and thesis.

Throughout the project I have also supervised many courses for students, and I would like to mention Elvis Ramovic and Christian Agger for particular strong endurance when facing never ending obstacles. Also Ask H Larsen, Martin F Laursen and Kasper Reck worked with great enthusiasm in the projects.

From Danchip there were also some that were helpful beyond my expectations. In no particular order, I will mention Svetolic Ivanovic, Thøger Eskildsen, Jan Vasland Eriksen, and Peixiong Shi.

From outside DTU I would like to thank Bill Milne and Ken Teo from Cambridge University, for inviting me to visit their group and for their invaluable collaboration. Also Christer Persson from Lund University is thanked for his collaboration on ESEM studies.

Abstract

In this thesis routes toward large scale integration of carbon nanotubes in microsystems have been explored. In the beginning of this thesis a background is given and essential state of the art knowledge presented.

In the first experimental part, the possibility of successful integration of carbon nanotubes into microsystems is explored. First growth tests are done on various probes and probe materials. The in situ grown nanotubes are investigated for usability as mechanical probes and electrodes. It is shown the in situ grown nanotubes are well attached to the substrate surface and also that the nanotubes can work as electrodes. A thorough investigation on control of nanotube inclination is also conducted. The inclination may be an important feature for nanotubes used as probe tips.

In the second part, properties of vertically aligned carbon nanotube forests are investigated. The wetting properties are studied both in ambient and in an Environmental Scanning Electron Microscope. It is further shown that the special properties of nanotube forests make them ideal surfaces for manipulation of micro and nanostructures, in this work demonstrated by latex beads and organic nanofibres. Pick and place nanomanipulation is made easy by the use of a nanotube forest as the workbench.

In the third part, the construction, and initial optimisation, of a combined CVD and PECVD chamber for carbon nanotube synthesis is described. Results from both PECVD and CVD growth is presented and discussed.

In the fourth part, the process recipes used or developed in this project for waferscale integration of catalytic nanoparticles for subsequent carbon nanotube growth in situ in microsystems is presented. Four methods are treated; 1) The *Direct* method, which is the standard method used for placing catalyst particles in microsystems. 2) The *In situ mask* method, which is a method developed for allowing integration of catalyst particles in complex microstructures, such as suspended cantilevers. The important innovation here is the integration of an in situ mask of poly silicon, which allows deposition of the catalyst material towards the end of the microfabrication. 3) The *Window mask* method, which is a method combining the strengths of the two preceding methods, using a poly silicon sacrificial layer to facilitate easy clean lift off on fragile nanostructures. 4) The *Encapsulation* method, the last method developed, uses poly silicon to encapsulate catalyst particles, made with the *Direct* method, allowing further cleanroom processing. These methods are presented and investigated, and it is seen that the three methods developed in this project are all capable of placing catalyst particles in microsystems. Most extensive studies are done on the *In situ mask* method, which was developed first, and optimisation results are presented.

Resume

Kulstof nanorør har mange egenskaber der kunne anvendes i kombination med traditionelle mikrosystemer, her især overlegne mekaniske og elektriske egenskaber. I denne afhandling bliver metoder til stor-skala integration af kulstof nanorør i mikrosystemer undersøgt, med henblik på anvendelse som mekaniske prober, elektroder og felt-emittere. Første del behandler kompatibilitet af silicium mikrofabrikation med in-situ katalytisk dyrkning af nanorør, hvilket er en metode der tillader kontrol af position, diameter og vinkel af nanorørene i et mikrosystem. I anden del blir kulstof nanorør "skove" studeret nøjere, hvor placeringen af nanorørene på underlaget er tilfældig men tæt. Det blir vist at sådanne nanorør skove kan bruges som slip-let overflader hvilket gør manipulering af mikro og nanostrukturer meget lettere. Objekter som latex mikrokugler og organiske nanofibre der normalt ikke manipuleres på grund af deres store vedhæftningsevne til de fleste overflader, kunne løftes op efter at have været spredt ud på en nanorør skov. I tredje del af afhandlingen beskrives konstruktion, optimering og første resultater fra et kombineret CVD (chemical vapor deposition) og PECVD (plasma enhanced CVD) katalytisk dyrkningskammer til kulstof nanorør. I sidste del præsenteres og sammenlignes fire forskellige mikro/nano fabrikationsprocesser udviklet i dette projekt, til wafer skala integration af katalytiske nanopartikler for efterfølgende syntese af kulstof nanorør i mikrosystemer.

Contents

<u>PREFACE.....</u>	<u>3</u>
<u>ABSTRACT.....</u>	<u>4</u>
<u>RESUME</u>	<u>5</u>
<u>1 INTRODUCTION.....</u>	<u>9</u>
Motivation.....	9
Background.....	10
Various approaches.....	10
Potential applications.....	13
Thesis goal and outline.....	15
<u>2 THEORY AND PRINCIPLES</u>	<u>16</u>
Carbon nanotubes.....	16
Introduction.....	16
Structure.....	16
Electromechanical Properties of CNTs.....	19
Synthesis of Carbon nanotubes.....	20
Introduction.....	20
CVD – Chemical Vapour Deposition.....	21
PECVD – Plasma Enhanced CVD.....	24
<u>3 INTEGRATION OF CNS IN MICROSYSTEMS.....</u>	<u>29</u>
Introduction.....	29
CN growth on cantilevers.....	29
The substrates.....	29
PECVD growth.....	30
Mechanics of PECVD grown CNs on microprobes.....	32
Electrical properties.....	35
Electrical field alignment.....	38
Introduction.....	38
On microprobes with cantilevers.....	39
Inclined CN growth on flat surfaces and in microchannels.....	41
Conclusion.....	46
<u>4 SURFACE PROPERTIES OF VERTICALLY ALIGNED NANOTUBE FORESTS</u>	<u>47</u>
Introduction.....	47

Wetting properties.....	47
Basic Wetting theory.....	47
Wetting of carbon nanotube forests.....	50
Summary.....	57
Stiction and friction on vertically aligned nanotube forests.....	58
Background.....	58
Latex beads.....	58
Manipulation of Nanowires.....	68
<u>5 CVD-PECVD CHAMBER.....</u>	74
Introduction.....	74
Construction.....	74
Vacuum system.....	74
Gas supply system.....	77
Heating.....	77
Plasma generation.....	80
CN growth with thermal CVD.....	82
CN growth with Plasma Enhanced CVD.....	89
Conclusion.....	93
<u>6 INTEGRATION IN MEMS USING E-BEAM.....</u>	94
Introduction.....	94
Electron Beam Lithography.....	96
Results from the four processing methods.....	98
Direct.....	98
In situ mask.....	102
Window mask.....	121
Encapsulation.....	127
Conclusion.....	129
<u>7 CONCLUSION.....</u>	131
<u>APPENDIX A.....</u>	133
List of Publications.....	133
List of workshop contributions.....	133
<u>APPENDIX B.....</u>	135
Process sequences.....	135
Direct method.....	135
In situ mask with oxide structures and leads.....	140
Window with oxide structures and leads.....	148
Encapsulation with oxide structures and leads.....	154

APPENDIX C 161

Additional material 161
Gas correction factor 161
Nitride removal in RIE with in situ etch mask 161

REFERENCES..... 162

1 Introduction

Motivation

Richard Feynman gave a fascinating talk at the annual meeting of the American Physical Society in 1959. The title of his talk was *There is Plenty of Room at the Bottom* [1], and Feynman challenged the research society to pursue the topic of miniaturisation in a new way. He called for a change in paradigm. From just making things a little bit smaller by improvement of existing technologies – to realising ways of making things really small by inventing new methods to accomplish it. Not the old fashioned way of miniaturisation, but through creating a new technology for this world of incredibly small dimensions, which he illustrated with some marvellous and mind-boggling examples. He put a challenge forth to the researchers to exploit the vast possibilities of the micro- and nano-worlds. With these thoughts, he anticipated what we today know as micro- and nanotechnology. Through examples he illustrated possibilities and potential problems that would be encountered on this scale, and envisioned the development of the computer technology. He had a strange fascination for infinitesimal machinery – something that he explores more in depth in a follow up talk in 1983 at the Jet Propulsion Laboratory (Pasadena, California) [2]. The very name of that talk was *Infinitesimal Machinery*, but, as Feynman himself pointed out, another suitable name could have been *There is Plenty of Room at the Bottom – Revisited*. In this talk he treats his ideas from his 1959 talk, and compares to what actually happened in the 23 years in between. Many of his ideas had been realised, and some not. Feynman continued treating the unrealised examples and could not resist from suggesting new possibilities, problems and potential solutions.

Today, another 23 years have passed, and the field of micro and nanotechnology is emerging as an ever more important area for both research and industry. Tools for both characterisation and fabrication are under continuous development, as well as the nanostructures themselves. In 1985, Richard Smalley and Harry Kroto discovered the Fullerenes [3], which are also known as Bucky-balls. The fullerenes are C_n molecules, with $n \geq 20$, forming a spherical or elongated ball consisting of one enclosed graphene layer. Then, in 1991, Sumio Iijima discovered carbon nanotubes [4], which is essentially a graphene layer tube, possibly with several walls, closed in each end with an appropriately sized fullerene cap. Nanostructures such as carbon nanotubes (CNTs), and nanowires of other elements [5-7], are potential components for integration in microelectromechanical systems (MEMS). To date, most demonstrated prototypes have been assembled in a serial way, either through nanomanipulation [8-10], or through contacting randomly dispersed nanostructures on a surface through electron beam lithography (EBL) [11, 12]. Although these methods are highly suitable for making prototype devices and investigating the fundamental properties of the nanostructures, they are not suitable for large scale industrial production. Here we need a parallel fabrication technique, provided by for instance in situ growth from pre-patterned catalyst particles [5, 13-15], where many CNTs can be grown in predefined positions on a full wafer.

The motives for research on carbon nanotubes (CNT) are numerous. The CNTs are immensely strong compared to any known macroscopic material. They may be used in electronics to produce faster, more durable and efficient devices thanks to excellent

current carrying properties. CNTs can in principle replace leads in electronic circuits, but on a much smaller scale – the molecular, where silicon and other standard semiconductors cease to work. The incentives for this miniaturisation are considerable due to the rapid increase of speed, density, and efficiency of microelectronic devices as the minimum feature decreases. Photolithography cannot produce devices on the scale of nanotubes. The nanotubes emerge as truly exotic conductors, combining graphite's semi metallic properties with the quantum rules of energy levels and electron waves. Thus, CNTs of different diameters and twists (chiral angle), as well as various multiwalled tubes, have different conducting properties. Since their discovery, CNTs have become one of the most likely candidates, together with carbon nanofibres (CNFs) and other nanowires (NWs), to be incorporated as nanocomponents in Microsystems. Much work has been done on integrating CNTs as components in functional devices such as for instance field effect transistors [10, 16-21]. Functional devices based upon nanocomponents require precise control of the growth parameters controlling the synthesis and thus the height, diameter, location, chemical structure, shape, etc. But the possible use of nanotubes does not stop with electronics. We can envisage chemical and biological probes [22, 23], supersensitive sensors [24, 25], and hydrogen and ion storage [26]. In the present work, it is the application of larger CNTs and carbon nanofibres (CNFs) as integrated parts in MEMS that is the focus. Thus the need for precise control of chirality and diameter is not crucial. However, the requirements of precise control of position in the microsystems still make the task very challenging.

Background

Although many experiments have been done in order to reveal the properties of CNTs, their formation mechanism, and to explore different ways of synthesising them – less work has been successful in integrating CNTs in Microsystems through an efficient in situ growth process. Whereas the synthesis of CNTs, CNFs and nanowires of other elements is not straightforward, there are many established routes and large amounts of research have been devoted to this (see [13, 14, 27, 28] and references therein). The main challenge presently is the integration of such nanostructures into MEMS. Since most research seem to point in the direction of nanostructures synthesised by in situ catalytically activated growth, the main obstacle lies not in the growth itself, but by placing appropriate catalyst particles in precise locations. Clearly, this challenge is greater the more precise the nanostructures have to be. Large CNTs and CNFs do not for instance require exact control of diameter, or, even more difficult, the chirality. Still, their successful integration into MEMS, is very challenging. But the level of difficulty depends strongly on the complexity of the MEMS structures on which the catalyst particles are supposed to be integrated.

Various approaches

On flat surfaces

Several research groups have shown in various studies how parameters, such as diameter and location, can be controlled by depositing the catalyst on planar surfaces in patterns defined by E-Beam lithography (EBL)[29]. The approach here is to spin an appropriate resist for electron beam lithography on the wafer, and expose the pattern

with an E-Beam writer. Single dots may then give rise to individual CNT growth, as seen in Figure 1A.

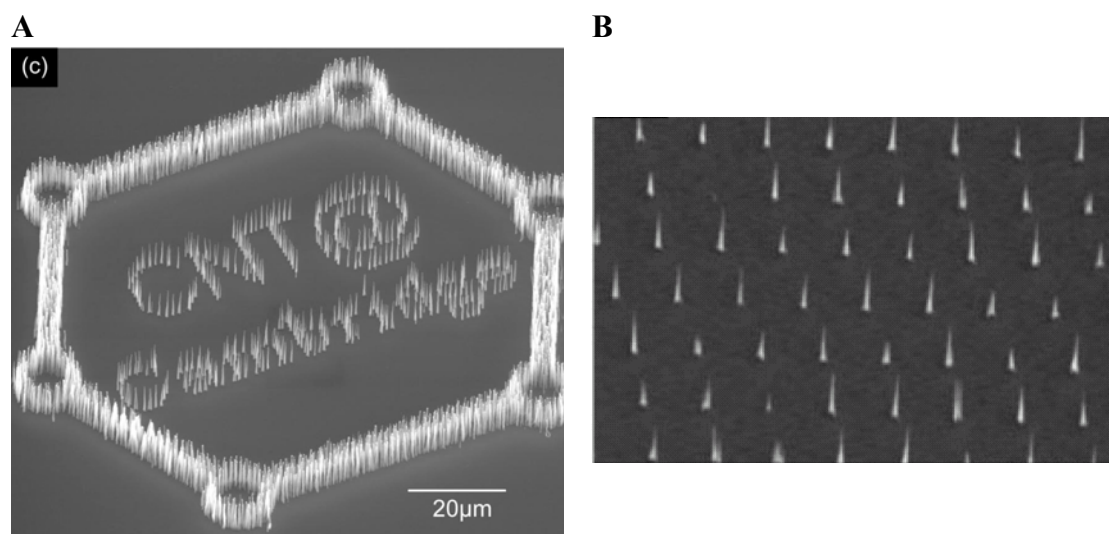


Figure 1 A) CNTs grown from precisely pre-patterned catalyst particles on a plain oxide surface (Reproduced from [29]). B) Arrays of CNTs grown from on plain oxide surface (Reproduced from [30]).

Interestingly, an alternative approach has been shown by Kim et al [30], where the small dots size is obtained by a reverse photolithography step. First a thin layer of nickel is deposited on the wafer, and conventional photolithography is used to define small dots and patterns of PR in places where nickel dots should remain. A subsequent nickel etch, removes the nickel in all exposed areas, and an overetch can be controlled to give very small nickel dots left underneath the photoresist. The array of individual CNs shown in Figure 1 B are synthesised from such a nickel pattern.

On flat surfaces with leads

For many applications, for instance in electronic circuits, the carbon nanotubes have to be grown on top of leads on the surface, and possibly between leads. The approach of patterning catalyst particles on top of leads by EBL is very similar to flat surfaces without leads. However, depending on the lead thickness, it may be necessary to ensure that the EBL resist is thick enough, thus avoiding edge effects. EBL has successfully been used by Jang et al [31], to define nickel catalyst dots for subsequent CNT synthesis on top of Niobium leads, to produce a nanoelectromechanical switch, see Figure 2 A. Guillorn et al [32] and McKnigh et al [33] fabricated tungsten interconnects with CNs, where each nanofibre could be individually addressed electrically. Integration of SWCNT between leads has also been shown. Tseng et al [34] placed catalyst islands on top of leads and after CVD growth SWCNTs was seen to bridge the gap between some electrodes as seen in Figure 2 C.

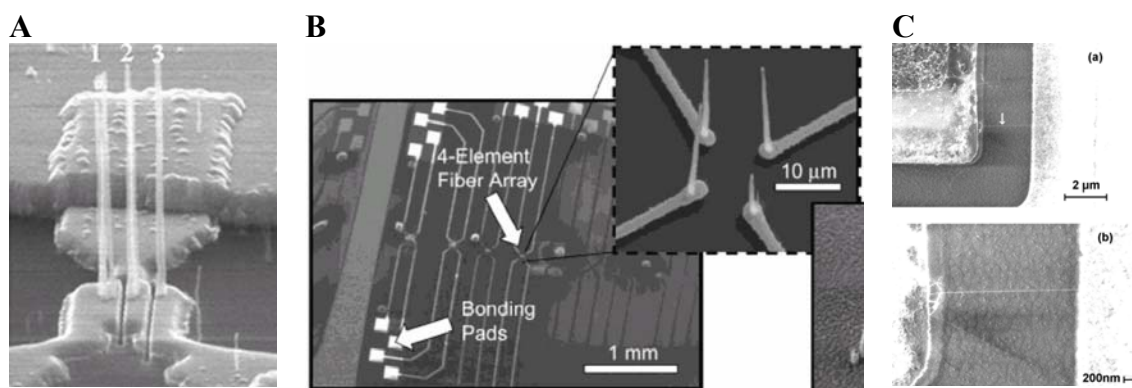


Figure 2 A) Three CNTs grown from EBL defined 10 nm thick 150 nm wide nickel catalyst dots on top of niobium leads (Reproduced from [31]). B) McKnight et al similarly produced CNTs on top of tungsten interconnects by EBL (Reproduced from [33]). C) SWCNT grown from a catalyst island bridging the gap between two electrodes (Reproduced from [34]).

On 3 dimensional microstructures

The biggest challenge is to integrate catalyst particles on 3 dimensional devices, such as microchips equipped with cantilevers. Examples of such devices are AFM tips and 4 point probes. Perhaps the most promising approach has been shown by Ye et al [35]. In their work, they define the nickel catalyst with EBL on the planar wafer surface, and then subsequently encapsulate the catalyst dot in silicon nitride. Conventional microfabrication then completes the chip structure with free hanging silicon cantilevers. After removal of the silicon nitride in a buffered oxide etcher, the nickel particle remained on the cantilevers and kept its catalytic activity (Figure 3).

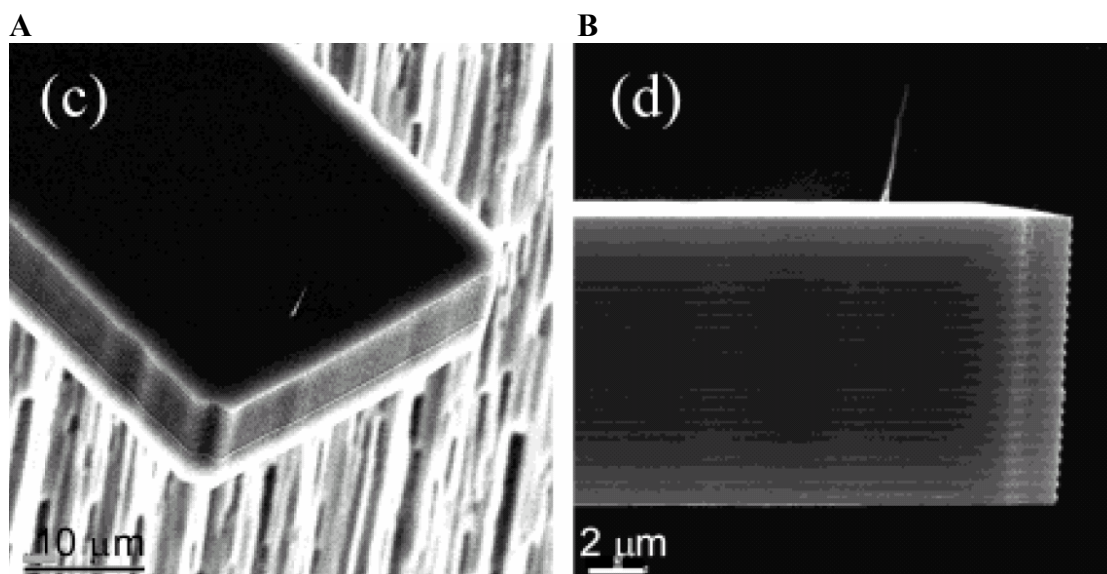


Figure 3 A) A CNT based AFM tip fabricated on waferscale by Ye et al [35]. B) A close up of the silicon cantilever with CN. (Reproduced from [35])

Potential applications

Four point probe

The four point probe is used to measure the electrical properties of the surface of a material. As compared to a more conventional two point measurement, a four point measurement measures the sheet resistance of a surface, without including the contact resistance between the probes and the surface. Four electrodes contact the surface, and a current is passed between the two outermost electrodes. The two centre electrodes measure the potential drop between those two electrodes. Since no current is passed through the inner voltage electrodes, the voltage drop across the contact barrier is very small, hence only the voltage drop in the sample is probed. This allows a value for the resistivity to be computed. In the area of material science, and in particular the microtechnology industry, it has become desirable to measure electrical properties of surfaces on an ever smaller scale. To reveal the local electrical properties of for instance deposited thin films of metal or semiconductors, and to describe their variation on the microscale it is advantageous to downscale the macroscopic four point measurement probe. Work on this has been going on for some years. A significant contribution was the development of a microscale four point probe by Petersen and co-workers [36]. The micro four point probe consisted of four metallised cantilevers suspended from the edge of a silicon support, with an electrode pitch down to about 4 microns. A schematic of this is shown in Figure 4, as well as a scanning electron micrograph of a micro four point probe in contact with a surface.

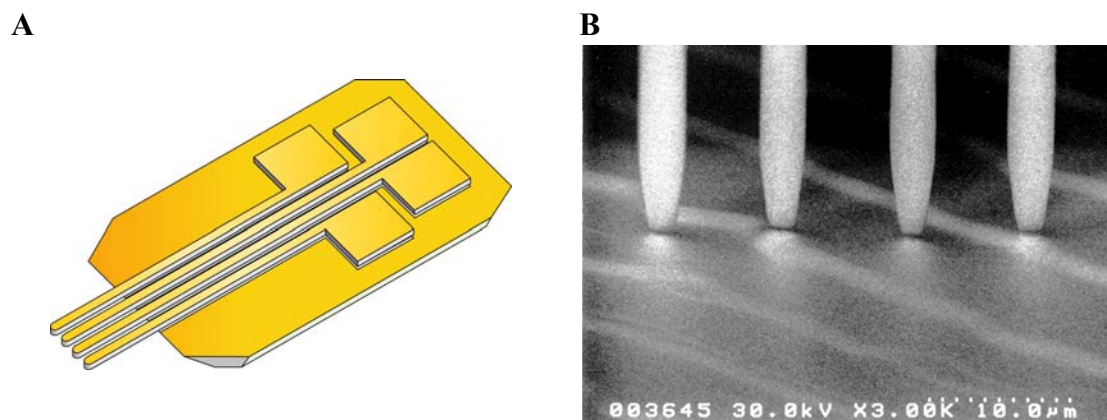


Figure 4 A) schematic of a micro four point probe. B) Scanning electron micrograph of a four point probe measuring on a surface.

The smaller the electrode pitch, the higher the sensitivity to the electrical properties in the top most layer. Thus there has been a continuous effort in reducing the scale of the microprobes. By conventional microprocessing the pitch has been reduced to 1.1 μm by Hansen [37]. In addition, four point probes with a pitch of only 300 nm was fabricated by Bøggild et al [38]. This was obtained by using electron beam deposition of carbon on the tips of an existing micro four point probes, and was therefore a serial process where each electrode had to be deposited one at a time. Another approach has been tried by Lin [9], where silicon nanowires was manually attached to a micro four point probe and subsequently covered in gold. An example of such a probe is shown in Figure 5A. Good measurements could be done with such probes, but it proved difficult to obtain a controlled reduction of the electrode pitch. A potential

improvement could be electrode tips made out of in situ grown CNTs, as illustrated in Figure 5 B.

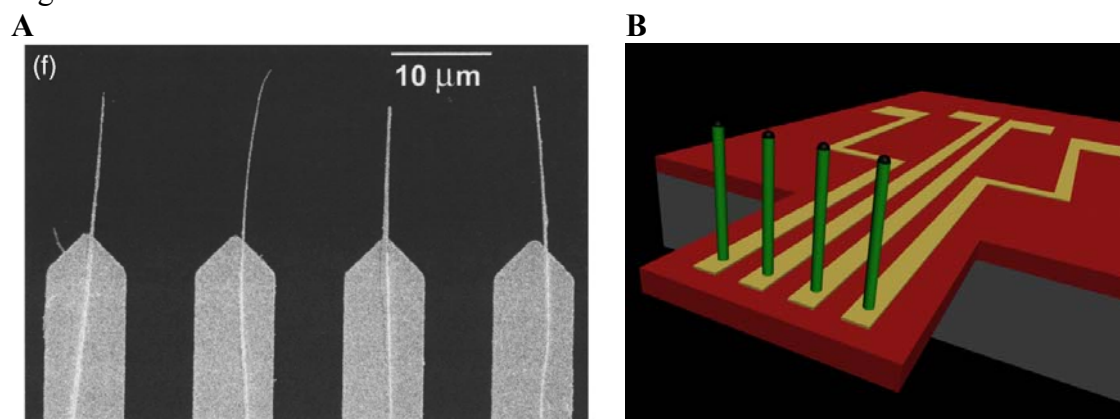


Figure 5 A) Silicon nanowires attached by a serial process to a four point probe, and subsequently covered in gold (Reproduced from [9]). B) Illustration of a four point probe, made out of a monocantilever with four electrode tips of in situ grown CNTs.

AFM tips

CNTs as scanning probe tips was first realised by Dai et al in 1996 where it was shown that tips with micrometer long CNTs had a superior ability to image deep trenches as compared to commercial tips [39]. However, in their work, the CNTs were manually mounted on the probe tips. More efficient ways of mounting CNTs on probe tips have been developed, for instance by the use of electric fields to transfer nanotubes from a nanotube sample and to the tip [40]. Waferscale production of AFM tips with CNTs grown by CVD has also been shown by Yenilmez et al [41]. However, Yenilmez et al spin coat the catalyst on the probe tips, which may result in a less controlled CNT growth. The superiority of CNT based AFM tips are shown in Figure 6, where a scan on a surface is compared to an equivalent scan with a conventional probe tip.

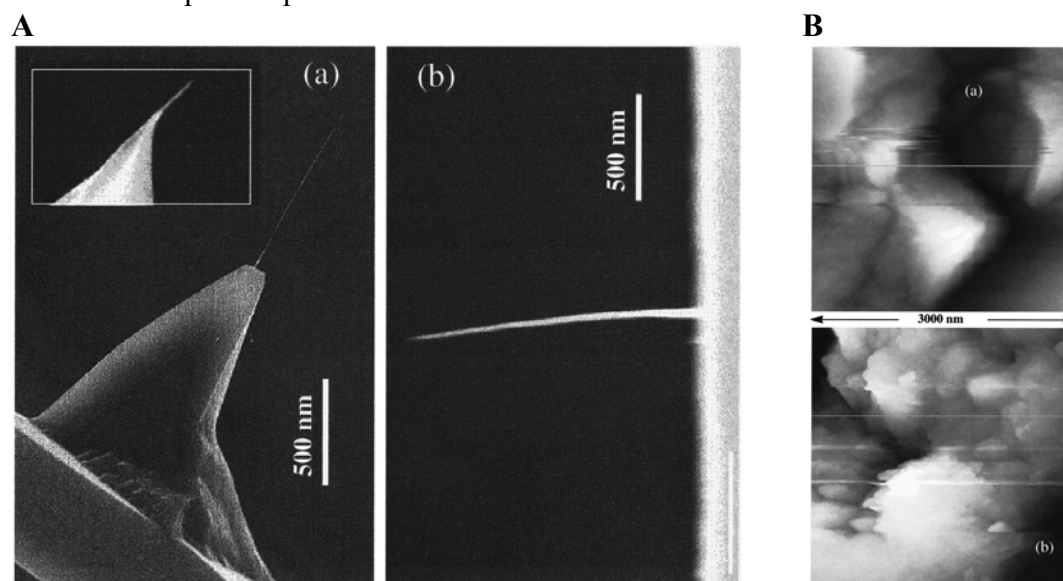


Figure 6 A) An AFM tip with an attached CNT (reproduced from [40]). B) Picture on top shows an AFM scan with a conventional tip of a sample. Bottom picture show the same area scanned with a CNT based AFM tip (reproduced from [40]).

Thesis goal and outline

The main goal of this work has been to explore routes that would allow fast and reliable integration of one dimensional nanostructures, such as carbon nanotubes and nanofibres (CNs), as components in microsystems. It is therefore important to control the dimensions, orientation and position of the structures. Furthermore, the fabrication should be done in a way compatible with standard cleanroom processing. Thus the task consists of;

- Show the feasibility of integrating CNs in microsystems, such as on cantilevers, for electrical and mechanical purposes.
- Investigate possibility of control of CN growth direction in microsystems
- Develop methods of integrating catalyst particles into microsystems on waferscale.
- The method should be compatible with standard cleanroom processing.

Important secondary goals have been to develop a CN synthesis setup that could allow CN growth on full 4 inch wafers, and to study the possibility to functionalise surfaces with carbon nanotube forests. In this thesis, our investigations toward reaching these goals and the results will be presented.

The thesis consists of 7 chapters. Chapter 1, gives the motivation and background for the work. Chapter 2 outlines important concepts. The presentation of the experimental work starts in chapter 3, where the initial investigations toward integrating CNs into MEMS are presented. Here the possibility of integrating CNs on various substrates, and explore the appropriateness of the CNs as electrical and mechanical components is looked into. A thorough study on the control of CN inclination in MEMS is also given. In chapter 4, some special characteristics of surfaces covered with vertically aligned CNs (nanotube forests) is explored. In particular the wetting properties are investigated and the friction and adhesion properties with regard to micro and nanomanipulation. Chapter 5 treats the construction and characterisation of a combined chamber for both chemical vapour deposition (CVD) and plasma enhanced CVD (PECVD). Chapter 6 presents various routes, with their challenges and obstacles, for successful integration of catalyst patterns in microsystems, with subsequent CN synthesis through in situ growth. Note that, here, the main focus has been to find routes for integrating catalyst particles in MEMS, in a way compatible with standard cleanroom processing. The final chapter 7 summarise the results from this thesis and provide an outlook of what is yet to be done. Extensive processing details are given in the appendices, where the most important process recipes are given.

2 Theory and principles

Carbon nanotubes

Introduction

Before 1985 there were only two known allotrope forms of Carbon – diamond and graphite. Today, another allotrope form of carbon is known, the fullerenes, discovered in 1985 [3], with the subcategory carbon nanotubes discovered in 1991 [4]. The fullerenes and the CNTs are similar structures, but whereas the fullerenes are one single layer spheres or ellipsoids of C_n molecules, the CNTs are essentially tubes of graphene layers, with one or several walls, closed at each end by a fullerene cap. The discovery of single wall CNTs (SWCNT) was done in 1993 [42, 43]. The electromechanical properties of CNTs have been extensively studied. It was shown in 1992 that CNTs could be both metallic and semiconducting [44-46]. It was soon shown that these tubular structures of graphitic carbon also had exceptional mechanical properties [47]. They may carry extremely high current densities and are highly flexible. They can undergo large distortions without suffering plastic deformation. Their elastic modulus is as high as 1 TPa, and the tensile strength is around 45 GPa – 20 times that of steel [48]. Work on CNT as field emitters started in 1995 by Rinzler et al [49]. Here, it was shown that CNTs are excellent field emitters due to their extremely low turn on fields and high current density.

Structure

Carbon nanotubes (CNT) are macromolecules with extraordinary properties, both mechanically and electrically. The building blocks of CNTs are carbon atoms. The atoms are bonded to each other in a hexagonal way in a 2 dimensional plane, as is sketched in Figure 7A. Such a 2 dimensional sheet of carbon atoms bonded into a hexagonal pattern is exactly what we also find in an individual graphene sheet of graphite. Although the formation mechanisms are completely different, we can think of a CNT as such a graphene sheet rolled up along a vector C_h (as seen in Figure 7A) to give a tubular structure. The tube will be hollow, with open ends. If we add two fullerene caps of appropriate diameter at each end to close the tube we have finally a single walled carbon nanotube (SWNT), see Figure 7B. It is the ability of carbon to form curved 2D sheets that makes it possible to have CNTs. The endcap curvature is obtained by including certain topological defects into the structure. A CNT can be regarded as an elongated fullerene with a vast number of hexagons but still only 12 pentagons to close the structure, six at each end cap.

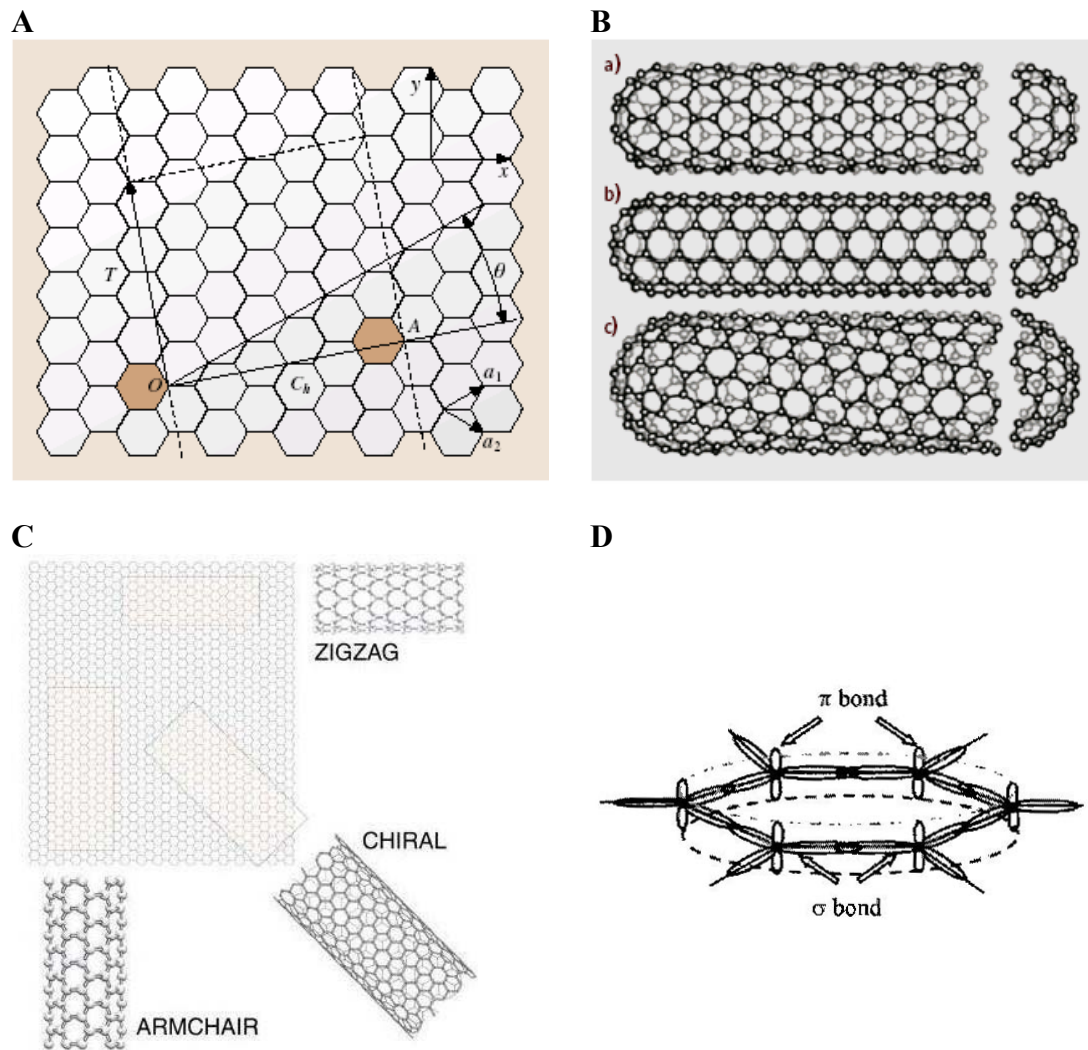


Figure 7 A) Hexagonal structure of a graphene sheet with roll up vector C_h and chiral angle θ . (Reproduced from [50]). B) The rolled up graphene sheets are closed at each end by an appropriate fullerene cap. C) Depending on the roll up vector (which again defines the chiral angle), the CNTs can be divided into three main classes; Zigzag, Chiral and Armchair. (Reproduced from [50]). D) Hexagonal bonding structure of graphite, showing both σ -bonds and π -bonds as they appear in the hexagonal lattice structure of graphite.

Figure 7A defines the roll up vector C_h and the primitive lattice vectors a_1 and a_2 . The C_h vector is a linear combination of the unit vectors;

$$C_h = n \cdot a_1 + m \cdot a_2 \quad (2.1)$$

This relationship also defines the chiral angle θ . The chiral angle is used to classify the different molecular structures of the CNTs.

- $\theta = 30$ ($n = m$) is called *Armchair*.
- $0 < \theta < 30$ is called *Chiral*.
- $\theta = 0$ ($m = 0$) is called *Zigzag*.

The integers n and m defines the diameter and chirality of the CNT. The resulting three categories are sketched in Figure 7C. Chiral tubes are sometimes also referred to as helical tubes. Calculations have predicted that all the armchair tubes are metallic

whereas the zigzag and helical tubes are either metallic or semi-conducting [51]. Theoretical analysis show that tubes are metallic when their set of base vectors (m,n) fulfil $n = m$. Tubes with $n-m = 3i$ where i is an integer, have a small curvature induced band-gap, and the rest ($n-m \neq 3i$) are semiconducting [52]. Due to the graphene-like band structure and the lateral confinement in the nanotube, it can be shown that metallic nanotubes not only are ballistic, but also contain two conducting channels, each contributing $2e^2/h$ to the conductance. Thus the resistance of any metallic SWCNT is $6.5 \text{ k}\Omega$.

The carbon atom has an electron configuration as $1s^2 2s^2 2p^2$ (6 electrons). Since the energy levels of 2s and 2p orbitals are very close, carbon is able to form hybrid orbitals. In graphite we have three sp^2 – orbitals that is formed by one s orbital and two p orbitals. These orbitals may form strong covalent bonds, called σ - bonds. They form in a plane separated with an angle of 120° . The remaining p orbital forms a bond perpendicular to that plane, and constitutes a weak bond called a π -bond. This is illustrated in Figure 7D. The π -bonds interact with the π -bonds on the neighbouring layer, and produces a weak interlayer bond of Van der Waals type, much weaker than the in-plane σ -bonds [53].

The typical diameter of a SWCNT is $d \sim 1\text{-}5 \text{ nm}$. However, carbon nanotubes can consist of several concentric helical tubes, thus forming a multiwalled carbon nanotube (MWCNT). An illustration of this is shown in Figure 8A, as well as a Transmission Electron micrograph of a MWCNT in Figure 8B. In MWCNT the interlayer spacing may be around 0.34 nm as compared to the interlayer spacing in planar graphite of 0.335 nm . The reason for this difference is the boundary requirements of the tubular graphene sheets, which needs to close onto itself after exactly one circumference. MWCNTs may have diameters from 3 to several hundred nm.

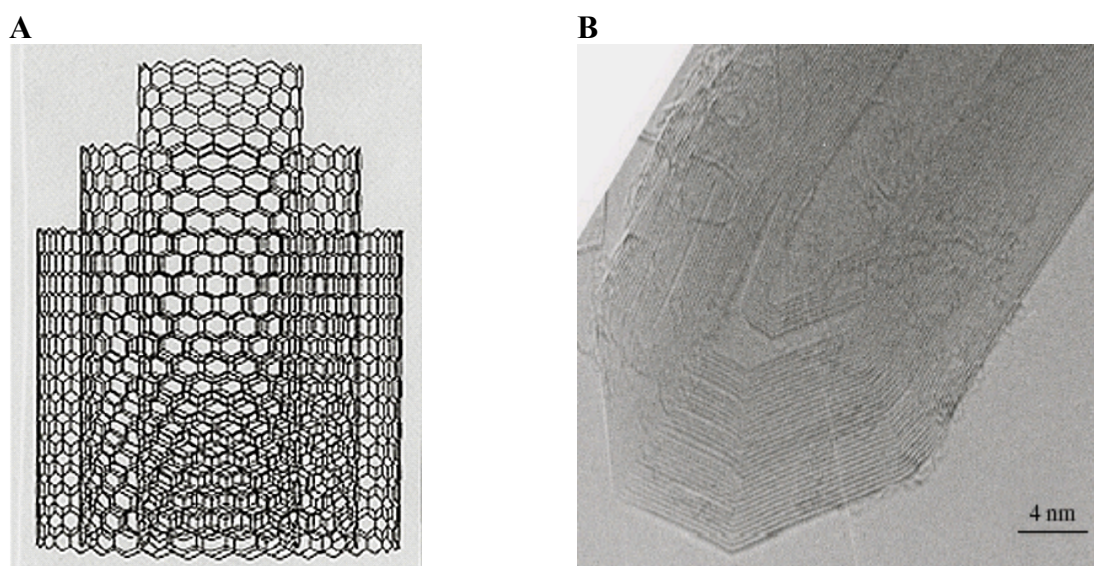


Figure 8 A) Schematic illustration of several single wall carbon nanotubes inside each other. B) Transmission Electron Micrograph of a multi wall carbon nanotube. The individual shells may be seen as black lines. (Reproduced from [50])

Often the largest MWCNT are less perfect, showing a multitude of defects and bamboo like structures. The difference between a MWCNT and a carbon nanofibre

(CNF) may then become vague. Carbon nanotubes are hollow structures, with graphene sheets parallel to the axis of the tube and coiled up around it. There exist several forms of carbon nanotubes whiskers and fibres that are more or less produced in the same manner. They are all grown by the diffusion of carbon through a catalyst nanoparticle (normally Fe, Co or Ni) and subsequent precipitation as graphitic filaments. The carbon is provided via catalytic decomposition of the carbon bearing gas on the surface of the catalyst particles. From this process several different types of filaments can grow. They are identified via the angle the graphene layers have with respect to the filament axis. Main morphological types are stacked, herringbone and nanotubular, see Figure 9.

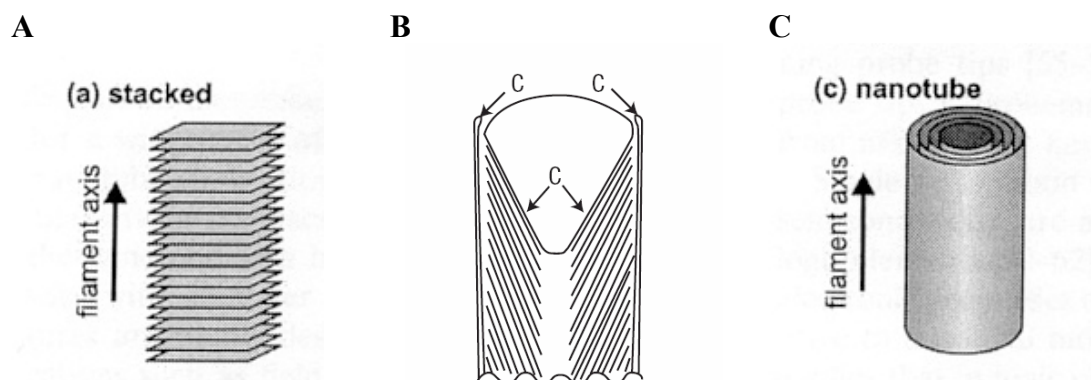


Figure 9 Different morphologies of Carbon filaments. A) Stacked (reproduced from [13]). B) Herringbone (Reproduced from [54]) C) Nanotube (reproduced from [13]).

Both the stacked and herringbone filaments are often classified as nanofibres. As can be seen the stacked form has the graphene layers normal to the filament axis, whereas the herringbone form graphene layers at an angle with the axis. Nanotubes are hollow and have the graphene layers parallel to the axis. Sometimes highly defective, more or less tubular structures are referred to as nanofibres instead of nanotubes. It has been proposed that the herringbone and stacked filaments are more easily synthesized when sufficient amount of hydrogen is available to satisfy the valences or dangling bonds at the cone edges. The herringbone or stacked cone structures are still mostly hollow and their graphene sheets normally form a small angle with the filament axis. Therefore they are sometimes referred to as multiwalled carbon nanofibers (MWCNF). In this manner we can separate them from graphitic carbon fibers (GCF) or vapour grown carbon fibers (VGCF) that are solid in the interior [55].

Electromechanical Properties of CNTs

Mechanical

The strength of the c-c bond is one factor making nanotubes one of the strongest and stiffest materials known. Young's modulus for both SWCNT ropes and MWCNTs has been estimated to be on the order of 1 TPa [13, 48, 56] and the tensile strength to 45 GPa [48]. This makes them stiffer and much stronger than steel. The strength of a CNT is furthermore strongly affected by defects in the molecular structure. Typically MWCNTs produced in a CVD process (low temperature) show a higher number of defects than MWCNTs produced by laser ablation and arc discharge.

Electrical

Carbon nanotubes can transport huge amounts of current. According to Collins et al [17] measurements show that a bundle of nanotubes one square centimetre in cross section could conduct about one billion amps. In comparison, copper burn out at about 1 million amps, one thousand times less. The conductance appears to be ballistic, even for several micron long tubes and at room temperature. This means that there is little dissipation in even long nanotubes and since the electrons move freely without scattering, the tubes can transport very high current densities. Even though it is not possible to define the resistivity for a ballistic conductor, the typical resistivity of nanotubes has been found to be about 10^{-6} Ωm [57, 58], and typical maximum current density is estimated at up to 10^9 Acm^2 [59-61]. In addition, the conductance depends on the degree of strain in the nanotube. Dai et al [62] have measured conductance versus strain and bending angle of individual SWNTs. In their experiments they found 2 orders of magnitude decrease in conductance at 14 degrees bending angle and 3 % strain. In addition to these excellent current carrying properties, the nanotubes also have a very high aspect ratio, making them excellent field emitters [63].

Synthesis of Carbon nanotubes

Introduction

Synthesis of Carbon nanotubes (CNT) can be done through three main approaches; arc discharge, laser ablation, and Chemical Vapour Deposition (CVD).

The first method discovered was arc discharge [4], where a voltage on the order of 20 V is applied between two carbon electrodes with a separation of 1 mm. This causes a direct current of 50-100 A to flow between the electrodes, vaporising some of the carbon, and re-condensation results in about 30% yield (by weight) of CNTs. The temperature in this process is above 3000 °C. The enclosure between the rods is normally filled with a low pressure inert gas, for instance helium or argon at 50-700 mbar. Because of different diffusion coefficients and thermal conductivities of different mixtures of helium and argon, the speed of the carbon and catalyst molecules varies. This causes a link between gas mixture composition and diameter of grown nanotubes. In addition, the anode may be doped with metal catalyst. The latter option will increase the yield of SWNT.

The second method is laser ablation [64]. Here the hot carbon gas is produced from laser pulses on a carbon target. Re-condensation produces primarily SWCNTs with a yield of 70 % or higher [58]. Also here the temperature is above 3000 °C. As for the arc discharge case, the atmosphere exists of helium or argon gas, and the pressure is kept around 500 Torr. From this method we get ropes of carbon nanotubes (SWNTs bundled together by van der Waals forces). There is no real big difference between laser ablation and arc discharge, and the reaction mechanism in both methods is thought to be the same. Also the optimum background gas and catalyst mix are the same. Laser ablation also needs doped electrodes in order to synthesise SWNT. Instead of pure graphite, a mixture of graphite and Co, Ni, Fe, or Y can be used. The

result becomes SWNT ropes with individual SWNT diameter between 1-2 nm, see Figure 10. Both arc discharge [4] and laser ablation [64] produce CNTs of high uniformity and quality. Graphitic by-products are also produced, which lowers the yield. Purification by oxidation or etching is therefore necessary afterwards.

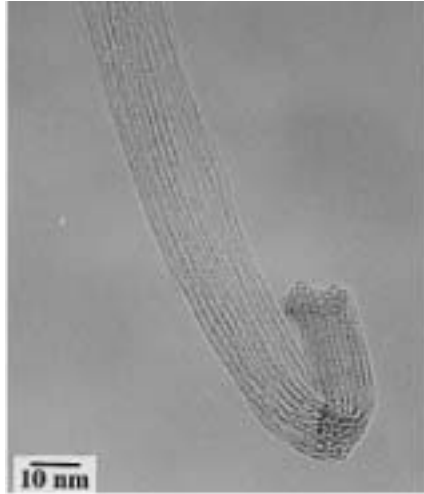


Figure 10 TEM image of a SWNT rope produced with laser ablation. (Reproduced from [50])

Neither arc discharge nor laser ablation can synthesise CNTs in-situ on substrates, due to the high process temperature. Chemical Vapour Deposition (CVD) on the other hand, can. CVD is therefore the method of choice for in situ integration of both CNTs and CNFs, and will be studied more in detail in the following subsections.

CVD – Chemical Vapour Deposition

The process

As mentioned, the CVD method is the only method capable of growing CNTs in situ on microsystems. A drawback however, is that the CNTs are often less perfect than those produced by arc discharge or laser ablation, and they are often all sorts of MWCNTS. The major advantage with CVD is that CNTs with high alignment and with great positional control can be synthesised. In addition both diameter and growth rate (and therefore height) can be controlled.

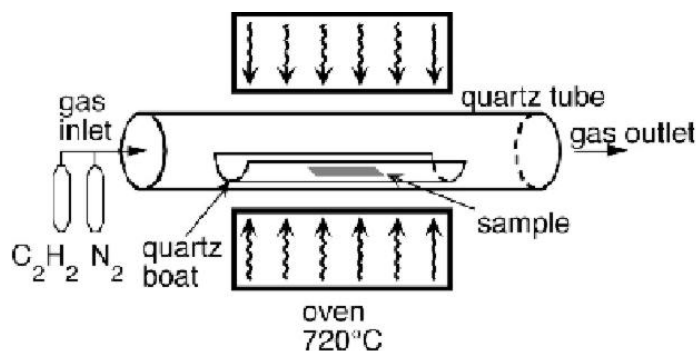


Figure 11 Typical CVD setup uses a heated quartz tube with the sample placed in the middle.

A typical setup for the CVD process is illustrated in Figure 11. A substrate is placed in the oven. The synthesis of CNT depends on a proper catalytic material being

present on the substrate. Normally this is a transition metal such as nickel, iron, or cobalt either deposited as nanoparticles on the substrate or as other structures on the micro scale. The process may take place in the temperature range from 600 °C to 1000 °C. Low process temperatures are between 600 and 750 °C, and high process temperatures in the range 850 to 1000 °C [65]. The oven is supplied with a steady flow of a carbon based gas, normally methane or acetylene [66]. The choice of carbon source may influence the resulting CNT structure. It has been found that the use of methane as the hydrocarbon source is critical to increase the yield of SWNT [65]. Usually there is a co-flow of either H₂ or Ar. During synthesis the carbonaceous gas is dissociated in a catalysis-enhanced thermal cracking reaction given as;



The reaction itself is constituted of three main parts. First we have the absorption and decomposition of hydrocarbon molecules on the surface of the catalytic nanoparticles located on the support surface. Second, the carbon atoms dissolve and diffuse into the interior of the nanoparticle to form a metal – carbon solid state solution [13, 50]. Third, the nanotube growth occurs when supersaturation leads to carbon precipitation into a crystalline tubular form. The size of the metal catalyst particle generally dictates the diameter of the synthesized nanotube. The process results in two modes that are controlled by the metal – support interaction. If the interaction is strong base growth will occur. The nanotube grows from the nanoparticle and the supply of carbon is from the base (interface with the anchored metal catalyst). The second mode occurs when the metal-support interaction is weak. This results in a detachment so that the catalyst particle lifts off from the support, resulting in tip growth. It seems to be important that the decomposition rate is not higher than the diffusion rate through the particle. If there are too many carbon atoms available, the excess atoms will accumulate on the catalyst particle and form graphene sheets. This effectively cuts off the carbon supply and the CNT stops growing. It is therefore crucial to balance the rate of the decomposition of the carbon bearing gas with the diffusion rate of carbon atoms through the catalyst particle. Both the catalyst composition and geometry are important for the resulting CNT structure. Not only is it observed that the catalyst diameter is strongly correlated to the size of the carbon nanotube [62], but the composition may even determine whether SWCNTs or MWCNTs are produced. For instance can addition of molybdenum in cobalt increase the yield of SWCNT tenfold [67].

Aligned CNT growth

If no electric field is applied to guide the growth direction of the CNTs, their directions will vary in a random way, only aligning themselves due to forces from other nearby CNTs (self-alignment). The self-alignment is caused by van der Waals interaction between the nanotubes. The tubes thus form a rigid bundle growing normal to the catalyst. This was demonstrated by Dai et al [65] where a catalyst array of squares resulted in the growth of square pillars of bundled MWCNTs as seen in Figure 12A.

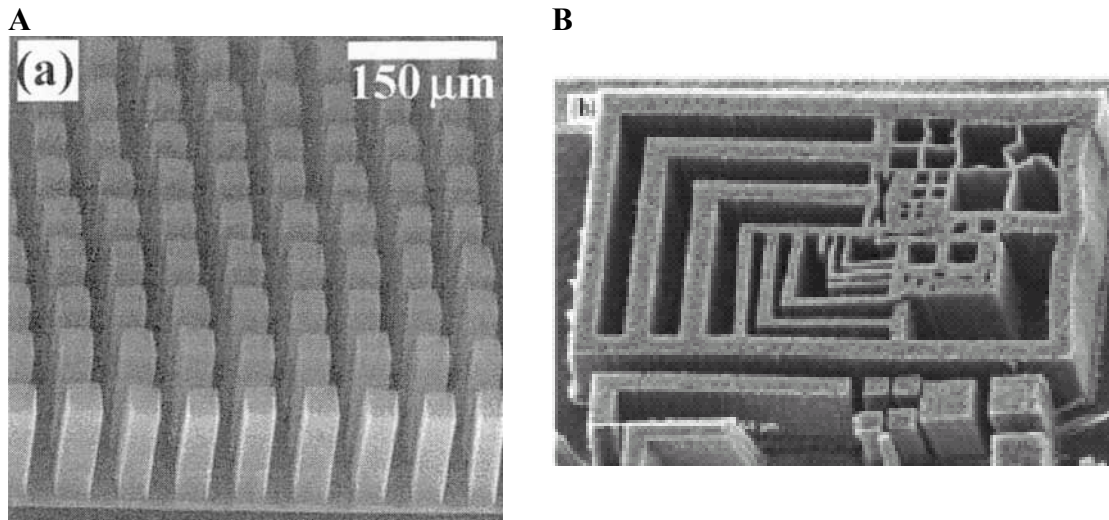


Figure 12 Bundled MWNT towers on top of square catalyst pattern (Reproduced from [65]) B) Bundled MWCNTs in complicated patterns (Reproduced from [68]).

There are mainly two routes toward aligned CNT growth in CVD. First, the catalyst pattern can be designed in a way that causes self-alignment, as was seen in with the CNT towers of Dai et al [65]. Another variation of that approach is to design microstructures in the substrate, which favours specific growth directions, or causes the CNTs to stick to opposing walls or pillars. Cassel et al [69] did just that when growing nanotubes on top of microfabricated silicon towers, as seen in **Error! Reference source not found.**

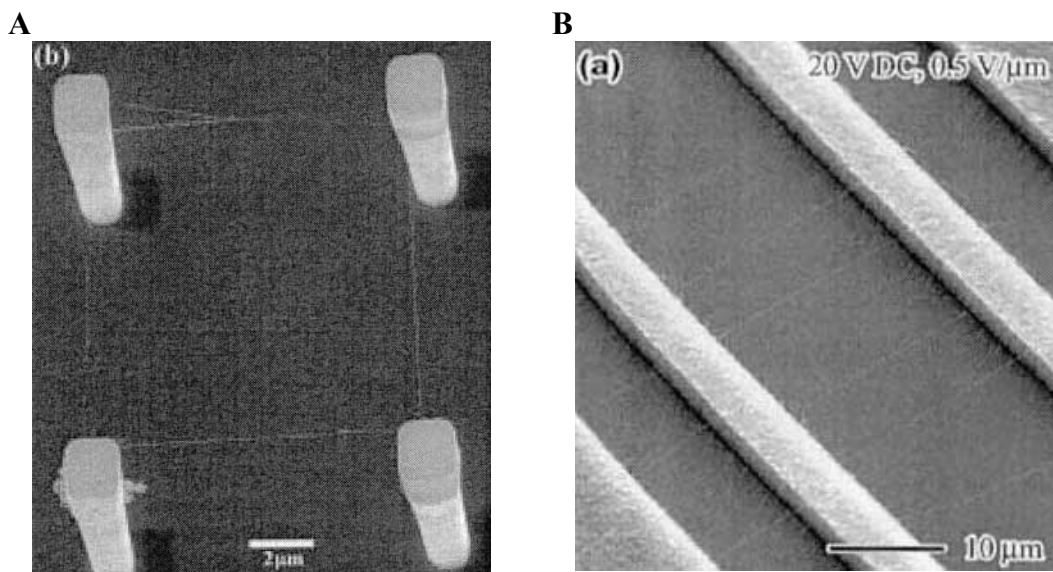


Figure 13 A) Carbon nanotubes suspended between silicon towers (Reproduced from [69]). B) Carbon nanotubes aligned during CVD growth by an applied electric field (Reproduced from [70]).

The second possibility for CNT alignment is the use of an electric field to guide the direction. Because of the dipole moment along the axis of the nanotube, they experience a force that aligns them with the electric field. During growth CNTs tend to vibrate due to the thermal energy. It has been shown that a 20 μm SWCNT, with a radius of 1 nm, will vibrate with a thermal vibration amplitude of 6.3 μm in a growth temperature of 900 $^{\circ}\text{C}$, whereas this is reduced to only 0.6 μm if an electric field of 1

V/ μm is applied [70]. Thus an appropriately strong electric field forces the CNTs to grow in the direction of the field. However, it is important to keep the nanotube at a distance from nearby surfaces, since the van der Waals forces are stronger than the alignment forces with the electrical field. **Error! Reference source not found.** shows SWCNTs, aligned using an electrical field, spanning the gap between electrodes [70].

PECVD – Plasma Enhanced CVD

The Process

In a PECVD process a plasma (an ionised gas) is generated by the use of dc, rf or microwave excitations of the present gas. PECVD gives aligned nanotubes of high yield and uniformity. The thermal CVD technique can also show vertical alignment of nanotubes. But in this case it is due to close-packing of the nanotubes and van der Waals interaction. Freestanding individual vertically aligned CNTs are only obtained through a PECVD process. The drawback of a PECVD process is that it tends to give CNTs of a poorer quality than a thermal CVD. The CNTs produced are often bamboolike in structure with many defects. They are therefore sometimes referred to as nanofibres or CNs. Methane and acetylene are common carbon feed gases, but the use of pure hydrocarbon gas may give substantial amounts of additional amorphous carbon (a-C) depositions, probably because the carbon feed gas is partly decomposed by the plasma. The a-C depositions can be avoided by diluting the hydrocarbon gas with argon, hydrogen, or ammonia, giving a hydrocarbon fraction of about 20 %. The addition of an etching agent, e.g. ammonia, in an appropriate ratio etches away the a-C but leaves the CNTs intact [29]. The plasma discharge produces a large amount of atomic hydrogen and different C_xH_y radicals. Those radicals decompose on the surface of catalyst particles at lower temperatures than more stable hydrocarbon species such as methane. Therefore PECVD allows CNT synthesis to be done at lower temperatures as well as it aligns the growth. The alignment of the CNTs is obtained from the electric field in the plasma sheath region. PECVD is a relatively new technique for producing vertically aligned CNTs, and was first demonstrated by Ren et al [71]. Today several PECVD techniques exist, like hot filament assisted PECVD, dc glow discharge PECVD, microwave PECVD, inductively coupled plasma PECVD and rf PECVD ([13] and references therein). These techniques represent different ways of generating the plasma. The rf PECVD method is able to synthesise CNs even at room temperature [54]. In our work we have used a dc glow discharge PECVD. The central part of the dc glow discharge PECVD chamber is illustrated in Figure 14A. A dc glow discharge PECVD consists of two electrodes, where the showerhead is the anode and the stage is the cathode. The cathode may require an independent heating source to achieve the desired growth temperature. This can be achieved with a resistive heater underneath the cathode. Alternatively a tungsten wire suspended in the plasma may serve as the heating source. This is called hot filament assisted PECVD. Plasma sheaths are formed at both electrodes, giving a plasma potential that is not the intermediate of the two electrodes but like the potential profile given in Figure 14B. It is important to note that the electric fields in this system only occur where there is a potential gradient. This is found exclusively in the plasma sheath regions close to the electrodes and the strongest field is found around the cathode.

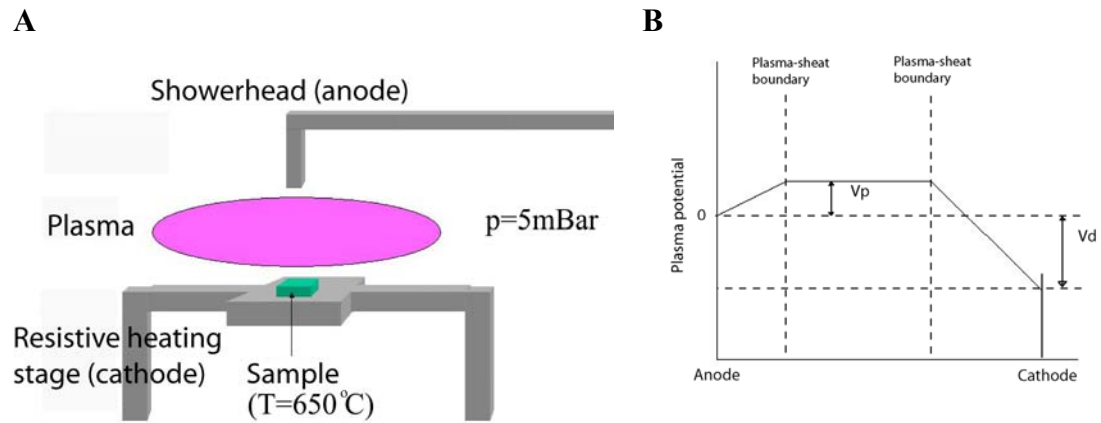


Figure 14 A) A dc glow discharge PECVD setup consists of a resistive heating stage (cathode), with an anode above. B) Illustration of the plasma potential between the anode and the cathode. The largest potential drop is in the plasma sheath around the cathode.

Plasma Physics

A plasma is a gas whose components are partially ionised. In the Plasma we find three species;

- Ions
- Electrons
- Neutrals

All species in the plasma resides in an electromagnetic field. On the macroscopic scale the total charge of the plasma is zero, giving us a neutral system. Therefore the electron density is given as the difference in positive and negative ions, which also is the definition of the plasma density.

$$n_{pl} \equiv n_i^{eff} = n^+ - n^- = n_e \quad (2.3)$$

The ionisation degree of the plasma is given as the ratio between all ions to the sum of the ions and the neutral constituents.

$$\eta = \frac{n^+ + n^-}{n^+ + n^- + n_o} \quad (2.4)$$

The typical ionisation degree for low pressure plasmas is from 0.01 % to 5 %. Every charge in the plasma creates a potential field. However, this potential field is screened by other charged species thus confining the Coulomb force range. This defines a characteristic length called the Debye length λ_D . The Debye length depends on the plasma density and the electron temperature T_e . At length scales L several times λ_D the plasma appears neutral. Furthermore, in time scales below 10^{-6} the ions are essentially fixed in their positions (due to their low mobility) and surrounded by a free electron gas. This is a situation similar to metals.

Correlation between catalyst and CNT growth

The PECVD process is catalytically defined. This means that the nanotubes will only grow where the catalyst is present on the surface. It has been shown by several research groups that the diameter of PECVD grown CNTs is strongly correlated to the amount of catalyst present. This is in particular evident for catalyst films, which gives forests of aligned CNTs, with the average diameter depending on the film thickness [61, 72], see Figure 15.

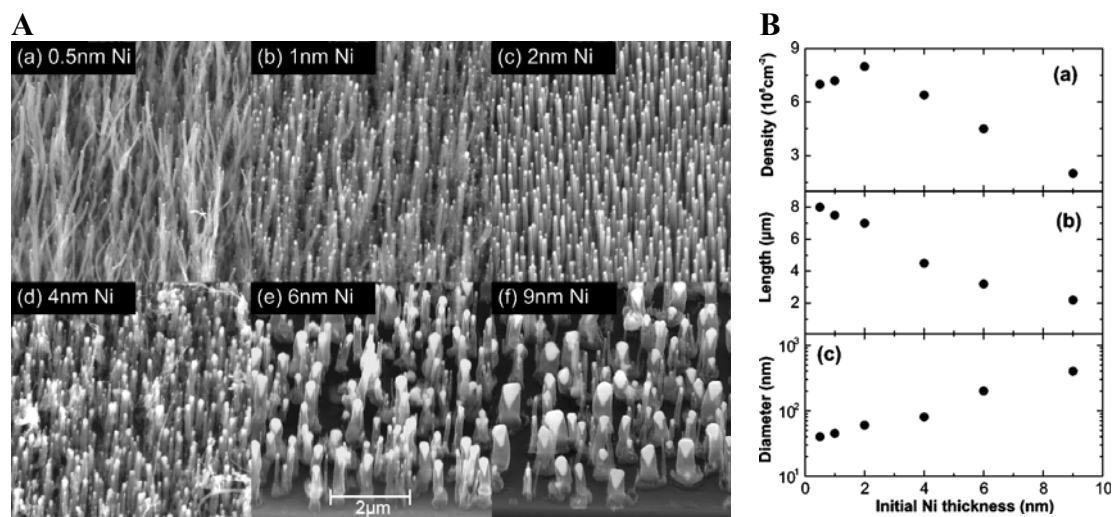


Figure 15 A) Nanotube growth on varying initial Ni thickness. From the nanotubes grown on 0.5 nm Ni to the ones grown on 9 nm, the CNT diameter increases from around 30 nm to 400 nm and the height decreases from about 8 microns to 3. The same growth conditions were used for all depositions (Reproduced from [72]). B) Plot of average a) nanotube density, b) nanotube length, and c) tube diameter as a function of the Ni thickness (Reproduced from [72]).

During heating the catalyst film breaks up into small particles due to surface tension and compressive stress due to the mismatch of the thermal expansion coefficients of Si and Ni. The size of the particles depends on the initial thickness of the metal film. Interestingly, it was shown by Chhowalla et al [72] that not only did the diameter of the resulting CNTs depend on the nickel thickness, but also the length and the areal density, as seen in Figure 15. The correlation between length and both growth time and pressure, was found to be close to linear with the nickel thickness. Other important parameters in the PECVD growth are the gas composition and temperature. It has been shown that a substantial co-flow of an etchant gas, for instance ammonia, is needed in order to synthesise CNTs of high quality. It has been shown that an acetylene content of 20-30% is optimal [29, 72, 73], as seen in Figure 16A.

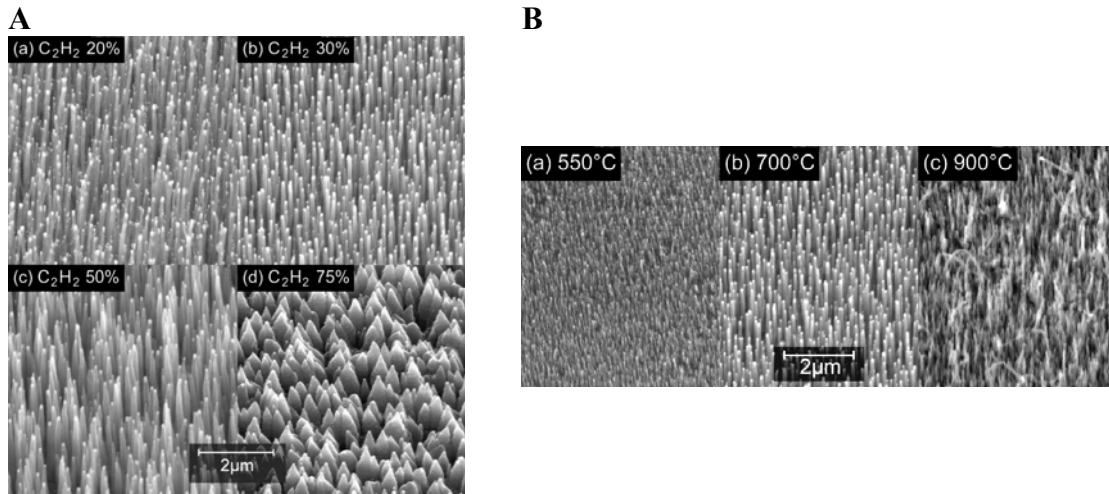


Figure 16 A) Nanotubes grown at different acetylene concentrations (the ammonia flow was kept constant while varying the acetylene flow). B) Carbon nanotubes grown at different temperatures under otherwise equal conditions. (reproduced from [72])

Furthermore, as can be seen from Figure 16B the growth rate is lower for low temperatures around 550 °C. At medium high temperatures around 700 °C the nanotubes are well aligned and uniform in size whereas higher temperatures give nanotubes that are disordered [72]. Characterisation of the PECVD grown CNTS by TEM reveals that they are far from perfect in morphology. They are quite bamboo-like in structure although the tubes deposited at medium temperatures around 700 °C have less defects.

Diffusion barrier

Diffusion barrier. A diffusion barrier is necessary to prevent the diffusion of nickel into the Si substrate which occurs at temperatures above 300 °C. SiO₂ and TiN are examples of such diffusion barriers [74]. The nickel catalyst is easily detached from the diffusion barrier layer giving rise to a tip growth process [73]. A typical thickness of a barrier layer is 10 - 20 nm.

Carbon nanotube uniformity

For most applications the reproducibility is important. For PECVD grown vertically aligned arrays from thin film catalyst the growth conditions should be very similar. However, this depends on the catalyst preparation. If the nanotubes are grown from a thin film or a catalyst line, the catalyst tends to agglomerate into catalyst nanoparticles of different sizes. If the dots are accurately defined, by EBL for instance, the size variation very small. Teo et al showed that CNT growth from nickel dots 100 nm in diameter and 7 nm thick gave growth of individual CNTs of small size distribution [75]. Furthermore, Teo et al found that dots smaller than 300 nm in diameter (7 nm thick) tended to give only one individual CNT (in 88 % of the cases), whereas several CNTs with various sizes was catalysed by larger dots, see fig XX.

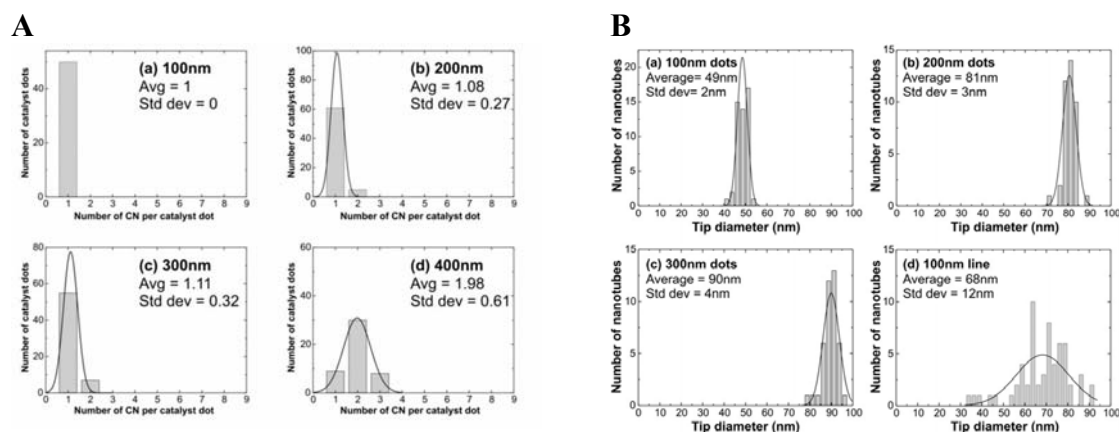


Figure 17 A) Histograms showing the occurrence of different number of CNs nucleated as the catalyst dot size was varied from 100 nm to 400 nm (Reproduced from [75]). B) Distribution in CN diameters from a) 100 b) 200 and c) 300 nm catalyst dot sizes. The distribution from multiple nanotubes nucleated from a 100 nm wide catalyst line is provided in d) (Reproduced from [75]).

The main observation is that the nucleation of multiple CNs from a large catalyst dot is a process with a significant degree of statistical spread in terms of number, height and diameter. But for smaller dots giving single CNs (100 % yield for 100 nm dots), the uniformity is much higher showing a standard deviation in diameter and height to be 4.1% and 6.8 % respectively.

Various groups have been preoccupied with exploring the controlling parameters for PECVD-CNT diameter, height, morphology and so on [14, 29, 72, 75-77]. Work has also been done investigating the control of the inclination of the CNTs with respect to the substrate [78-80].

3 Integration of CNs in microsystems

Introduction

Position controlled growth of CNs on cantilevers or other types of microsystems, requires two main conditions to be fulfilled;

- It must at all be possible to grow the CNs on the materials involved.
- Methods to deposit the catalyst material in the desired pattern must be available.

This chapter will mainly focus on the first condition. Here, the compatibility of CN growth with the microsystems will be investigated. It also involves growth condition control and the applicability of the CNs as components in microsystems. The second condition, precise placement of catalyst material, will be explored in chapter 6. In the present chapter, simple techniques for catalyst deposition are used, resulting in catalyst films synthesising forests of CNs.

CN growth on cantilevers

The substrates

The substrates are microprobes fabricated via conventional microfabrication techniques in silicon and oxide [36, 37]. The probes have oxide cantilevers protruding from their front. An illustration of such a microprobe, here a four point probe, can be seen in Figure 18 A.

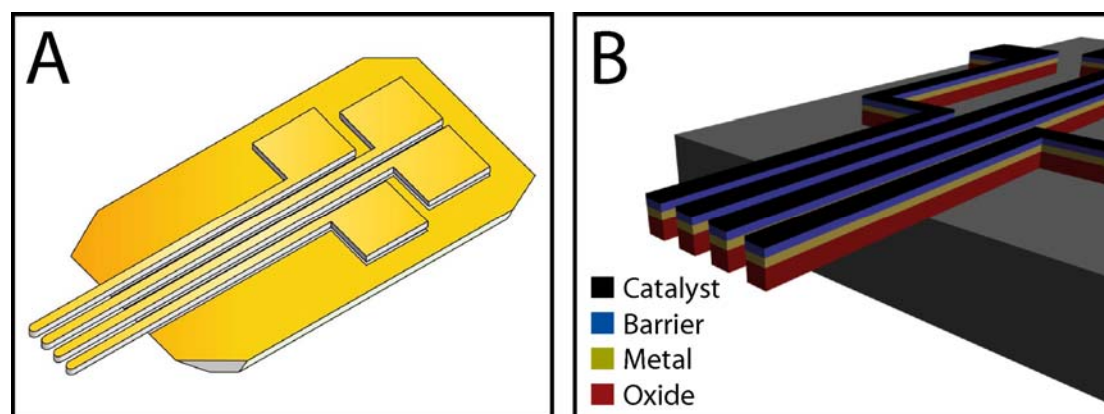


Figure 18 A) An example of the microprobes used as substrate for CN growth. Structures on top of the silicon chip are fabricated in SiO₂. B) Illustration of the layering of thin films on top of the microprobes.

A variety of microprobes differing both in terms of geometry and material composition, were chosen for preparation for CN growth by PECVD. While most microprobes had pure oxide cantilevers, a series of microprobes with metal coated cantilevers were also prepared. Here, 100 nm of either gold, silver, or wolfram was deposited by e-beam evaporation. See Figure 18 B for a sketch of the layering on top of the microprobes. The pre-treatment consisted of deposition of a diffusion barrier layer by sputtering. A diffusion barrier is necessary to prevent the diffusion of nickel

into the Si substrate or the metal that may occur at high temperatures [13]. Commonly used diffusion barriers are SiO₂ and TiN [74, 81]. In this sputtering of a SiO₂ target was used to deposit the barrier layer. Since the sputtering was done in pure argon plasma, the deposited barrier layer became SiO_{1.4} which is a conducting silicon oxide [82]. In the examples here where this barrier layer has been used, the thickness has been 20 nm. After barrier deposition the catalyst are deposited. Here nickel in various thicknesses between 2 and 16 nm has been used.

PECVD growth

The process and results

Direct Current PECVD (DC-PECVD) was used to grow the CNs on the substrate. The growth was performed with acetylene (C₂H₂) as carbon feed gas and ammonia (NH₃) as co-flow, at a chamber pressure of 5 mbar and a temperature of 650 °C. The main role of ammonia is to act as an etchant to avoid depositions of amorphous carbon (a-C) on the synthesised tubes which would make them cone-shaped, or elsewhere on the substrate as a carbon film [29]. A discharge voltage of -600 V initiated the plasma necessary to facilitate the dissociation of the carbonaceous molecules. During the heating the Nickel film breaks up and agglomerates into many small nanoparticles, which each become a catalyst particle for a single CN [72] (see Figure 19). Bulk nickel has a melting point of 1450 °C, so the breaking up of the film is controlled not only by the temperature, but also of the surface energy, which is sought minimised. The nickel catalyst is easily detached from the diffusion barrier layer giving rise to a tip growth process [83].

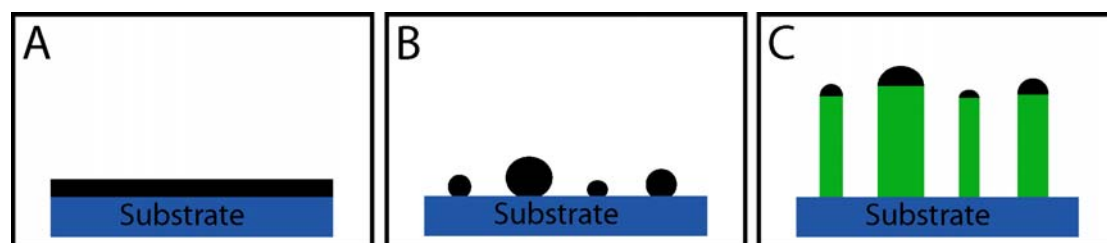


Figure 19 A) A substrate with barrier layer, having a thin nickel catalyst film on top. B) During heating above 500 °C the nickel film breaks up and agglomerates into small particles, with a small size distribution. C) During PECVD synthesis, each catalyst particle synthesises one single CN.

It is important to investigate which substrates are compatible with the PECVD growth of CNs. The PECVD growth process was found not to damage the SiO₂ cantilevers, which has a melting point of 1700 °C, as can be seen in Figure 20. However, not all metals are suitable for forming leads since both the gold and silver thin films break up and agglomerate into chaotic patterns due to the high temperature. This happens in spite of the growth temperature (~650 °C) being considerably lower than the macroscale melting point of both gold, 1063 °C, and silver, 961 °C. The break up process is driven by a minimisation of the surface energy. As expected, the samples with tungsten as leads were found to be undamaged by the growth process. Tungsten has a very high melting point at 3410 °C, preventing even the thin film from breaking up. Other potential candidates for forming leads exists, such as other metals with sufficiently high melting point (for instance molybdenum) and other conducting materials such as ITO, TiN, and TiW.

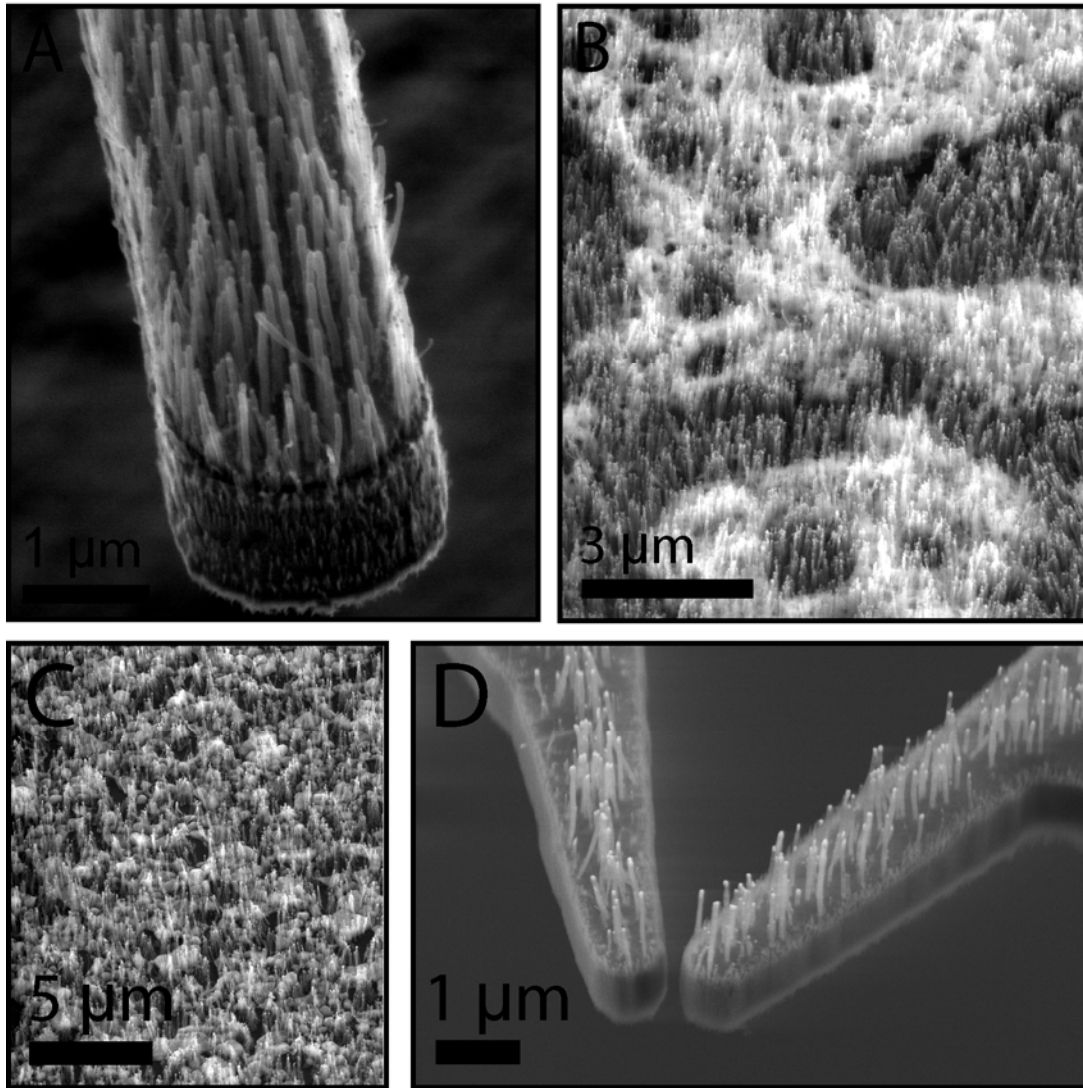


Figure 20 A) CNs grown on an oxide cantilever without metal layer are seen to be well defined. B) On substrates with 100 nm gold the CNs still grow, but the gold breaks up during the PECVD process, thus ruining the leads. C) On silver coated probes, the same behaviour is observed. D) CNs grown on cantilevers with Wolfram as the metal lead material are seen to grow well defined, and the metal layer is not destroyed during PECVD growth. All cantilevers here had also a barrier layer between the substrate and the catalyst.

Effect of catalyst film thickness

As has been shown by several other research groups, the thickness of the catalyst film influences strongly the resulting CN growth [72, 84]. All of these tests have been made on planar surfaces, and, although a similar correlation for CNs grown from catalyst films on top of cantilever structures can be expected, we have verified that these correlations indeed seem to hold for the cantilever growth as well. The length diameter and density are governed by the thickness of the catalyst [13, 72]. The rate of heating of the substrate before deposition starts may also affect the diameter and density distributions [13] – a slow heating allows the catalyst particles to agglomerate into larger particles thus giving a sparser forest of CNs of larger diameter. Figure 21 shows a series of SEM pics of CNs grown on cantilevers from a nickel catalyst layer of thickness 2 nm to 10 nm. It may be observed that the CN diameter become larger

with increasing catalyst thickness. We also note that the height of the CNs seems to be smaller for thinner films.

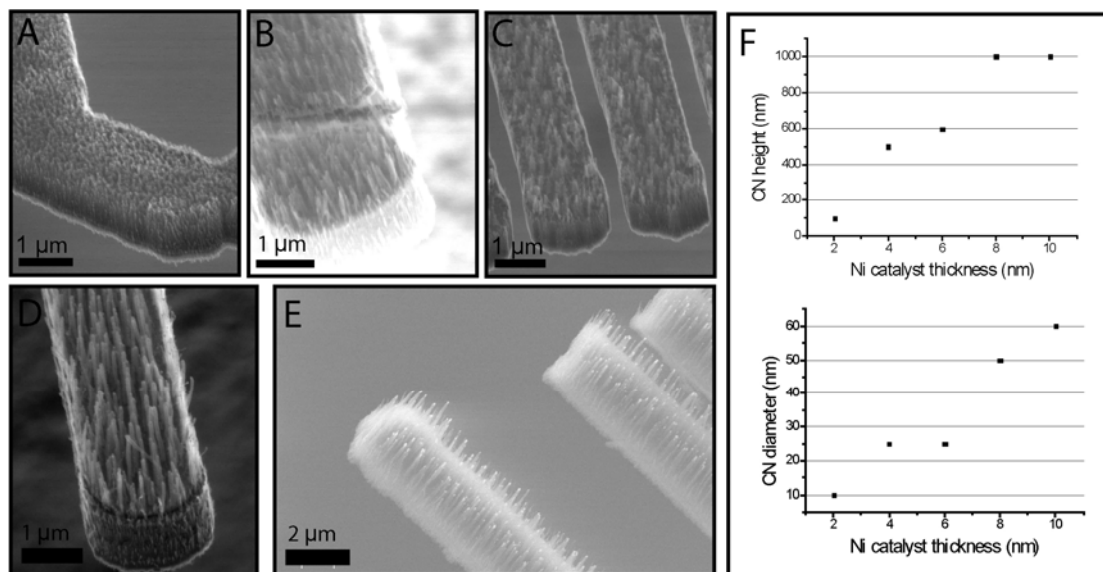


Figure 21 Sem images of MWNT synthesised in PECVD from a nickel thin film layer of A) 2 nm B) 4 nm C) 6 nm D) 8 nm E) 10nm. The deposition time (PECVD) was 15 minutes. F) Plot of the CN height and diameter as a function of nickel thickness.

The data in Figure 21F have been drawn from a study of a few SEM images. The samples were all oxide cantilevers without metal coating, however the samples have been grown in different PECVD runs, which may influence the results. The conclusion that can be drawn is that the diameter of the CNs is strongly correlated to the nickel catalyst thickness – giving smaller diameter for thinner layers. The CNs also tend to become shorter for thinner catalyst layers.

Mechanics of PECVD grown CNs on microprobes

The mechanical properties of CNs have been extensively studied and it has been shown that CNs are extremely strong and highly flexible at the same time [47]. In order for the in situ grown CNs to function as probe tips or electrodes, the mechanical strength is important. But perhaps more important is the attachment strength to the surface. In the present section the feasibility of CNs as probe tips will be investigated.

The experimental setup uses either an STM tip of wolfram or an AFM tip mounted on an XYZ manipulator, from Klocke Nanotechnik, inside a SEM. With this equipment it was possible to approach even single CNs and bend them. Figure 22 shows such an experiment, where an AFM tip is bending a single CN tip protruding above the CN forest.

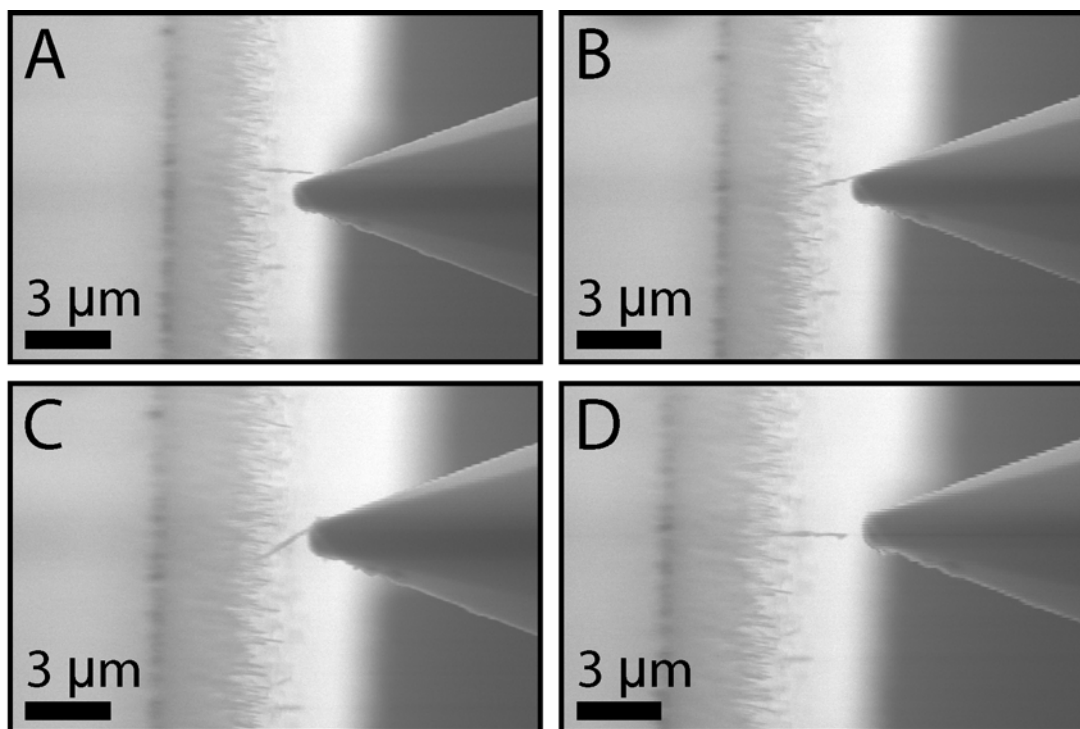


Figure 22 A series of SEM images that show a CN being manipulated by an AFM tip (used passively as a poking instrument). **A)** The initial approach. **B)** Contact between AFM tip and CN accomplished, slight bending of CN. **C)** Large deflection of the CN can be seen just before CN snaps back to its initial position as shown in **D)**.

It is seen, from the series in Figure 22 A-D, that a single PECVD grown CN on top of the oxide structure can be bent more than 45° without breaking or releasing from the substrates. In fact, at this bending the CN slips on the side of the AFM tip, and return to its initial position without any visible damage, as seen in Figure 22 D. If the AFM tip was pushed slightly into the CN forest, and then moved horizontally above the CN forest, it was seen that the AFM tip bent up and down with amplitude of about 400 nm as it encountered different resistance in the CN forest, but no visible damage was observed on the nanotube forest.

However, AFM pictures of this surface are not easy to make. An effort was made to measure differences in frictional force on the surface, dependent on the CN inclination. Measurements were made with a lateral force AFM in contact mode, but the AFM images obtained were of poor quality due to the mechanical flexibility of the CNs. Upon inspection with SEM afterwards, it was discovered that the areas scanned by AFM were severely damaged, as can be seen in Figure 23. Also depicted in Figure 23 D and E, is a SEM study of an AFM cantilever being pushed strongly into the CN forest. It is seen then that the CNs are permanently removed from their initial positions, enabling us to draw patterns in the CN forest. Our results indicate that the CNs are fairly well attached to the substrate surface and that they may sustain a moderate force exerted on them before breaking off. However, there is a limit where the CNs become permanently damaged by detaching from the surface.

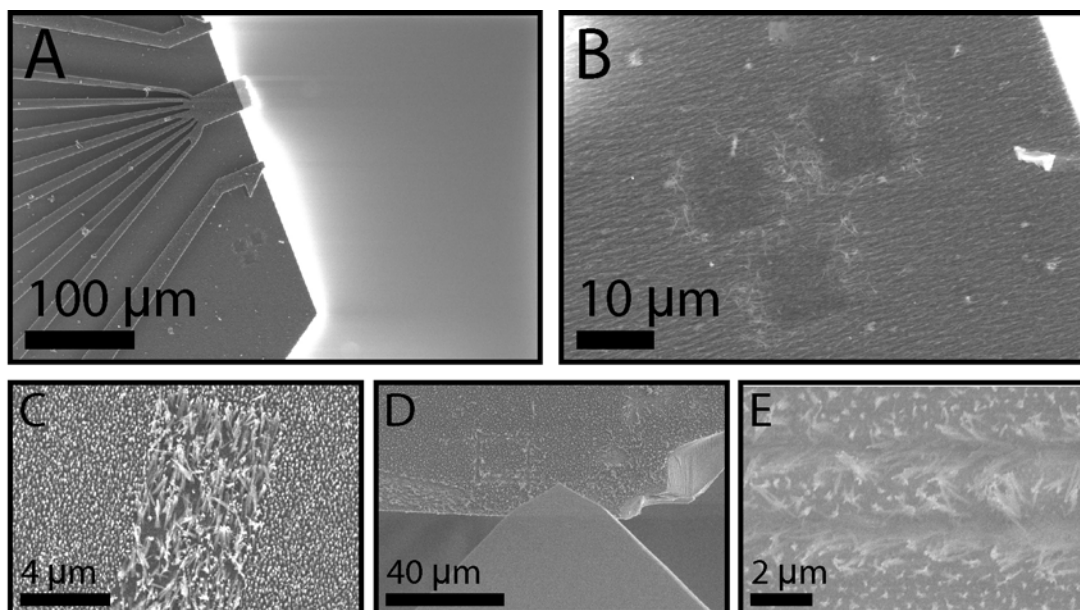


Figure 23 A) A microprobe with inclined CNs. Here three AFM scans have been made just to the right of the cantilever structures. B) A close up of the region shown in A, reveals that the CNs in this area have been partly released from the substrate. C) On another substrate with vertical CNs similar damage is found. D) An AFM tip mounted on an XYZ manipulator within a SEM is used to draw a square in the nanotube forest. E) A close up of the lines in the square, shows CNs bent away from the trace. It is difficult to say whether the CNs were detached from the surface in the process.

Pick and place with CN probes

Pick an place of objects on the micro- and nano-scale is extremely difficult due to the strong adhesion and stiction forces [85]. CN covered probes were tested as pick and place tools, using the same experimental setup as explained above. A pick and place manipulation sequence is shown in Figure 24. Here the CN covered cantilever can be seen to pick up the particle resting on top of the nanotube forest on the opposing surface. It is also seen, that if the CN covered probe is pushed hard into the substrate forest, and then pulled downwards, the CN forests on both surfaces become severely damaged.

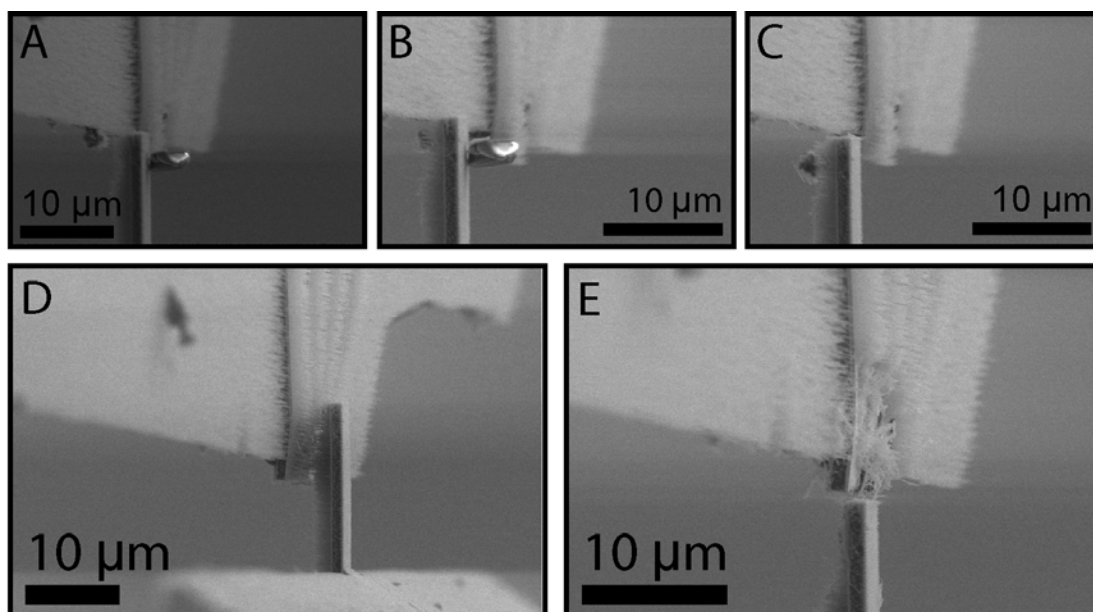


Figure 24 A-C) A cantilever with nanotube forest is approached to a dust particle and picks it up. D) Two microprobes with forests of CNs on them approach each other. Vertical penetration of the forests shows little or no damage to the forest. E) Probes are squeezed well into each other vertically, for then to be dragged horizontally from each other – resulting in major damage to the CN forests on both cantilevers.

Electrical properties

Introduction and Experimental setup

The electric properties of CNTs have been extensively studied. Important studies were done in 1992 showing that CNTs could be both metallic and semiconducting [44, 45, 86]. It was soon shown that these tubular structures of graphitic carbon had exceptional electrical properties. They may for instance carry extremely high current densities. Work on CNTs as field emitters started in 1995 by Rinzler et al [49] where they showed that CNTs are among the best candidates for field emitters due to their extremely low turn-on field and high current density.

It is desirable to have electrical contact to the CNs on the cantilevers in order for the electrodes to work as for instance probes for surface conductance measurements. We designed an experimental setup to measure both the conductance properties and the field emission properties. The set up consisted of a homemade STM tip controlled by a high precision xyz manipulator with possible step resolution down to about 50 nm. The STM tip was etched in KOH from a 0.5 mm tungsten wire prior to the electrical tests [87]. It is important that the tips are freshly etched to avoid surface oxidation. In the SEM the STM tip was approached to the microprobe surface covered in vertical PECVD grown CNs, see Figure 25. By careful manoeuvring the xyz manipulator, it was possible to obtain contact with a few or an individual CN at a time.

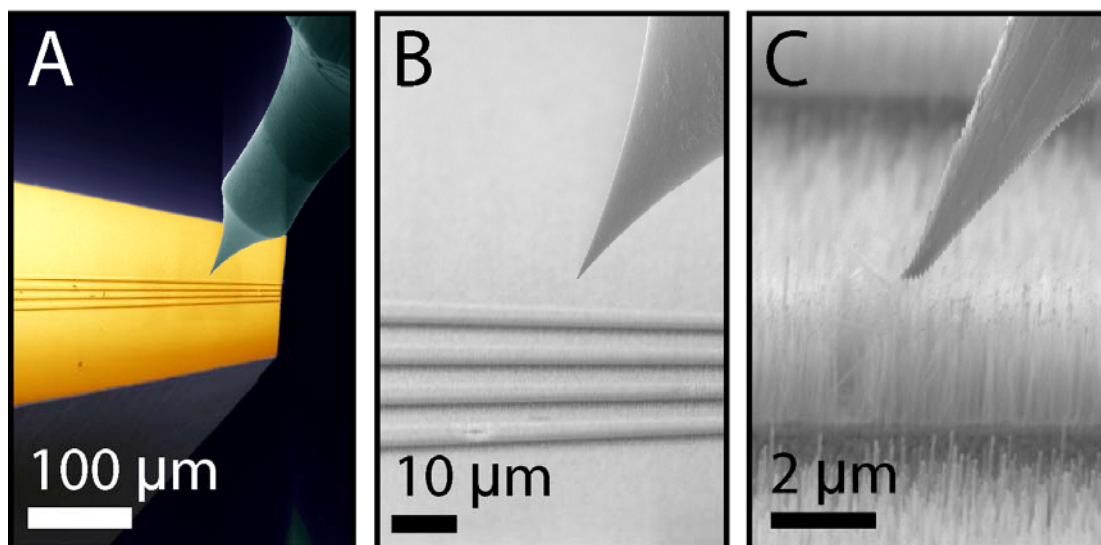


Figure 25 A) SEM picture of an STM tip approaching the substrate. B) SEM picture of a substrate used for electrical characteristics. C) The CNs can be seen to have a length of 2-2.5 μm .

Electrical resistance and field emission of the CNs

The electrical resistance and the field emission properties of a CN forest on microprobes were measured. The CNs had a diameter of about 100 nm and lengths in the range 2-2.5 μm , as shown in Figure 25 C. The density of the CNs is estimated to be around 10^9 tubes/ cm^2 , corresponding to 10 tubes/ μm^2 . This density corresponds to what Teo et al [88] referred to as dense forests. The sample had been grown on a micro four point probe with 8 nm nickel as catalyst. The probe had an initial layer of 100 nm W and 20 nm $\text{SiO}_{1.4}$. In the experiment an STM tip was used as the anode, whereas the nanotube forest worked as cathode, where the electrons are emitted from the CN tips. Figure 26 A shows an STM tip touching the CN in front of the tip. After electrical measurement the CN is burnt off, as is seen by the shortened CN in B. The resistance was found from fast I-V sweeps from 0 to 15 V, which resulted in the CNs being burnt over before the higher voltage was reached. A typical I-V measurement is shown in Figure 26 C, where the burn off voltage was around 2.5 V. The resistance of the CNs were measured to be of the order a few tens of $\text{k}\Omega$, ranging from 3 $\text{k}\Omega$ to 200 $\text{k}\Omega$ in our measurements, as can be seen in Figure 26 D. Corresponding burn off voltages are shown in Figure 26 E. Common resistance values found elsewhere for CNs are normally in the range of 5-10 $\text{k}\Omega$ [89]. Our mean value of 26 $\text{k}\Omega$ (excluding the highest measurement) is somewhat higher and may be caused by an increased contact resistance caused by the measurement technique. After all, the STM tip and the CNs are just touching each other, and, together with the vibrations in the system, this may not be a stable low resistance contact. The important result is, however, that we have electrical contact to the in situ grown PECVD CNs on microprobes.

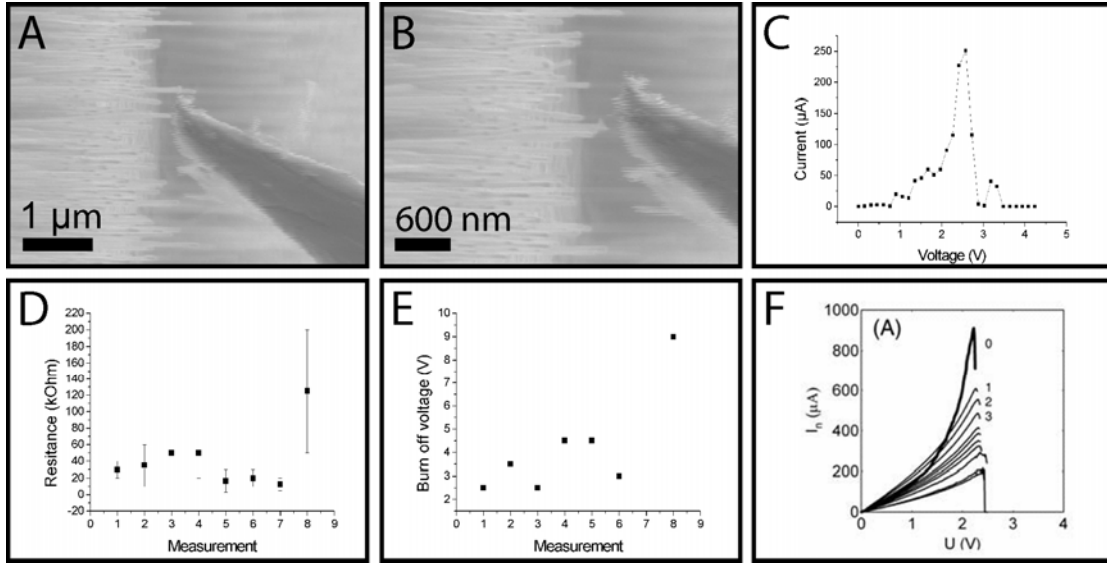


Figure 26 A) An STM tip is just touching a single CN. B) The CN is burnt off during I-V sweep. C) A typical I-V sweep. D) CN resistance measured on 8 different CNs. E) Corresponding burn off voltages to the measurements in D. F) I-V sweeps on CNTs obtained by Dohn et al [89], using a 4 point probe (Reproduced from [89])

The I-V plots show some resemblance with measurements on CNTs obtained by Dohn et al [89] and reproduced in Figure 26 F. Those measurements were obtained through pushing a four point probe down on the CNTs. Both methods show burn off voltages around 3 volts and burn off currents on the order of a few hundred μA .

By using the same experimental set up as described above, we could also successfully measure field emission on a local area on the microprobe. Again, with careful manoeuvring of the xyz manipulator, the STM tip could be placed in a very short distance from the tips of the CN forest. This step introduces some uncertainty, since it is difficult to estimate the precise distance from the STM tip to the field emitting CNs. The Fowler Nordheim theory treats the correspondence between field strength E and emission current I . The Fowler Nordheim plots are based on a modification of the Enhanced Fowler-Nordheim equation for total current. In the plot $\ln(I/E^2)$ is plotted as a function of $1/E$;

$$\frac{I}{E^2} = \frac{CA}{\Phi} \beta^2 \exp\left(-\frac{B\Phi^{\frac{3}{2}}}{\beta E}\right) \quad (3.1)$$

In a Fowler-Nordheim plot we would expect to find a linear portion that allows estimation of the field enhancement factor β . The field enhancement factor is a correction in the field strength, which is mainly due to the geometrical shape of the CNs, which has a very high aspect ratio [90]. However, the calculation of β is also dependent on the estimate of the distance between the anode and cathode (which basically defines the field strength). We aimed at a distance of about 400 nm between the STM tip and the CN tips through visual inspection in SEM, and this distance was used in the calculations. A negative bias was applied to the microprobe with CNs, so that the field emitted electrons would be emitted from the CNs and not the STM tip. Examples of the field emission data obtained may be seen in Figure 27. The plot in B

shows that the I-V sweeps exhibit the characteristic linear field emission portion in the Fowler-Nordheim plots. Values from 50 to 2000 cm^{-1} were obtained for the field enhancement. The uncertainty is large due to the experimental setup. Values reported elsewhere are around 700-1200 cm^{-1} [21, 74, 91]. The experiments show that it is possible to use PECVD CNs grown in situ on microprobes as field emitters. As mentioned earlier, the β value is dependent on the estimate for the anode – cathode distance. The relation varies in a linear way which is seen from the factor βE in the Enhanced Fowler Nordheim formula. Clearly, a too low estimate of the field strength E (based on the estimated distance between the cathode and anode) will result in a higher β value. The factor is highly dependent on the density of the CN forest, with higher density showing lower enhancement effect due to shielding effects between the nanotubes [88].

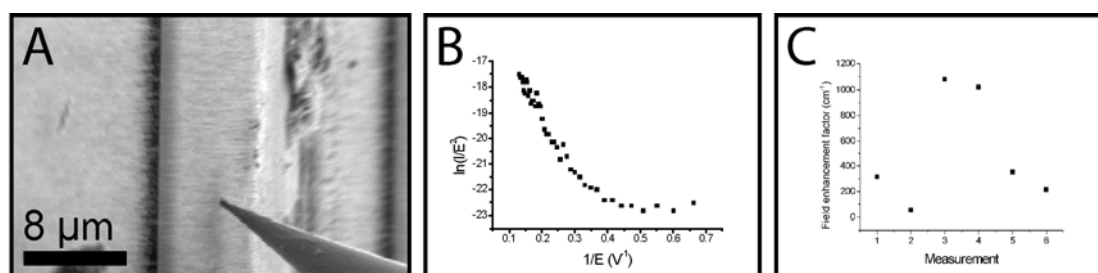


Figure 27 A) The STM tip is placed very close to the nanotube forest. B) Fowler Nordheim (F-N) plot for a successful field emission measurement. Field emission occurs in the linear portion to the left, from which the field enhancement factor β can be estimated. C) β values between 50 and 2000 cm^{-1} was found. The large variation is probably due to the measurement technique.

Electrical field alignment

Introduction

In a PECVD system, the electrical field in the plasma sheath region guides the growth direction of the CNs. Electrical field lines are always perpendicular to the surface on conductive materials. In free space, or dielectrics, they may bend and become distorted due to geometrical constraints such as inner and outer corners on conductive materials nearby. Recently it has been shown that it is possible to grow CNs with an inclination angle different from the vertical in local areas [27, 78-80, 92, 93]. CNs on conductive surfaces will always be aligned parallel to the surface normal. A material with a low conductivity will not affect the directions of the field lines substantially, and thus may have inclined field lines on the surface depending on the shape of and distance to conducting geometrical features. It is believed that the field alignment in the PECVD process is mainly caused by the catalyst particle in the tip of the CN [30, 94]. Merkulov et al [80] showed that it is possible to obtain inclined growth by placing the substrate in the immediate proximity of the sample holder edges. In this region the electric field lines accommodate the corner of the sample holder by bending sharply after leaving the conductive sample holder. Since the sample has a finite height (typically 350 – 500 μm for a Si Wafer), the field lines that leaves the sample surface in the vicinity of the sample holder corner will have an inclination angle different from 90° , and thus give rise to inclined CN growth. A problem with this method is that the edge effect drops off rapidly, and for distances larger than

about 1 mm the CN orientation to the surface normal is already below 10° (e.g. the inclination angle). Control of inclination could be a route towards making microsystems with highly customised surfaces. It should be possible to control the growth direction of the CNs with the electric field by imposing an electric field that is inclined to the substrate. In this subchapter we work with local distortions of the electrical field to grow CNs with various angles on microprobes, on plane silicon chips, and inside microchannels fabricated on silicon wafers.

On microprobes with cantilevers

The setup consisted of a small graphite block with trenches and holes. During PECVD synthesis, the microchips, with SiO₂ cantilevers, were positioned in these trenches, as shown in Figure 28 A, with the probe tips extending slightly out from the trenches. The graphite block with the microchips was then put on the ordinary growth stage. Since the probe tips effectively were tilted in the plasma sheath region, the synthesised CNs grew inclined with respect to the cantilever surface, as seen in Figure 28 B and C. The inclination angle was measured to around 40° , corresponding to the angle of the sample during deposition.

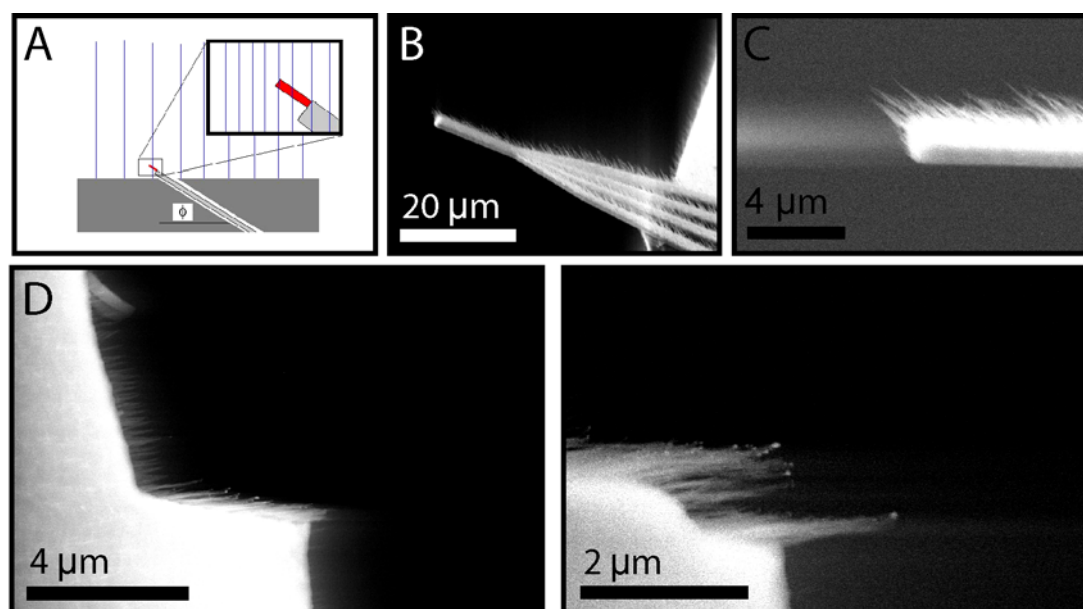


Figure 28 A) Estimated field lines around inclined microprobes during the PECVD process. Field lines are undisturbed by SiO₂ cantilevers which are non-conducting, thus giving rise to inclined CN growth. B) Inclined CNs on a microprobe. C) A close up of the inclined CNs on the cantilever. The inclination angle can be measured to about 40 degrees. D) Lateral growth of CNs. The sample was placed sideways in the holder, giving CNs growing to the right in the image. E) A close up of the tubes shown in D, reveals that they have catalyst particles at their tips.

In Figure 28 D and E inclined CNs on another microprobe which was placed sideways in the holder are seen. Here, the CNs point upwards, thus extending out of the right hand side of the probes as can be seen in Figure 28 D and E. Interestingly, Figure 28E shows that the CNs have the catalyst particle at the tip. In general, the morphology of these inclined CNs seems to be different than was seen for the morphology of the CNs grown vertically on microprobes. The cylindrical structure is not clear, and it is generally difficult to spot an individual catalyst particle at the tip of each CN (see Figure 29A and B). The difference in morphology may be due to a different

temperature, since the substrate in the inclined case was placed on an extra graphite holder, with the tips protruding slightly out from this. Figure 29C and D shows CNs that are inclined with a homogenous angle all over the probe tip, thus comprising an inclined forest of CNs. The CNs on this particular chip were inspected with TEM. The analysis revealed that the CNs had a very irregular shape, with many secondary CNs extending from the main fibre (see Figure 29E to H). It also showed that the CNs had graphitized planes running along the length axis of the CNs, but they did not appear to have a hollow core, and thus not a tubular structure.

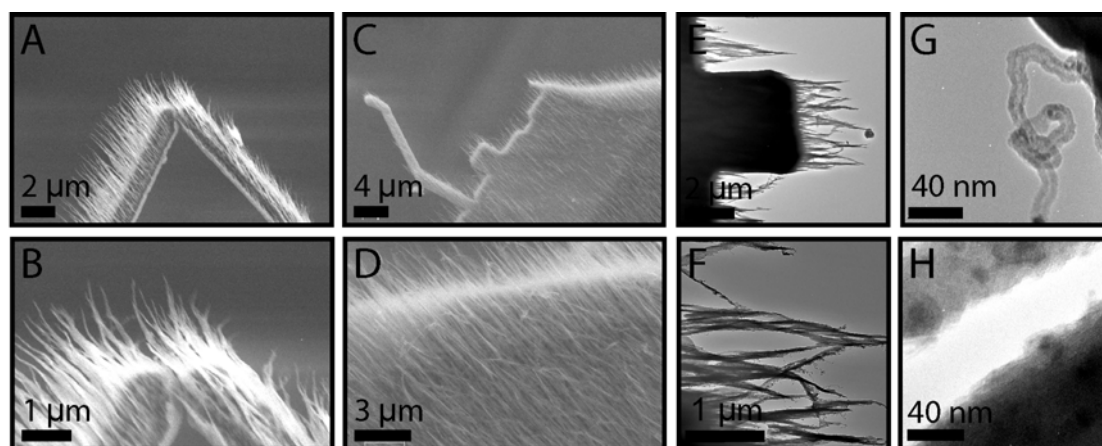


Figure 29 A) Inclined growth of CNF on microprobe. B) A close up shows that the CNs seem to be fiber like. C) Another microprobe with similar CNs grown D) A close up of the CNs on the probe shown in C. Also here the CNs appear to be quite long and thin, almost hairlike, without an apparent catalyst particle in the tip. The CNF can be seen to grow towards the upper left corner, which corresponds to the anticipated direction of inclined growth. This is not an effect of stage tilting in the SEM. E) TEM picture of CNs on the same microprobe as shown in C and D. F) A close up shows that the CNs are not tubular, but rather fiberlike. However, small secondary CNs appear to extend from the larger fibres. G) A close up of a secondary CN. These seem to be more tubular in shape. H) A large magnification picture of the fiberlike structures reveals that graphitized planes exist along the axial direction of the fiber. The void space in the middle is here between two fibers.

It is a goal to grow a precise number of CNs in precise locations on the cantilevers. In these initial investigations, the catalyst was not deposited precisely on the cantilevers, but rather through the deposition of a catalyst film. However, tip growth was attempted on a few probes by placing them vertically during catalyst sputtering and PECVD synthesis. Examples of CNs grown in this way are shown in Figure 30. The structure of the CNs appear to be rather poor, however, it is seen that many CNs grow in the desired direction protruding out over the cantilever edges. Furthermore, some ridge-like structures were found growing on the surface of such microchips, as seen in Figure 30C. These ridges are probably poorly defined CNs, that, due to the strong inclination of the chip, grows along the surface in the direction of the electrical field. The growth is probably catalyzed by a small amount of nickel that got deposited on the surface during the sputtering process.

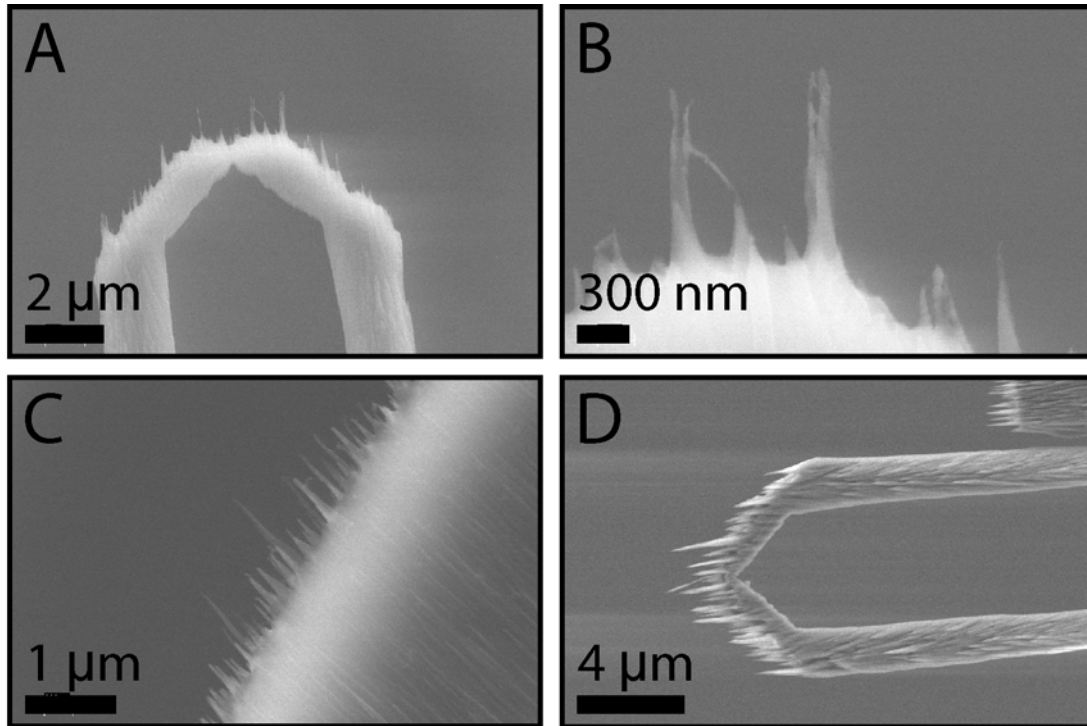


Figure 30 A) Carbon nanofibers grown on the tip of a microtweezer. The close up in B) shows the structure to be rather fiber like than tubular, although we cannot rule out some tubular structure. C) Example of carbon ridges along the field direction on the sample surface. The structures extends over the substrate edge. D) On another cantilever, large CNs are formed on the tip, and on the surface almost horizontal CNs are seen, probably catalysed by a small amount of nickel deposited there during sputtering.

Inclined CN growth on flat surfaces and in microchannels

In the following we will study the ability to control the inclination angle of CNs grown in situ in microsystems such as microchannels, as well as on flat substrates. The microchannels (made by Tommy Schurmann) were fabricated by conventional KOH etching in silicon wafers using a single lithography step. Channels with widths in the range of 1 to 80 μm were made with depths in the range of about 1 μm to 5 μm , leaving both narrow channels with a V-shaped profile and wider channels with flat floors. The inclined sidewalls are due to the KOH etch. Ni of various thicknesses was used as the catalyst and was deposited by evaporation inside the fabricated microchannels through a photolithographically defined lift-off resist mask. Either Native SiO_2 or about 0.2 μm SiO_2 grown by thermal oxidation was used as a barrier layer to avoid diffusion of Ni into the substrate [29]. The planar silicon chips without microstructures had a 15 nm thick PECVD SiO_2 layer underneath 10 nm Nickel without surface patterning. Direct current PECVD (DC-PECVD) was used to grow the CNs [72]. The CN growth was performed at 650 $^\circ\text{C}$, 5 mbar pressure, and at a discharge voltage of -600 V, with acetylene (C_2H_2) as carbon feedstock. The substrates were placed in contact with a vertical face on one side, and tilted at angles ϕ (see Figure 31) from 0° , to 60° with respect to the horizontal. Figure 31 A to C illustrates the experimental setup here. The catalyst (nickel) is deposited inside the KOH etch microchannels by ebeam evaporation (Figure 31 A), and the CN forest grows straight up during PECVD when the substrate is placed horizontally on a flat substrate holder as sketched in Figure 31 B.

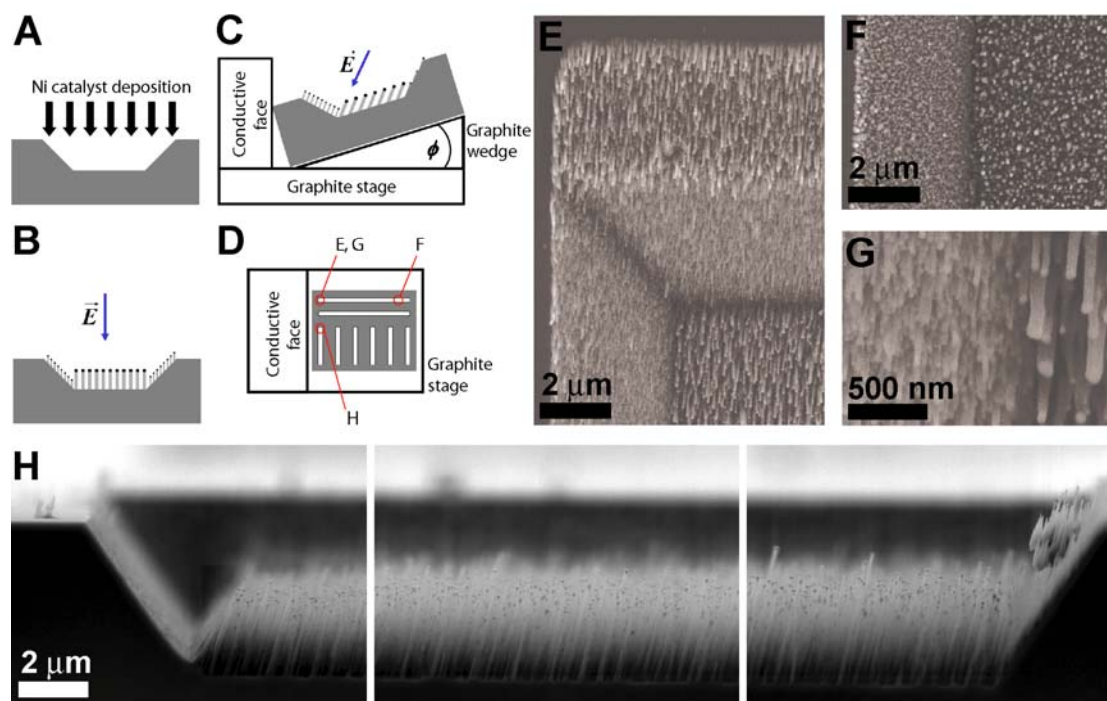


Figure 31 A) Deposition of Ni catalyst by evaporation. B) Illustration of synthesised CNs, showing smaller size on the sidewalls as was observed experimentally. C) A conductive face of graphite and different sample tilt angles ϕ obtained with graphite wedges bends the electrical field and gives growth of inclined CNs. D) Top view of a sample on the graphite stage, showing the locations of the micrographs in E, F, G and H. E) Top view of a channel 1 mm from the conductive face, the CNs (grown with $\phi = 0^\circ$) are inclined inside the microchannel, on top of the substrate and on the sidewalls. F) Further 3 mm down the channel the CNs are seen to grow vertical. G) A close up of the region shown in E reveals that the CNs grown on the sidewalls are smaller both in diameter and height. H) A cross section of an 80 μm wide channel, made from three micrographs, shows that the substrate geometry does not substantially interfere with the growth direction of the CNs.

Here, we introduce a field distorting conductive face as illustrated in Figure 31 C. The conductive face is made out of graphite. In addition, a graphite wedge is placed beneath the substrate, tilting it an angle ϕ with respect to the horizontal. The geometry of the graphite deforms locally the electrical field lines within the plasma sheath. In the experiments, the wedge is placed there to increase the field distorting effect of the opposite face, by squeezing the field lines into a narrower region. As seen in Figure 31 E, the CNs grow inclined both on the top of the substrate, inside the channels and on the channel sidewalls. Moreover, the CNs grow with the same orientation and apparently undisturbed by the substrate geometry. The sample shown here was grown with $\phi = 0^\circ$. The micrograph in Figure 31 E is taken approximately 1 mm from the position of the conductive face, see Figure 31 D. Figure 31 F shows the situation at the other end of the channel 3mm further away from the conductive face, see Figure 31 D. Here the CNs, both on the channel floor and on the sidewalls, grow close to vertical. Thus the effect of the conductive face of the sample holder diminishes fast. Another observation can be made from Figure 31 G which is a close up of the region shown in Figure 31 E. The CNs on the channel sidewalls, which are inclined due to the KOH etch, are smaller both in diameter and height but have a larger areal density. This is probably caused by a thinner catalyst layer on the sidewalls as a result of reduced catalyst flux landing on the angled sidewalls during evaporation of the nickel layer. In Figure 31 H a cross section of a channel that was oriented parallel to the

conductive face is shown. The picture is constructed from three different micrographs, and large portions of the 80 μm wide channel are not shown. From comparison of the left and right side, it can be seen that the angled sidewalls of the channels do not influence the inclination angle of the CNs substantially. It is important to investigate how the field distorting effect, and the resulting inclination angle, changes with increasing distance from field distorting features. Samples with different wedge angles ϕ were made, and the resulting CN inclination was measured as a function of the distance from the field distorting face. Figure 32A and B show SEM images of inclined and vertical CNs on the same substrate for $\phi = 0^\circ$. Their respective positions are indicated with the connections to Figure 32C.

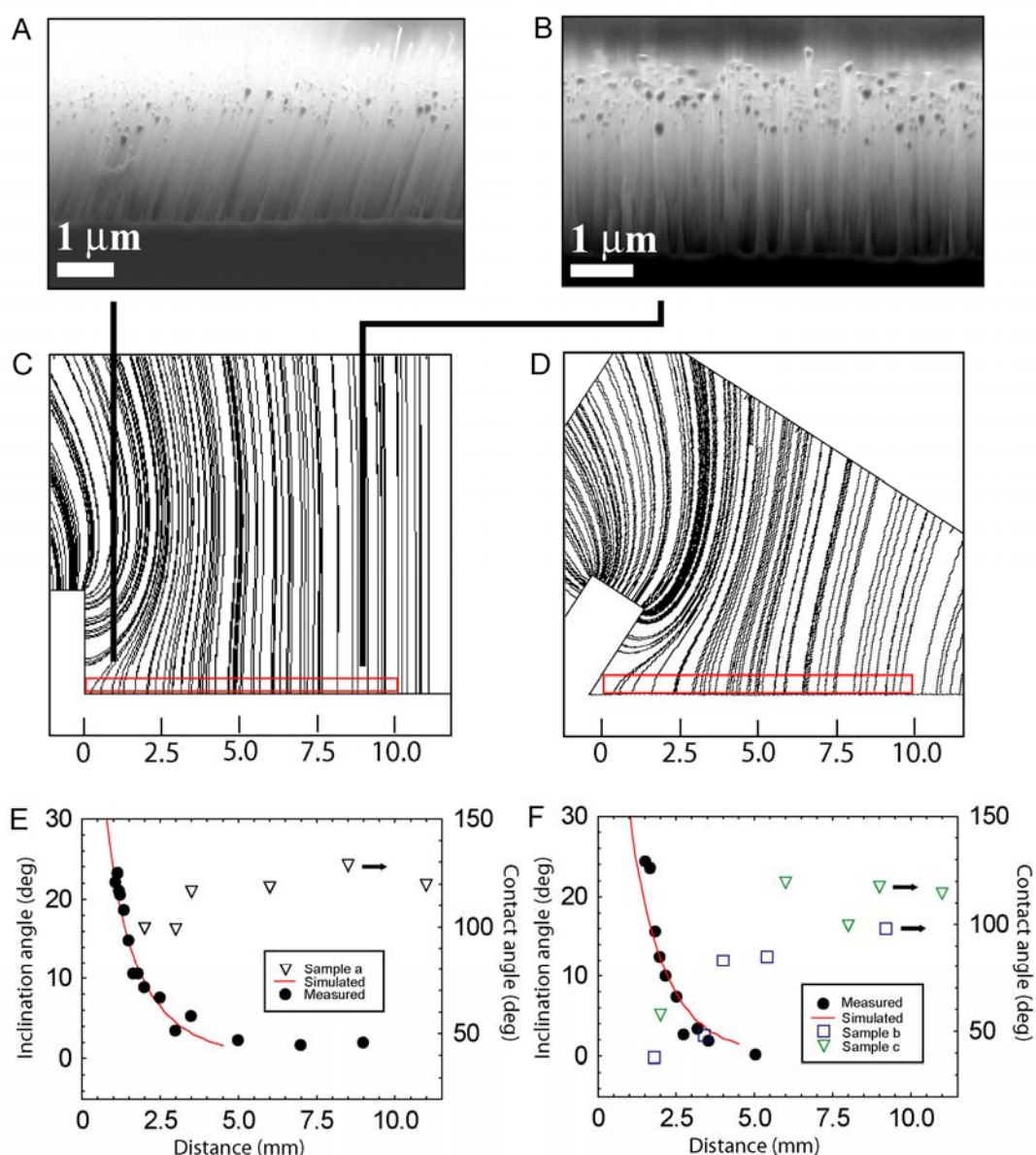


Figure 32 A) and B) SEM images of inclined and vertical CNs imaged 1 and 9 mm from the conducting face of the sample holder, respectively. C) and D) show finite element simulations of the electric field that guides the CNs during PECVD synthesis on stages with 0° ($\phi = 0^\circ$) and 30° ($\phi = 30^\circ$) tilt respectively. E) and F) The simulated and measured inclination angles as well as the measured contact angle with water for an equivalent substrate, are shown as a function of distance from the conductive face for $\phi = 0^\circ$ and $\phi = 30^\circ$ in E and F respectively. The inclination

of the CNs rises sharply close to the conductive face, whereas the contact angle tends to have a lower value for the highly inclined CNs.

Figure 32C and D show 2 D finite element simulations of the electrical field lines around the stage geometries. In these simulations the field lines runs from the stage to a planar anode above. In reality the field lines would only run through the plasma sheath. However, the CNs grow so close to the cathode surface, that this simplification can be done. In the location shown in A the field lines are strongly bent as shown by the simulations. Far from the substrate holder face, the field lines approach the vertical. Other values of ϕ gave the same overall behaviour. In Figure 32C and D the result for the stage geometries with $\phi = 0^\circ$ and $\phi = 30^\circ$ are shown. Since the CN inclination is supposed to match the direction of the electrical field lines, measurements of the CN inclination is compared with the simulated field line inclination at the sample surface. The results are shown in Figure 32E and F where both the measurements and the simulations are plotted as function of the distance from the field distorting feature for ϕ equal to 0° and 30° . Excellent agreement between simulation and experiment is found. However, there is a general uncertainty in the determination of the x-position that may give rise to an offset of up to 100-200 μm , due to ragged edges of the sample. It is seen that field distorting effect reaches only some millimetres from the conducting face. To grow inclined CNs on an entire wafer requires a different approach, like the use of conductive geometrical features either above or beneath the substrate. That would open up the possibility to precisely control the inclination angle of CNs in local areas on a wafer scale basis. This may be useful in producing for instance AFM tips or micro four point probes with inclined CNs as probe tips. Another possibility is to have dense arrays of inclined CNs in a microfluidic channel, functioning as a valve or a filter. In light of this, the wetting properties of inclined CNs grown on samples without microstructures were investigated. Three samples were checked, sample *a* was grown with a stage geometry with $\phi = 0^\circ$, and samples *b* and *c* were grown with $\phi = 30^\circ$. Measurements of the contact angle with water are shown in Figure 32 E and F. All samples show a lower contact angle for higher inclination angles. Inclined CNs expose more of their sidewalls toward the water, which reduces the surface roughness and thus the apparent contact angle.

An investigation was done on the possibility of controlling the inclination angle locally by either shaping the graphite stage underneath or by placing small graphite blocks on top of the sample during growth. The CN inclination can be modified by placing graphite blocks on top of the substrate as shown in Figure 33. Figure 33A shows a micrograph taken vertically above a substrate grown with the graphite block placed as shown in Figure 33B. In Figure 33C another micrograph from another area on the same substrate is shown. Clearly, the CNs point away from the graphite block in both areas. For waferscale fabrication of microprobes with CNs an array of graphite blocks on top of the wafer, possibly hovering slightly above, is suggested. In such a scenario, the region of interest is fairly small (e.g. the tip of an AFM cantilever) and the array should be shaped in such a way that it gives the desired inclination at the region of interest. In Figure 33D the inclination angle is plotted for a substrate grown in the same way as the one shown in Figure 33A and C and shown from the leftmost edge and all the way to the graphite block.

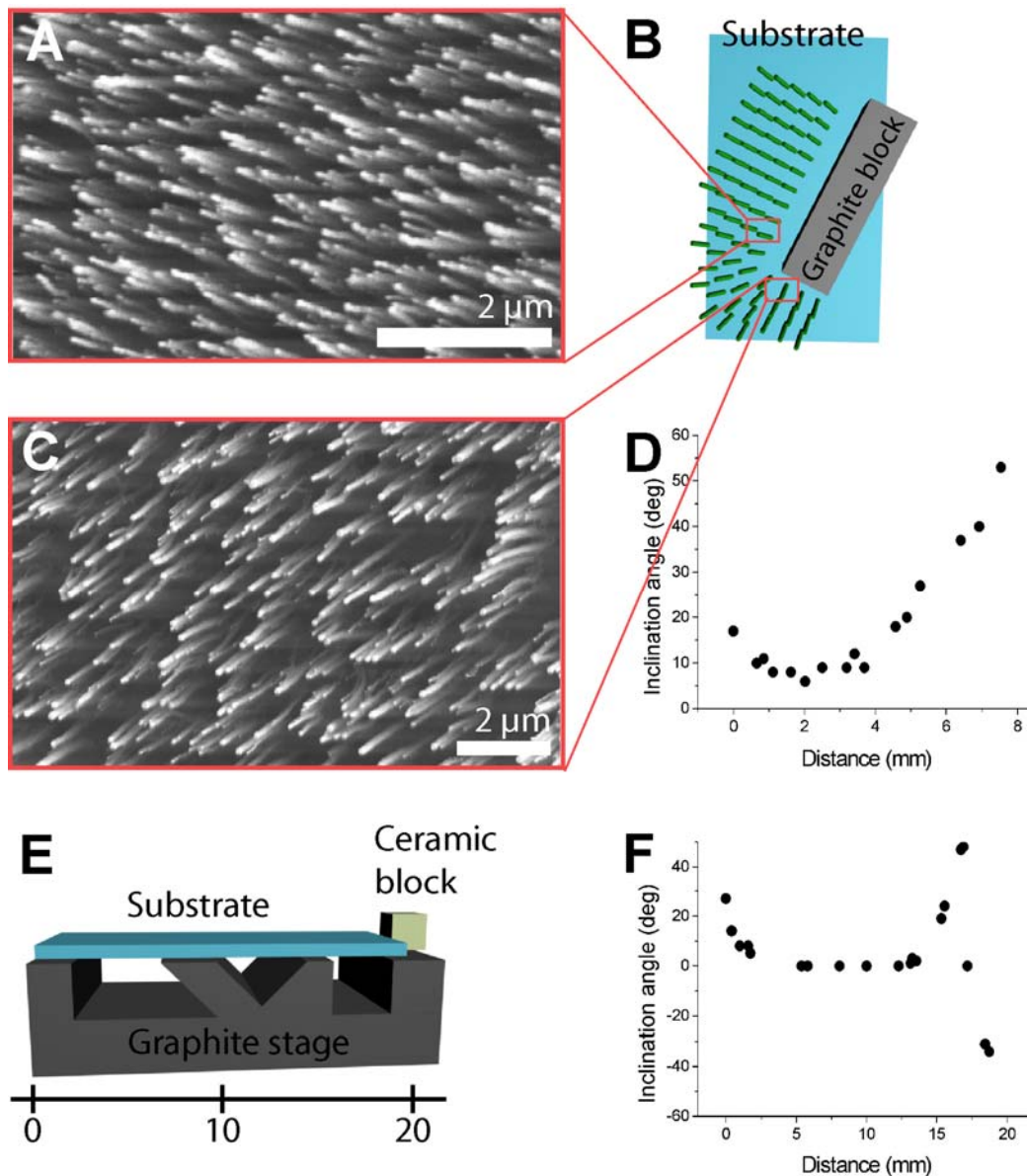


Figure 33 A) A micrograph taken vertically above a CN forest shows that the local inclination is pointing away from the field distorting graphite block placed on top of the substrate as shown in the sketch in B. C) In another region the CNs point in a different direction, but still away from the graphite block as seen by comparison with B. D) The inclination angle is plotted from the leftmost edge to the graphite block. A positive inclination signifies a tilt away from the graphite block. E) A sketch of the shaped graphite stage that was placed underneath another substrate. A ceramic block was added to avoid the substrate from sliding off. F) The inclination angle is plotted for a sample grown with the setup shown in E. No apparent correspondence to the underlying structure is seen, apart from edge effects.

The graphite block gives rise to large inclination angles. The figure shows positive inclination angles close to 60° in the vicinity of the graphite block. A positive inclination angle is here taken as to point away from the graphite block on the left side. It is also seen that the CNs have an increase in the inclination angle close to the leftmost edge of the sample. This may be caused by the stage underneath. To investigate the effect of a shaped graphite stage underneath the substrate, CNs were grown on a substrate on top of a stage as sketched in Figure 33E. The resulting inclination angle is plotted in Figure 33F. It is seen that the inclination angle is positive at the leftmost edge (e.g. pointing to the left), but remains close to 0 over the

central part of the substrate. Clearly the field is distorted only at the edge and not in the central parts. However, on the rightmost edge a sharp increase in the inclination angle up to about 45° followed by an equally sharp drop down to about -40° (e.g. pointing to the right), is seen. Such a shift indicates that the electrical field is distorted back and forth over this small distance, but this is probably not a result of the geometry of the underlying stage in this region. A ceramic block had to be placed close to this region to avoid the substrate to slide off the stage. This ceramic block is insulating and may hold a lot of charge during the growth. The shift in inclination angle is therefore more easily explained by the presence of this ceramic block, than the shape of the underlying stage. However, for waferscale fabrication of probes with inclined CNs it would probably be possible to distort the electrical field in the regions of interest simply by shaping the stage underneath, since wafers with probes will have holes through the wafer, thus enabling the field distortion similar to the edge effects seen in both Figure 33D and F. The results indicate that inclinations in the range 0° to at least 50° may be obtained by careful design of the substrate holders.

Conclusion

It has been found that CNs can be successfully integrated in microsystem such as microchannels and microprobes with cantilevers. Moreover, electrical contact could be made to the CNs when grown on conductive material such as W. Furthermore, the CNs were attached strong enough to the surface to allow bending up to at least 45° without releasing. Furthermore, integration of CNs with a high degree of control over the inclination angle was found to be possible. This was made possible by;

- The growth direction of the CNs is guided by the electrical field in the PECVD process.
- It is possible to distort the electrical field on substrates such as silicon and oxide.
- The field distortion can be made by shaped graphite geometries above the growth surface, and possibly below for some structures.
- The microstructures do not interfere substantially with the inclination angle.
- It is possible to calculate the field distortion by finite element modelling

This opens up the possibility of tailor designing conductive stages with features that distorts the electrical field in local areas on an entire wafer. For integration on cantilever probes, this could be done with a shaped stage underneath, but for integration in the interior of large chips the field distorting features would have to come from above. In these ways it is possible to have wafer-scale production of devices with integrated inclined CNs in specific areas. Furthermore, it was also seen that the contact angle with water depends on the inclination angle, the contact angle being smaller for smaller inclination angles. This may have special significance for the use of inclined CNs in microfluidics.

4 Surface properties of vertically aligned nanotube forests

Introduction

In micro- and nano-manipulation the inevitable stiction and adhesion forces prevents controllable and repeatable manipulation on most surfaces. On the nanoscale, adhesion and stiction are mainly caused by van der Waals forces or capillary forces. In order to realize the potential of structures such as nanotubes and nanowires, as components in electronic devices or other microsystems, methods for reliable pick and place assembly has to be found. This will enable fabrication of prototype devices for subsequent characterisation. Although pick and place assembly is suitable for fabricating prototype devices and small production series, it can never become a method for industrial scale fabrication. Here, other methods, such as directed growth of nanostructures on microelectrode have to be used [92, 95]. A major obstacle for the pick and place assembly method, is the delicate balance required of the stiction forces between the manipulated object to the surface and to the manipulation tool. It is essential to control the balance of these forces [85]. Nanostructures, such as carbon nanotubes, various III-IV nanowires and organic nanofibers are all potential candidates for future NEMS devices. In particular organic hexaphenylene (p-6P) nanofibers show great promise as components in future nanophotonic applications [7, 96], such as waveguides, lasers and blue-light nanosized LEDs. All these nanostructures are very difficult to place controllably in devices. Most devices fabricated to characterise these structures, rely on methods to make electrical contact to randomly dispersed nanostructures [11, 12]. The ability to pick one particular nanostructure for a sample, place it in a device, and make successful electrical contacts, is much needed. The wetting properties of a surface are important for how well micro-objects stick to a surface, due to the capillary forces. It has been known that vertically aligned carbon nanotubes may exhibit highly hydrophobic behaviour, especially when covered with a hydrophobic coating, like Teflon [97]. In this chapter a study on the wetting properties of uncoated vertically aligned nanotube forests, as well as an investigation on the stiction and friction properties related to micro and nanomanipulation will be presented.

Wetting properties

Basic Wetting theory

It is not the scope here to treat wetting theory in full depth, but to introduce a few basic concepts. The first important term is the contact angle of a surface or material. This is illustrated in Figure 34, where illustrations of three water droplets are seen resting on three different substrates. Depending on the surface energy of the surface, the water either forms a spherical drop in the hydrophobic case (low surface energy) as seen in A, or, via intermediate states as seen in B, an almost flat water drop in the hydrophilic (high surface energy) case as seen in C. The contact angle θ is the angle formed between the water surface and the baseline d at the contact line, as illustrated in Figure 34C. Here the contact line is the line around the base of the droplet, where the water is in contact with both the surface and the surrounding atmosphere. Furthermore, the baseline d is the diameter of the droplet at the interface between the

water and the surface. Normally, a contact angle larger than 90° is said to be hydrophobic, while contact angles less than 90° are hydrophilic. Superhydrophobic surfaces have contact angles in excess of 150° , showing almost no contact between the droplet and the solid surface.

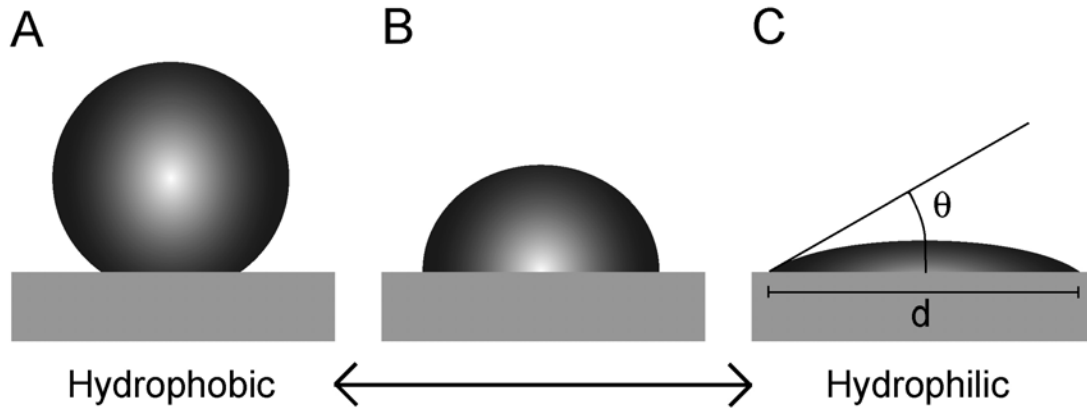


Figure 34 A) A water drop resting on a low energy surface forms a spherical drop. This is the hydrophobic case B) A surface with intermediate surface energy. C) On a surface with high surface energy, the water drop flows out towards a flat film. This is the hydrophilic case.

It is the interfacial energy between the solid and the liquid that decides which form of wetting will occur, hydrophobic or hydrophilic. For a water droplet in air, a minimisation of the interfacial energy is obtained through forming a sphere – the geometrical shape that has the least surface area per volume, and thus least interfacial energy. When the drop on the other hand rests on a surface, the interfacial energy of that surface comes into play. For a low energy surface, as compared to the water, the drop will not wet much of the surface since that will increase the surface of the drop and thus the energy. However, for a large surface energy, the total interfacial energy is minimised when the water wets a large part of the surface, trading off an increase in the surface energy on the water for a decrease in the surface energy of the solid surface. This is the case for planar ideal surfaces, and the total interfacial energy of the system is given as [98] ;

$$E = \sigma_{SL} |\Sigma_{SL}| + \sigma_{SV} |\Sigma_{SV}| + \sigma_{LV} |\Sigma_{LV}| \quad (4.1)$$

Here $|\Sigma_{AB}|$ is the area of the interface between the phases A and B, where we have the three different phases Solid, Vapour and Liquid. σ_{AB} is the corresponding interfacial energy density. Minimisation of the interfacial energy gives the classical Young law for the contact angle;

$$\cos \theta = \frac{\sigma_{SV} - \sigma_{SL}}{\sigma_{LV}} \quad (4.2)$$

The surface energy of a surface is also called the surface tension. Surface tension is measured in newtons per meter (N/m), which is equivalent to Joules per square meter (J/m^2). In a liquid, it is this surface tension that causes the liquid surface to behave like an elastic membrane, making it possible for insects to walk on water.

Wetting of rough surfaces complicates the issue. It is observed that a rougher surface tend to amplify the property of a system, thus increasing the contact angle in a hydrophobic system, and decreasing it in a hydrophilic system [98]. There exist two main models for rough wetting, one based on Wenzel drops [99], and another based on Cassie-Baxter drops [100]. The main difference lies in how the rough surface is wetted. If one assumes a complete contact at every point between the rough surface and the liquid, then we have a Wenzel drop following the Wenzel law (wetting of both peaks and valleys). In this case the apparent contact angle is given by;

$$\cos \theta_W = r \cdot \cos \theta \quad (4.3)$$

Here, r is the roughness of the surface, and θ is the equilibrium contact angle of the corresponding flat surface. The roughness r of a surface is given as the ratio between the actual contact area and the apparent macroscopic contact area, see illustration in Figure 35A. The Wenzel law predicts that the intrinsic wetting behaviour of a surface, will be amplified by a factor which depends only on the roughness r of the surface.

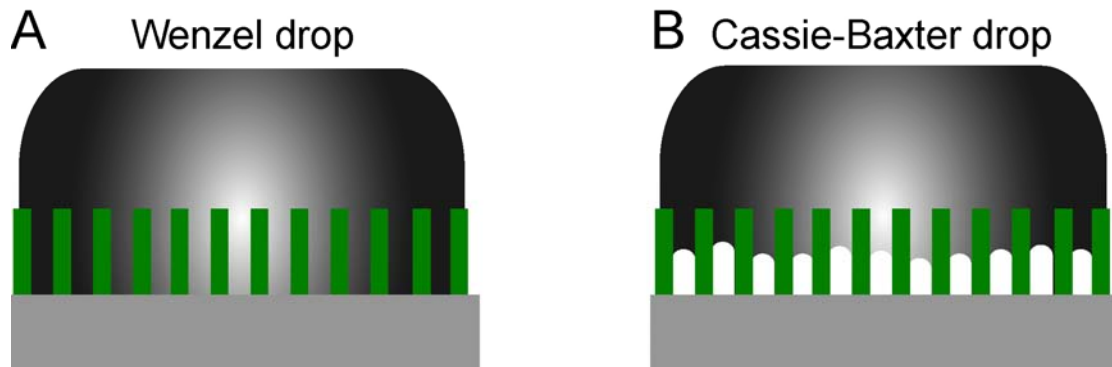


Figure 35 A) A Wenzel drop following the Wenzel law completely wets the rough surface. B) A Cassie-Baxter drop following the Cassie-Baxter law does not wet the rough surface entirely. Small pockets of vapour is trapped within the asperities.

If on the other hand one assumes that vapour is trapped inside asperities of the rough surface, as illustrated in Figure 35B, the drop is called a Cassie-Baxter drop, which follows the Cassie-Baxter law for composite surfaces;

$$\cos \theta_{CB} = f_1 \cos \theta_1 + f_2 \cos \theta_2 \quad (4.4)$$

Here, the fractions f_1 and f_2 corresponds to the respective fractions of the projected planar area of the two species the liquid is in contact with. Note that $f_1 + f_2 = 1$. The liquid has the equilibrium contact angles θ_1 and θ_2 on the two species respectively. Of the two possible mechanisms, a minimisation of the energy for a given system, can only be obtained by one of the them at a time [101, 102]. In fact, Alberti et al [98] showed that the minimal energy configuration is obtained by the model that predicts the least roughness induced enhancement of the hydrophobic or hydrophilic properties.

In the real world the wetting of a rough surface become even more complicated. The above explained theory is valid for liquid droplets in equilibrium on a solid rough surface. Pinning and contact angle hysteresis, are phenomena that need to be

addressed. Rough structures on a surface work in a way to prevent the extension of a droplet, and this effect is called the pinning effect. The roughness can pin the contact line directly so that the wetting dynamics is completely changed [103]. Contact angle hysteresis is the variation of the contact angle in a receding or advancing liquid droplet, and this hysteresis, caused by chemical or physical imperfect surfaces, is typically enlarged on a rough surface due to pinning. On a perfectly flat surface, the difference between an advancing and a receding water drop should be very small. However, the advancing contact angle would be slightly larger than the equilibrium contact angle, and the receding contact angle would be slightly smaller. Pinning may be divided into three main groups, strong pinning, medium pinning, and weak pinning. In strong pinning the contact line does not recede (receding contact angle equal to 0), while it can advance. In medium pinning, the liquid can both advance and recede, but the receding contact angle is much smaller than the advancing one. On surfaces with weak pinning, the receding contact angle is only slightly smaller than the advancing contact angle.

Wetting of carbon nanotube forests

The wetting properties of carbon nanotube forests have been a topic of interest for some time and Li et al. [104] and Lau et al. [97] have reported on strong hydrophobicity, and even superhydrophobicity (contact angle larger than 150°) on such surfaces. Lau and co-workers observed that the superhydrophobicity can only be maintained given that the carbon nanotube forest was treated in a special manner, for instance covered in PTFE (Teflon) coating. Recently Cheng and co-workers investigated the superhydrophobic property of the Lotus leaf [105, 106]. Raindrops on Lotus leaves form droplets with a contact angle of around 160 degrees. The superhydrophobic effect is due to a combination of a micrometer sized roughness covered with nanometer scaled wax hairs. Cheng and co-workers found that the Lotus leaf could show superhydrophobic behaviour as well as hydrophilic behaviour, depending on exactly how the surface was wetted. They found that the Lotus effect can vanish when water is condensed onto its surface from the water vapor phase. By wetting through condensation, they observed both rolling droplets with superhydrophobic contact angle, “sticky” droplets with a high contact angle, and droplets with a contact angle of less than 90 degrees. A SEM micrograph of a Lotus leaf surface is shown in Figure 36, together with an illustration showing the surface roughness in detail with the two different wetting possibilities as suggested by Cheng et al [105].

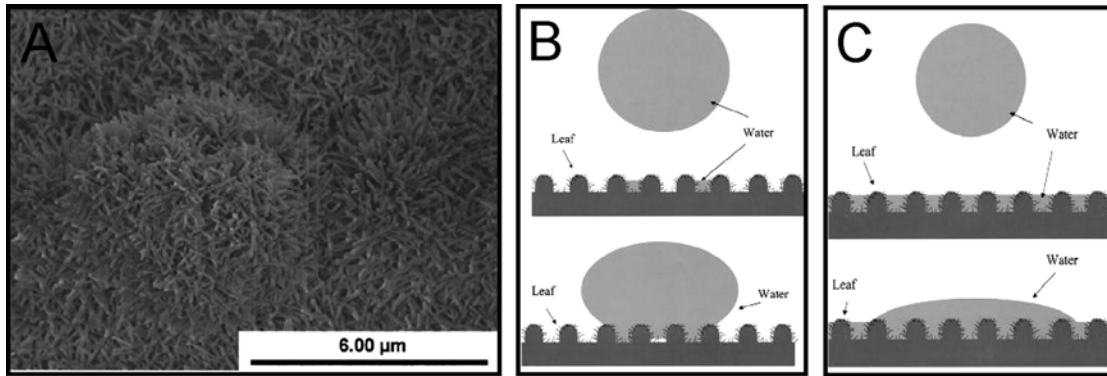


Figure 36 A) A SEM micrograph of the lotus surface [105]. The nanoscale hairs have a striking resemblance to carbon nanotube forests. B) & C) Two wetting states of the Lotus leaf as suggested by Cheng et al [105]. In B the drop behaves like a Cassie Baxter drop and in C it does not behave like a wenzel drop, but rather as a drop in the film regime[107], where the rough surface is filled with a liquid film from before (in Chengs work from condensation). In the film regime the contact angle is drastically reduced, whereas a wenzel drop is pinned along the contact line, preventing the spreading out of the liquid.

The micro scale roughness on the lotus leaf is covered in nanoscale hairs with dimensions similar to that of carbon nanotubes. The apparent similarity between a carbon nanotube forest and the nanoscale hairs of the Lotus leaf in Figure 36A is striking. It is tempting to ask the question whether or not the carbon nanotube forests exhibit similar wetting properties as well.

In ambient air

At first the wetting properties of a nanotube forest is studied in ambient air. The nanotube forest, prepared at Cambridge University, was synthesised in a PECVD process for 5 minutes, using a film of 4 nm nickel as catalyst. A computer controlled syringe was used to deposit 1 μl of water on the surface forming small water droplets. The development of such water droplets was observed with an optical microscope. In Figure 37, series A to D shows optical microscope pictures of two water droplets at times 0, 5, 10, and 13 minutes after initial deposition on a nanotube forest, respectively. Besides the difference in volume, the two droplets are equivalent.

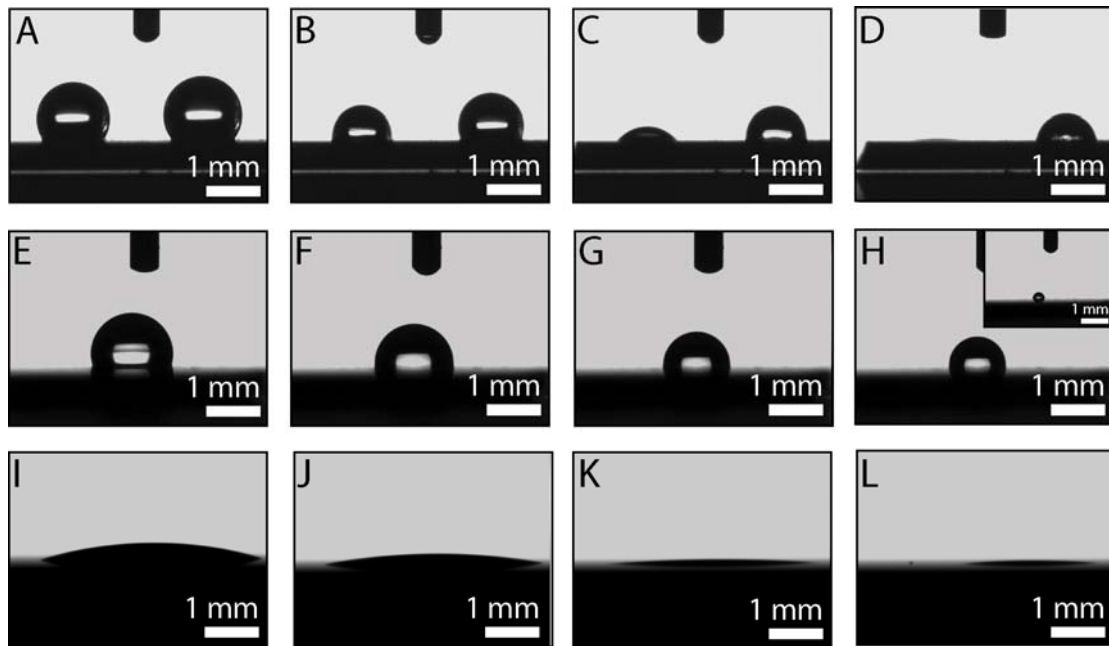


Figure 37 A-D) Evaporation of water droplets on a carbon nanotube forest, for times of 0 min, 5 min, 10 min and 13 min, respectively. E-H) Evaporation of a water droplet on a Teflon surface, for times of 0 min, 5 min, 10 min and 13 min, respectively. I-L) Evaporation of a water droplet on a Silicon surface, for times of 0 min, 5 min, 10 min and 13 min, respectively.

Initially, the contact angle is about 125° , corresponding to strong hydrophobicity. Due to evaporation, the liquid volume is reduced, and accordingly either the base line of the drop or the contact angle has to change, to accommodate the shrinking water volume. For a smooth surface the contact lines move almost freely, and the advancing angle, which is comparable to the angle just after deposition, is only slightly larger than the receding contact angle. Furthermore, the contact lines shrink (moves) with almost constant contact angle. In Figure 37B it is clear that the contact angle is reduced, whereas the base line is virtually constant. Figure 37C and D, 10 and 13 minutes after deposition respectively, support this observation. In fact, in D only a very thin water film is still present, but is seen to cover practically the entire area initially covered by the drop. Accordingly, the water droplets on the nanotube forest experience strong pinning, and the contact line cannot be made to recede. Apparently, it looks as if the surface has turned hydrophilic. But this is not the case, in contrast it is a strongly hydrophobic surface showing strong pinning, and thus a large contact angle hysteresis.

For comparison, equivalent measurements were done on Teflon, a well known hydrophobic substrate, and a hydrophilic silicon surface. Series E to H in Figure 37 shows a water droplet deposited on a Teflon coated silicon surface, at times 0, 5, 10, and 13 minutes after deposition respectively. It is here seen that the receding contact angle is only slightly less than the advancing, and that it appear to be rather constant during the evaporation process. The loss of liquid is accommodated by a reduction of the baseline, not the contact angle which remains close to the initial 105° . In the end, 20 minutes after deposition, a small spherical droplet is all there is left as seen in the inset in H. Apparently, there is only a weak pinning on this Teflon surface, leading to a small contact angle hysteresis. On the silicon surface, a similar development of the water droplet during evaporation is seen (Figure 37 I-L). Initially the advancing

contact angle is seen to be very low (less than 20°), while the receding contact angles in J, K, and L show have a basically constant value during the evaporation. Again it is the baseline, and accordingly the contact line, that shrinks and accommodates the shrinking water volume.

Without any contact hysteresis, there should be no difference in the evaporation process between the hydrophobic and the hydrophilic case. In both cases the base line should shrink with a constant contact angle. This is seen for both the hydrophilic silicon surface and the hydrophobic Teflon surface. However, the hydrophobic carbon nanotube forest is seen to have a large contact angle hysteresis, probably due to strong pinning of the contact line. In Figure 38 the development of the contact angle and the base line for the three different substrates are shown.

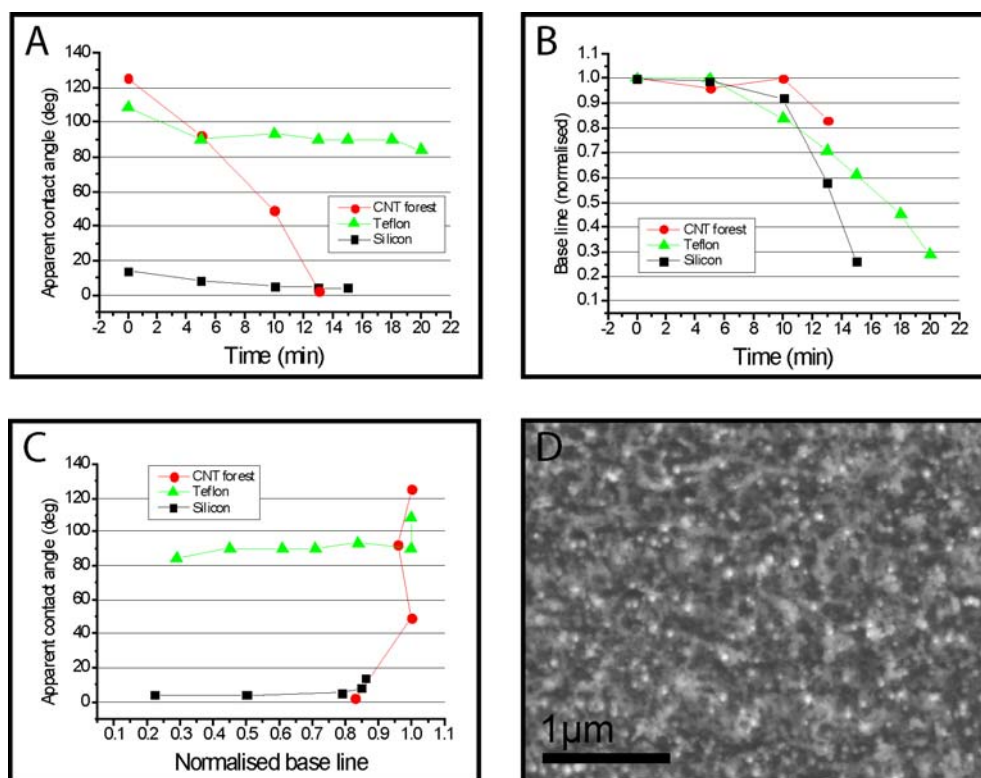


Figure 38 A) The apparent contact angle as a function of time for the three surfaces. Notice that the contact angle of the nanotube forest drops sharply as compared to the two other substrates. B) The base line as a function of time for the three surfaces. Notice that the base line on the nanotube forest almost remains constant during the entire evaporation process. C) The apparent contact angle as a function of the base line for the three surfaces. Notice that the base line shrinks with close to constant apparent contact angle for both Silicon and Teflon. On the nanotube forest, the case is almost the opposite, where the contact angle shrinks with almost constant base line. D) A SEM micrograph of the carbon nanotube forest used here. The nanotubes were synthesised in a PECVD process for 5 minutes, using 4 nm nickel as catalyst. This yielded about 1 μm long tubes.

In ESEM

Inside an ESEM chamber it is possible to control the condensation rate of water on the substrate by both carefully regulating the temperature of the substrate with a Peltier element, as well as the water vapour pressure, or total vapour pressure in the ESEM chamber. Condensation of water inside the ESEM starts when lowering the

temperature and rising the water vapour pressure sufficiently. It is a delicate balance, for each temperature. If the temperature of the substrate is kept below 0 °C, ice will occur instead of water.

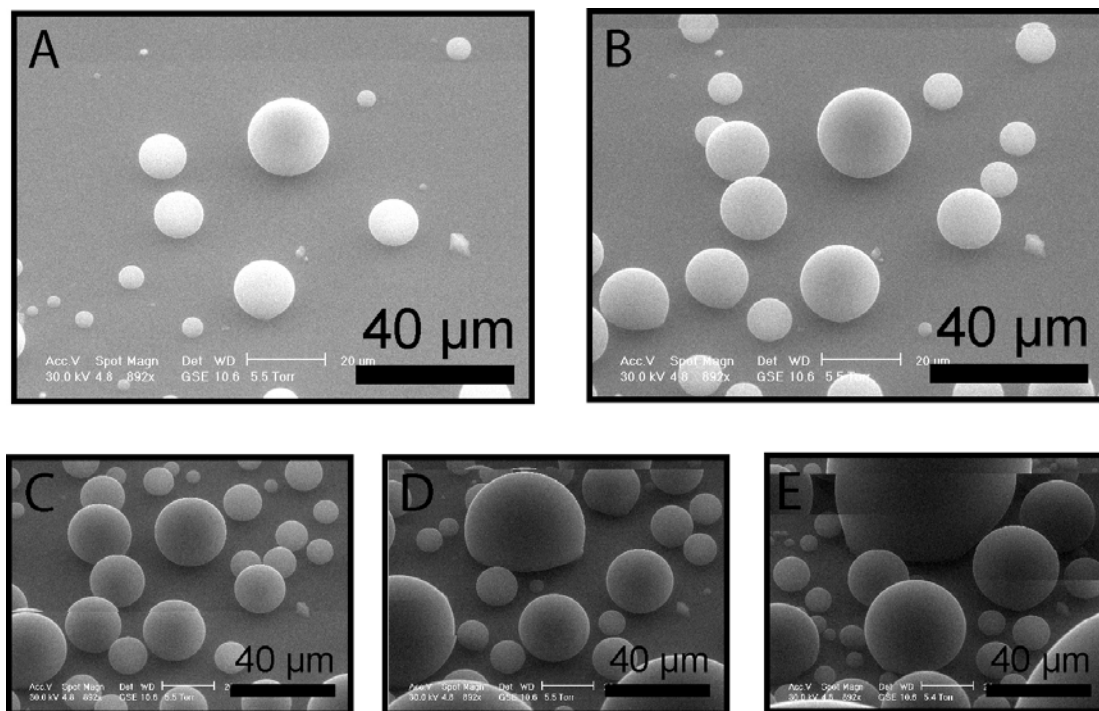


Figure 39 A) Condensation starts with appearance of spherical microdroplets. B-E) The droplets grow by further condensation.

The condensation starts with the sudden appearance of many microdroplets randomly distributed over the substrate surface. Existing droplets accumulate water vapour and grow in size, while new droplets are nucleated at the same time, see Figure 39. The equilibrium between condensation and evaporation is very sensitive to small changes in substrate temperature and water vapour pressure. Here the temperature was 3.0 °C and the pressure 5.5 torr. The water droplets continue to grow due to condensation. When two droplets touched each other they merged, and it was noticed (Figure 39D and E) that larger droplets do not have a contact angle as high as the one seen for the smaller droplets. The ESEM images here are recorded with a substrate stage tilt of 45 °. To measure the contact angle correctly from the pictures, a correction for the stage tilt has to be made. From trigonometry we find that the actual contact angle, θ_{act} , is given as

$$\theta_{act} = \arctan\left(\frac{1}{\sin(\theta_{tilt})} \cdot \theta_{measured}\right) \quad (4.5)$$

Here, $\theta_{measured}$ is the contact angle measured directly on the images.

In a new condensation, after complete drying of the sample outside the ESEM chamber, the surface was seen to exhibit the same behaviour (Figure 40). Micrometer sized water droplets formed here at 5.3 torr and 2.9 °C.

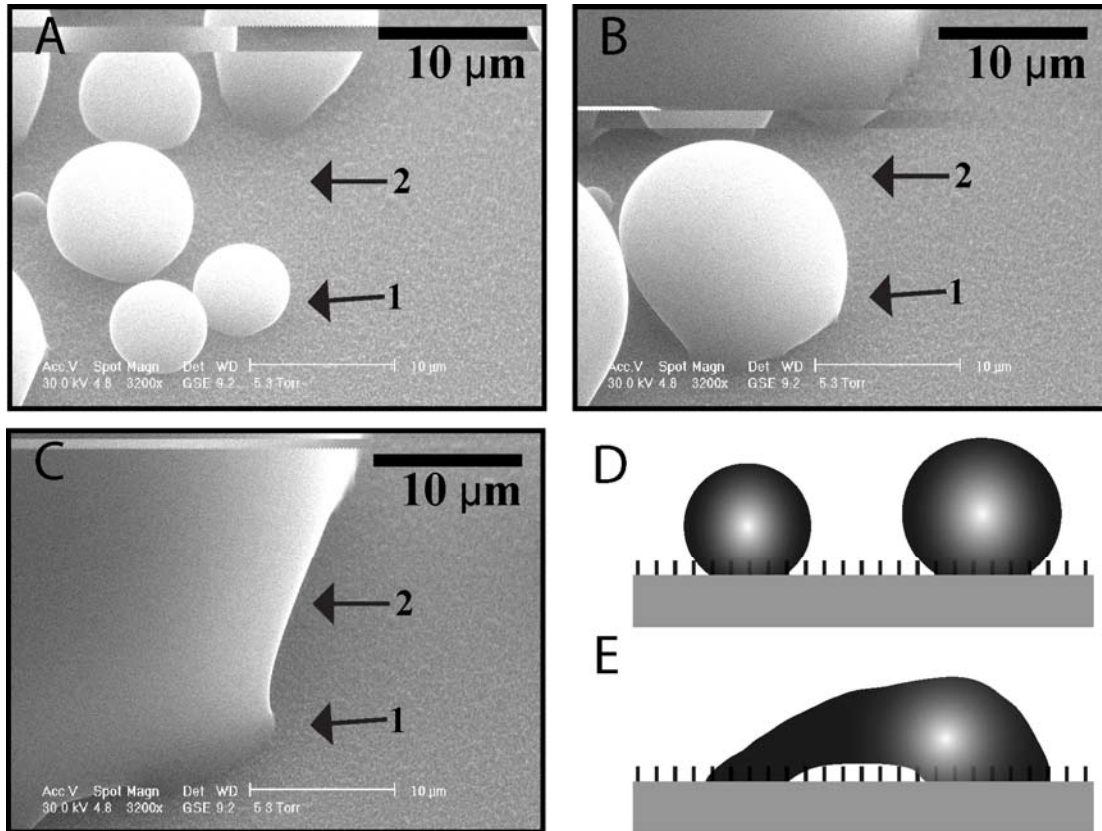


Figure 40 A) New droplets condense on the same surface after drying. B) Smaller droplets merge into larger ones, exhibiting pinning at the previous droplet centres. C) A close up of an area where the droplet is prevented from receding due to pinning. D & E) Sketch illustrating two droplets merging. After merging (E) the new droplet is pinned at the two previous droplet centres.

In Figure 40A we find θ_{measured} to be about 135° , from which the actual contact angle is estimated to be about 125° , which is in agreement with the findings in ambient environment. The same area is shown in Figure 40B approximately half a minute later. More water has condensed, and smaller water droplets merge when their surfaces come in contact. Specifically, three smaller droplets in A have merged into one larger in B, and the larger droplet appears to have lost the spherical shape and is now more irregular. In Figure 40 C further water droplet merging has occurred. It now becomes apparent that the irregular shape is caused by pinning points on the surface. When the droplets grow by condensation only, their contact angle is the advancing one. However, when the droplets merge, they have too little liquid volume to maintain the advancing contact angle over the combined surface area. Thus the contact angle is lower due to the receding liquid. However, due to the strong pinning of the nanotube forest, the liquid will not let go of the nanotubes already wetted, such as below the centres of previous droplets. Arrow 1 in Figure 40 points to such a centre of strong pinning, whereas arrow 2 points to an area still not wetted in Figure 40C, where the contact angle is still very high. It is clear that upon combination with neighbouring droplets there is not enough water to maintain the high contact angle with a larger droplet. Instead of retracting itself to a smaller area, the droplet stretches between the centres of the initial droplets where the contact line is strongly pinned. When the droplets stretch like this, dry areas in between still cause high contact angles on some sides of the droplets. This process is sketched in Figure 40D and E. Such a wetting

may potentially cause the carbon nanotubes to bundle together and lose much of their roughness, thus making the substrate less hydrophobic. This depends probably on the morphology of the nanotube forest. However, it was found that the hydrophobic behaviour was the same after drying. This indicates that the surface has not changed permanently due to the wetting.

Interestingly, this form of wetting of the nanotube forest was not the only one observed. When the substrate had been completely wetted in water, it was possible to condensate and evaporate a water film on the nanotubes, without any hydrophobic droplets occurring at all. This could not be done on a perfectly dry substrate. Such a condensation series is shown in Figure 41.

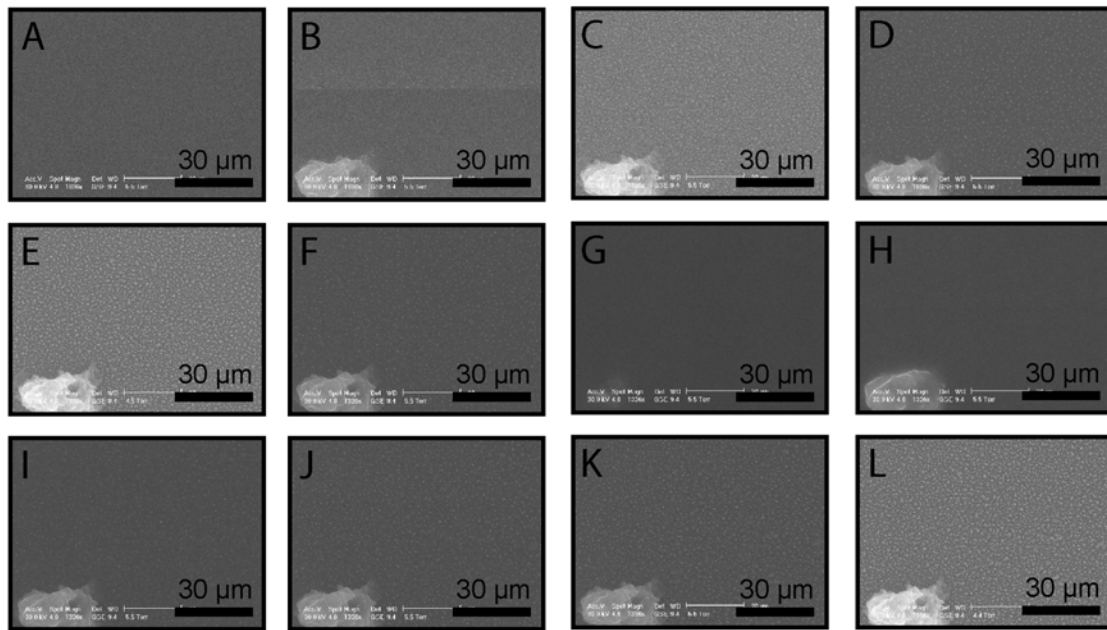


Figure 41 A) An already completely wetted nanotube forest is wetted in the film regime. It is almost impossible to see the nanotube forest, which is soaked in water. B-C) By raising the temperature, the nanotube forest dries gradually and the nanotubes re-appear. D) By lowering the temperature slightly, the water films condensate again. E) At 3.9 ° and 4.5 torr the nanotube forest appears almost dry. F-G) An increase in the vapour pressure again causes the film to condensate again. H-L) An increase in temperature again causes the nanotubes to re-appear.

On a dry nanotube forest, the droplets touch only the tips of the MWCNTs and the vapour between the tips. Quantitatively, the contact angle of water droplets on top of a surface consisting of two materials, can be treated by the Cassie-Baxter equation for composite surfaces of two species [100, 105].

$$\cos \theta_{CB} = f_1 \cos \theta_1 + f_2 \cos \theta_2 \quad (4.6)$$

In this picture, f_1 and f_2 represent the fractions of the contact area of the water droplet to the material between the nanotubes and the tips of the nanotubes, respectively, while θ_1 and θ_2 represent the corresponding contact angles. For a water droplet resting on top of the nanotube tips with vapour (or almost vacuum) in between ($\theta_1 = 180^\circ$), the equation becomes

$$\cos \theta_{CB} = -1 + f_2(\cos \theta_2 + 1) \quad (4.7)$$

Here, we have used the fact that $f_1 = 1 - f_2$. Furthermore, since the area of the nanotube tips is relatively small, $f_2 \ll f_1$, the apparent contact angle approach the contact angle to vapour, i.e. $\theta_{CB} \rightarrow 180^\circ$. On the other hand, if the space between the nanotubes is filled with water, the equation becomes

$$\cos \theta_{CB} = 1 + f_2(\cos \theta_2 - 1) \quad (4.8)$$

Here $f_2 \ll f_1$ gives a contact angle approaching zero, corresponding to the hydrophilic state. As the space between the nanotubes are filled with liquid, the contact angle changes from 180° to 0° . This corresponds to the film regime if the entire structure is wetted. Accordingly, the two different condensation behaviour observable on the nanotube forest, may be explained by this.

Summary

Cheng et al [105, 106] concluded that Lotus leaves could show both hydrophobic and hydrophilic behaviour. They found that water drops on Lotus leaves that had experienced water vapour condensation could be categorized into three types; (1) Rolling drops with superhydrophobic contact angle, (2) sticky drops with high contact angles, and (3) drops with contact angles less than 90° , i.e. hydrophilic. On the untreated nanotube forest two of these three behaviours were observed. The sticky drops were observed as the drops either deposited or condensed on dry nanotube forests. These drops showed a strong pinning, and the contact line could not be made to recede, but still maintained large contact angles, unless they merged with other nearby droplets. Water in the film regime, corresponding to the third category, was also seen, and the nanotube forest appeared to be fully hydrophilic once the asperities between the tubes had been wetted. To observe the last category, rolling superhydrophobic drops, it is probably necessary to coat the nanotubes in a hydrophobic material, for instance Teflon. Lau et al [97] showed that Teflon coated nanotube forests became superhydrophobic with contact angles around 160° . But then, even the nanohairs on the Lotus leaves are coated with a wax to enhance their hydrophobicity.

It can also be concluded that the sticky drops are Wenzel drops. The Wenzel drops completely wets the rough surface underneath, but the surface is dry ahead of the contact line, thus the contact angle remain large in contrast to the film regime. Furthermore, in these investigations the nanotube forest consisted of short tubes with a length of $0.5 - 1 \mu\text{m}$. Long nanotubes will bundle together during evaporative drying due to the attractive capillary forces as shown by Lau et al [97] and studied on a similar silicon nanorod surface by Fan et al [108], and this will make the carbon nanotube forest change its surface roughness, between consecutive condensations. Thus carbon nanotube forests can only be permanently hydrophobic, resisting penetration of liquid into the asperities, by surface treatment (for instance coating by Teflon [97] or Thiol molecules [109]). However, small objects resting on top of a dry nanotube forest will still have a very small contact area as compared to on a flat surface. Thus adhesion and sticktion forces, and in particular capillary forces, should therefore still be expected to be very small on this surface. That is the topic of the next subchapter.

Stiction and friction on vertically aligned nanotube forests

Background

The purpose is to investigate the stiction and friction properties of micro-sized objects on the nanotube forest compared to the other substrate surfaces. It is important to understand the distinction between the different terms adhesion, stiction and dynamic friction. Adhesion is a term relating to how much force is required to lift objects vertically off a surface. Thus it is a force acting along the surface normal. Stiction and dynamic friction on the other hand are forces that act parallel to the surface. Stiction is short for static friction, which is the force required to set an object into motion from initial rest. This is always slightly larger than the dynamic friction, which is the force required to keep the object in motion once it is released. Every time the object comes to a complete halt, the static forces have time to settle, and we need to overcome the static friction again in order to release the object. In the ideal situation, if the objects only slide, the measured force is stiction. However, if the objects roll instead, it is adhesion [110]. In addition to the two established friction forces, a third type may be relevant for micro and nanomanipulation [111]. There appears to be a significantly higher initial stiction on most materials. The objects to be manipulated have been deposited on the surfaces, often through the deposition of a liquid solution containing the objects. The objects appear to be sticking much harder to the surfaces, due to a gluing effect – perhaps from contaminant particles (dust) in the solutions. Once the objects have been released, this initial stiction cannot be observed again. It may be very difficult to come around this problem, since better cleaning of the samples may not always be possible. If the samples are provided in a liquid solution, which nanofibers and filaments often are, the potential dust or remaining liquid constituents that helps gluing them to the surface may not be removed, since they are part of the sample.

Latex beads

Experimental setup

Manipulation experiments of objects on the micro- and nano-scale are inherently problematic due to the minute size of the objects. Therefore, precise experimental equipment with xyz manipulators of high precision is required. Experiments can be either performed beneath an optical microscope with a high magnification, or inside the chamber of a scanning electron microscope. Here the experiments have mainly been done in a SEM (LEO 1550 SEM) due to the increased magnification, and thus the increased control of the pick and place operations.

The experimental setup consists of a precise xyz manipulator mounted inside the SEM chamber. The manipulator, from Klocke Nanotechnik (Figure 42), can be independently operated by an external computer. On this manipulator, different manipulation tools may be mounted, one at a time. Siliconchips fabricated through conventional microfabrication techniques were used as manipulation tools. The chips were equipped with cantilevers made of glass. The substrates were placed on the SEM stage, which can be moved in xyz. Thus there are two xyz manipulators inside the

SEM, which enables independent movement of the substrates and the manipulation tool and accurate approach of objects on the micron and submicron scale with the cantilevers.

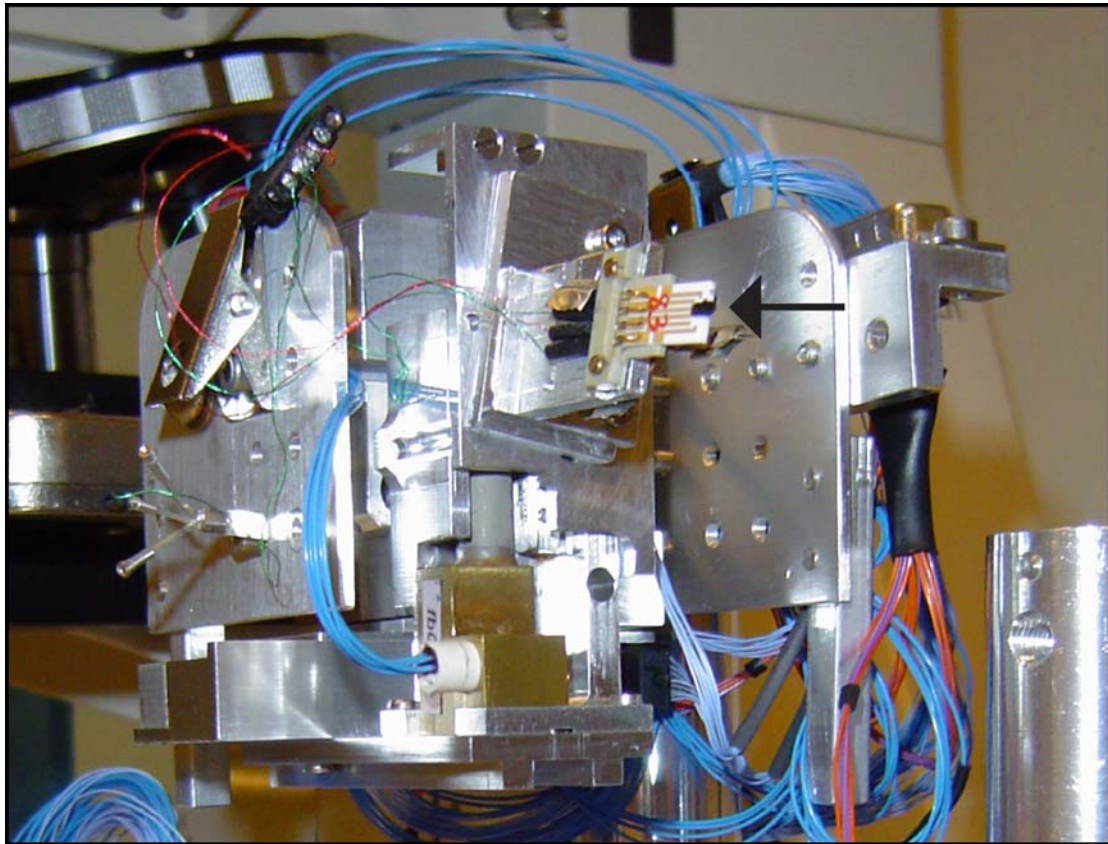


Figure 42 The xyz manipulator with a mounted microchip. The arrow points towards the manipulation tool, which is the silicon chip (black) with cantilevers, attached to a ceramic holder (white).

To compare the stiction and dynamic friction forces on nanotube forests to other substrates it is necessary to find a way to estimate the forces required to push objects around on the substrates. Here, the approach is to use the cantilevers on the chips to push homogenous objects, and estimate the forces from the deflection of the cantilevers. As objects, latex beads were chosen, since they in a particular sample have a very small size distribution allowing comparison of force estimates between different substrates. For a point force on the tip of the cantilever, the force can be estimated from the deflection by [112];

$$F = \Delta X \cdot \frac{3EI}{L^3} \quad (4.9)$$

where ΔX is the deflection of the cantilever at the tip, L is the length of the cantilever, E is the elastic modulus of the cantilever material and I is the plane moment of inertia. The cantilevers used were made from silicon dioxide with E equal to 70 GPa [112]. The moment of inertia for a beam with rectangular cross section is given by;

$$I = \frac{w \cdot t^3}{12} \quad (4.10)$$

where w is the width of the cantilever and t is the thickness of the cantilever. The thickness is here taken as the dimension in the bending direction, parallel to the surface. That means that the width and thickness have been interchanged as compared to conventional terminology (see Figure 43A). In some cases multiple cantilevers were bending against a single object, in which case the total force was taken as the sum of the individual forces.

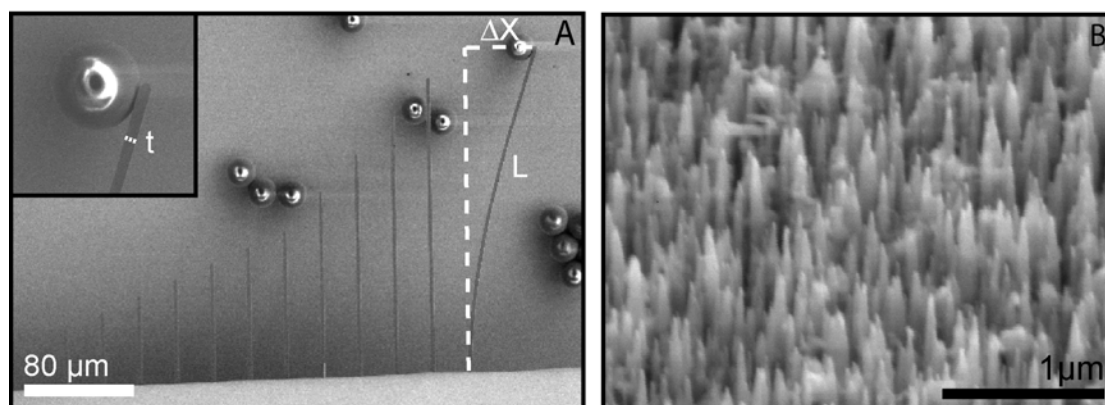


Figure 43 A) The longest cantilever on our xylophone chip is clearly bent while pushing on a 20 μm latex bead resting on a gold surface. The parameters L and ΔX are indicated, as well as the thickness t in the inset. The thickness t is measured to 3 μm and the width is 1 μm . Measured length of longest cantilever is 225 μm . B) A SEM micrograph of the carbon nanotube forest used.

The manipulation tool shown in Figure 43A is equipped with 12 cantilevers, with varying lengths. The longest cantilever, which is seen deflected against a latex bead, has a length of 225 μm , and all cantilevers are separated by 25 μm . Their thickness is measured to 3 μm , and they have a uniform width of 1 μm . The manipulation tools were fabricated using conventional microprocessing [36, 37, 113]. The tool is here mounted on the XYZ manipulator stage within the scanning electron microscope (SEM).

Five different substrates were used for the latex bead stiction studies I) gold, II) Teflon, III) silicon, IV) diamond-like carbon, and V) a nanotube forest. The gold substrate was prepared by depositing 100 nm of gold by e-beam evaporation onto a 500 μm thick silicon wafer. Similarly, the “Teflon” substrate was made by deposition of a 80 nm thick Teflon-like coating from a C_4F_8 plasma onto a 500 μm thick silicon wafer [114]. The silicon substrate was taken as a clean, untreated 500 μm thick silicon wafer, and the diamond-like carbon substrate, prepared by Ken Teo at Cambridge University, was made by depositing a 70 nm DLC film onto a 500 μm thick silicon wafer using an S-bend filtered cathodic vacuum arc system [115]. Finally, the substrate with nanotube forest was prepared in a plasma enhanced chemical vapour deposition (PECVD). Here, a 4 nm thick nickel catalyst film was first deposited by evaporation onto an oxidized (15 nm thick) silicon wafer (500 μm thick). The carbon nanotubes were then grown by PECVD at 650°C from a 50:200 sccm mixture of acetylene:ammonia for 5 minutes. This yielded about 1 μm tall nanotubes, see Figure 43B. Due to the electrical field present in the plasma sheath region, the nanotubes are

automatically vertically aligned in the PECVD process [13, 27, 71]. All the substrates were rinsed in ethanol and blow-dried with nitrogen, except the nanotube forest due to the risk of collapse of the nanotube forest. Subsequently, an aqueous solution of latex microbeads was deposited on the different samples in small droplets using a micropipette. The solvent was evaporated by a low-power heating for 20 minutes.

Measurements on 5 μm latex beads on various surfaces

Friction on carbon nanotube forest

After approaching the manipulation tool to the sample surface, the cantilever is positioned with the tip slightly touching the side of a latex bead. Then the sample stage is moved slowly towards the cantilever. An example of this is shown in Figure 44 A where the cantilever deflection is measured to be 3.2 μm . Such a deflection corresponds to a friction force of 0.1 μN .

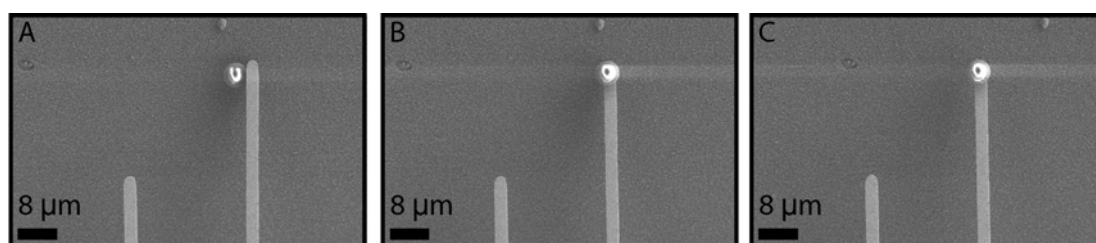


Figure 44 A) The cantilever of the manipulation tool is pushing on the latex bead, and the cantilever deflection is measured to 3.2 μm . B) The bead releases from the surface and jumps on to the cantilever. No deflection can be measured. C) The cantilever with bead can then be moved freely over the surface.

In this case the bead releases from the nanotube forest and jumps onto the cantilever as seen in Figure 44 B. Here, no deflection of the cantilever can be measured, which means that the cantilever itself did not contribute to the friction force by touching the nanotube forest. The found friction force can then be attributed solely to the initial stiction force between the latex bead and the nanotube forest. This is supported by Figure 44 C, where it is shown that the cantilever with the bead on top could be moved over the surface, without any deflection at all, meaning that the cantilever itself did not touch the nanotube forest. Sometimes it could be difficult to judge whether the cantilever contributed to an increase in the measured friction force by touching the nanotube forest. The cantilever could also potentially have a force component pushing the bead toward the surface. However, in both these cases, the potential contribution from the cantilever would be to increase the measured friction force. Thus our measured data are an upper limit of the real frictional forces.

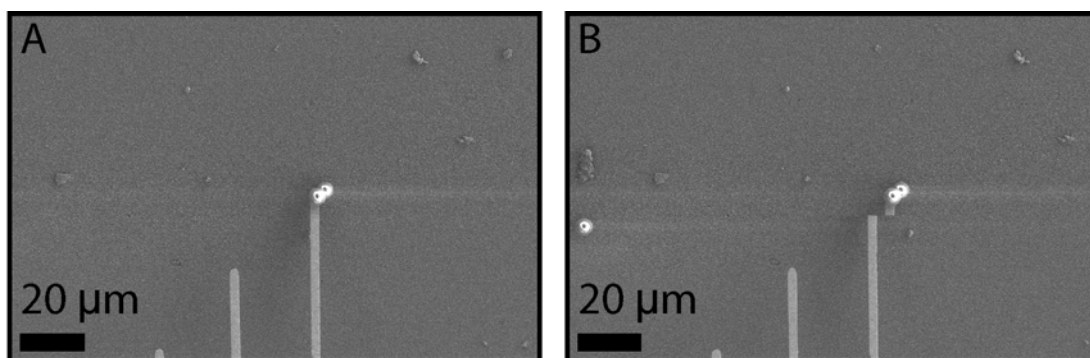


Figure 45 A) The cantilever pulls on a bead B) The bead jumped on to the cantilever during picture registration. The entire deflection of 5.8 μm can be assigned to the initial stiction of the bead.

In Figure 45 another measurement is shown, where we actually pull the bead instead of pushing it. The deflection in Figure 45A could be attributed to the cantilever sticking into the nanotube forest. But as shown in Figure 45B, the bead jumped on to the cantilever during picture registration, and the cantilever has no deflection afterwards. Thus the entire estimated force of 0.2 μN can be attributed to the initial stiction of the bead. Interestingly, the stiction between the bead and the oxide cantilever is stronger. Several measurements on single beads had no measurable deflection of the cantilever at all. However, in these cases it could be uncertain whether the beads had jumped completely off the nanotube forest, and was only stuck to the cantilever. Apparently, the stiction between the beads and the nanotube forest is not very large. It was even possible to move large clusters of 5 μm latex beads, almost without any cantilever deflection. In fact a cluster of 11 beads released from the nanotube forest and attached to the cantilever instead.

The measurement of the dynamic friction force, is done on beads that slide over the nanotube forest due to a continuous push of the cantilever, and then come to rest. The deflection of the cantilever in this situation is a measure of the dynamic friction force. On average, the dynamic friction force was found to be 0.1 μN for the 5 μm latex beads on the nanotube forest, as compared to an average of 0.2 μN for the initial stiction.

Friction on the other substrates

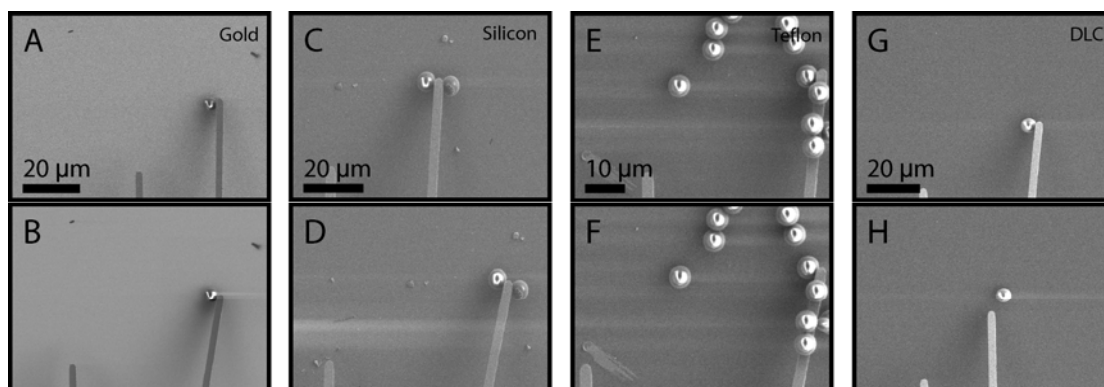


Figure 46 A-B) The cantilever is unable to release any 5 μm latex beads on the gold substrate. C-D) The cantilever is unable to release any 5 μm latex beads on the silicon substrate. E-F) The

cantilever is here seen unable to release a single 5 μm latex bead on the Teflon substrate. G-H) The cantilever is able to release 5 μm latex beads on the DLC substrate.

The other surfaces examined here give mostly entirely different results than the nanotube forest. A typical measurement on the gold surface is shown in Figure 46A and B. Here the cantilever is unable to release the latex bead, with the maximum deflection of the cantilever corresponding to a force larger than 1.1 μN . This was the general results of the gold surface, where no beads could be released by pushing. Equivalent results were found on the silicon surface, where similarly no beads could be released with the maximum force of 1.1 μN , as seen in Figure 46C and D. The maximum force of 1.1 μN was mostly unable to release beads on the Teflon surface as well, as illustrated in Figure 46E and F. However, in one case, a group of three beads released with a force of only 0.8 μN . It was possible to re-approach these released beads, and measure the stiction of the beads after the initial release to 0.3 μN . In these measurements it seemed as if there was no difference between the stiction and the dynamic friction. That is understandable since the coefficients of static and dynamic friction of Teflon on Teflon are equal to each other [116]. The DLC surface showed a behaviour more resembling that of the nanotube forest. It was possible to release the beads, with an average force from the cantilever of 0.6 μN . An example of such a release is given in Figure 46G and H. The bead was released during saving of picture G, and it came to rest as shown in H. The released beads were quite easy to push around, requiring only 0.1 μN on average, which is equal to the value of the nanotube forest. On a slightly different DLC film, which was 40 nm thick instead of 70nm, we found both an initial stiction of 0.2 μN and a dynamic friction of 0.2 μN . The results are summarized in Table 1.

Table 1 Initial stiction and dynamic friction found on various surfaces for the 5 μm beads.

Substrate	Initial stiction (μN)	Dynamic Friction (μN)
Nanotube forest	0.2	0.1
DLC 40	0.2	0.2
DLC 70	0.6	0.1
Teflon	0.8*	0.3
Si	> 1.1	No release
Au	> 1.1	No release

The values are averaged. Several measurements on the nanotube forest with no measurable deflection is not included. The value for initial stiction on Teflon is for a group of three beads that released simultaneously. Several other attempts could not release even individual beads using a force in excess of 1.1 μN

Measurements on 20 μm latex beads on various surfaces

Friction on carbon nanotube forest

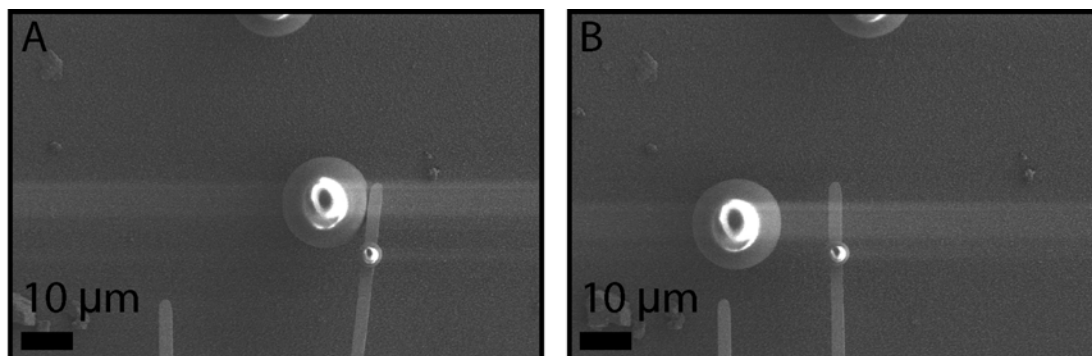


Figure 47 A) The cantilever deflects against a 20 μm latex bead. B) A slight increase in the force releases the bead.

The measurements of initial stiction and dynamic friction are performed in the same manner for the 20 μm beads on the various substrates as was done for the 5 μm beads. A typical measurement result is shown in Figure 47, where the cantilever is seen to push on the bead in A. The force is increased slightly resulting in a release of the bead as seen in B. The deflection of the cantilever was here measured to 20.4 μm , corresponding to a force of 0.7 μN , which equals the average of the measured initial stiction of these 20 μm beads on the nanotube forest. However, sometimes the initial stiction was measured as low as 0.2 μN . The dynamic friction can be estimated from the deflection when a sliding bead stops its movement. The estimated value for this is also 0.2 μN . It has to be stressed, that it is not trivial to evaluate the difference between deflections due to stiction or dynamic friction on this substrate. Also there does not appear to be any significant difference between initial stiction and the subsequent stiction, and all measurement on stiction has been put in the same category. It can be noted that the nanotube forest seems completely undamaged after removal of the beads, see for instance Figure 47B. This strengthens the argument that there is no gluing effect on this substrate causing a higher initial stiction.

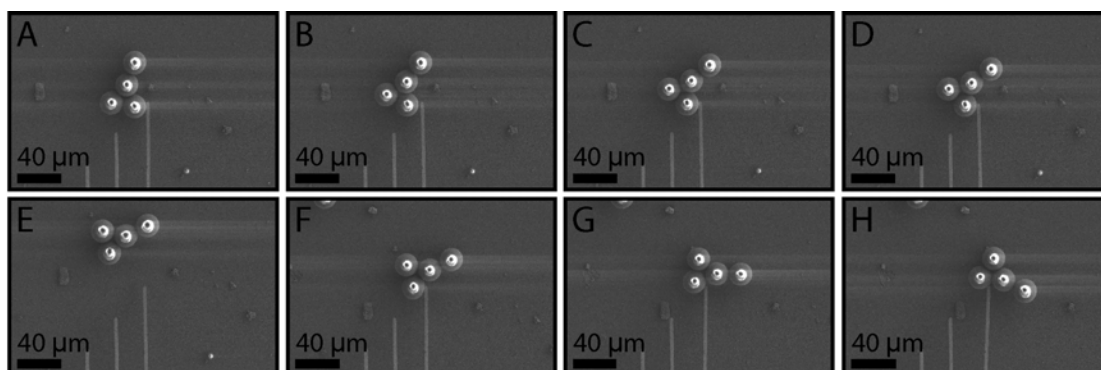


Figure 48 A) A large cluster of 20 μm beads is approached. B-D) By pushing slightly it is possible to rotate the cluster. E) The cluster jumped away. F-H) Re-approach allowed further rotation of the cluster.

As was seen for the 5 μm beads, it was possible to move clusters of 20 μm beads almost without any cantilever deflection. In Figure 48, four 20 μm latex beads are moved on the nanotube forest. Here the beads are rotated freely in Figure 48A to D, where the cluster then jumps to a new position as seen in E. Subsequent re-approach allowed further rotation (Figure 48F to H).

Friction on the other substrates

As for the 5 μm beads, the 20 μm beads could not be released on the gold or silicon substrates by pushing the beads with the cantilever even with a force in excess of 2 μN . However, it was possible to release a few beads on the gold surface by driving the cantilever under the bead from below. On those released beads the dynamic friction could be measured, which were on average 0.6 μN . The initial stiction appear to be very high on gold, whereas the dynamic friction is more comparable to that of the nanotube forest. What is interesting to note is that after releasing beads on the gold surface, the surface underneath the beads were damaged, as well as the beads appeared to have some material attached to them. This can be seen in Figure 49 A, where the bead has been released from the black spot in the centre of the picture. On silicon it was completely impossible to release any beads, even when pushing very hard from below, as shown in Figure 49 B.

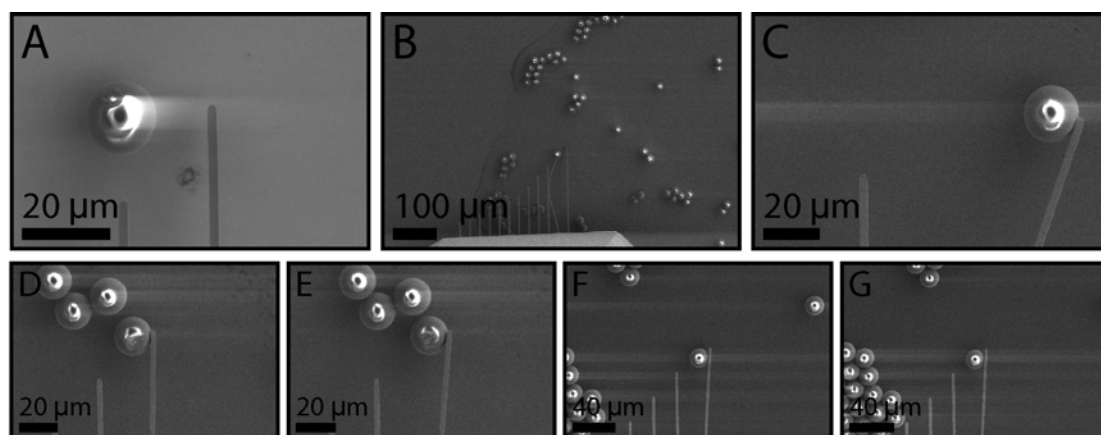


Figure 49 A) A bead released on gold by pushing from underneath. Note the damaged surface (black spot in the center). B) On Silicon it was impossible to release any beads. C) On Teflon, large cantilever deflections was not enough to release the beads. D-E) A released bead on Teflon (by pushing from below) can be moved on the surface. F-G) On the DLC substrate, released beads (by pushing from below) could also be moved.

On Teflon the behaviour was similar to that of gold. It was impossible to release any beads by pushing from the side as shown in Figure 49 C. Only when pushing underneath the beads from below could a few beads be released. Such a released bead is shown in Figure 49 D and E. Here it is seen that the bead is moves sideways towards the small cluster of other beads, due to the cantilever push. The average dynamical friction for such 20 μm beads sliding on Teflon was estimated to 0.8 μN . Note that also this bead appear to have some kind of residual material on the top. Interestingly, the DLC substrates behaved here more like the other substrates than

the carbon nanotube forest. On the thinnest DLC sample (40 nm thick), it was completely impossible to release any beads, even when using the push technique from below. It has to be said, that on this substrate, no single bead could be found and the release attempts were done on the smallest groups of three beads. On the thicker DLC substrate (70 nm) the situation was similar. However, here some single beads could be released by pushing from below. Such a bead is shown in Figure 49F and G, where it is seen moved towards the large cluster of beads to the left. The average dynamical friction for 20 μm beads on the DLC (70 nm) substrate was estimated to 0.4 μN . The results found for the 20 μm latex beads are summarized in Table 2.

Table 2 Initial stiction and dynamic friction found on various surfaces for the 20 μm beads.

Substrate	Initial stiction (μN)	Dynamic Friction (μN)
Nanotube forest	0.7	0.2
DLC 40	> 2	no release
DLC 70	> 2	0.4
Teflon	> 2	0.8
Si	> 2	no release
Au	> 2	0.6

The values are averaged. Several measurements on the nanotube forest with no measurable deflection is not included. With this soft cantilever it was impossible to release the beads on most substrates (all other than the nanotube forest). However it was possible to release some beads on some substrates by pushing from underneath (along the axis of the cantilever).

Shorter, stiffer cantilevers

The results obtained with the manipulation tool used in the previous sections, suggest the need of a shorter, stiffer cantilever, to get quantitative data on the surfaces with high stiction. Thus microfabricated probes, with four short (20-40 μm) cantilevers were used. The stiction of 5 μm latex beads was then measured on the gold, silicon, Teflon, and carbon nanotube forest substrates.

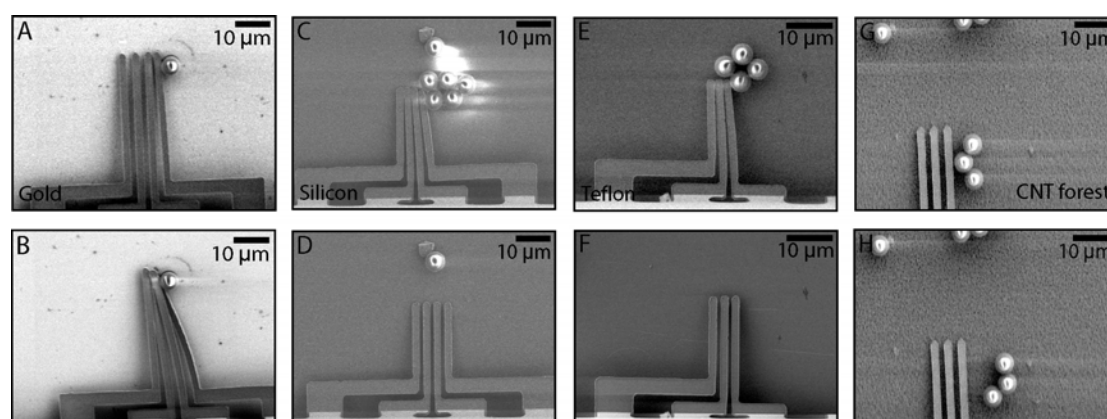


Figure 50 A) A micro four point probe is moved in contact with a latex beads resting on a gold covered surface. B) Even by applying a force on the order of 70 μN it is not possible to move the latex bead. C) A force of 57 μN is applied to a group of five beads on the silicon surface. D) By increasing the force slightly, all beads are released. E) A force on the order of 25 μN is applied to one latex bead situated in a small cluster on a Teflon coated silicon surface. F) By increasing the force slightly, all the latex beads detach from the substrate and, due to the built up tension in the cantilevers, are shot away. G) Latex beads resting on top of a nanotube forest are approached by

a microchip with three cantilevers. H) Without any visible deflection of the cantilevers, the latex beads are easily moved around on the surface.

By pushing laterally on latex beads lying on the gold substrate, it was generally not possible to release them, as shown in micrographs A and B in Figure 50. A huge force on the order of 70 μN was only enough to bend the cantilevers on top of each other. This was experienced on several beads. However, a group of three beads were released with a mere force of 41 μN in one situation. On the silicon surface it was possible to release groups of beads by employing a force of 57 μN per bead on average. One such case is shown in Figure 50 C and D. A similar behaviour was found on the Teflon substrate. Micrographs E in Figure 50 shows that a force estimated to about 6.4 μN per bead was not enough to release a cluster of four beads on the Teflon substrate. A slight increase in the exerted force, however, was enough to release all four beads instantly, Due to the built up tension in the cantilevers the beads where shot away, as seen in Figure 50 F. On the nanotube forest the situation was again remarkably different. In Figure 50 G the microprobe approaches a small cluster of three latex beads. On this substrate the latex beads can be easily pushed around without any observable deflection of the cantilevers, as seen in H. In fact, in some cases the beads start to move simply due to electrostatic attraction or repulsion of the cantilever, which is slightly charged due to the electron beam in the SEM. The results are summarised in Table 3.

Table 3 Stiction and dynamic friction on various substrates compared to each other. Results found with short cantilever and 5 μm latex beads

Substrate	Initial stiction (μN)	Dynamic Friction (μN)
Nanotube forest	0 ?	0 ?
Teflon	6.4	No measurement possible
Silicon	57	No measurement possible
Gold	>70*	No measurement possible

* Most beads on the gold substrate could not be released by a force in excess of 70 μN . However one group of three beads were released with a force of only 41 μN , corresponding to an average of 14 μN per bead.

Additional comments

During the work a special behaviour of the latex beads was discovered. It could be difficult to approach the cantilever to the surface in a controlled way, since the distance between the cantilever and the surface is hard to judge. However, it was discovered that the latex beads give a sort of mirror reflection of the beam descending in the vicinity of the bead. This is probably some sort of charge shadow, but, as can be seen in the picture series in Figure 51, the result is a mirror image of the cantilever approaching the surface. This could be used to calibrate the movement, since a particular position of the shadow meant a particular distance above the surface.

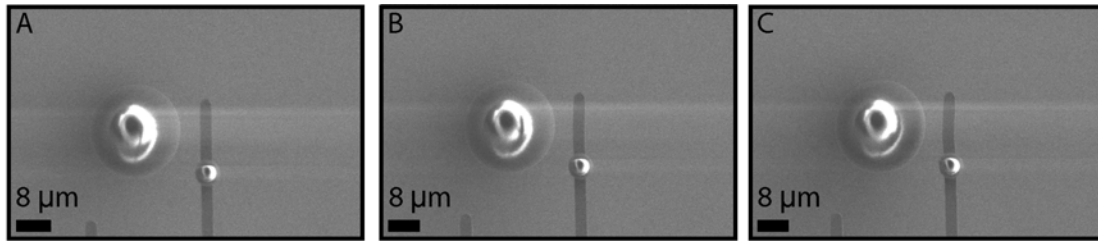


Figure 51 A-C) As the cantilever was approached the surface, a mirror reflection of the cantilever could be seen on the latex beads. This was used to control the height of the cantilever above the surface during the experiments

Summary

The latex beads had a very low stiction on the nanotube forest. It is very hard to tell whether or not there is a difference between the initial stiction and the stiction after first release on this substrate, and to distinguish that from the dynamic friction. Typical measurements of the necessary force to move the 5 μm beads were in the range 0.1 μN to 0.3 μN . However, examples of no measurable deflection of the cantilever were also seen, corresponding to a measured force of 0 μN . On the 40 nm DLC film, an average of 0.2 μN was enough to release the 5 μm beads, and the dynamic friction was also found to be 0.2 μN . Interestingly, the 70 nm DLC film had a higher initial stiction of 0.6 μN , but here the measured dynamic friction was as low as 0.1 μN . It was extremely hard to release any beads on the silicon and gold surfaces, and even on the Teflon surface. By using the shorter and stronger cantilever, it was possible to measure extremely high stiction values on these surfaces as compared to both the DLC surfaces, and especially the nanotube forest surface. The main finding is that whereas all the other surfaces seem to have a very high initial stiction as compared to the dynamic friction (perhaps with DLC as an exception), this is not the case for the nanotube forest. On the nanotube forest, there seems to be no real difference. It is remarkable how large clusters of beads can be moved on the nanotube forest, almost without any cantilever deflection. Such behaviour was not seen on any other surface.

Manipulation of Nanowires

Introduction

The special stiction and friction properties of carbon nanotube forests suggest that this kind of surface could be appropriate for nanomanipulation. In pick and place assembly of nanostructures one of the main problems is to pick up the nanocomponents. Nanotubes and nanowires tend to stick very well to any surface, and traditionally it has only been possible to pick up such components if parts of them were sticking up from the surface, or over an edge [85]. These issues have been a major problem for decades, and effectively prevented nanomanipulation to become a relevant technique for assembly of devices. P-6P nanofibres are very soft and fragile. They break at a shear stress of just 20 MPa [111], making manipulation very challenging. It has been shown that once the p-6P nanofibres were dispersed on a Teflon-like surface, only short pieces of these roughly 50 nm tall, and 300 nm wide, nanofibers could be pushed along the surface using the tip of an atomic force microscope [111]. To lift up such nanofibres is then practically impossible. The low friction, combined

with the compliant property of the nanotube forest, suggest that it can be an appropriate manipulation surface for these nanostructures. The fragility of the p-6P nanofibres makes them suitable for evaluating the usefulness of the nanotube forest as a nanomanipulation workbench.

Manipulation of nanostructures

Some initial pick and place tests on the nanotube forest is shown in Figure 47. The experimental setup was similar to the one used for manipulating latex beads, but rather than a microchip equipped with cantilevers, an electrochemically etched tungsten tip was used as the manipulation tool. The tip was also mounted on the xyz manipulator inside the SEM.

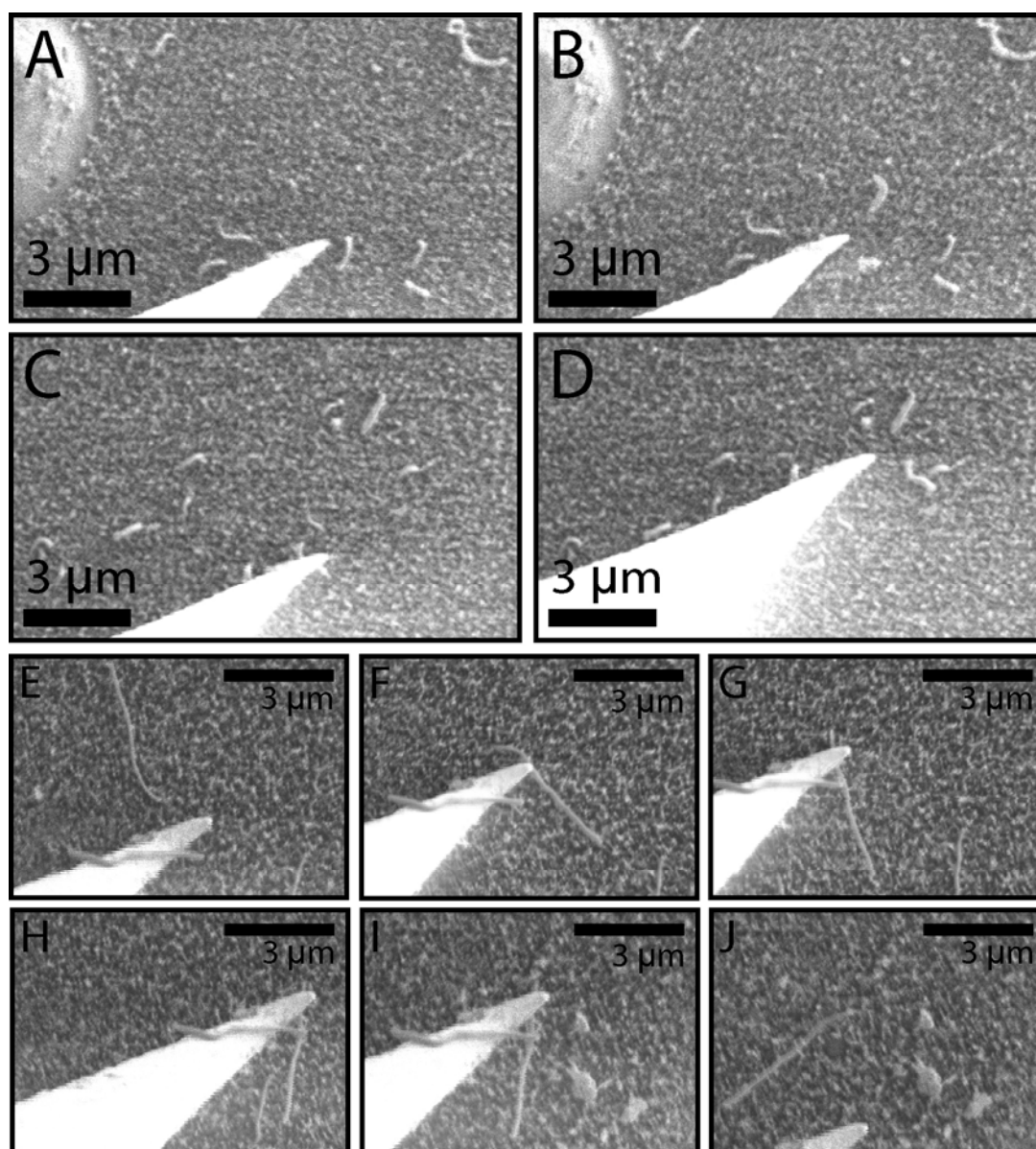


Figure 52 A) An STM tip approaches a larger CNT on top of the nanotube forest. B) The CNT is displaced 1-2 μm by pushing. C) Another CNT is picked up by touching it from above. D) By lowering the tip into the nanotube forest it is possible to place the CNT on the forest again. E) An STM tip is approached to a p-6P nanofibre resting on top of the nanotube forest in the upper part of the micrograph. F) Comparison between micrograph A and B show that one single nanofibre has been moved. G) The nanofibre is now attached to the STM tip and can be easily

moved to other places as seen in H. I) By approaching the STM tip to the surface again we try to place the nanofibre in a new location. J) The nanofibre is seen to have been successfully placed on the substrate.

Figure 47A shows the tungsten tip approaching one large carbon nanotube resting on top of the carbon nanotube forest. In B, the same nanotube is seen to have been pushed 1-2 μm s upwards. Another nanotube is approached in C and touched from above by the tungsten tip. Interestingly, the nanotube attached better to the tip and could be lifted off the nanotube forest. However, the attachment to the tip was not stronger than that it was possible to place the nanotube on the forest again by lowering the tip into the forest, and pulling it sideways. In Figure 47 E to J a similar manipulation is shown for a p-6P nanofibre. In this experiment, the sample was first prepared by depositing an aqueous solution of the nanofibres on the nanotube forest and then dried in air. Comparison between Figure 47E and F shows that a nanofibre over the tip in E has been moved a small distance downwards in F. There is also one nanofibre lying on top of the tip without interfering. In Figure 47 G the nanofibre has released from the surface, also here by pushing gently on it from above, and it is now attached to the tip. It is then possible to transport it over the surface as shown in H. In Figure 47 I the surface was approached again with the tungsten tip and the nanofibre was placed on the surface again, as shown in J. Clearly, the organic nanofibres adhere only very lightly, on the nanotube forest. It was sometimes possible to lift off the nanofibres simply by touching them from above, indicating that the adhesive forces between nanofibre and tool were stronger than the forces between nanofibre and nanotube forest.

Pick and place of nanostructures with integration into microsystems

On the nanotube forest the nanostructures adhere only very lightly. Moreover, the ability of each individual carbon nanotube to deflect in any direction as a response to an applied force makes the nanotube forest mechanically compliant. This enables the nanofibres to be lifted up, not only by touching them from above, but also by pushing the tungsten tip slightly into the nanotube forest, under the nanofibre and pull it up. In order for this to be possible, the tip of the manipulation tool needs to be very sharp. It was found that tips with a radius of curvature comparable to the diameter of the nanofibres were suitable. The sharpness of the tungsten tip, combined with its mechanical strength, seem to make it highly suitable as a manipulation tool. Furthermore, it was observed that if a freshly etched tip was used, the nanofibres were less likely to stick to the tip. Storing the tips in ambient conditions for several days causes the growth of a thin native oxide layer. The nanofibres adhere better to such oxidized tips thus facilitating easier pick up of the nanofibres, and consequently more difficult release.

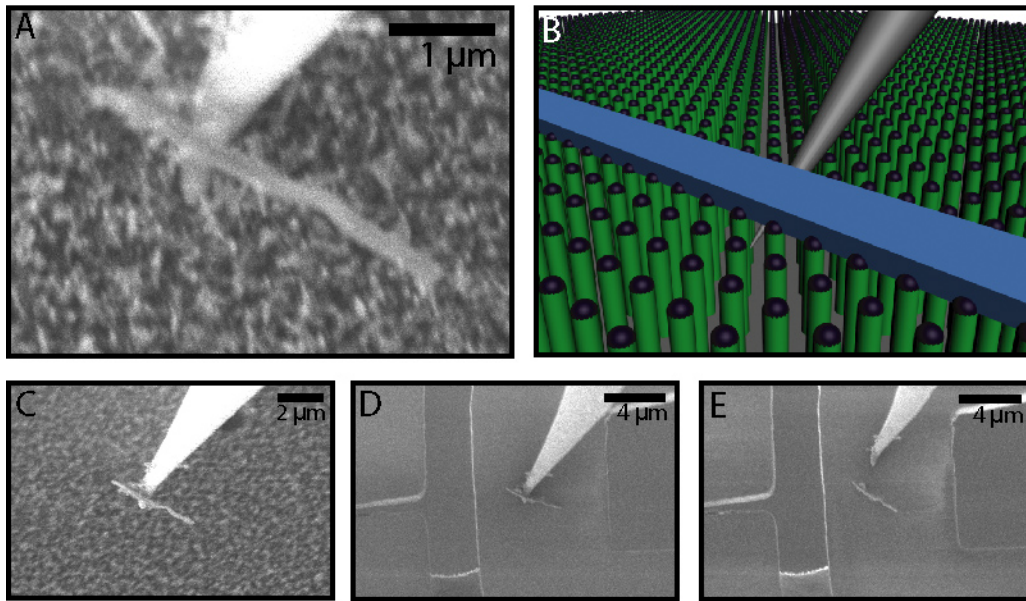


Figure 53 A) A tungsten tip is approached to a p-6P nanofibre resting on top of a nanotube forest, and moved underneath the fibre. B) Illustration of the technique used for manipulation of fragile organic nanofibres. An electrochemically etched tungsten tip is moved beneath the nanofibre slightly into the mechanically compliant nanotube forest. The nanofibre may then be lifted by pulling the tip vertically up. C) The nanofibre is lifted off the nanotube forest by pulling the tip up. D) The nanofibre is then placed onto electrode supports on another microchip. E) By pulling the tip away, the nanofibre remains on the electrode support, as it has been moved from a surface with low adhesion to a surface with higher adhesion.

In Figure 53A a tungsten tip was moved underneath the nanofibre, as shown in the illustration in B. By lifting the tip, the nanofibre was successfully released from the surface as seen in Figure 53C, and was now attached to the tip. The nanofibre could then be moved and placed controllably onto electrode supports on another microchip, see Figure 53D. The tip was successfully retracted as seen in Figure 53E. Furthermore, a custom-built manipulation set-up [117] was used, by Casper H Clausen, to perform equivalent manipulations in ambient conditions under an optical microscope. Also here was it possible to pick up nanofibres from the nanotube forest, and place them on electrode supports. Also, manipulation in SEM has been successfully used to transfer bismuth nanowires to electrode supports.

Once an organic nanofibre is successfully placed in the desired position on the electrode supports, it is possible to do electrical characterization of the particular nanostructure. With a nanomanipulation-based, resist-less shadow mask technique [117], electrical contact can be made to the nanofibre to characterize its electrical properties (see Figure 54A).

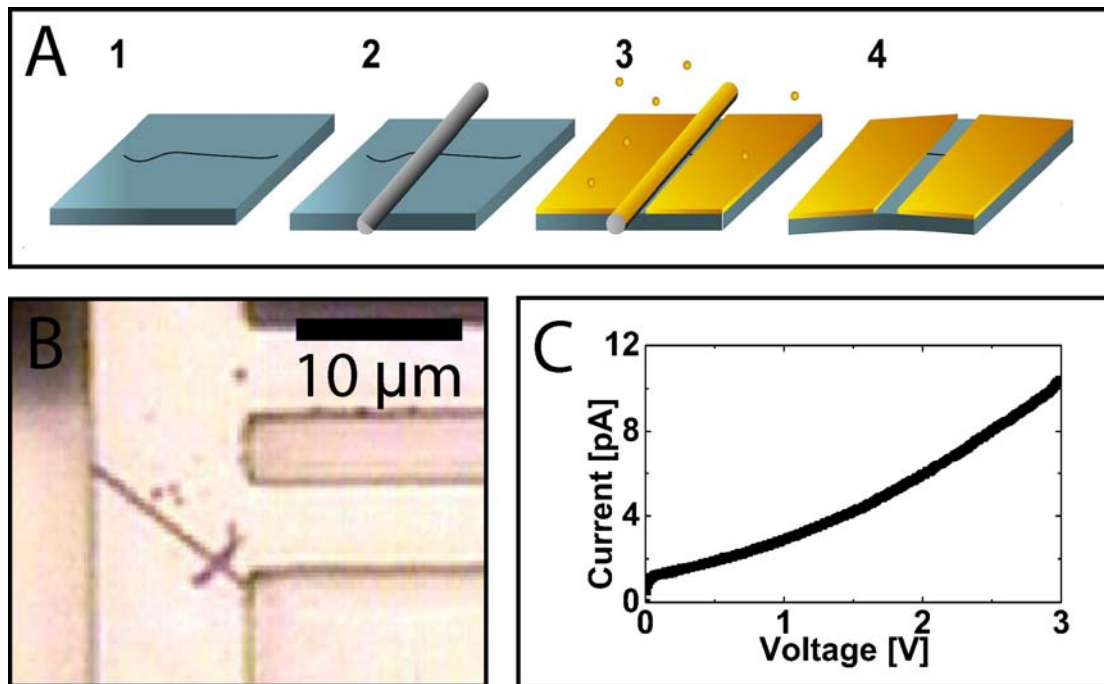


Figure 54 A) An illustration of the shadow mask technique. (1) The nanofiber rests on electrode supports. (2) A SiNW is placed on top. (3) Metal is deposited. (4) After removal of the SiNW the nanofiber is left between two electrodes. B) After lift off of the shadow mask, the nanowires is seen to lie on the electrodes, which a black line crossing over and cutting the electrical contact through the gold electrodes C) Electrical characteristics of a p-6P nanofiber mounted via assembly in a SEM. The measurement shown is consistent with other p-6P measurements, made using manipulation as well as other methods [118].

The shadow mask technique works by manually placing a silicon nanowire across the nanostructure to be characterised, in such a way that the SiNW covers the oxide electrode support underneath from one side to the other (2). Subsequent electrode metal deposition by evaporation is then done (3), and the SiNW is lifted off (4) using a custom built manipulation set up [117]. The nanofiber is then left on the electrode support, spanning a gap between the two electrodes, as seen in Figure 54B. Electrical measurements can then be done and Figure 54C shows the electrical characteristics of a single p-6P nanofiber, electrically contacted with two electrode supports via manipulation in SEM and nanowire shadow masking (Electrical measurement done by Jakob Kjelstrup-Hansen). As demonstrated in Figure 54, it is possible to contact and study individual nanofibres manipulated onto a target structure, however the analysis and interpretation requires invoking additional theoretical models, which are beyond the scope of this work.

Summary

Previous work have shown how difficult it is to overcome the attraction forces between the surface and the objects [85], and this remains one of the main challenges of micro and nanoscale pick and place manipulation. Here it was shown that it was possible to grab individual nanofibres resting on a nanotube forest, and place them controllably on desired locations in other microsystems. Thus, surfaces coated with vertically aligned carbon nanotubes appear to be highly suitable as a workbench for the manipulation. When dispersed on a nanotube forest, only the nanotube tips are in contact with the object, minimizing the effective contact area greatly and hence

lowering the total stiction and adhesion forces. The compliance of the nanotube forest helps further the manipulation through allowing the manipulation tool to grab underneath the fragile nanofibres. In comparison, this type of manipulation on surfaces such as gold or Teflon is practically impossible.

5 CVD-PECVD chamber

Introduction

In this chapter, the construction of a setup for growing CNs is presented. In situ integration of CNs into microsystems requires good and convenient access to equipment for growing CNs. In this project it was important to construct a setup that could allow CN growth on full 4 inch wafers, since our ultimate goal is have waferscale integration of CNs into microsystems. Another important point was to have a setup available for testing CN growth on microfabricated structures made with the process recipes developed in this project. There exist many different types of CVD and PECVD chambers for growing CNs [13]. We wanted to build a flexible system that could work as thermal CVD, PECVD (dc glow discharge PECVD [72]), and finally thermal CVD with electrical connections to in situ electrodes. Furthermore, the chamber should eventually allow growth of CNs on full 4 inch wafers. Thus a vacuum chamber was chosen, that could fit a stage for a 4 inch wafer. The heating stage cannot hold 4 inch wafers at the present time, and should be modified when that is needed. Some parts of this work, notably the design of the heating stage and programming of a software for controlling the massflow controllers, were results from a special course co-supervised with Jakob Kjelstrup-Hansen.

Construction

Vacuum system

The central core of a CVD reactor consists of the vacuum chamber itself, with connected vacuum tubes and valves, as well as pump system and exhaust. The system has been developed over several stages to accommodate the needs. Figure 55 shows an overview of the system, including the gas supply lines. The vacuum system consists of the following main parts;

- The vacuum chamber, which is constructed of stainless steel with a glass plate as lid (see Figure 55B and C). The glass plate allows us to monitor the growth process. The chamber has three separate connections. One connection is used for introducing the reactant gases, and another is used for pumping. The pump is necessary both for pumping vacuum and flushing the system, but also in order to keep the gas composition and pressure stable during growth. The last connection is used for feed through of electrical connections. There are in total 4 possible feed throughs, two from each side of the T fitting as seen in Figure 55. However, only three are in use - one for the thermocouple, one for the resistive heating of the stage and one for the plasma generation.
- The pump line, seen to the left of the vacuum chamber in Figure 55B. It consists of QF tubes with connections and two valves. One valve is placed close to the pump inlet, and the other is placed close to the vacuum chamber. In between the vacuum chamber and the valve a Pirani pressure gauge is located. The gauge monitors the pressure in the chamber during growth. It is crucial to maintain the pressure in the chamber at a controllable and stable

level. Therefore a parallel tube of much smaller dimensions, using VCR-2 fittings and swagelock, is placed to short-circuit the main valve between the pump and the vacuum chamber. This secondary line has a needle valve that allows control of the pressure in the main chamber with high precision, when the main valve is closed. The needle valve allows pressures in the range 10-50 mbars with a precision of 1 mbar, given the usual gas flow into the chamber. Ideally we should have better control also from 0.5 mbar to 10 mbar, and this could be achieved by changing the needle valve. However, it is possible, although difficult, to control the pressure in the range 0.5-2 mbar with the main valve.

- The exhaust system consists of a rotary pump (Alcatel OME 25S) that pumps the exhaust gases into the general ventilation system. Since the pump is pumping on potentially explosive gases, some extra considerations had to be made. First, the pump has to work on silicon oil. Silicon oil will not ignite even when pumping on gases such as hydrogen, methane or acetylene. However, as an extra precaution, an extra line gas line introduces a co-flow of nitrogen immediately in front of the pump (Figure 55D). This co-flow is controlled by another needle valve. The valve is set to a level that dilutes the exhaust gases by about 10 times as much nitrogen as reactant gases.

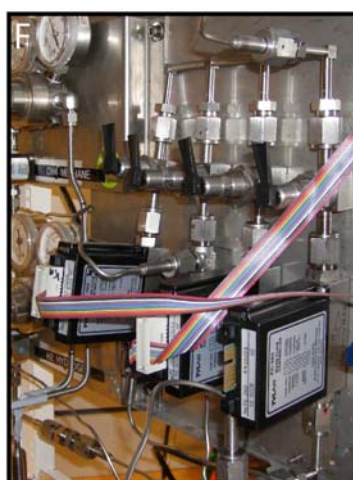
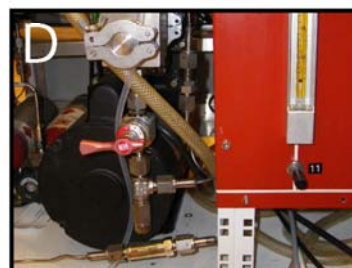
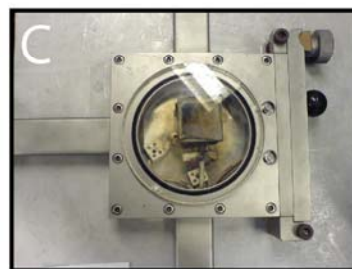
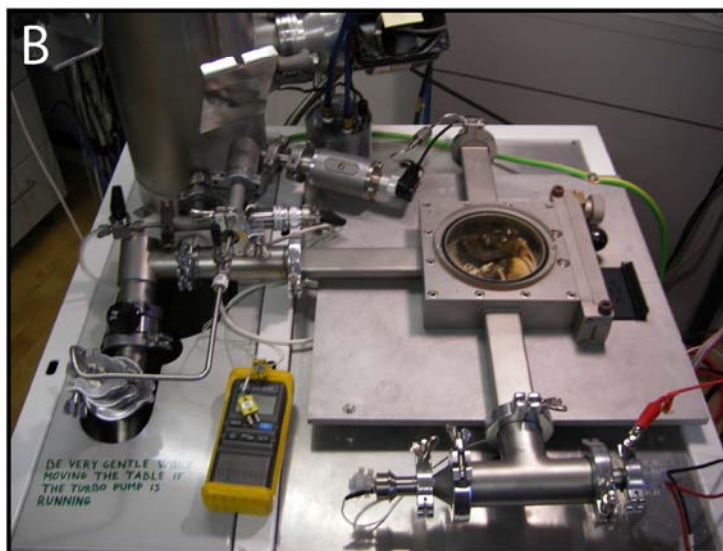
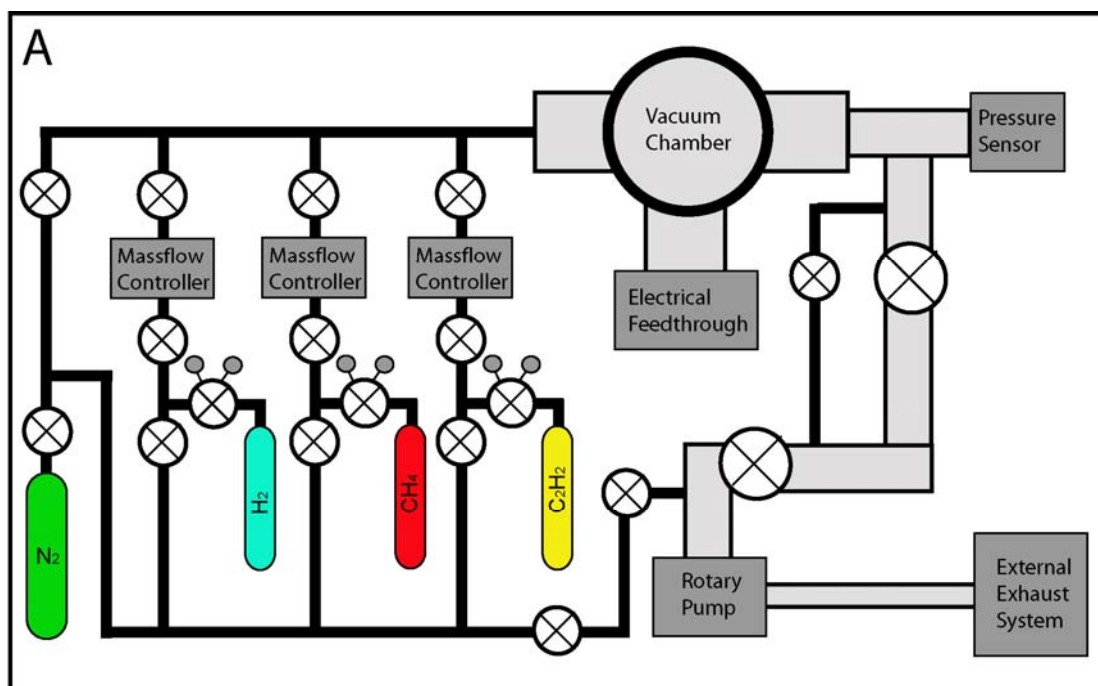


Figure 55 A) Sketch of the gas line system and the vacuum system. B) The CVD reactor system, showing both the vacuum chamber, the exhaust tubes to the pump, the inlet of gases, and the T-fitting with electrical feed-throughs. C) The CVD vacuum chamber, with the sample stage. D)

Immediately in front of the rotary pump a co-flow of nitrogen is let in, diluting the exhaust gases by 10 times. E) The pressure reduction valves for two of the gas lines, with additional valves. F) Massflow controllers with valves in front of the mixing point. G) Two of the gas bottles lies on the floor. The acetylene bottle is attached standing on the outside.

Gas supply system

The reactant gases in the system are methane, acetylene, and hydrogen. The flows of these three gases are individually controlled by three separate massflow controllers. Before entering the reaction chamber, the reactant gases are mixed. In addition to these three reactant gases, nitrogen is connected in a separate line to both the mixing point of the gases, and to each separate gas line. All the three gas lines can also be flushed with nitrogen separately. The three gas lines are constructed identically. The tube fittings are of swagelock and VCR-2 types. From the gas cylinders a high pressure tube fitting connects to a pressure reduction valve system. The operating pressure is reduced and on the low pressure side it is in the range 2-3 bars. As can be seen in the schematic in Figure 55A, the line divides into two lines, each blocked with a valve, on the low pressure side. One valve controls the access of nitrogen, the other valve controls the reactant gas flow towards the massflow controller. When open, the mass flow controller allows the reactant gas to flow through at a given rate set in a controlling software. Between the massflow controller and the reaction chamber there is another valve. The flows through the mass flow controllers are controlled by a National Instrument Labview software program. The controllers are operated by a voltage between 0 and 5 V, where an input of 0V closes the flow, whereas 5 V opens it fully to a flow of 10 sccm (standard cm³ per minute). The flow is calibrated for N₂ gas, which means that the actual gas flow has to be corrected with a factor. These factors are given in Table 4.

Table 4 Gas flow correction factors.

Gas	Factor
H ₂	1.01, [119]
CH ₄	0.72, [119]
C ₂ H ₂	0.62*

* Calculated from formula given in appendix C

The mass flow controllers also measures the actual flow they let through, and this signal is sent back as a voltage between 0 and 5 V as well. In the software, the gas flow is given as a percentage of the maximum flow, and the measured flow is shown in a corresponding display. The software has the possibility to control only two mass flow controllers at a time. However, during runs of the system, only two gases will be used, and the control cable is simply switched between the methane and acetylene mass flow controllers according to which gas is required.

Heating

CNs are synthesized at a high temperature. This is partly due to the need for energy in order to dissociate the reactant gas molecules, and partly due to the need of a high temperature to activate the catalyst material [13, 14]. Most CVD systems normally

use a tube oven to supply the heat. However, a tube oven is not suitable for waferscale synthesis of CNs. Therefore a small vacuum chamber is used. It is then necessary to have a heating stage inside the chamber. A common way of constructing a heating stage is by using wolfram filaments through which a high current is sent. Thus the resistive dissipation in the Wolfram filaments provides the necessary heat [72]. Here, a novel approach using two high power light bulbs of 400W each placed inside a stage fabricated in graphite (Figure 56A and B). The graphite stage absorbs all the energy from the bulbs, including the radiation energy. The graphite stage rests on a layer of ceramic, insulating it from the chamber floor.

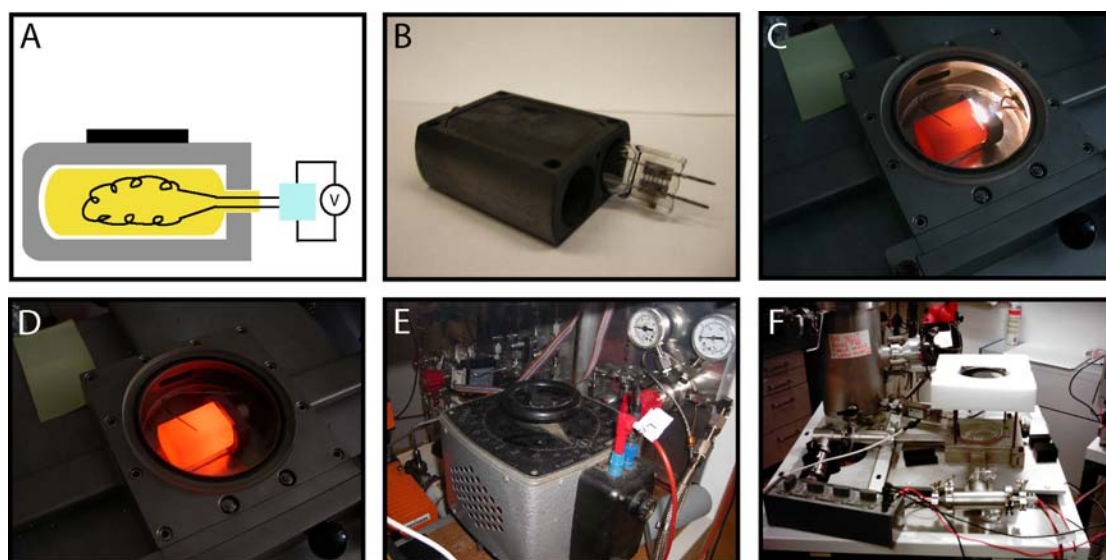


Figure 56 A) Sketch of the graphite stage with light bulbs. The substrate is placed on top. B) Picture of the graphite stage. C) Picture of the heating stage when light bulbs are on. D) Picture of the heating stage just after turning off light bulbs. E) The power supply used for heating the stage. It can provide a current up to 10 A. F) After growth the cooling is assisted by an electric fan placed on top of the chamber

In Figure 56 C, the light bulb is on and heating the stage to a glowing orange colour. Very little light from the bulb escapes, since it is trapped inside the graphite cavity. An added value of this approach is that the light bulbs are long lived, as compared to open Wolfram filaments which need to be changed frequently. In Figure 56 D the stage is shown with the light bulb just turned off. The power to the light bulbs is provided with a power supply (Figure 56 E) capable of delivering up to 10A. The system heats the stage rapidly. However, after growth the cooling process is slower. An efficient approach has been found to cool it down to less than 100 °C in about 20 minutes. The chamber is evacuated after growth, and flushed with nitrogen three times once the temperature is below 500 °C. The valve towards the rotary pump is then shut, and the chamber is filled with nitrogen and left at atmospheric pressure, to increase the heat conduction. A fan, as seen in Figure 56 F, is placed on top of the vacuum chamber throughout the cooling process. Once the temperature reaches 100 °C, the chamber can be opened and the samples taken out.

Heating characteristics

The temperature is measured by a K-type thermocouple, mounted with its end into a hole drilled in the graphite stage. This hole is drilled close to the surface of the stage, where the substrate rests. The signal from the thermocouple is converted into a temperature with an ISO-Tech ITA11 temperature converter, and displayed on a Keithley voltmeter for manual readout. A routine has also been made to record the temperature by the software controlling the massflow controllers. The signal from the thermocouple is taken out through the electrical feed through in one end of the T-fitting on the vacuum chamber. The other feed through is reserved for high voltage and current, used for heating and plasma generation.

The capacity of the heating system to heat the stage with the substrates fast is important. Initially we run several heating tests to find the operating range of the system, using methane as the atmospheric gas. In Figure 57 a graph for several heating series are shown. The heating here is done simply by turning the power supply to a given voltage, and record the rise of the temperature as a function of time.

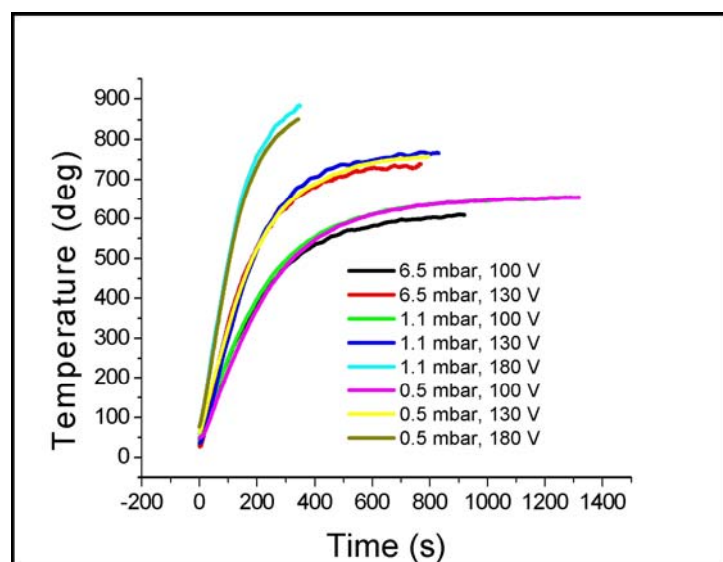


Figure 57 The heating characteristics of the temperature stage for different applied voltages, and pressures. These tests were run with one 1000 W light bulb (in a one bulb stage) and methane gas in the chamber. The data were obtained by Elvis Ramovic and Christian Agger in a supervised course.

It is interesting to note that in this low pressure regime, there does not seem to be a large influence on the heating characteristics from the pressure variation. In fact, for 180 V applied heating, the 1.1 mbar case is seen to heat to a higher temperature than the 0.5 mbar case. This is the opposite of what might be expected since a higher pressure leads the heat away from the stage. The influence of the pressure is expected to be more important the higher operating pressure. This is supported by the fact that both test runs at 6.5 mbar heat to considerably lower temperatures than the 1.1 mbar and 0.5 mbar at equivalent applied voltages. This trend should continue for higher operating pressures. As expected, there is a response to the applied voltage. The 180 V cases heated very rapidly to over 800 °C, whereas the 130 V cases stabilised around 750 °C and the 100 V cases at around 600 °C. These measurements were done on a graphite stage having one 1000W light bulb. The applied voltage could have been

increased to 220 V if needed. It is seen that the current setup provide a sufficient amount of heat to reach the growth temperature range of 600-900 °C. In real runs, however, the heating approach will be to turn on a high voltage in the beginning, and gradually reduce this voltage when approaching the desired temperature.

Plasma generation

As discussed in chapter 2, a plasma-enhanced CVD facilitates growth synthesis at lower temperatures, as well as providing an electrical field that aligns the nanotubes during growth. The plasma helps dissociating the reactant gases, thus speeding up the synthesis. A plasma generating stage was built by modifying the thermal CVD stage. A sketch of the system and some pictures of the stage are shown in Figure 58. The stage was wired up as a cathode with a graphite plate on top as an anode, separated from the cathode by four 10 mm ceramic rods (Figure 58B and C). The anode is placed on top of the ceramic supports in a way that allows easy replacement of the substrates between the anode and the cathode. The stage, which effectively is a plate capacitor, is connected to a high voltage supply through the electrical feed throughs in the T-fitting of the vacuum chamber. The high voltage supply used here could deliver up to 600 V and 0.25 A. Ideally, since the reaction chamber is grounded, and due to the geometry of our stage, we would have liked to put the cathode (the lower part) to a potential of 0 V and the anode at + 600 V. However, it has not been possible to achieve stable plasma under these conditions. Therefore we do not force the cathode to 0 V but allow it to be set by the plasma power supply. During runs we have measured the cathode at -500 V and the anode a 100 V, roughly. This configuration causes plasma to be formed all around the cathode, since the wall of the reaction chamber itself effectively becomes an anode. However, the resulting plasma becomes very stable. Examples of such stable plasmas are shown in Figure 58 D and E. Stable plasmas are most easily obtained with pressures above 10 mbar. For lower pressures, arcing between the anode and the cathode may burn the fuse in the plasma generator. To avoid this problem, an adjustable resistance was placed in series with the plate capacitor (the stage). Thus, if arcing occurs, there will still be resistance high enough in the circuit to avoid the plasma generator to shut down. As mentioned, another problem with the design is that the plasma is not only formed between the anode and the cathode, but all around the cathode. This is due to the vacuum chamber itself, and in particular the aluminium plate on which the stage rests (isolated with ceramics), effectively works as an anode as well. Thus the plasma is not only confined to between the designed anode and cathode, but cause the entire cathode to be covered in a plasma glow, as seen in Figure 58 D and E. However, this does not seem to cause any problems with the stability of the plasma. But the problem can be avoided if the chamber is replaced with a larger one, allowing the stage to be better isolated from the chamber walls. Furthermore, the plasma shown in Figure 58 D is without thermal heating and the plasma in Figure 58 E is with thermal heating. The shape of the plasma is seen to be very similar in the two cases, thus indicating that the thermal heating does not disturb the plasma. In the two images the plasma colour appears to be different. This is just an artefact of the camera, which give different colours when the light bulb in the thermal heating is on.

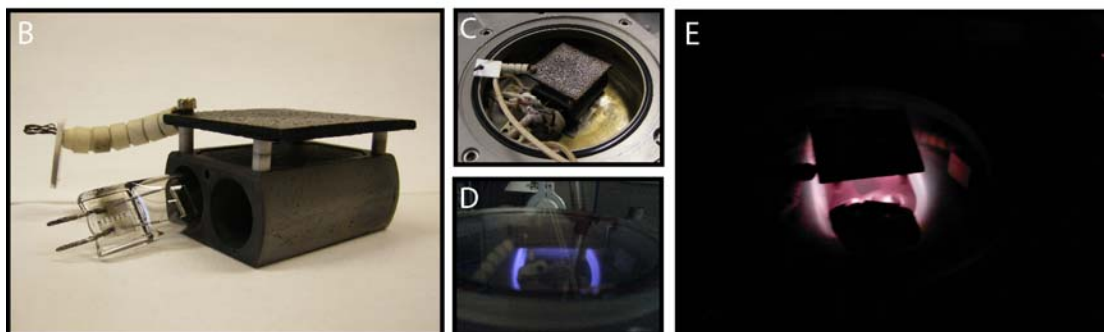
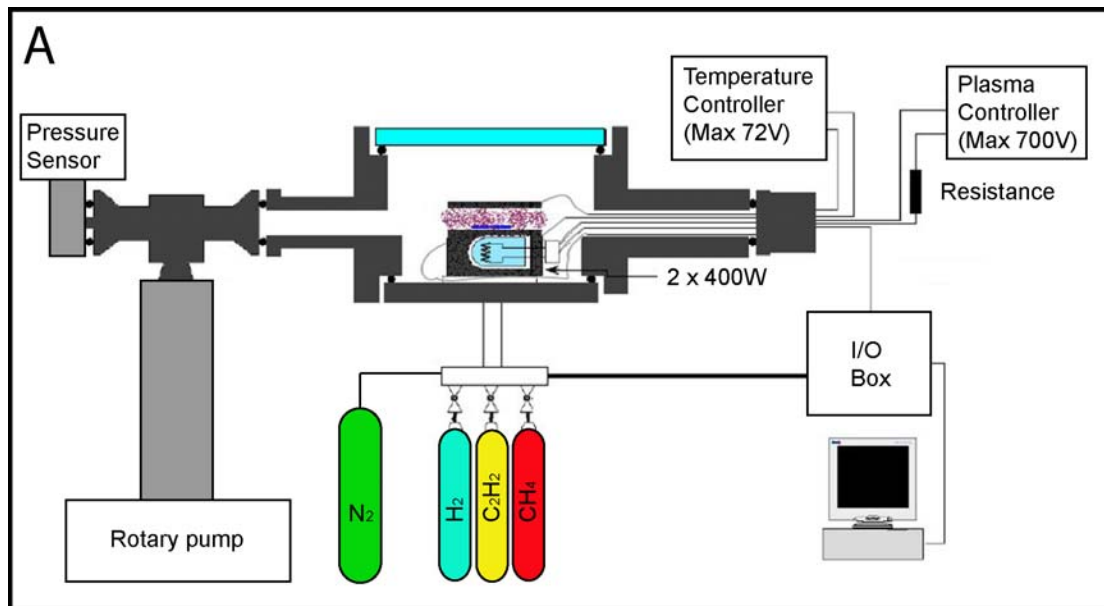


Figure 58 A) Schematic of the entire PECVD system. B) A picture of the heating stage (cathode) with the graphite anode on top, suspended by four ceramic pillars. C) The PECVD stage in the chamber. D) Plasma with without heating stage on. D) Plasma with with heating stage on (plasma colour is still blue, but appears white on this image).

CN growth with thermal CVD

Here, the results from growth attempts with the thermal CVD setup will be discussed. The first runs were all done at around 1 mbar using methane as carbon source. The sample substrates were chips from a silicon wafer with 1 μm oxide and some TiN leads defined through conventional photolithography. Electron Beam Lithography had been performed on top of this, and a layer of 10 nm Ni had been deposited by e-beam evaporation. The sample had had a very bad lift off, so remains of e-beam resist and nickel were left in various parts. The CVD run was performed at 650 $^{\circ}\text{C}$ for 15 minutes, using an atmosphere of 100% CH_4 at 1 mbar.

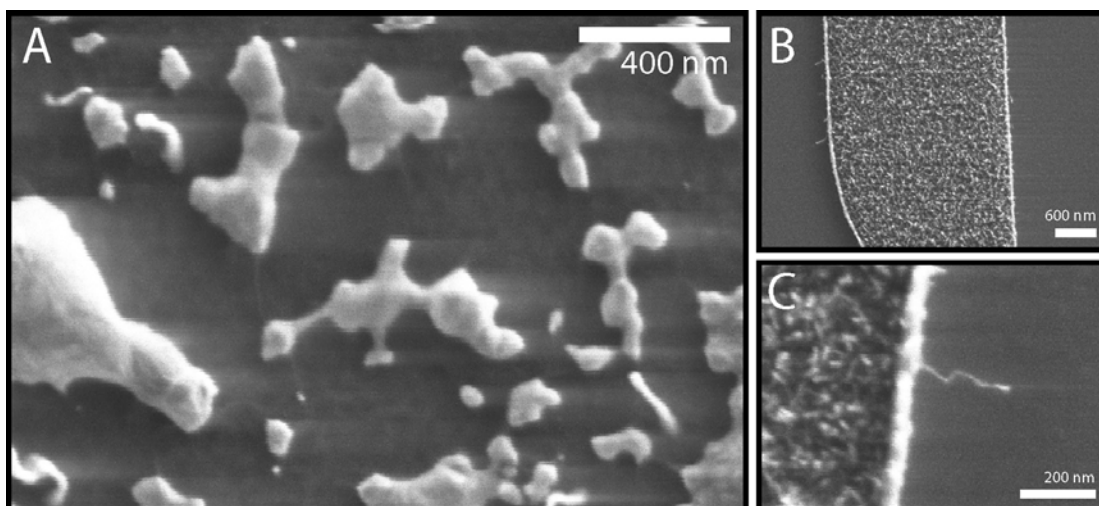


Figure 59 A) Large amorphous depositions are found on the chip with apparent wire-like structures spanning the open areas. B) On the TiN leads larger CNs are seen to grow. C) A close up of a CN shows the catalyst particle in the end.

Figure 59 A shows that wire-like structures were formed around and between larger clumps of catalyst and graphite. The wire-like structures could resemble CNs, protruding out from larger particles of amorphous graphite depositions. The diameter of these wire-like structures is below 10 nm, and close to the SEM resolution. This kind of growth occurred in regions where both e-beam resist and nickel remained. Even more convincingly was the discovery of wire-like structures on the TiN leads. In principle we did not expect any CN growth here, however the TiN leads had a very rough surface, and remains of nickel may very well have been left after lift off. It is clear that wire-like structures have been synthesised all over the leads, and we can see some of them sticking out sideways in Figure 59 B. Figure 59 C shows that CNs with catalyst particle in the tips have been synthesised. Although we do not have any TEM images of the crystallisation degree, the wire-like coiling structure with a clear catalyst particle at the end is a clear fingerprint of CNs. Other test runs with the same parameters showed that the CN formation was repeatable.

Further test runs with methane

In an attempt to optimise the system, test runs with variations in temperature, gas composition and pressure was done. The parameter space was studied by varying one parameter at a time. Thermal CVD with methane is expected to give better CN growth

for higher temperatures. Thus a focus was given on increasing the temperature in the system. A summary of the results from these test runs are given in Table 5.

Table 5 Optimisation runs of the CVD chamber with methane

Gas flow	Temp (°C)	Pressure (mBar)	Growth time (min)	H ₂ pre-treatment (min)	Result
100% CH ₄ , 0% H ₂	650	1	15	0	Some CNs
100% CH ₄ , 0% H ₂	750	1	15	0	Some CNs Graphite/catalyst balls
100% CH ₄ , 0% H ₂	750	10	15	0	Some CNs Graphite/catalyst balls
100% CH ₄ , 0% H ₂	750	1	15	5	Some CNs Branched Graphite/catalyst
59% CH ₄ , 41% H ₂	750	1	15	5	Many CNs Branched Graphite/catalyst
15% CH ₄ , 85% H ₂	750	1	15	0	Graphite/catalyst balls
94% CH ₄ , 6% H ₂	750	1	15	0	A lot of branched Graphite/catalyst
24% CH ₄ , 76% H ₂	750	1	15	0	Some CNs
15% CH ₄ , 85% H ₂	850	1	15	0	A lot of small CN formation
100% CH ₄ , 0% H ₂	850	1	15	0	Some small CN formation

Neither an increase in temperature to 750 °C nor an increase in pressure to 10 mbar affected the resulting structures significantly. A pre-treatment of the catalyst in H₂ flow for 5 minutes showed an effect of more branched graphite depositions. A more important effect is seen in introducing a co-flow of hydrogen during the process. In a run where hydrogen was added as a co-flow at a ratio of CH₄:H₂ = 3:2, the growth showed evidence of more fiber-like CN synthesis, see Figure 60.

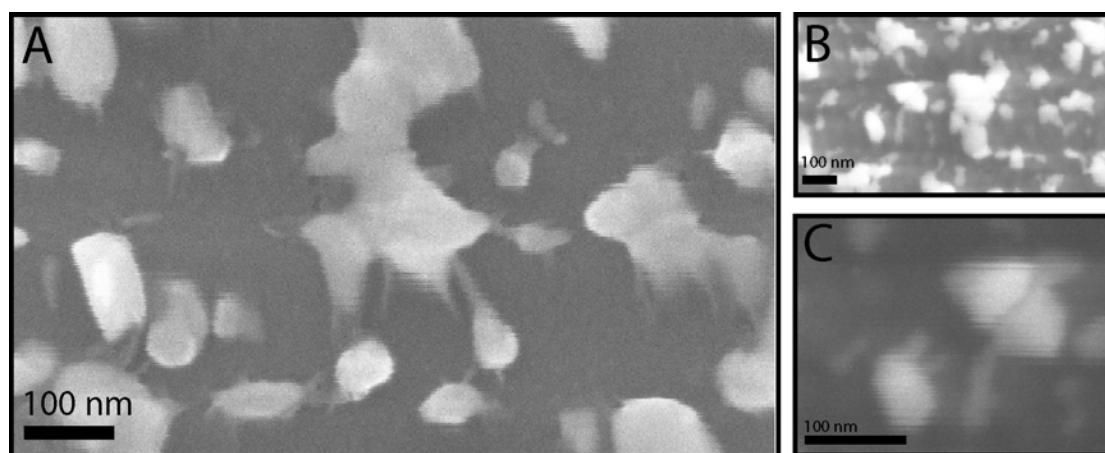


Figure 60 A) A lot of wirelike CN formation is seen, when adding hydrogen as a co flow. B) Even larger CNs form. C) A close up of a large CN.

Based on these first runs, it seems probable that the gas mixture is one of the most crucial parameters. The pressure, at least within the tested range, does not seem to influence the results substantially. The temperature is important, although we could not see a significant difference between runs at 650 °C and 750 °C. This may indicate that the temperature needs to be even higher. Nanotube growth from methane in conventional tube ovens normally occur around 900 °C [13]. In a new run the temperature is therefore raised to 850 °C, and the methane flow is at 15 %. With these parameters a sample (a) with 10 nm nickel on PECVD glass showed similar resulting carbon deposits as before, whereas another sample (b) also with 10 nm nickel, but with resist remains, showed a lot of fiber-like structures, see Figure 61.

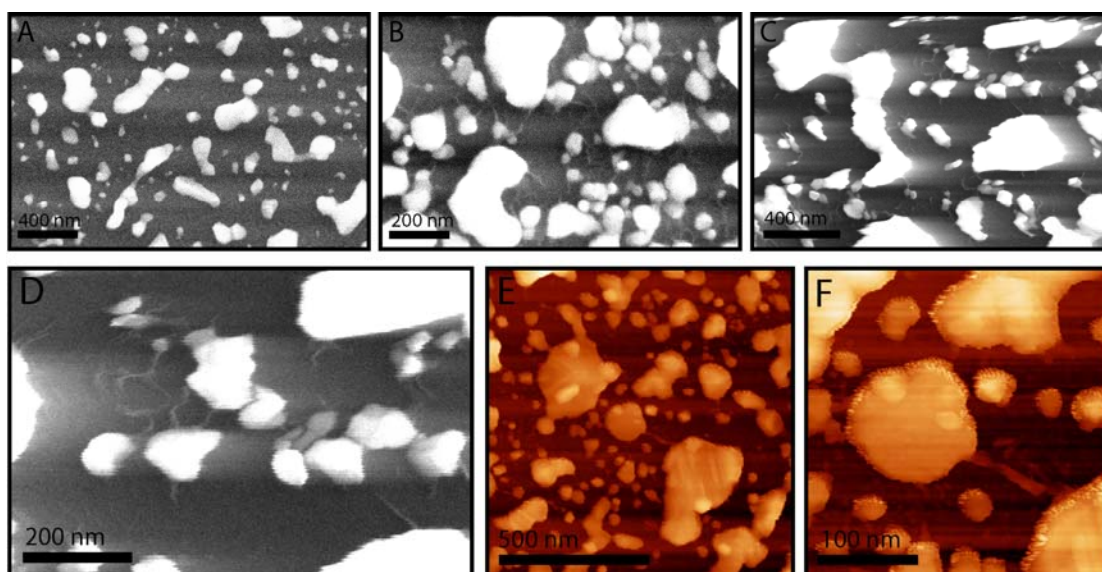


Figure 61 A) A sample with 10 nm nickel on top of PECVD glass does not show much CN growth. B-C) A sample with nickel and resist remains does show CN growth. D) enlargement of area in C. E & F) AFM pictures show fiberlike structures on the surface.

Although the wire like structures in Figure 61 D resembles CNs, it is not possible to be sure, due to the minute size of these structures. An investigation with AFM, which has a higher resolution but records images much slower, as seen in E and F did not lead to a definitive conclusion. However, some wire like structures were found with AFM as well, as shown in Figure 61 E and F. The results indicate that a higher temperature increases the amount of nanotubes grown. A last test run is made with a high temperature of 850 °C, but where the co flow of hydrogen is removed. In fact the difference is not evident, as can be seen in Figure 62. CNs can still be found spanning gaps between larger graphite depositions. However, there appears to be less of them. An interesting observation is made. The red circle in Figure 62A encircles a thick bridge like graphite deposition. This may indeed be a thin CN that has been covered in amorphous carbon after formation. A similar formation can be seen in Figure 62D where both a thin CN is seen and thicker connection between the larger graphite depositions.

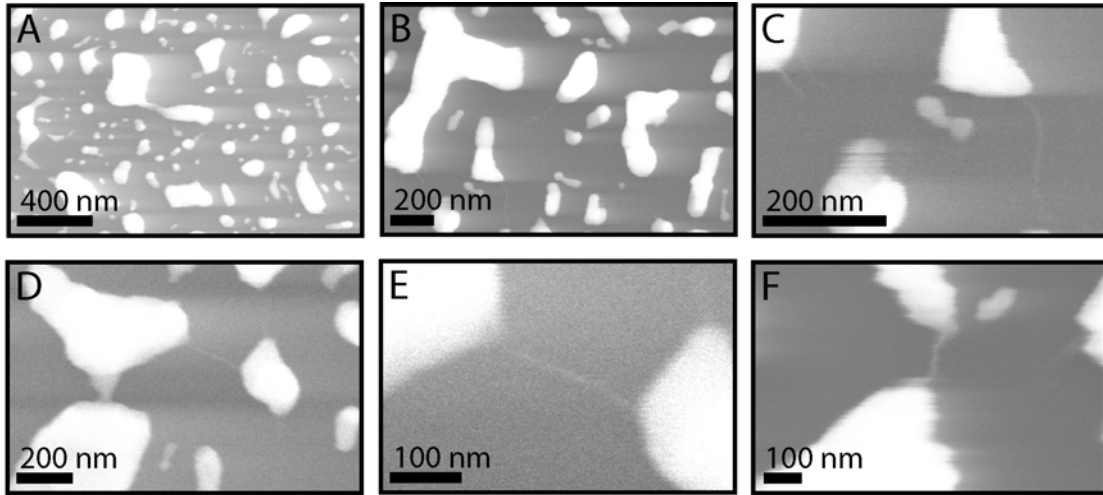


Figure 62 A) A sample with 10 nm nickel on top of PECVD glass does not show much CN growth. B-C) A sample with nickel and resist remains does show CN growth. Notice the long CN in the circle which is enlarged in C. D-F) Several CN like structures are seen to span gaps between larger graphite depositions.

CVD runs with acetylene

Whereas the dissociation of methane to carbon and hydrogen is an endothermic reaction consuming energy, the dissociation of acetylene is exothermic. However, acetylene needs an activation energy before dissociation occurs. In a thermal CVD process acetylene will dissociate more easily than methane and give a different growth result.

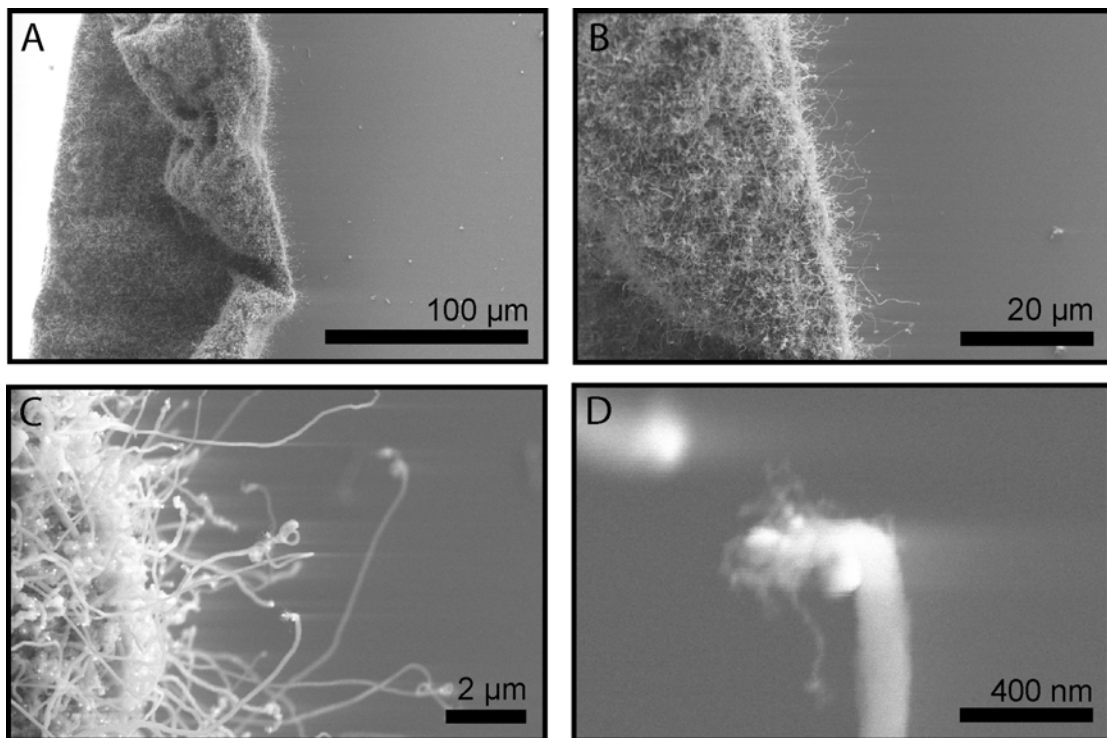


Figure 63 A) CVD growth at 700 °C and 25 mbar, from 17% acetylene mixed with 83% H₂. B) Thick carpets of CNs are seen to form. C) Close inspection indicate high quality of the CNs. D) A large magnification of the tip of the CN shows secondary smaller CNs extending from the tip.

A first test is performed on a sample with 10 nm nickel on PECVD glass. The sample shows a dense coverage of CNs, see Figure 63. The CNs were grown at 700 °C and 25 mbar for a duration of 20 minutes, with a gas composition of 17 % acetylene and 83 % hydrogen. Several important observations can be made. During growth, the CN synthesis forms a large carpet of CNs, as seen in Figure 63 A. This carpet actually detaches from the oxide surface and curls up. The larger magnification image in Figure 63 B shows that the carpet consists of large amounts of CNs and yet a larger magnification in Figure 63C shows that no amorphous carbon can be seen. The CNs appear to have a diameter of about 150 nm (Figure 63D), but as the close up of one of the tips shows, the CN tip appear to divide into many, much smaller CNs. This phenomenon is seen on all CNs, and a possible explanation may be that as the process is shut off, the rapid pressure drop or the rapid temperature drop splits the catalyst particle into many smaller parts synthesising growth of smaller CNs for a brief moment.

Gas composition optimisation

A series with acetylene, varying the gas composition from 3% acetylene to 17 %, keeping the temperature at 700 °C and the pressure at 25 mbar was done (in collaboration with Jakob Kjelstrup-Hansen). These growths were done on structured substrates with 5 nm nickel in patterns and lasted 20 minutes. The results are shown in Figure 64.

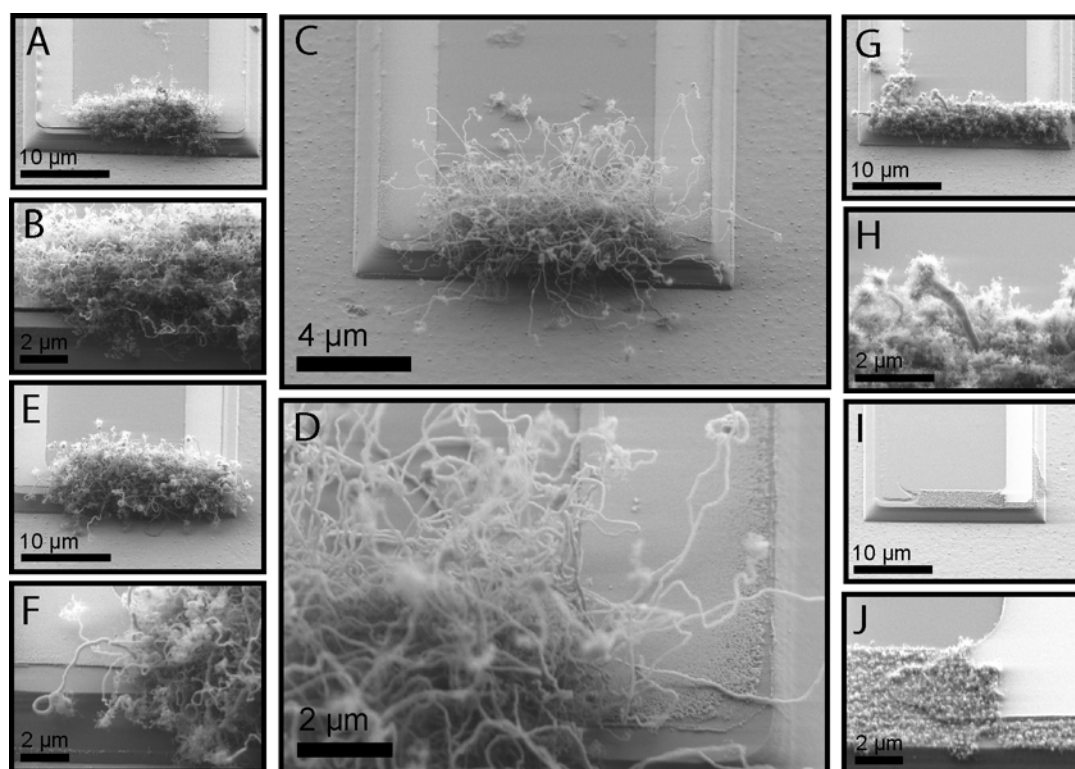


Figure 64 A & B) 17 % acetylene. C & D) 13 % acetylene. E & F) 10 % acetylene. G & H) 6 % acetylene. I & J) 3 % acetylene.

By visual inspection it seems clear that the best CNs are obtained for the 13 % acetylene 87 % hydrogen mixture. There is a significant difference between the results for the various compositions. A composition with 17 % acetylene gives CN

growth as seen in Figure 64 A and B. There are many tubes, of various dimensions. It is also noted that the tips of the CNs seem to divide into much smaller CNs. At 13 % acetylene, the CNs looks more homogenous in thickness, as well as being longer, as seen in C and D. Further reduction in the acetylene content results in gradually lower quality of the CN growth. This is shown in Figure 64 for 10 %, 6 %, and 3 % acetylene content. In fact 3% acetylene does not give much CN growth at all. These results are summarized in Table 6.

Table 6 Optimisation runs of the CVD chamber with acetylene

Gas flow	Temperature (°C)	Pressure (mBar)	Growth time (min)	Result
3% C ₂ H ₂ , 97% H ₂	700	25	20	Amorphous carbon
6% C ₂ H ₂ , 94% H ₂	700	25	20	CN formation Thick and nonuniform
10% C ₂ H ₂ , 90% H ₂	700	25	20	CN formation low uniformity ~100nm and much smaller
13% C ₂ H ₂ , 87% H ₂	700	25	20	CN formation High uniformity Long and thin ~70 nm
17% C ₂ H ₂ , 83% H ₂	700	25	20	CN formation High uniformity Shorter less straight ~60 nm

Temperature optimisation.

Figure 65 shows results from temperature optimisation runs. There were two samples, one with 2 nm nickel and another with 10 nm nickel. The gas composition was kept at 13% C₂H₂ and 87% H₂ at 25 mBar. The temperature was varied between 650 °C, 750 °C, and 850 °C. On the 10 nm nickel The best CNs are formed with T = 750 °C. Interestingly, the CN formation is much worse at 850 °C. At this temperature we even have formation of cube like catalyst blocks, see Figure 65 D. The 2 nm nickel sample shows a less conclusive trend. Here the growth at 750 °C is the worst, with irregularly shaped CNs. Also here the formation at 850 °C seems to be more amorphous, but the CN that do form appear to be of higher quality. The various diameters found for the CNs are summarised in Table 7.

Table 7 Diameter of the CNs formed at various temperature on two different substrates.

Temperature	Diameter on 2 nm nickel (nm)	Diameter on 10 nm nickel (nm)
650 °C	20-40	30-120
750 °C	30	200 and 30
850 °C	30	100

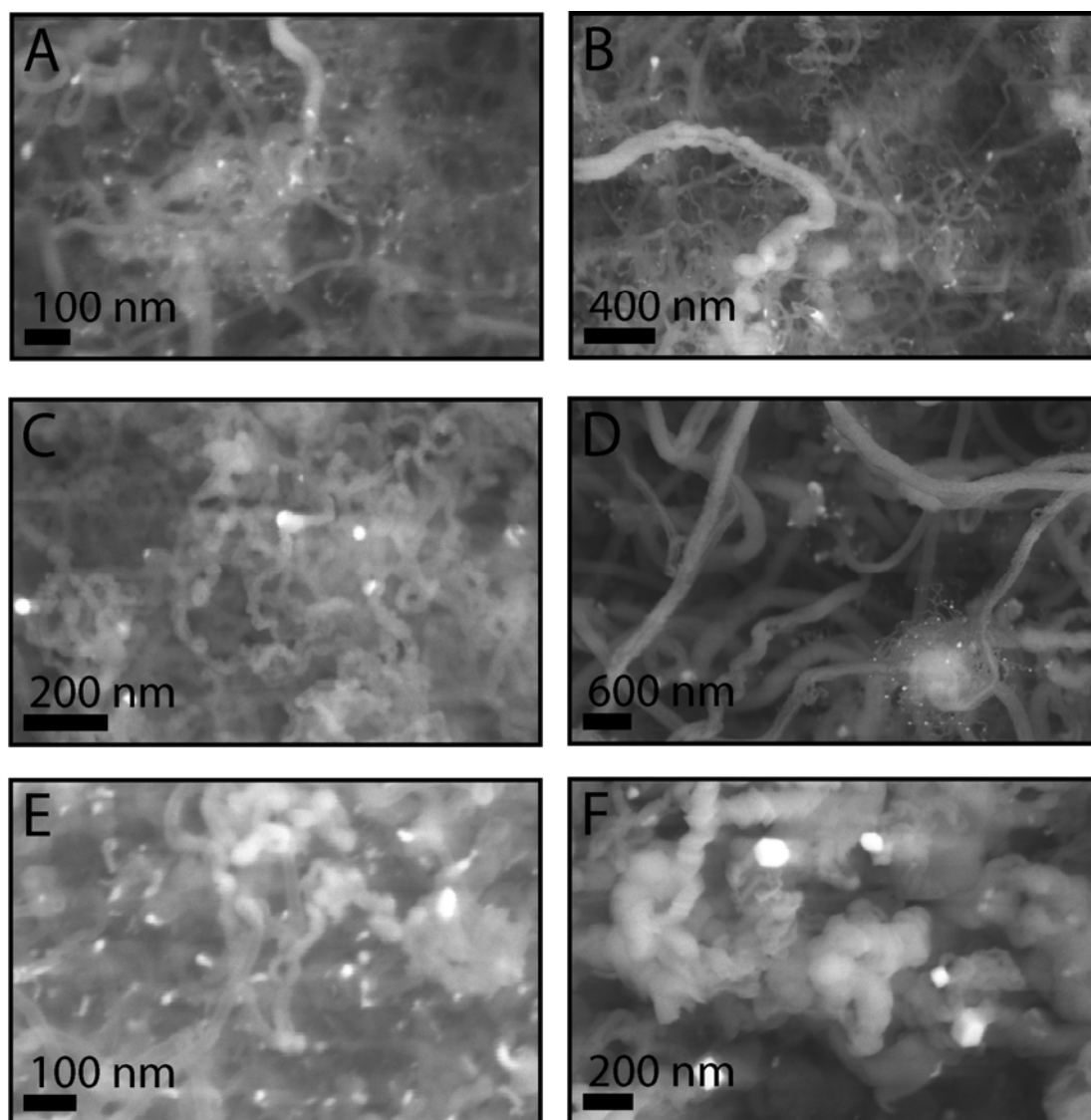


Figure 65 A) CN growth from 2 nm nickel at 650 °C. B) CN growth from 10 nm nickel at 650 °C. C) CN growth from 2 nm nickel at 750 °C. D) CN growth from 10 nm nickel at 750 °C. E) CN growth from 2 nm nickel at 850 °C. F) CN growth from 10 nm nickel at 850 °C.

Pressure optimisation

A run where the pressure was increased to 50 mBar was also done. Figure 66 shows results from this run, where the temperature was at 750 °C and the gas composition the same as above. Also here good CN formation is seen. In fact the CNs on the 2 nm nickel sample show increased quality. The diameter remained unchanged at 30 nm.

The 10 nm nickel sample had CNs of worse quality, and the diameter was found between 30 to 60 nm.

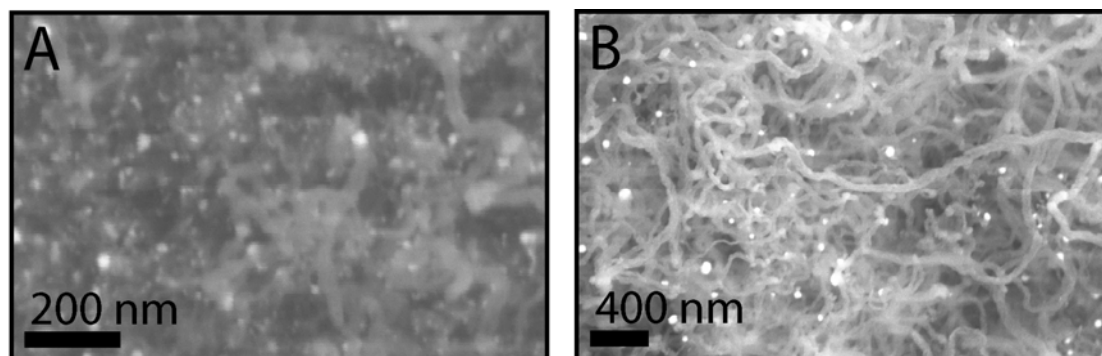


Figure 66 A)CN growth from 2 nm nickel at 750 °C and 50 mBar. C) CN growth from 10 nm nickel at 750 °C and 50 mBar.

Conclusion

In conclusion from these tests, thermal CVD with methane gives most CNs with a temperature of 850 °C and a gas composition of around 15 % (and lower) methane and 85 % hydrogen. From these tests, no difference was observed between 1 mbar pressure and 10 mbar, although 10 mbar was not tested at the highest temperature. Higher temperatures can possibly improve the CN growth as well, but caution has to be taken with the present design of the chamber, since the O-ring sealing the glass lid may be damaged by the heat.

The runs with acetylene give far larger CNs, which are more easily characterised. The CNs grown at 700-750 °C, 25 mbar and 13 % acetylene, are several tens of micrometers with a diameter of around 100 nm. For this thermal CVD setup, operating at relatively low pressures and temperatures, acetylene is a good choice for the carbon bearing gas. Further optimisation with respect to temperature, pressure and catalyst material, may give a variety of CN qualities.

CN growth with Plasma Enhanced CVD

Plasma Enhanced CVD allows CN growth at lower temperatures, and could possibly facilitate better CN growth with methane as carbon source. Another benefit from PECVD grown CNs is that the CNs will be aligned with the electrical field. Thus CNs suitable for use as probes, for instance AFM or four point probes, have to be made by PECVD. Various initial experiments with the PECVD set up taught us that the most stable plasmas were obtained with pressures in the range 10-50 mbar. These high pressures are easily obtained by choking the main pump line and only pump through the secondary pump line where the pump efficiency can be controlled by the needle valve. However, the secondary pump line was first implemented after realising its need, thus our initial tests were done by choking the main pump line to obtain the desired pressures. This gives a larger variation of the pressure during growth. The secondary pump line allows pressure control within 1 mbar, whereas the main pump line gives variations within a couple of tens of mbar. Most initial runs are done with five sample substrates where four have 1, 2, 5, 10 nm nickel on glass and the fifth has 5 nm of nickel on 100 nm of TiW.

Initial PECVD CN results

In one of our first optimisation runs we found some very interesting CN formation. This run was carried out with 15 % CH₄ and 85 % H₂, with a pressure varying between 15 to 40 mbar, and the temperature between 650 – 700 °C, with a total growth time of 20 minutes and a plasma potential of 600 V. Carbonaceous depositions were given on all substrates, resembling vertically aligned CNs. However, on the 2 nm nickel sample ringshaped and toroidal CNs were found, as shown in Figure 67.

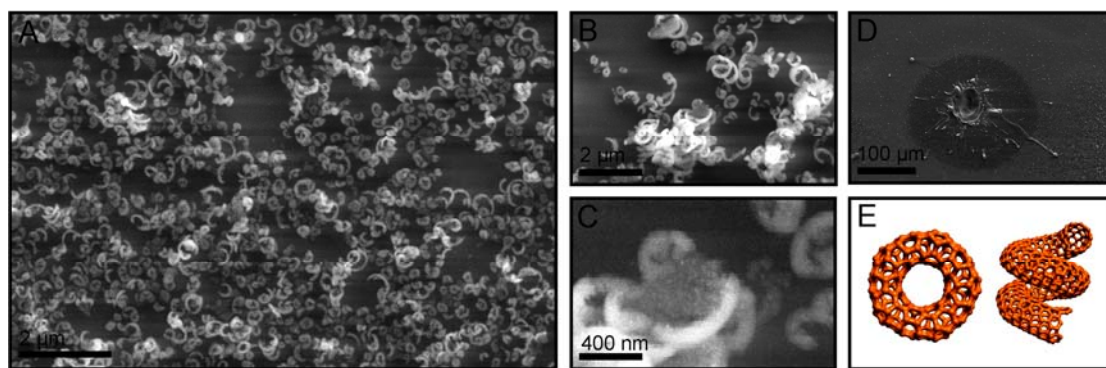


Figure 67 A) Large amounts of toroidal and ringshaped CNs are found. B) A close up of the CNs. C) Clusters of much smaller CNs are seen on the larger structures. D) The toroidal and ringshaped CNs were found in the vicinity of craters made by discharges. E) Sketches of these structures.

Figure 67 A shows that in certain areas many toroidal and ringshaped CNs had been formed, with a quite homogenous size. The close up in B shows that these structures clearly are toroidal shaped. Interestingly, some of the CNs also have clusters of much smaller CNs on them as seen in C. We discovered that the sample had been damaged in some places by what is known as arcing. During runs too much electrical charge can be concentrated in certain points on the anode/cathode constellation leading to discharges in that local region. On our sample, this caused craters of melted glass and silicon, as seen in Figure 67 D. Solidified glass was observed around the impact region. The toroidal shaped CNs were found in the vicinity of such craters, and not in other places. The arcing may have caused the temperature to rise significantly in a brief time, thus altering the conditions of the synthesis. The homogeneity of these structures indicates that this should in principle be a controllable type of process in the system. The structures are known from both theory and experiment beforehand [120], and sketches of such structures are shown in Figure 67 E.

Although circular and toroidal CNs are fascinating, they are not the kind of CNs we aim at synthesizing. In a new run with the same gas composition, the pressure varied between 15-50 mbar and the temperature between 650-720 °C with a total growth time of 10 minutes and a plasma potential of 600 V. Inspection with SEM revealed CN formation on all substrates, as shown in Figure 68, although the grown CNs are not longer than a few hundred nm. Furthermore, the CNs seem to be of best quality on the 5 nm nickel sample.

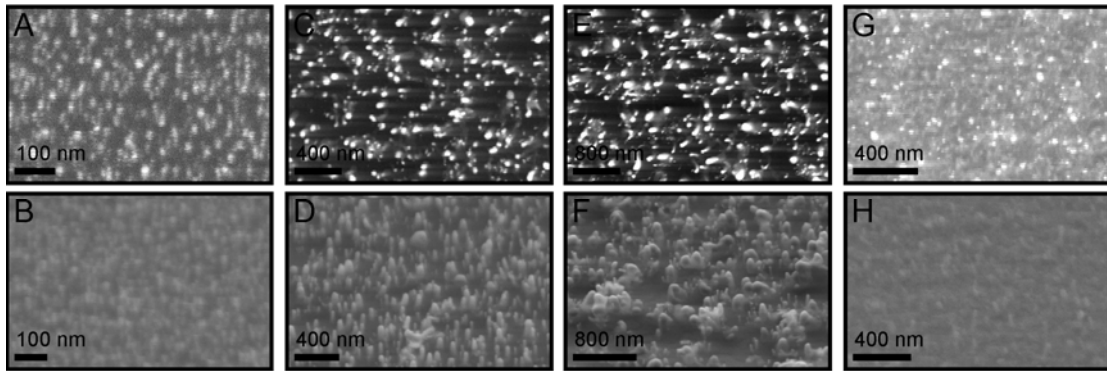


Figure 68 Series of CNs grown from 2, 5, 10 nm nickel respectively. The last sample had TiW underneath 5 nm nickel. The CN forest seem to be best defined in the region 2-10 nm nickel (1 nm not shown), with 5 nm nickel to be best.

Also in this run did we find unexpected structures. On the 10 nm nickel sample long tubes and bundles of tubes were discovered in a local region, as seen in Figure 69. These tree-like structures were several microns tall, and appeared to consist of several tubes. They were also clearly aligned with the electrical field. It is unclear what caused this exceptional growth in this local region.

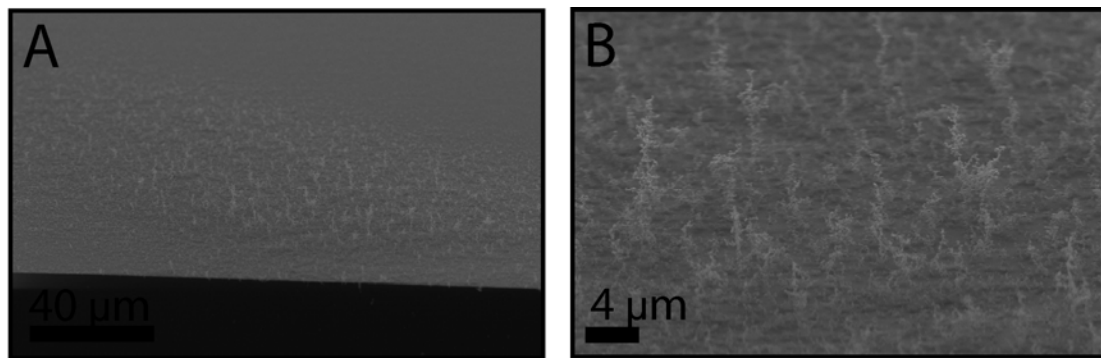


Figure 69 Very tall, perhaps as tall as 15 – 20 μm, treelike structures of interwoven CNs. They all appear to be guided by the electrical field.

Runs with lower methane content, at 4% and 1%, gave a much worse CN growth, which resembled particles of graphite depositions. It is also observed from all these runs, that the CN formation on top of the TiW substrate seems to be similar to the CN formation on the other substrates. This is important, if TiW is supposed to be used as leads for electrical contact. These results are summarised in Table 8.

Table 8 Test runs of the PECVD chamber with methane

Gas flow	Temperature (°C)	Pressure (mBar)	Growth time (min)	Result
15% CH ₄ , 85% H ₂	650-700	15-40	20	Vertically aligned CNs, plus toroidal CNs
15% CH ₄ , 85% H ₂	650-720	15-50	10	Vertically aligned CNs, plus bundles of CNs taller than 10 μm
4% CH ₄ , 96% H ₂	650-720	15-50	10	Some CN formation
1% CH ₄ , 99% H ₂	650-70	15-50	15	Some CN formation

Runs with improved control of pressure and temperature

Clearly, several of the initial runs did not have good enough control on pressure and temperature. In order to get better control, a parallel pumping line was constructed with a needle valve able to control the pressure within 1 mbar accuracy as previously described. With this implemented the temperature became controllable within a couple of degree Celsius. In Figure 70 results from growth from a nickel pattern on microfabricated structures are seen (processed in collaboration with Jakob Kjelstrup-Hansen).

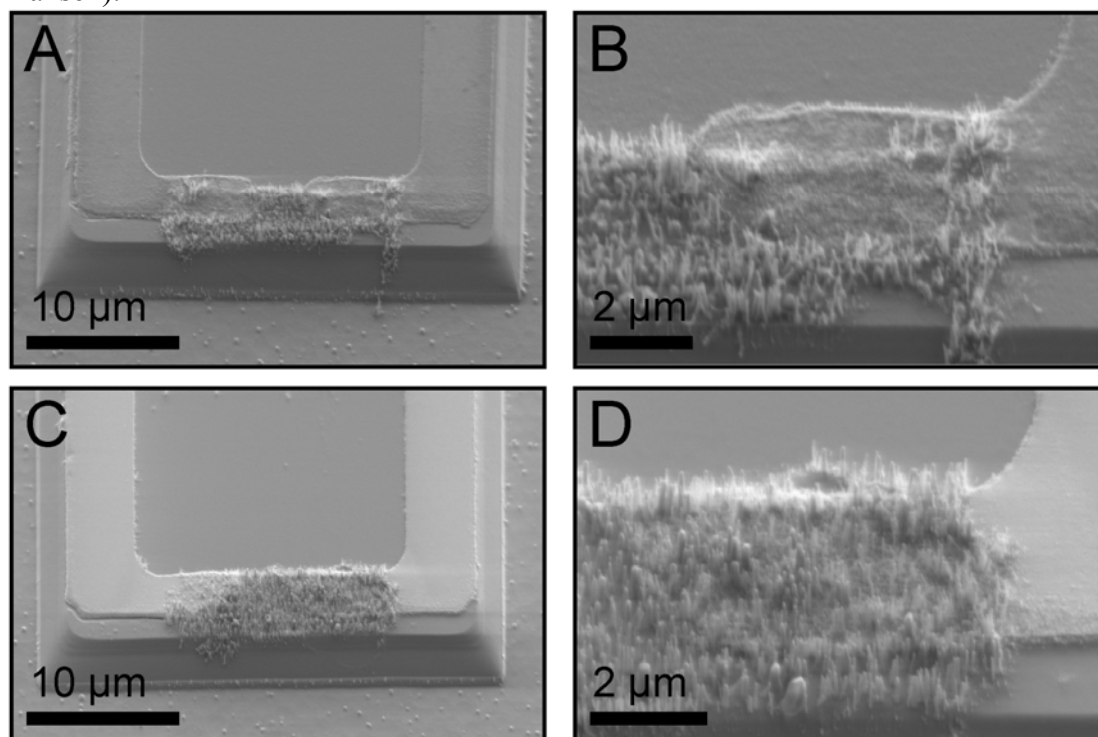


Figure 70 A & C) Vertically aligned CNs grown from nickel pattern on a microstructure. B & D) Close up of the CNs show that they are around 1 μm tall.

Parameters of the run were 750 °C, 25 mbar, 600 V plasma potential, and a methane content of 15 %. As compared to previous runs, the CNs synthesised here are longer, between 500 nm and 1 µm. However, the diameter seems to vary substantially between the CNs, which is particularly noticeable in Figure 70 D, where CNs with diameters between 40 and 150 nm can be found.

CN growth from acetylene

As seen with the thermal CVD, acetylene gives higher deposition rates. There has not been much time to work on PECVD runs with acetylene but one series has been attempted with a gas composition of $H_2:C_2H_2 = 6:1$. The temperature was kept at 700-720 °C for about 25 minutes, and the pressure was stable at 25 mbar. By visual inspection it was seen that the samples were completely black after deposition, and inspection in SEM revealed that thick depositions of carbon material had been obtained, as well as many CNs. Better results for acetylene would probably be obtained with a smaller acetylene fraction in the gas flow or a lower temperature.

Conclusion

A combined CVD/PECVD growth chamber for CNs has been constructed. The chamber is under continuous development, and initial test runs for both CVD and PECVD has been presented, using both methane and acetylene as carbon sources. The best growth conditions found for the two different types of growth was;

- CVD
 - 13% C_2H_2 , 87% H_2
 - $T = 700 - 750$ °C
 - $P = 25$ mbar
- PECVD
 - 15% CH_4 , 85% H_2
 - 750 °C
 - 25 mbar
 - 600 V plasma potential

More work needs to be done on CVD growth with methane. The results this far indicate that a CNs are formed at temperatures of 850 °C, and even better results could perhaps be achieved by raising the temperature even more. However, the current design of the vacuum chamber does not allow much higher temperatures. PECVD growth on the other hand, needs to be optimized further. Reasonably good results have been achieved with methane a carbon source. Here more work needs to be done on optimizing the growth from acetylene. Interestingly, the current results indicate that the temperature needs to be lower than the tested 700 °C.

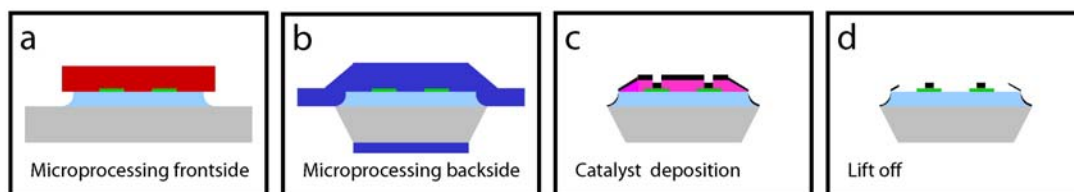
6 Integration in MEMS using E-Beam

Introduction

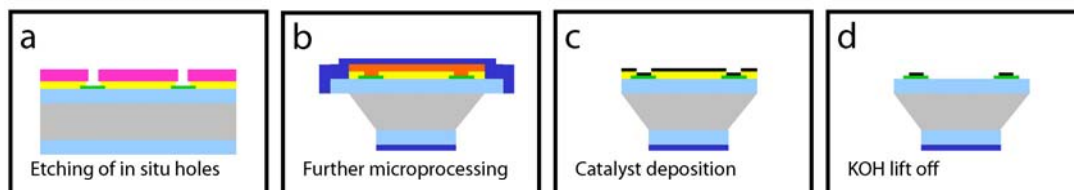
The Methods

In this chapter, four routes toward waferscale integration of nickel catalyst dots into microsystems will be presented. The four routes are called, I) the *Direct* method, II) the *In situ mask* method, III) the *Window mask* method, and IV) the *Encapsulation* method. The principles of these four methods are shown in Figure 71.

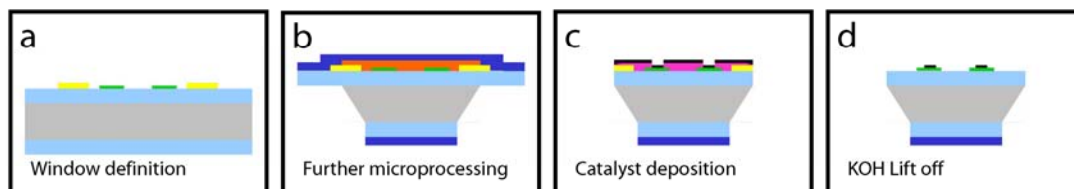
I Direct



II In situ mask



III Window mask



IV Encapsulation

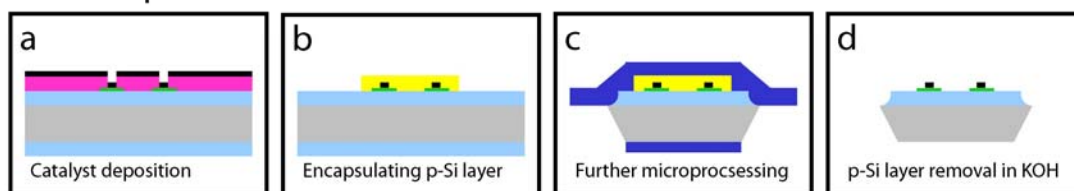


Figure 71 The four different methods for integration of nickel catalyst dots into microsystems investigated here. I) The Direct method has the EBEAM patterning in the end of the processing. II) The In situ mask method starts with the EBEAM patterning in the beginning of the process and transfers the pattern into a p-Si layer which is used as a lift off mask in the end. III) The

Window mask method is a combination of the two preceding methods, where a p-Si layer with open areas is deposited early on in the process. In the end, the EBEAM steps are performed inside the open areas, with lift off accomplished for both the EBEAM resist and the p-Si in KOH. IV) In the Encapsulation method, the EBEAM patterning and catalyst deposition is done in the beginning. The catalyst pattern is subsequently encapsulated in p-Si, allowing further processing before it is removed in KOH.

In the *Direct* method, all microprocessing is finished first as illustrated in Figure 71 Ia and Figure 71 Ib. The EBEAM patterning step is performed on the finished structures, as seen in Figure 71 Ic. If the wafer at this time has holes through the interior, for instance defining separate chips, the EBEAM resist must be spun on with the use of mechanical support and not vacuum. Lift off after nickel deposition (Figure 71 Id) on such structures is accomplished with microposit 1165 nanoremoval. The *In situ mask* method starts with the EBEAM patterning in the beginning of the process (Figure 71 IIa). By reactive ion etching (RIE) the dot pattern is transferred into holes in a p-Si layer on top of the microstructures. Further microprocessing (Figure 71 IIb) define the structures, and the nickel catalyst are deposited on finished structures were the p-Si layer, which has been carried through the process, plays the role of an EBEAM resist layer (Figure 71 II c). Lift off is accomplished in KOH (Figure 71 II d), leaving the nickel dots on the structures. The *Window mask* method is a combination of the two preceding methods, where a p-Si layer is deposited early on in the process, but where a window through the p-Si layer is present around the area the nickel dots will be defined (Figure 71 IIIa). After further processing (Figure 71 IIIb) the EBEAM steps are performed on finished structures just like the *Direct* method, but now there is a p-Si layer along all edges (Figure 71 IIIc). After lift off in KOH, the nickel pattern is left on the structures. Finally, in the *Encapsulation* method, the EBEAM patterning is done in the beginning, followed immediately by the nickel catalyst deposition (Figure 71 IVa). The catalyst pattern is subsequently encapsulated in a p-Si layer (Figure 71 IVb) by conventional photolithography and lift off. The p-Si encapsulation of the nickel dots allows further microprocessing to be done (Figure 71 IVc). The encapsulating p-Si layer is lifted off in KOH on the finished microstructures, leaving the catalyst dots in place. Refer to appendix B for complete process sequences. In this work, we have mainly focused on the integration of nickel catalyst dots, capable of synthesising growth of CNTs. However, the main knowledge gained in this work, will also have direct relevance towards integration of catalytically grown nanowires of other elements in similar systems with various catalysts. Obviously, the process sequences may have to be slightly changed for some catalyst materials.

Several success criteria for the process methods have been identified. The most important criterion is whether or not the method is able to define catalyst dots on the finished structures. This is not a trivial criterion, since several routes have been investigated without a successful outcome. However, the four methods discussed in this chapter do fulfil the first criterion on getting catalyst dots on the structures. We can then identify the success criteria as follows

- Compatible with standard cleanroom processing
- Possible on flat and nearly flat surfaces (including thin leads)
- Possible on micro-structured surfaces
- Possible on suspended structures (i.e. cantilevers)
- Acceptable precision on dot size

- Acceptable yield on nickel dots
- Catalytic activity of catalyst remains
- Range of dot diameter
- Range of dot thickness

An important note may be done to the first criteria. In standard cleanroom processing, which should be CMOS compatible, there are strict rules on which materials can be present or exposed in various processing equipment. Specifically, doping by metal particles is unwanted. Accordingly, most metals including nickel are strictly forbidden in many equipments. Therefore the methods have to either deposit the nickel towards the end of the processing, or the nickel dots will have to be encapsulated safely within a material that can be removed later.

In the following subchapters results from the four investigated methods will be shown in detail. Advantages and drawbacks will be discussed, as well as how well the methods meet our success criteria. However, first an initial study of the E-Beam lithography system used in defining the dot patterns is presented.

Electron Beam Lithography

Ebeam lithography is (EBL) is a technique for patterning structures such as catalyst dots around 100 nm. It would be beneficial to use photolithography instead of EBL, due to the parallel exposure where the whole wafer is exposed at once, as compared to EBL where the electron beam scans the wafer surface and expose the pattern in a serial way. However, conventional photolithography has a minimum line width around 1 μm , which makes it impossible to make small structures on the order of 100 nm. Some alternatives to conventional photolithography exist, such as UV lithography and deep UV lithography, but these are very expensive and impractical for research. In addition, the physical limit for optical lithography systems is close to 100 nm [121], whereas the corresponding limit for EBL is about 10 nm [122].

EBL use a high voltage, between 10 to 100 keV, to accelerate electrons emitted from a filament [122]. These electrons are then focused into a beam that is scanned over the wafer surface according to the mask design, using a shutter to block the beam when moving across areas that should remain unexposed. EBL is a serial process where the writing time t depends on the writing area A , the beam current I and the exposure dose D , as given in equation 6.1.

$$t = \frac{D \cdot A}{I} \quad (6.1)$$

For very small patterns, like a few catalyst dots per microchip, the writing time for a whole 4 inch wafer is on the order of 10 minutes, which is short enough for development work. A common resist used for EBL, and the one used in this work, is ZEP-520. The resist requires a certain dose to break the polymer chains to become successfully exposed. This dose depends on the designed pattern, and therefore a small study of the dots size as a function of dose was done for various dot sizes. Arrays of dots of sizes ranging from 30 nm to 500 nm were designed. These patterns

were written on a wafer, varying the exposure dose from $\mu\text{C}/\text{cm}^2$ to $800 \mu\text{C}/\text{cm}^2$, while the beam current was kept constant at 0.8 nA. The results of this study can be seen in Figure 72.

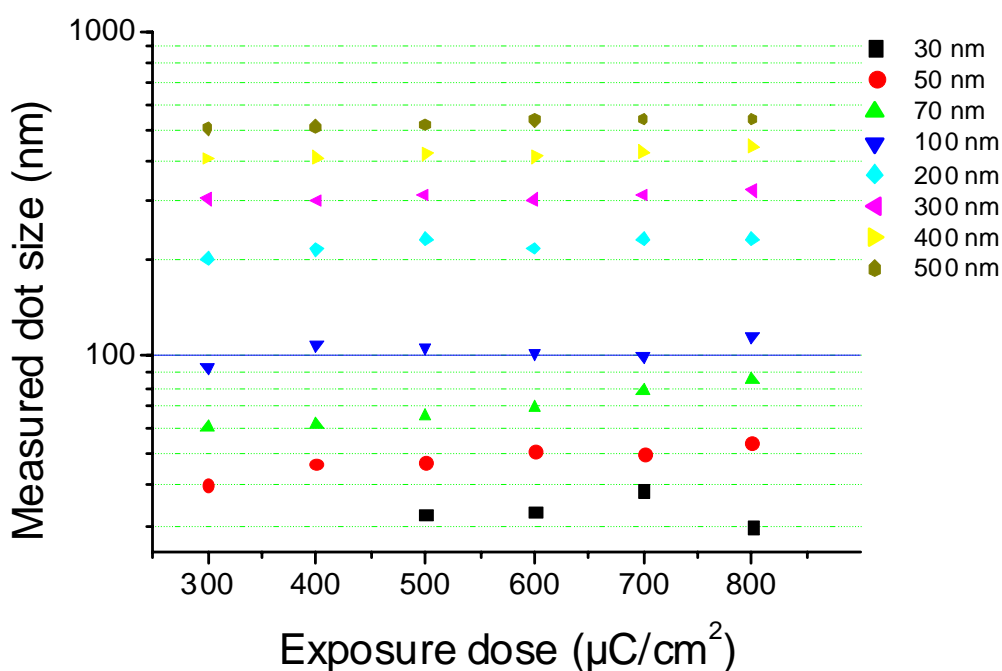


Figure 72 Dot size as a function of exposure dose for dots 30 nm to 500 nm in diameter.

The graph in Figure 72 shows that an increase in exposure dose gives an increase in dot size. For fabrication of catalyst dots, we are mostly interested in dots with a size of 100 nm or less, corresponding to the four lowest series in Figure 72. Here, an exposure dose of $600 \mu\text{C}/\text{cm}^2$ gives the best consistence between the designed dot size and the resulting size after EBL. For the larger dots in Figure 72, the deviation from the designed size is less in percent. It is observed that the dose should be $300 \mu\text{C}/\text{cm}^2$ or perhaps even lower, in order for the dots to match the design. Integration of catalyst dots into microsystems for subsequent nanotube or nanowire growth does not always have strict requirement on the dot size. The dots themselves will be transformed into catalyst particles and give rise to the CNT or NW growth, with a diameter depending on the size of the catalyst particle. In this process there are also other factors influencing the final size of the CNT or NW, which makes it less crucial to have an exact dot size. It is perhaps more important that the uniformity of the dots produced in one batch is large, which is also seen. Therefore, the accuracy obtained with an exposure dose of $600 \mu\text{C}/\text{cm}^2$ seems to be good enough.

In all investigations done in this chapter the ebeam resist used was ZEP 520 A7. The resist was spun on the wafers using an acceleration from 0 to 500 rpm in 5 s, followed by a rapid acceleration to 3000 rpm where the speed was kept for 30 s. For an undiluted ZEP resist, this results in a resist thickness of about 300 nm. In some cases the resist was diluted in anisole in the ratio 1:2. The same spin recipe then gives about 100 nm resist thickness. The wafers were baked at $160 \text{ }^\circ\text{C}$ for 2 minutes prior to EBL exposure.

Results from the four processing methods

Direct

The *Direct* method of integrating catalyst dots in existing microsystems is to cover the finished microstructures with an appropriate resist for subsequent electron beam lithography, catalyst deposition and lift off. In this subchapter the investigation will focus on three main structures – flat surfaces with leads, microchannels patterned in silicon wafers, and suspended cantilevers on microchips. The results from microstructured surfaces and suspended structures were obtained in collaboration with Tommy Schurmann and Lauge Gammelgaard.

Flat and nearly flat surfaces

The test structures here are silicon wafers with metal leads on top. The nickel dots should be placed on top of the metal leads, similarly to what McKnight et al has shown [33]. It is a nearly flat surface, only with thin leads typically 50-100 nm thick. Both 100 nm and 300 nm ZEP resist was tried, without any noticeable difference on these very thin structures. However, it is anticipated that thicker leads will result in a poorer lift off with a too thin resist layer. Figure 73 a resulting structure with nickel dots on top of 50 nm thick TiW leads is shown. In this case a 300 nm thick ZEP resist was used and 50 nm of nickel was deposited.

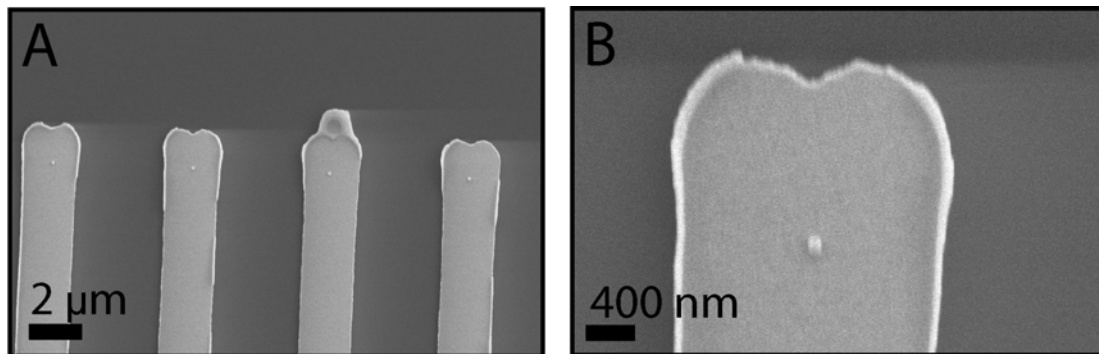


Figure 73 Ni dots 100 nm in diameter deposited on TiW leads by the direct method. The inset shows an enlargement of one of the dots.

After lift off the dots are well defined on top of the TiW leads. Similar tests were done with both thinner resists and thinner nickel thickness. It is observable that the lift off is easier for nickel layers thicker than 20 nm, as thin layers of 10 nm tend to be more stuck on the surface. In some cases a successful lift off could not be accomplished on the entire wafer. The increased difficulty is thought to be a combination of the lesser thickness of the resist, as well as the lesser thickness of the catalyst. For small structures like dots on the order of 50 – 100 nm in diameter it is a clear advantage to use 300 nm ZEP resist to facilitate the lift off.

It is furthermore important to note that the lift off on these flat surfaces does not show any problem with the lift off along the structure edges. The structures are so thin that no unwanted catalyst remains. The exception is in some locations where the lift off made in the lead definition step was not good, leaving flaps on the sides. When the

catalyst deposition step is done on top of badly defined lead structures the ebeam resist coverage may be poor on the largest protruding parts.

Microstructured

The test structures here are silicon wafers with microfabricated channels. The channels are made by conventional photolithography on a silicon wafer combined with a subsequent etch in 20% KOH at 80 °C. At these conditions the etching rate of KOH is about 1.2 µm/min. An etch of 4 minutes thus gives roughly 5 µm deep channels. The KOH etch of silicon is anisotropic; it etches with different speed in different directions, defined by the silicon lattice structure. The etching rate given here, 1.2 µm/min, is the etching rate of the (100) plane. Since the etching of the (111) plane is 400 times slower (at 85 °C [122]), etching of a (100) wafer gives channels with inclined sidewalls. In our mask definition channels of varying widths were made. The narrowest channels became v shaped with a depth lower than the etching depth of 5 µm, due to the anisotropic etch. As a barrier layer between the Ni and the silicon a 20 nm thick PECVD SiO₂ layer was used. After the e-beam exposure, the wafers were developed and subsequently the catalyst material (20 nm Ni) was deposited by ebeam evaporation. Lift off was accomplished with a 12 h bath in Microposit remover 1165, with use of ultrasonic treatment towards the end (3-4 pulses of 10 s duration).

The main challenge with the *Direct* method is that the resist, which is spun on, will not have a uniform thickness. It is very difficult to show this for ZEP resist, due to it being so thin. However, the problem is illustrated in Figure 74 A, where the coverage of conventional photoresist (1.5 µm thick) inside and in the vicinity of a microchannel is shown by a SEM image of a cross section. After spinning, the photoresist is seen to be thick in the channels, increasingly so close to the channel walls. Outside the channels the resist is very thin close to the channel walls. The results shown in Figure 74 B and C reveal two important points. First, the e-beam defined dots are very well defined, with homogeneous size despite the fact that the resist inside the channels were inhomogeneous and thicker towards the sidewalls of the channels. Second, it reveals a problem with poor lift off along the edges close to the channels. Due to the spinning effect of the resist, there is a very thin resist layer close to the edges, which prevents lift off. Therefore, a film of nickel is left along these sharp edges. Figure 74 D and E show that the catalyst dots give rise to homogeneous and well defined MWCNTs within the channel. As expected only one individual freestanding MWCNT is obtained for each deposited Ni dot. Unfortunately, it is also observed that the catalyst remains on the side edges also give rise to unwanted CNT growth. The problem of the remaining resist may be solved by using a sacrificial layer, along the edges, which is lifted off before the CNT growth. However, this remains to be investigated further.

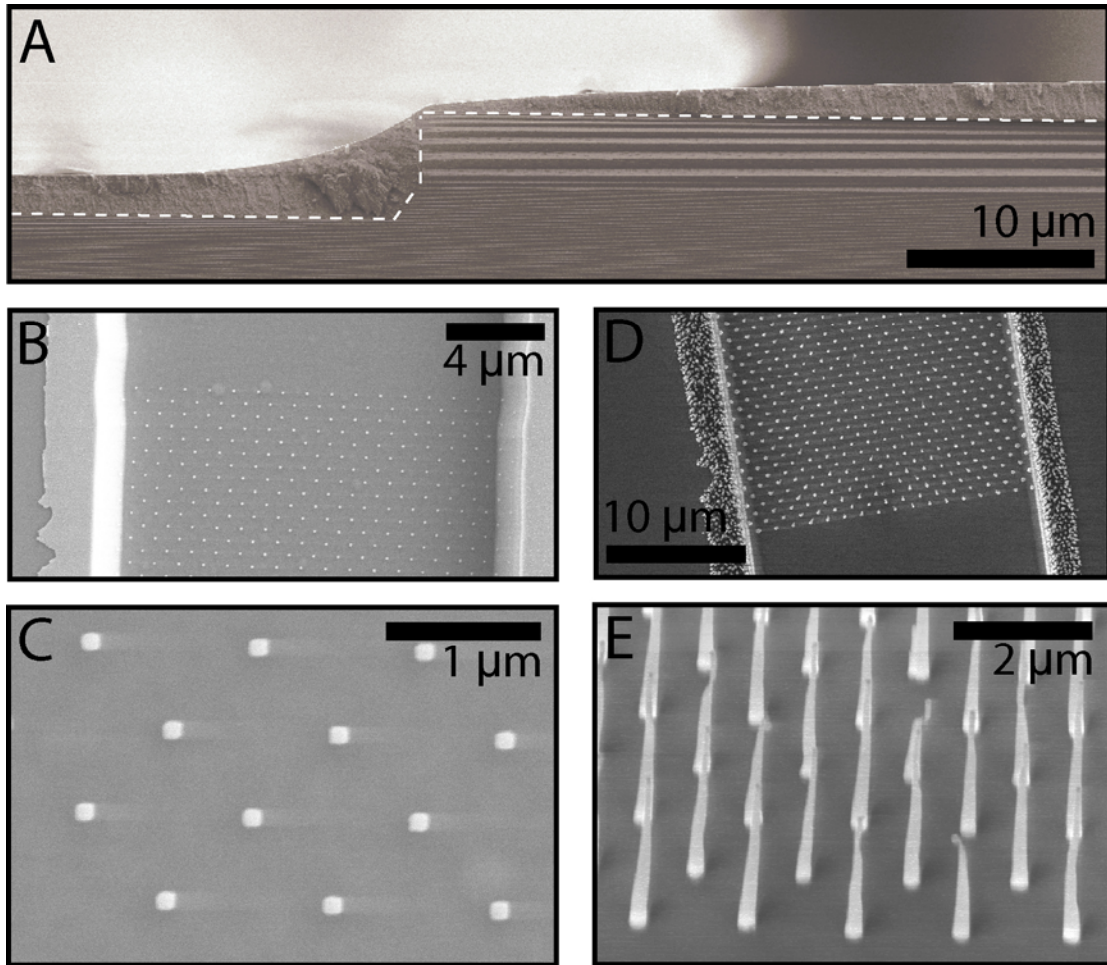


Figure 74 A) A SEM micrograph showing photoresist coverage on a wafer with microchannels. The dotted white line separates the photoresist from the wafer surface. Conventional photoresist is used to illustrate the resist coverage. The resist is seen to be thick inside the channels, especially close to the channel walls. However, the resist is also very thin directly outside of the channels, close to the channel walls. B) An array of Ni dots 100 nm in diameter defined within a 5 μm deep microchannel. Some Ni remains along the edges next to the channel. The lift off is poor in this area due to a very thin resist layer caused by the channel edge. C) A close up of the Ni dots show that they are uniform in size. D) After CNT growth in a PECVD process the MWCNTs grow uniformly all over the channel. However, the remains of catalyst material at the edge also give rise to an disordered CNT growth. E) Within the channel the CNTs are well defined and of similar size.

Suspended

The *Direct* method for integrating catalyst dots on suspended microstructures is more complicated due to the fragility of the wafers. Ideally, the best way to deposit resist on such structures would be by a spray coating. This would also give a more uniform coating of the system – possibly completely avoiding the problem with poor lift off around sharp edges in the microstructures. However, we have not had access to spray coating equipment. The alternative is spin coating, but without the use of vacuum. This spin coating follow the same spin parameters as normal spin coating, but the wafer is supported by pins instead of vacuum. First, microchips with freestanding monocantilevers were fabricated with a standard photolithographic process involving several masks. The actual processing details here are given in the original work of

[36, 37]. After the microprocessing, the wafer contains several hundred microchips, each with an individual monocantilever. There is no need for an extra barrier layer on these structures, since the cantilevers are made of silicon dioxide, which is a barrier itself. 100 nm ebeam resist was spun on. After the e-beam exposure, the wafers were developed and subsequently 5 nm of nickel was deposited by ebeam evaporation. Lift off proved to be problematic, and optical inspection showed that nickel remained in parts on the cantilevers, especially along the edges, see Figure 75. The lift off was done with a 12 h bath in Microposit remover 1165. Since the nickel remained along the edges, it was necessary to use some ultrasound treatment. Short pulses of ultrasound cleaned the cantilevers more. However, many cantilevers broke off under this harsh treatment. Ultrasound on suspended cantilevers drastically reduces the yield. The problem with remaining nickel along the edges of the microstructures after lift off, is the same problem that was observed for the channel structures on the microstructured surface. In Figure 75 C and D the results after nanotube growth is shown. As seen from above, the patterns seem to be well defined. However, as expected there is a lot of unwanted carbon nanotube growth along the edges, were the nickel remained after lift off. Furthermore it was observed that pattern designed in the interior of the microchips, far from any edges, became well defined with a successful lift off. Subsequent CNT synthesis gave the designed patterns.

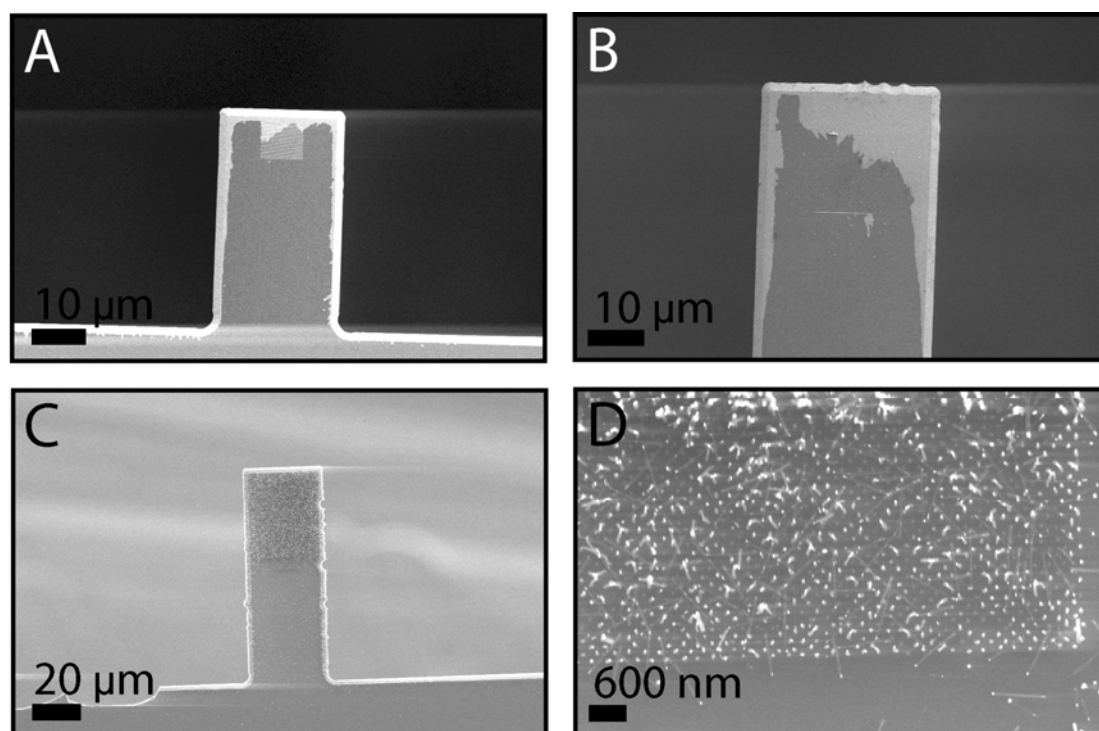


Figure 75 A) A suspended cantilever with nickel pattern after lift off. The e-beam defined pattern is seen as the square structure on the tip. There is also remaining nickel along the edges. B) Another cantilever with a different pattern, showing the same results as in A. C) After CNT synthesis, the CNTs are seen to grow from the nickel left on the cantilever. D) A close up shows that the pattern of CNTs seems to be well defined in the areas were the lift off has been successful.

Conclusion

The *Direct* method is capable of placing nickel dots on flat surfaces, microstructured surfaces, and suspended structures in a way compatible with cleanroom processing. However it is only on the flat surfaces that it is possible to obtain a good lift off. The poor lift off on the other structures is caused by the thin resist layer along the sharp edges of the microstructures. However, a possible solution to this problem could be to use a sacrificial layer, for instance p-Si, along the edges. When the resist is later spun on, the regions with too thin resist and subsequent poor lift off will be located on top of this sacrificial layer. These remains will then be removed together with the sacrificial layer by etching. This idea forms the basis of the *In situ* and the *Window* methods to be discussed in the next subchapters. A lift off obtained by a sacrificial layer, without the need of ultrasound, will also avoid the problem of cantilevers breaking off.

In situ mask

The method

The *in situ mask* method starts with a wafer where some microprocessing may have been done in advance, for instance fabrication of leads or trenches. The polysilicon (p-Si) is sputtered on top of these structures. The deposition rate in the used sputtering equipment has been estimated to be about 18 nm per minute. A 5.5 minute deposition gives then a 100 nm thick p-Si cover. The most important factor determining the optimal thickness is mainly how well the p-Si covers the underlying structures. It is also necessary to etch holes with RIE, and remove the layer in the end with KOH. These factors should also be considered. The EBL is done directly after the p-Si has been deposited, see illustration in Figure 76 A.

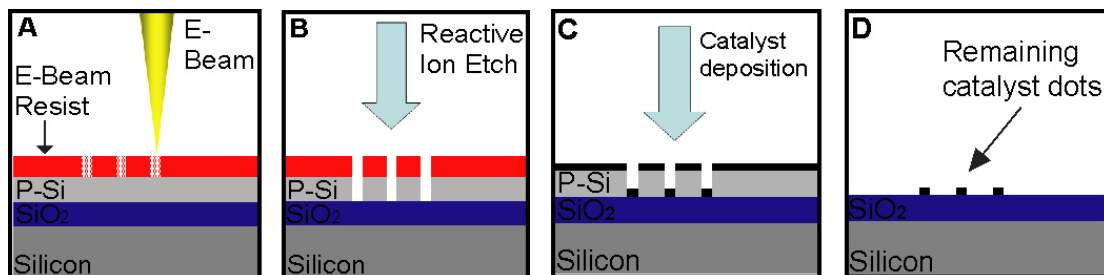


Figure 76 Illustration of the sacrificial layer approach. A) EBL is done on top of a wafer which has two layers, one 1 micron thick SiO₂ and one 100 nm thick p-Si. B) After development, reactive ion etching is used to etch holes through the p-Si layer. C) After all microprocessing has been done, the catalyst material may be deposited. D) The sacrificial p-Si layer is removed by a short etch in KOH, leaving a catalyst pattern on the substrate.

A 100 nm thick resist has been used in all tests with the in situ mask. The pattern is exposed with the ebeam, using an exposure dose of 600 $\mu\text{C}/\text{cm}^2$ and 0.8 nA beam current. After development the resist covers all the structures except the patterned holes. A short etch (about 60 s) in RIE, transfers these holes into holes in the p-Si layer, see Figure 76 B. The etch recipe consist of 32 sccm SF₆ mixed with 8 sccm O₂ at 30 W and 80 mTorr. There is also a slight isotropic etch component that will

enlarge the diameter of the holes, as compared to the ebeam defined mask. It is therefore important not to overetch, but to stop the etching when the etch is through the p-Si. The resist can then be removed, and the wafer is ready for subsequent microprocessing. Moreover, since no metal is present on the wafers, there is no risk of contaminating any cleanroom equipment. In the end, the catalyst material can be deposited on the three dimensional structures (Figure 76 C). The sacrificial layer is then lifted off, together with unwanted catalyst material. This is done with a 1 min dip in 80 °C KOH, which removes the p-Si. Table 9 shows the etch rate of some materials in KOH. It can be seen that the silicon is etched extremely fast as compared to the other materials present. Thus the p-Si comes off fast and leaves the catalyst dots on the microsystem, as sketched in Figure 76 D. The full process recipe is given in appendix B.

Table 9 Etch rates in KOH

Material	Etch rate in 30 % KOH at 80 °C (nm/ min), [123, 124]
Si (100)	1100
LPCVD p-Si	670
LPCVD SiO ₂	~8
PECVD SiO ₂	~15
Ni	~0
TiW	~1

By depositing the catalyst material in one of the very last steps and do a lift off, it should be possible to obtain a sample free of catalyst remains in unwanted areas. The choice of the sacrificial material for the in situ mask was crucial. It had to be physically and chemically appropriate for the remaining processing. However, it should also be possible to remove it – without damaging the underlying structures. The structures underneath will in most cases consist of silicon dioxide, lead material and catalyst. From Table 9 it is seen that p-Si is an excellent candidate. It is compatible with the microfabrication steps, as well as removable in a short KOH etch. The selectivity over nickel as catalyst and TiW as lead material is very large.

In situ holes

The etching recipe for p-Si has an etching rate of 440 nm/min in silicon. According to this, 100 nm of p-Si should be etched through in less than 20 s. It was necessary to try different etch times on several wafers, and see the trend. It is possible by visual inspection in an optical microscope to check whether or not the etching is finished. The actual holes are obviously too small, but a test structure was added to be monitored in optical microscopes. This test structure should have a homogenous colour all over the wafer, if all the p-Si is gone.



Figure 77 A) A sketch showing a cross section of the wafer at the current step in the processing. B) After just 30 s in the RIE, the test patterns still had a white colour. This was seen all over the wafer. C) After 50 s, all test patterns had a uniform red colour – indicating that the etching had come through the p-Si layer. Note that the colour of the surrounding surface also changes due to the resist also being etched.

After 30 s in RIE, the test patterns still had a uniform white colour all over the wafers, as seen in Figure 77 B. This indicated that there were still remnants of p-si present. The pattern along the edges of another wafer that got 40s changed to a red colour, whereas the patterns in the centre still had a white colour. This is not unexpected since the RIE process etches mostly along the edges of a wafer. A wafer that was etched for 50 s had a uniform red colour on all patterns. This indicates that 50 s is enough to etch through the p-Si in all patterns over the entire wafer. Therefore a series of four wafers with etching times 50 s, 60 s, 70 s and 80 s was prepared. For waferscale fabrication it is necessary to come through the layer all over the wafer. However, the downside is that microchips along the edges of the wafer will tend to have overetched holes.

In the following the results on three of the wafers, with etching times of 60 s 70 s and 80 s, will be discussed. Figure 78 shows the average hole size with standard deviation on one cantilever from each of the three wafers. The design size of these holes was 100 nm.

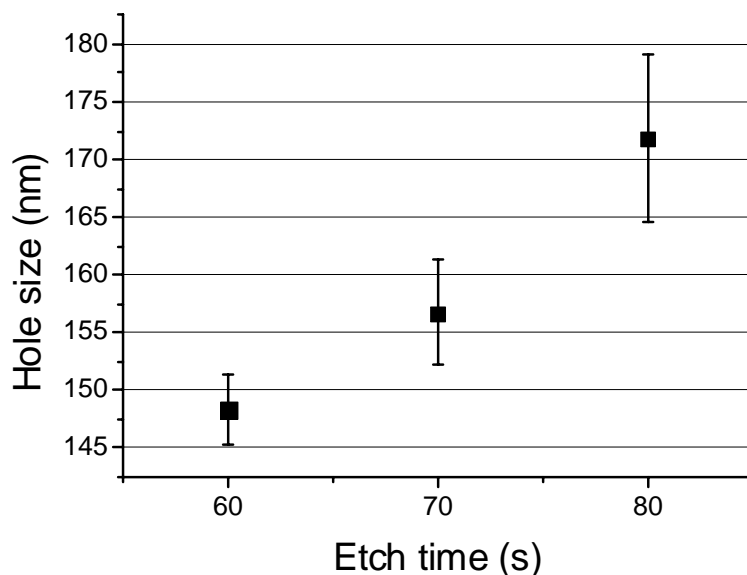


Figure 78 Average hole size and standard deviation on one cantilever from each of the three wafers.

It may be seen from Figure 78 that the average hole size decreases from an average of 172 ± 7 nm via 157 ± 5 nm to 148 ± 3 nm for the etch times 80s 70s and 60s respectively. There is some variation of the holes on each cantilever, but more important is the amount of overetch. For the 80s etch the holes size has increased by 72 % whereas this is only 48 % for the 60s etch. Apparently a 20 s etch time reduction gives a 24 nm decrease in overetch, corresponding to a lateral etch rate of 0.6 nm/s. An equivalent study of the hole size variation in some test array in the interior of the chips are shown in Figure 79. These test arrays consisted of 10 times 10 dots of 25 nm, 50 nm, 75 nm, and 100 nm, all with a pitch of 500 nm.

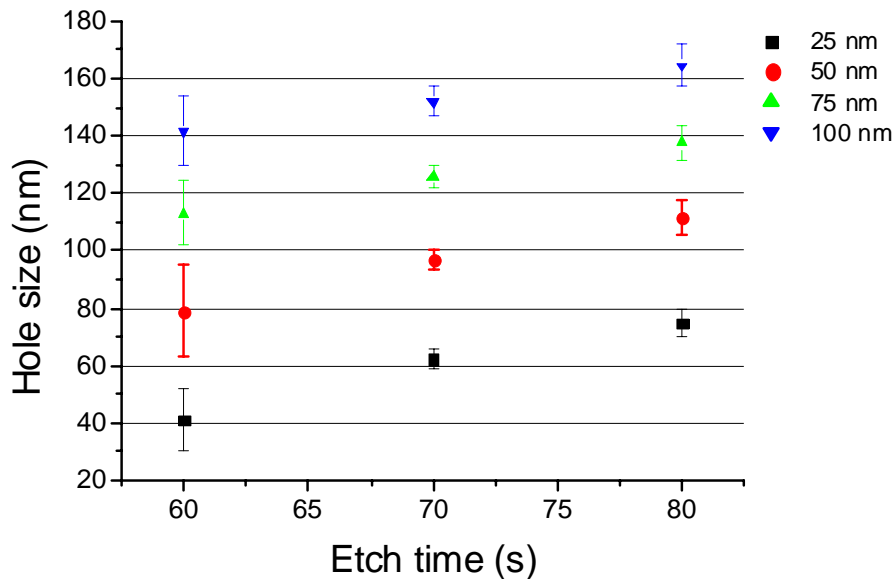


Figure 79 Average hole size and standard deviation for various hole size designs in several test arrays as a function of etching time.

Similar results are found for the hole sizes in the test arrays. However, the hole increase seems to be slightly smaller, giving a hole size of 165 ± 7 nm for the 80 s etch and 142 ± 12 nm for the 60 s etch. This also corresponds to a lateral etching rate of 0.6 nm/s. The lateral etching rate can also be estimated from the total overetch of 65 nm for the 100 nm design and 80s etch. This gives a lateral etch rate of 0.4 nm/s. The first estimate is probably the best, since it does not depend on the initial holes in the ebeam resist to be exactly the size of the design. Since the lateral etch works at the same rate for all hole sizes, the size increase is relatively larger for the smaller designs. However, the total overetch seems to be reduced for smaller holes as seen in Figure 80. This is important to consider when making designs with various hole sizes. In order to obtain the correct hole size in the p-Si layer, the design can be made smaller than the wanted size.

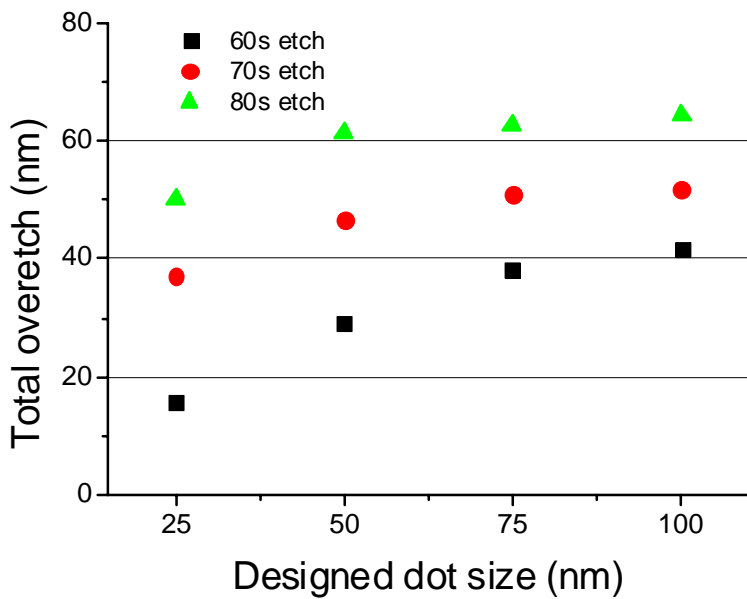


Figure 80 Total overetch of holes in the test arrays.

As was seen in Figure 79, the standard deviation of the hole sizes for the 60 s etch was larger than for the other etch times. This is probably not a consequence of the etch time, but rather of the fact that we got a chip from the edge of the wafer included. The RIE etch etches more along the edges, thus the overetch is increased. Figure 81 shows the hole size variation between three test arrays from the 60 s etch. Array 2 corresponds to the chip close to the edge of the wafer. Here it can be observed that the hole sizes resembles those found for the 70 s etch.

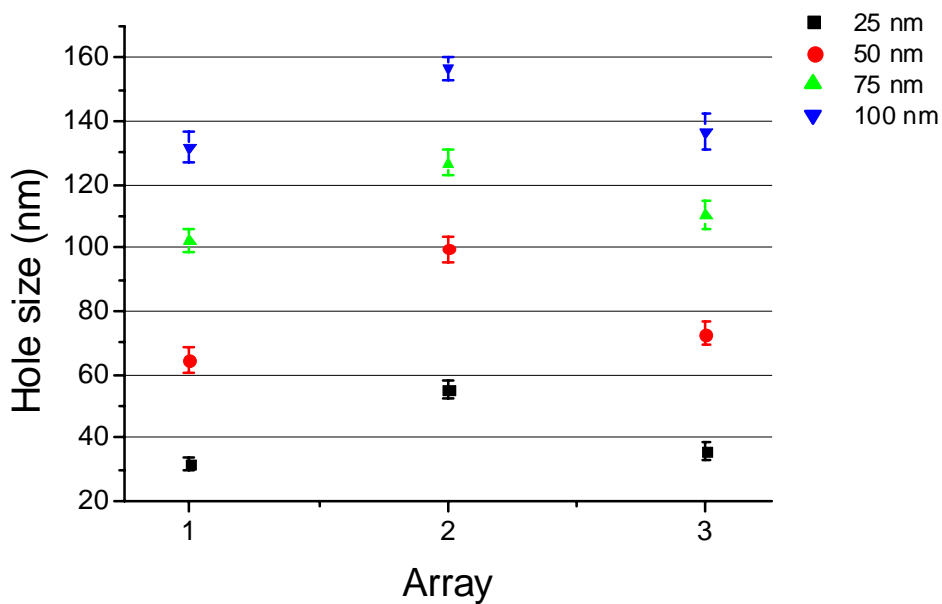


Figure 81 Hole size variation between different test arrays from the 60s etch.

On each chip another test pattern with arrays of dots was designed. Here the dot size was the same as for the smaller arrays, but the pitch was 10 times larger, at 5 μm . Figure 82 shows the measured dot size in these arrays for the three different etch times.

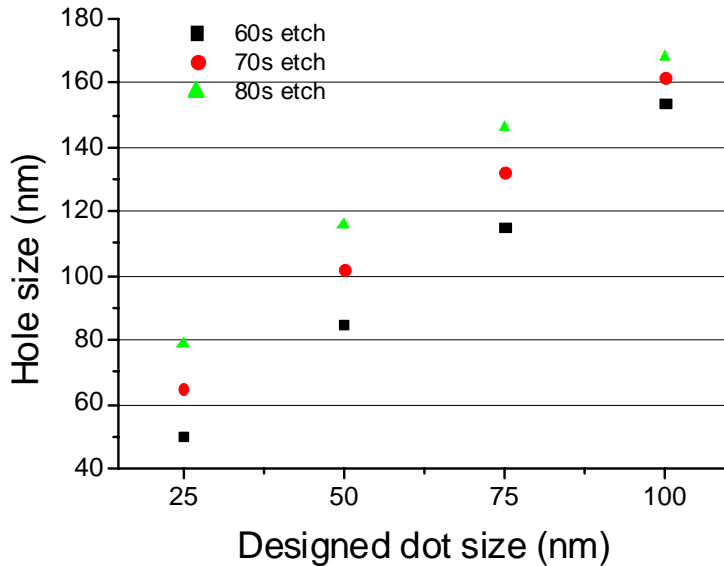


Figure 82 Measured dot size in arrays with large pitch

The hole sizes of the arrays with larger pitch may seem to be slightly larger than that of the small arrays, supporting the findings that the holes also on the cantilever tend to be larger. On the cantilevers the holes have a similar spacing as in the large arrays.

Microprocessing

According to the process recipe given in appendix B, the steps after etching of the holes involve the definition and fabrication of the cantilevers. However, unlike the process recipe, which use aluminium as an etch mask for the cantilever structures, the cantilevers were here fabricated using photoresist as etch mask. The resulting structures after oxide etch in RIE is shown in Figure 83 (see appendix B for etching recipes).

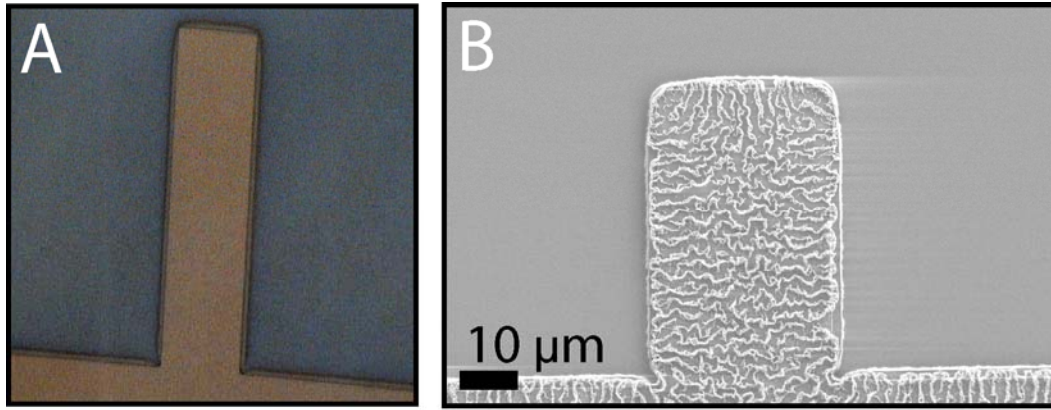


Figure 83 A) An optical microscope picture of a cantilever structure after resist strip clearly shows that the oxide structure (seen protruding along the edges) is not as well defined as the same structure in the above lying p-Si layer, here seen in a yellowish colour. **B)** A closer inspection of another cantilever with SEM shows that the resist has been smeared out. Also even after an hour in the plasma asher it is impossible to remove all of the resist – which leaves threadlike structures on the surface in some areas of the wafer.

It is seen that the geometry of the photoresist is deformed during the etching, resulting in a deformation of the cantilever structure as seen by the rounded red edge around the cantilever in Figure 83 A. This red edge is oxide protruding out underneath the yellow p-Si layer on top. The p-Si layer is seen to keep the designed geometry. In addition, it was observed that the removal of the resist was extremely difficult. Normally this is achieved with a 10 min dip in acetone – possibly with some ultrasound treatment. This was not effective in this case. A plasma asher with an oxygen plasma at 1000W for about an hour removed most of the resist, but still threadlike structures could be observed on some chips as seen in Figure 83B. However, if metal leads had been present underneath the resist, for instance at the bottom of the in situ holes, it would have been removed as well in the plasma asher. To preserve the cantilever geometry and avoid problems with resist removal, it is therefore recommended to use aluminum as etch mask, and remove this in an aluminum etch afterwards.

Figure 84 A shows a SEM picture of a clean cantilever, where eight well defined holes are visible. The holes were etched for 80 s in RIE on this wafer. One of the test patterns are shown in Figure 84 B-E, where the arrays with 25 nm , 50 nm, 75 nm, and 100 nm dots are shown in B, C, D, and E respectively. Even the 25nm small holes in Figure 84 B are clearly defined.

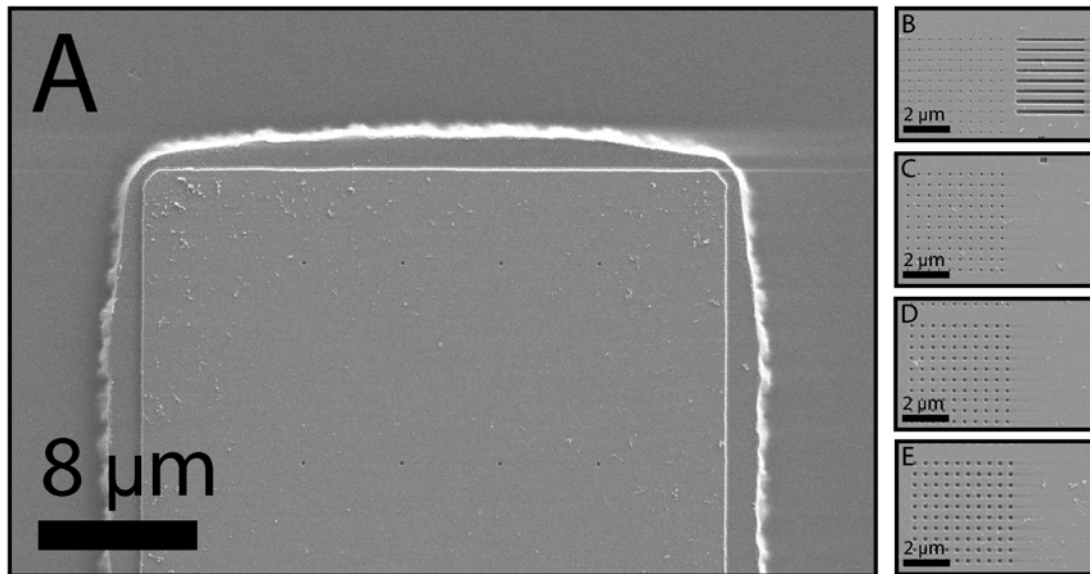


Figure 84 A) Eight well defined holes are seen on the cantilever. Note the rounded shape of the underlying oxide layer. B-E) Arrays of holes in test structures with hole sizes on mask design of 25 nm, 50 nm, 75 nm and 100 nm respectively.

On some chips remaining resist material was seen in the hole regions, possibly blocking some of the holes, as seen in Figure 85 A. During later catalyst deposition, this may cause a lower yield on the catalyst dots. Some surface damage on the p-Si was also observed, again only on some chips, see Figure 85 B. This may have been created during the etching of the cantilevers. Alternatively, the damage arose during etching of the holes, if the ebeam resist was too thin in some areas. Still, the holes are well defined, as seen in the close up in Figure 85 C. The use of aluminium as etch mask, and possibly a thicker ebeam resist during in situ hole etching will prevent this kind of surface damage.

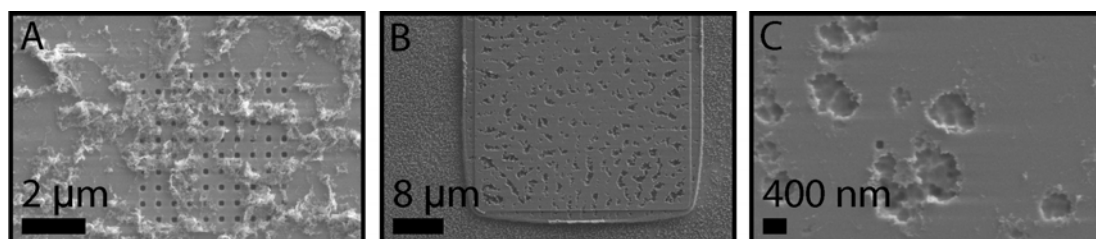


Figure 85 A) Resist remains on some chips partially blocking the in situ holes. B) A damaged p-Si layer on top of a fabricated cantilever. C) A close up shows that the in situ holes are well defined even on the damaged layer.

At this stage the structures qualifies for being a microstructured surface. However, to produce suspended cantilevers further processing is required. The microchip structure have to be defined through a photolithographic patterning step on the backside of the wafers, with subsequent etching. To protect the structures and define the etch pattern the wafers are covered in 450 nm of PECVD nitride on the frontside and 150 nm on the backside. Subsequent photolithography defines the etch pattern on the backside, which is transferred through the nitride and oxide layers with RIE. The wafers are then ready for the KOH etch that etches through the entire wafer, from the backside. A 350 μm thick wafer requires about 4 h 50 min in KOH at 80 °C. This is a very

delicate step, and often the wafers break into several pieces during the etch. However, at this stage the microprocessing is finished and even wafer pieces is suitable for the few remaining steps; nitride removal, catalyst deposition and KOH lift off.

In Figure 86 A-C optical images of some cantilevers after the KOH etch is shown. Figure 86 A shows a suspended cantilever where the p-Si is seen intact on the cantilever surface. The green and yellow colour corresponds to the p-Si layer on top of the suspended cantilever and on top of the silicon chip, respectively. The red colour corresponds to the nitride membrane. It is also possible to see the oxide edge around the rim of the cantilever. Most cantilevers are unharmed by the backside etch. However, some have a damaged p-Si layer. Figure 86 B shows a cantilever where the p-Si layer has been partly etched away. Here, the nitride did not encapsulate the p-Si entirely, thus allowing the etchant to start etching the p-Si layer once it got through the wafer from the backside. The green part of the cantilever is where the p-Si still remains, showing that it is not attacked from the upper rim. It is also observed that the p-Si on top of the silicon chip is also partly etched away. It is important to note that the etchant seems to have etched in areas that was unclean. Both on the solid chip and on the cantilever there are black particles where the etchant has entered. Figure 86 C shows a cantilever completely covered in these particles, and all p-Si has therefore been etched. It is suggested that these black particles are photoresist remains that could not be removed, as was seen in Figure 85A.

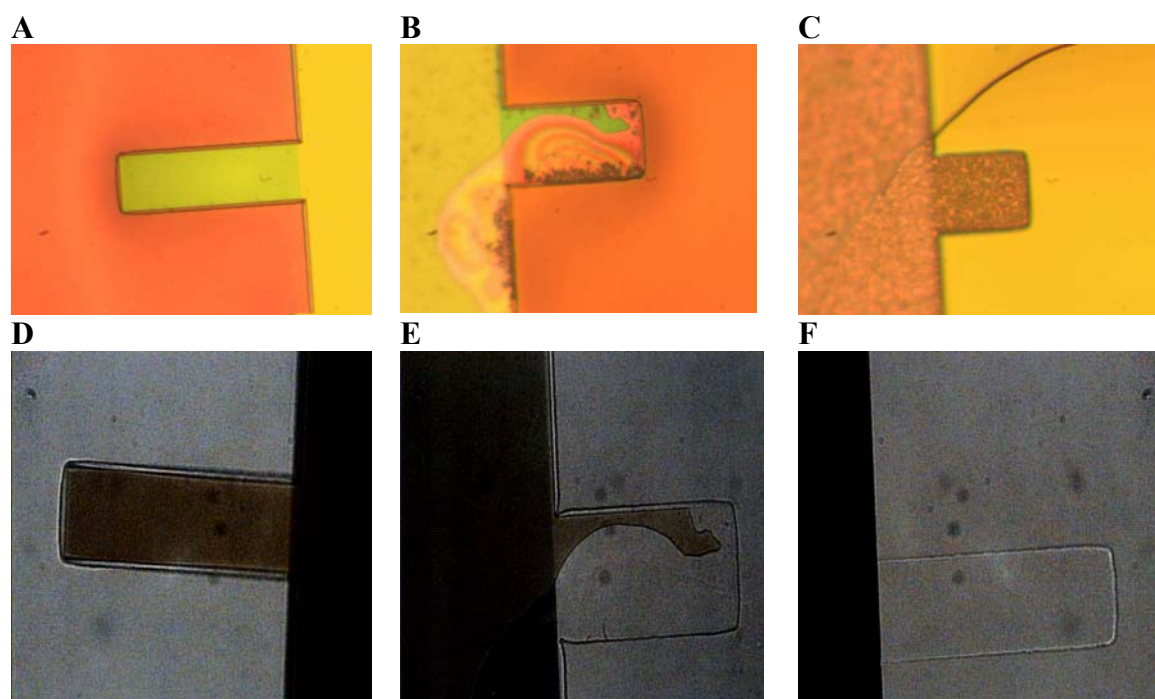


Figure 86 A) An undamaged cantilever after KOH etch of the backside B) A cantilever where the p-Si (green and yellow) has been partly etched away. Note that the etch of the p-Si has started along dirty edges with black particles, probably resist remains. C) A cantilever where the p-Si has been completely etched away. Here the entire surface is covered in resist remains. D-F) The nitride etch does not damage the p-Si layer or the oxide cantilevers. B and E are the same cantilever.

Before the nickel catalyst can be deposited, the nitride layer on top of the structures needs to be removed. A phosphoric acid etch (nitride etch) at 160 °C and a pH of 2 is

used to remove the nitride. Tests have shown that the p-si layer is undamaged even after 50 minutes in this etch. Figure 86 D-F shows some optical images of cantilevers after 20 minutes nitride etch. Subsequent inspection of the structures in SEM reveals two things. First it confirms that the p-Si layer is intact, as can be seen in Figure 87 A where also the holes on the cantilever can be observed. Second, there still appears to be some layer on top of the holes, thus clogging them up. This is clearly seen in Figure 87 B. The etch time was increased to 30 minutes, but even then hole in some areas were clogged up. It was later discovered that the nitride coating had been oxygen contaminated, thus preventing removal in some areas. This explains that some cantilevers had a nitride cover that could not be removed as seen in Figure 87 C.

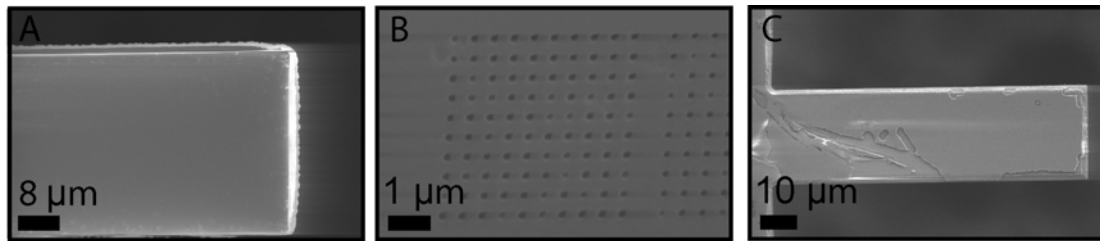


Figure 87 A) Inspection in SEM shows that the p-Si is undamaged. B) Still after 20 minutes of nitride etch the holes appear to be clogged up. C) A cantilever with nitride cover that cannot be removed.

Even though some microchips could not have the nitride removed, the yield of successfully cleaned microchips was high enough to give many test structures.

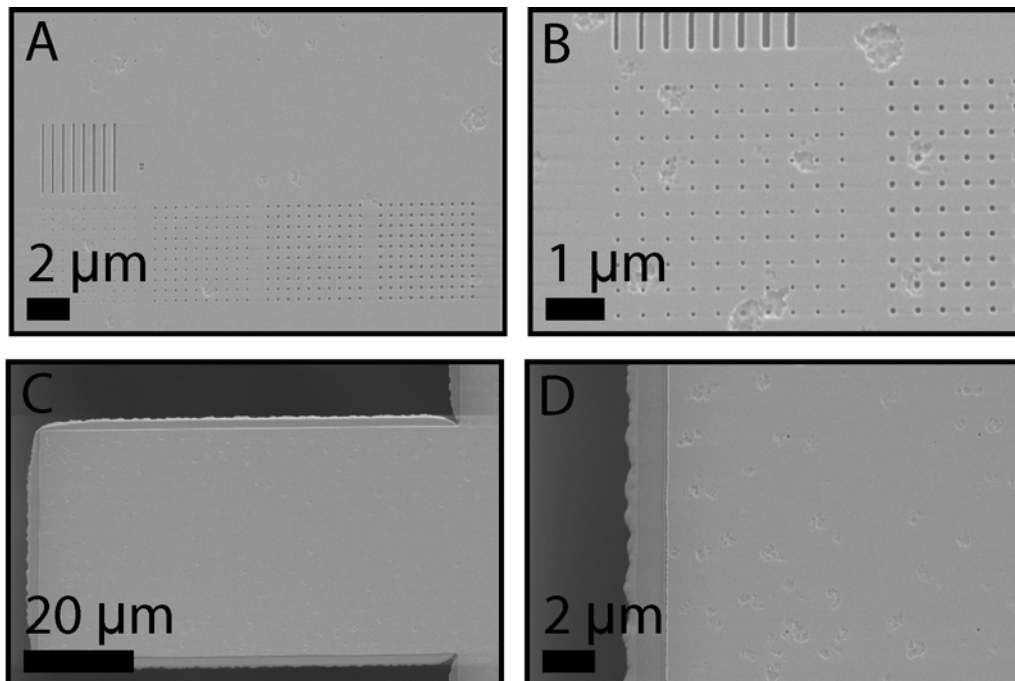


Figure 88 A) A test array of holes after nitride removal. B) A close up of the structures in A. C) A cantilever with holes after nitride removal. D) A close up of the cantilever in C.

Figure 88 A and B show holes in test arrays where the nitride layer have been successfully removed (after a 30 minute etch). It can be noted in addition to that the holes are clean, that there is no damage caused to the p-Si layer from the phosphoric etch. This can be seen by inspection of the hole structures, and indicates that the pieces can be treated with phosphoric etch for a long time. The damage that is, is probably caused during either etching of the holes or the cantilever structure. Figure 88 B shows a successfully cleaned cantilever with holes (see close up in Figure 88 D).

Microstructured

The *in situ mask* method has not been tested on flat structures, where the *Direct* method already works satisfactorily and also is a far simpler method. However, on microstructures surfaces it was necessary to develop alternative methods. In this subchapter the results of the *in situ mask* method on microstructured surfaces will be presented.

A wafer with cantilever structures, but without backside processing is used to assess the applicability of the *In situ mask* method for microstructured surfaces. The RIE etch time of the *in situ* holes were 80 s on this sample. Parameters to be optimized in this study are the thickness of the nickel catalyst, and the lift off time in KOH. Nickel with thickness 5 nm, 10 nm, 20 nm, and 30 nm was deposited on four different pieces. The etch rate of p-Si in KOH is more than 10 nm per second [123], however it is covered in a nickel film that has to break up before the p-Si can be etched away. It is possible, by visual inspection, to see when the lift off is complete, as the nickel film, with an etch rate of 0, comes off in continuous pieces. The lift off takes about 60s. Figure 89 shows resulting nickel patterns both on cantilevers and in test arrays for the various nickel thicknesses.

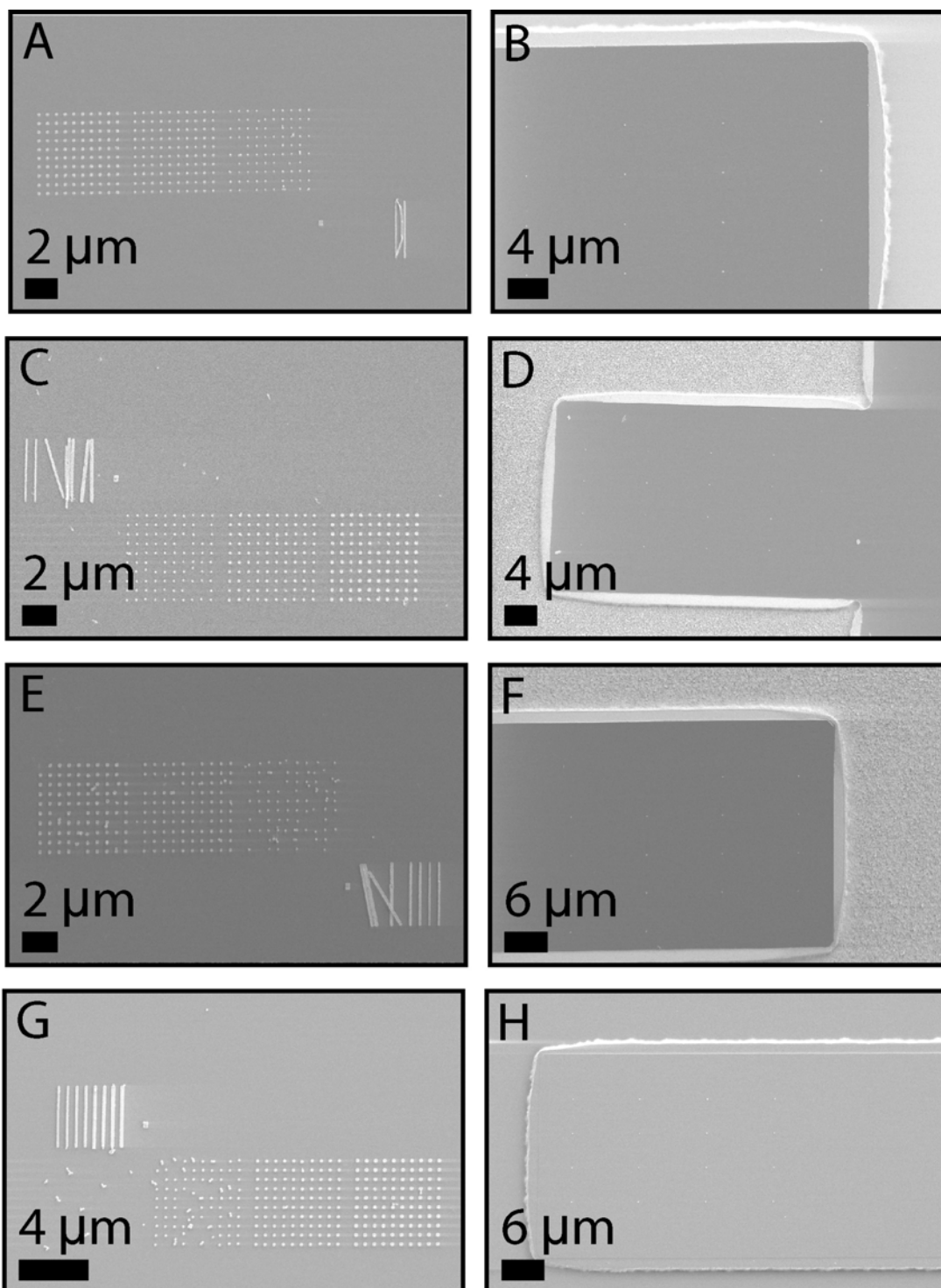


Figure 89 A) Array pattern with 5 nm Nickel. B) Dots (5 nm nickel) on cantilever. C) Array pattern with 10 nm Nickel. D) Dots (10 nm nickel) on cantilever. E) Array pattern with 20 nm Nickel. F) Dots (20 nm nickel) on cantilever. G) Array pattern with 30 nm Nickel. H) Dots (30 nm nickel) on cantilever.

It is seen that most catalyst dots remains in the patterns, and that there is no obvious difference between the samples with different nickel thickness. However, it can also be noted that the smallest dots in the design, the 25 nm in diameter, are poorly defined and almost missing on all samples. Also, the larger test lines seem to have been

moving around slightly. This seems to have occurred more the thinner nickel layer there was.

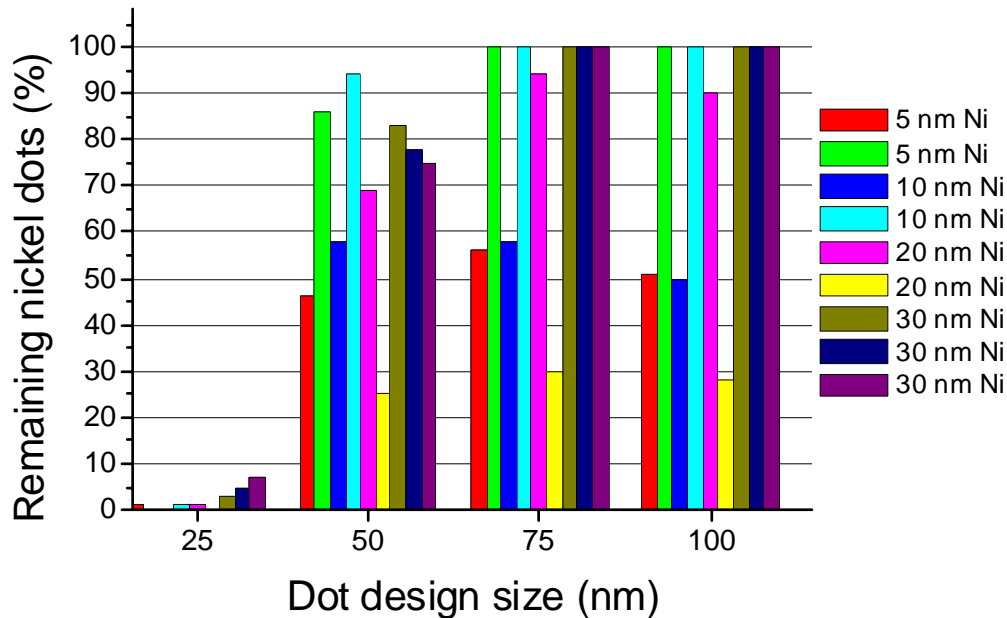


Figure 90 Remaining nickel dots in the test arrays as a function of dot design size and nickel thickness.

Figure 90 shows how many dots that remained in the different arrays, where the variable parameters are both the nickel thickness and the dot design size. It is evident that the smallest dots are not surviving. Only a few percent of the designed dots are present. It is unclear whether this is caused by insufficient etching of the holes or that the small nickel dots simply are lifted off by the KOH etch. It was seen that the larger lines are displaced by the KOH, which indicate that lift off may be the problem. However, the remaining designs show higher yield. The yield is still lower for the 50 nm designs where we see yield of 40 – 80 %. The individual variation between different samples seems to be large. For both 75nm and 100 nm design the yield is 100% for good chips, but around 50 % for bad chips. Overall the larger the dot design is the more dots survive. When considering the effect of nickel thickness it does not seem to have too large influence. For instance is the worst example from the 20 nm nickel catalyst. It is believed that the individual variation from chip to chip is larger than the effect of varying nickel thickness. However, a trend is seen, showing a higher yield for the 30 nm nickel samples, and more consistently close to 100 %.

Inspection of the test arrays with large pitch shows the same results, see Figure 91. It is seen that the yield increases as the dot design size increases. Virtually no 25 nm dots remain whereas around 80 % of the largest dots remain. The yield also increases with increasing nickel thickness.

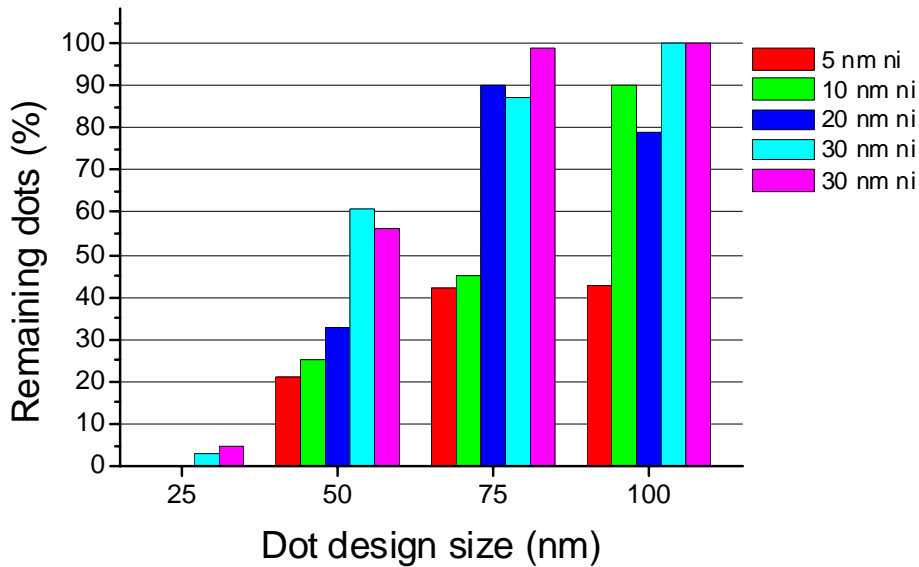


Figure 91 The yield of nickel dots in large test arrays as a function of dot design size and nickel thickness.

On the cantilevers, all dots were designed to be 100 nm. Figure 92 shows the nickel dot yield on cantilevers as a function of nickel thickness. It is interesting to note that in this case, the yield is highest for the 5 nm nickel thickness, where all 5 investigated cantilevers had a yield of 100%. The occurrence of bad cantilevers with lower yield increases with increasing nickel thickness. This is actually the opposite of what was expected from the test array findings. This discrepancy could be caused by the limited statistical basis, although 5 different chips on average were inspected for the different nickel thicknesses on the cantilevers.

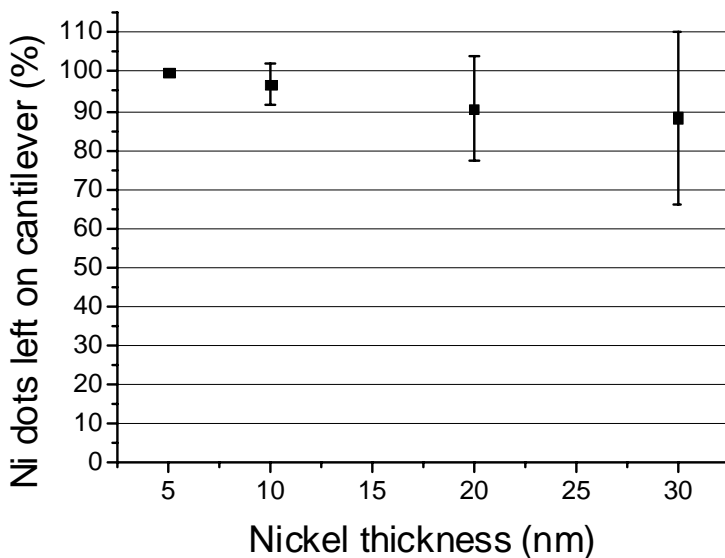


Figure 92 The yield of nickel dots on cantilevers, as a function of nickel thickness. A trend is seen, where the yield is highest for the thinnest nickel thickness. On average 5 cantilevers were

inspected for each nickel thickness. Remarkably all 5 inspected samples with 5 nm nickel showed a 100 % yield.

The size of the nickel dots has been investigated for the small test arrays. Figure 93 A shows how the size corresponds to the different designs, as well as for different nickel thicknesses. The size seems to be independent of nickel thickness, as could be expected. Furthermore, the dots are significantly larger than the designed size. The dots appear to be about 60 to 80 nm larger than the design. This corresponds well to the overetched holes measured in Figure 79 for 80s RIE etch. Inspection of the dot size on one cantilever with 30 nm nickel showed a dot size of 192 nm with a standard deviation of 6 nm.

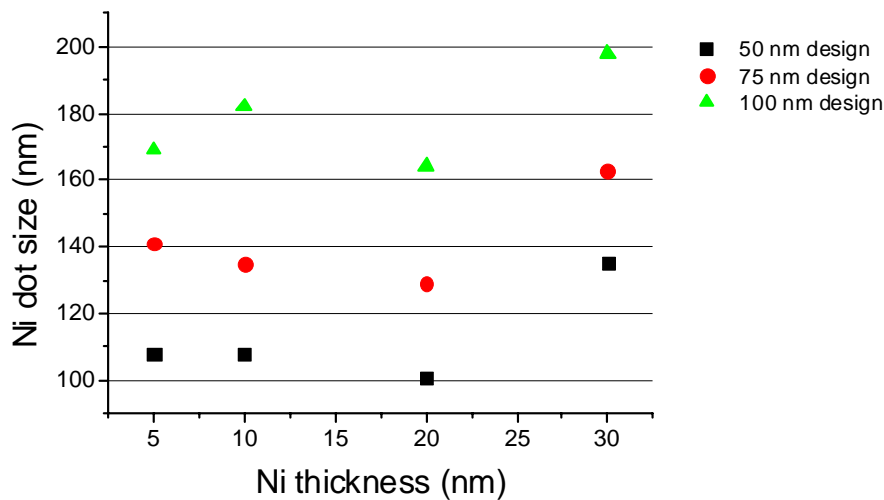


Figure 93 Size of nickel dots in small test arrays as a function of nickel thickness and designed dot size.

Figure 94 A shows a cantilever structure after KOH lift off. The nickel dots on the cantilever can be seen as small white dots. Also note that the nickel also covers everything around the cantilevers. Even on the ill defined sides of the oxide cantilever the nickel can be seen, here appearing as white. The nickel was deposited directly on the oxide cantilever edges, since the p-Si did not cover the edges entirely. This should not be a problem if the cantilevers were fabricated with aluminium as an etch mask. However, a method was developed to avoid the problem. As shown in the sketch in Figure 94 B, the p-Si layer does not cover the edges of the oxide cantilever. A short dip in BHF after the cantilever fabrication step solves this problem by etching the oxide underneath the p-Si layer. This can be done irrespective of whether aluminium or photoresist is used as etch mask. Subsequent deposition of nickel leaves the cantilever without nickel along the edges, and the p-Si can thereafter be lifted off leaving no nickel but the desired pattern. Results from a batch, made by Marc Fornes Mora, where this has been implemented are shown in Figure 94 C and D. The SEM micrograph in Figure 94 C shows the cantilever structure after CNT growth, and it shows a very good definition of the CNT pattern on the cantilever, with only very few stray CNTs.

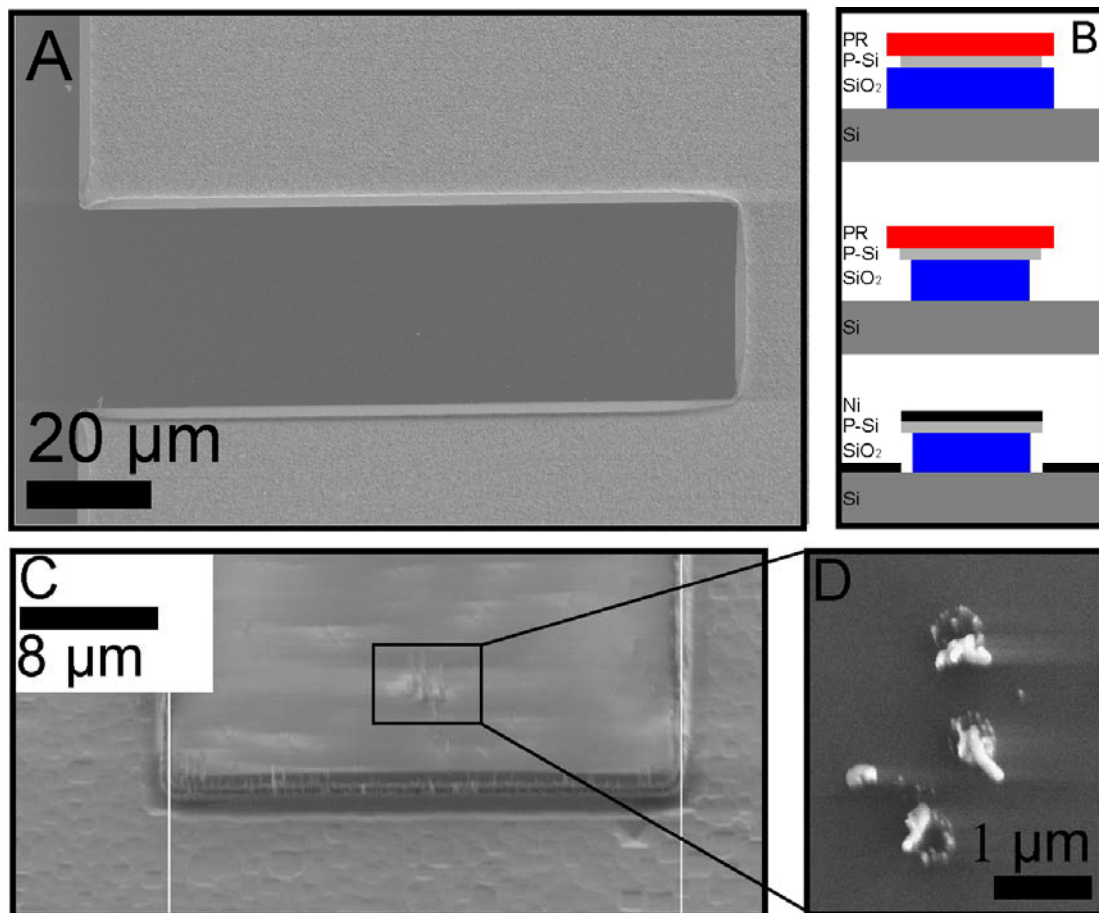


Figure 94 A) A cantilever structure as seen from above after p-Si lift off. The nickel dots are seen as light dots on the cantilever. The light area around the cantilever is also nickel. Note that the nickel remains on the sides of the poorly defined oxide cantilever. B) A method to remove the protruding oxide sides of the cantilever is suggested. The situation is sketched in the topmost sketch, where the p-Si does not cover the underlying oxide completely (The coverage is vastly improved by using aluminium as etch mask). A very short dip in BHF etches the edges of the oxide cantilever – improving the p-Si coverage. Subsequent deposition of nickel then leaves the cantilever edges clean of nickel. C) An improved batch where the p-Si layer is slightly underetched avoids the problem with catalyst material along the edges. D) A close up shows that the CNTs are fairly well defined.

Suspended

Microchips with suspended cantilevers are used to assess the *In situ mask* method for suspended structures. The RIE etching time for the in situ holes was here 70s. Figure 95 shows a suspended cantilever with 5 nm thick nickel dots after KOH lift off. On this particular cantilever the yield is 14 out of 16 dots. In fact on this particular piece the KOH lift off lasted 2 minutes due to a slow lift off in some areas. However, it was later discovered that slow lift is caused by a poor nitride quality (oxygen rich), and 1 minute is KOH lift off is enough on well defined samples. The inset show the nickel dots in the test arrays. It can immediately be seen that the smaller dots have a low yield.

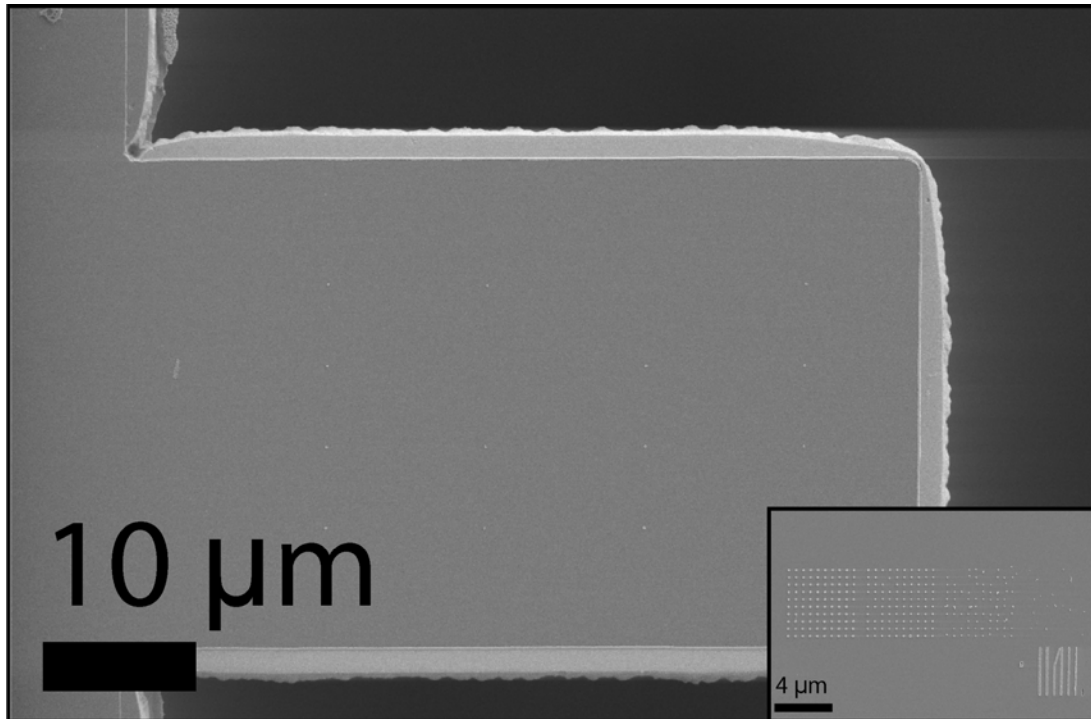


Figure 95 A cantilever with 5 nm nickel dots. The yield is here seen to be 14 out of 16 designed dots. The inset shows the nickel dots in the test array.

The yield of nickel dots on the cantilevers has been found to be $56 \pm 24 \%$, which is rather low. However it is believed that this yield is lowered by the problems identified, such incomplete photoresist removal and nitride removal, thus it should be possible to increase the yield significantly. Equivalent structures without the backside processing showed a 100 % yield (Figure 92). To test how well nickel dots survive the KOH lift off, piece was given a 7 minutes lift off. Interestingly, 12 out of 16 catalyst dots were still left on the inspected chip. This indicates that the nickel dots on oxide can withstand the KOH etch for a substantial time. Nevertheless, even a yield of around 50% will be acceptable for fabrication of AFM tips, where only one tip is required. In this case half of the chips on an entire wafer would work. The dot size on the cantilevers was found to be 161 nm with a standard deviation of 7 nm, for these 100 nm designed dots. This corresponds well with the hole size found in Figure 78 of 157 nm. Figure 96 shows the dot size and yield for the test arrays.

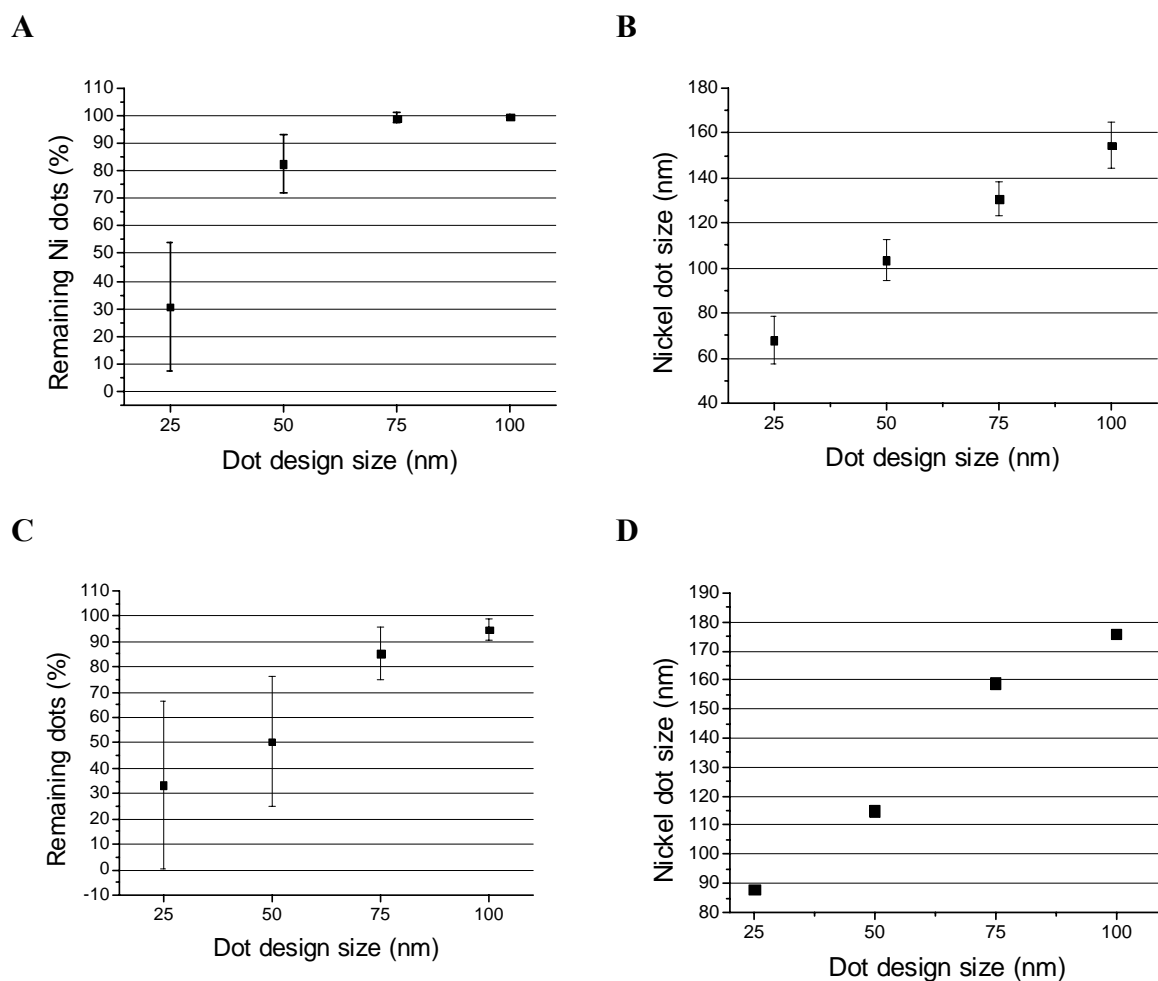


Figure 96 A) Remaining nickel dots in small test arrays. B) Nickel dot size in small test arrays. C) Remaining nickel dots in large test arrays. D) Nickel dot size in large test arrays.

Figure 96 A shows that the yield of nickel dots in the small test arrays is high for the larger dots. Even for the 25 nm design the yield is more than 30%. The actual dot size, shown in Figure 96B, is about 50 nm larger than the design. Thus it is the 50 nm design that gives a dot of about 100 nm. In order to achieve a 100 nm dot it is then possible to design 50 nm dots, and accept the overetch in the RIE etch of the in situ holes. Alternatively the etching time can be further reduced to give better correspondence between design and dot size. It is also observed that the yield of the dots having physical dimensions of 100 nm (the 50 nm design) is around 80% (Figure 96 A). Inspection of the test arrays with large pitch shows a smaller yield than that for the small pitch arrays, see Figure 96 C. This is indeed strange, since the physical dimensions of the dots are actually found to be larger than in the small pitch arrays, see Figure 96D.

Carbon nanotube synthesis has been performed on microhips fabricated in an equivalent way as described above by master student Marc Fornes Mora. Figure 97 A shows a four point probe with one single catalyst dot on each cantilever. Figure 97 B shows a close up of such a cantilever. However, also here we can see the bright rim around the cantilever, which corresponds to the nickel catalyst deposited on the oxide rim. Figure 97 C shows the cantilevers after CNT synthesis. Larger central tubes can

be seen in the area where the catalyst dots were deposited. However, there is also a lot of unwanted CNT synthesis along the rim of the cantilevers, caused by the catalyst layer deposited on the exposed oxide.

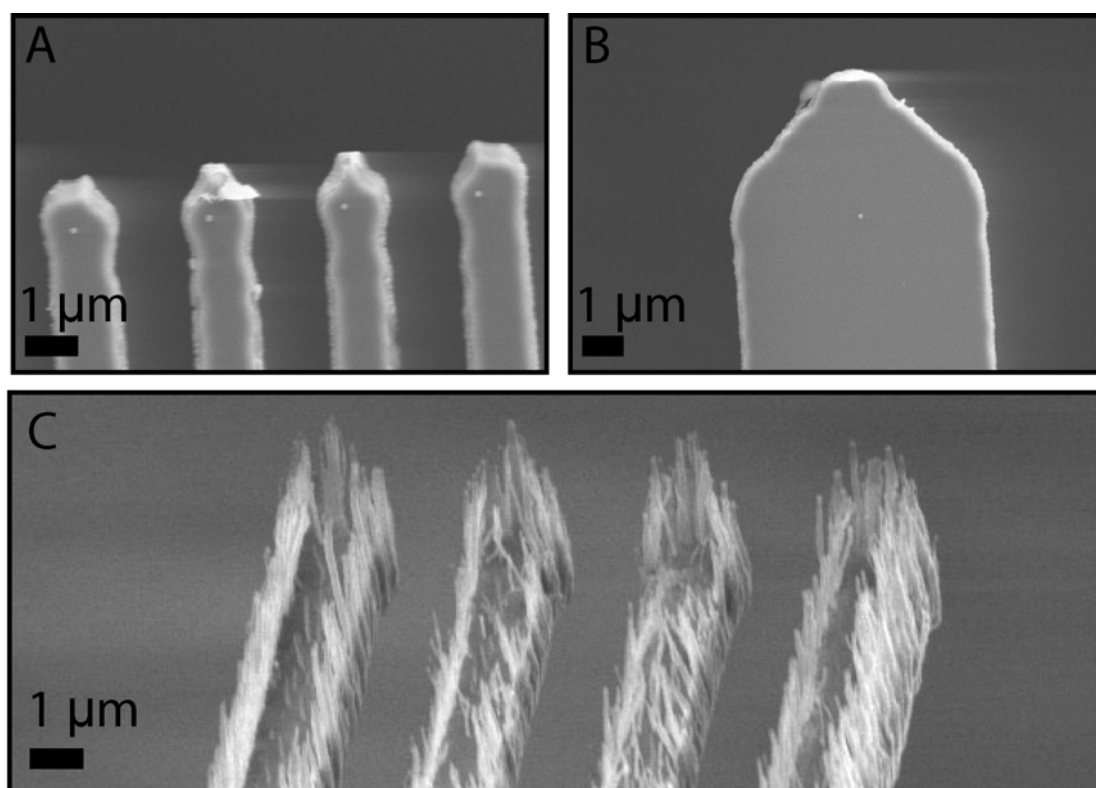


Figure 97 A)-B) After lift off of the p-Si mask, the catalyst dots are seen left on the substrate. Catalyst material is also left along the rim of the cantilever, and can be seen here as a bright edge. C) The PECVD process synthesizes CNTs also along the edges of the cantilevers, as well as from the catalyst dots. However, the CNTs seem to be smaller, at least in diameter, than the main tubes on the tip centre.

Conclusion

The *In situ mask* method was seen to be fully capable of integrating nickel catalyst dots on microstructured surfaces. Here the yield of dots were as high as 100 % for 5 nm thick nickel dots on cantilever structures (Figure 92). Also on suspended cantilevers was the method capable of placing the catalyst dots, although the yield was not as high. However, it is believed that this yield can be increased by using aluminum as an etch mask for the cantilever fabrication, and by using a better quality nitride. Furthermore, there seems to remain a problem with nickel along the edges of the cantilevers. A method to accommodate this has been developed, where an in situ aluminum etch mask is carried through on top of the p-si layer. In this approach, the final cantilever geometry is etched out after the backside etch (see appendix B for process details). This method is further explained in the next subchapter on the *Window mask* method.

Window mask

The method

The *Window mask* method is a combination of the *Direct* and the *In situ mask* methods, as explained in the introduction. The method uses a p-Si layer deposited early in the process as a lift off layer much like the *In situ mask* methods does. However, in stead of fabricating small holes in this layer, larger open *window* areas are made by photolithography. After the microprocessing has finished, the ebeam steps are then performed on the finished structure much as was done on the *Direct* method. However lift off is here accomplished with a short etch in KOH, lifting the p-Si layer and the resist, without the need of ultrasound which was so detrimental to the *Direct* method. Furthermore, since the p-Si covers the oxide and lead structures, no remaining nickel catalyst will be present in unwanted areas. Schematics of some important steps are shown in Figure 98.

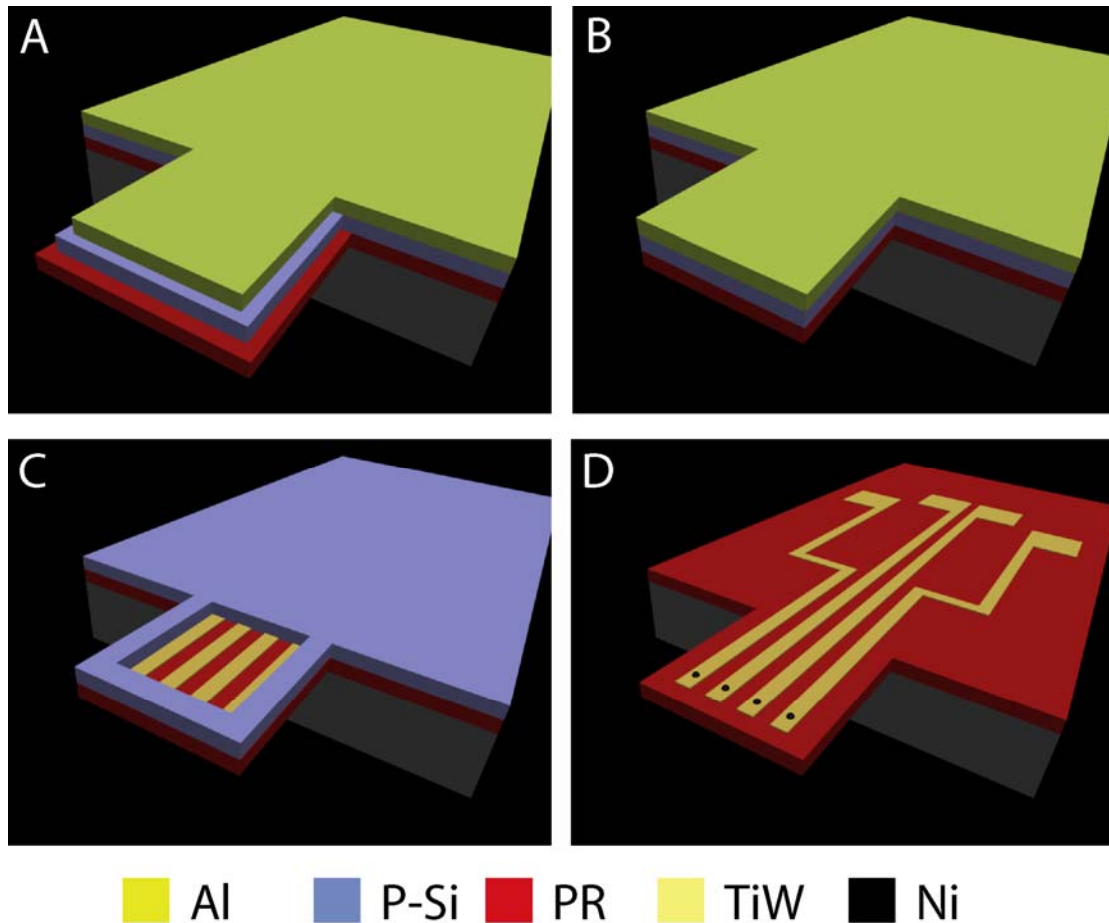


Figure 98 Important steps in the Window mask method A) After KOH etch of the backside the chip consists of three layers; Oxide (with leads) in red, p-Si (with window) in blue, and Aluminium (in situ etch mask) in yellow. There is also a nitride layer on top of everything (not shown). B) The nitride layer is removed in RIE. At the same time the final geometry of the suspended structure is defined (by RIE). C) A selective aluminium etch removes the in situ etch mask. D) After the ebeam steps, a lift off in KOH leaves the structure with nickel dots in the defined locations.

Figure 98A Shows the structure after the KOH etch of the backside. At this stage the structure is covered in nitride as well, which is not shown in the sketch for clarity. The sketch shows the first of two new innovations in this method. The last microprocessing step on the frontside put an in situ aluminium etch mask (yellow) on top of the microchip. It is this layer that defines the final cantilever geometry in the end. The aluminium layer lies on top of the patterned p-Si layer which again is on top of the oxide layer with leads (if applicable). It is important to note the steps between the layers. Since there is a free oxide surface around the cantilever, the nitride cover will protect the p-Si completely against the KOH during backside etching. The removal of the nitride and etching of the final cantilever geometry is accomplished in RIE (see process recipe in appendix B for details). In this way the sidewalls of the cantilever becomes vertical (Figure 98B), with perfect coverage of the p-Si over the oxide. It is even possible to include a short BHF dip to etch the oxide further underneath the p-Si, however, the cantilever will also be thinned. After removal of the aluminium in an aluminium etchant the structure is left as shown in Figure 98C. The p-Si layer covers everything except small window areas (the second new innovation) where ebeam writing is supposed to be done. As for the *Direct* method the ebeam resist is spun on using mechanical fixation of the wafer instead of vacuum. After metal deposition and lift off in KOH the structures are left with nickel dots in the patterned areas (Figure 98D). The idea with the *Window* method is to use the advantages of both the *Direct* and the *In situ mask* method, avoiding their drawbacks. We preserve the writing precision of the *Direct* method and combine that with the easy lift off of the *In situ mask*.

Microstructured

We will in this subsection study the results from the *Window mask* method on microstructured surfaces. The microstructures are here oxide structures (cantilever shaped) with leads (50 nm TiW) on top. Conventional photolithography is used to define the pattern of the p-Si. The P-si is sputtered on for 5.5 min at 640 W, which deposits about 100 nm on the wafer. Lift off in the window areas is accomplished in acetone, with ultrasonic treatment till the structures are clean. Subsequent photolithography defines the etch mask of the cantilever structures, see Figure 99A. Aluminum is deposited as an etch mask and the oxide structures are fabricated in RIE. Figure 99B shows the cantilever structure with the aluminium mask on top, corresponding to the sketch in Figure 98B (without backside). Figure 99C shows a close up of the cantilever corner in Figure 99B. It is noted that the sidewalls are very well defined and close to vertical. If needed, a short dip in BHF will etch the oxide further underneath the p-Si layer. The aluminium will also be slightly etched (11 nm/min [123]), but it is going to be removed in the subsequent step.

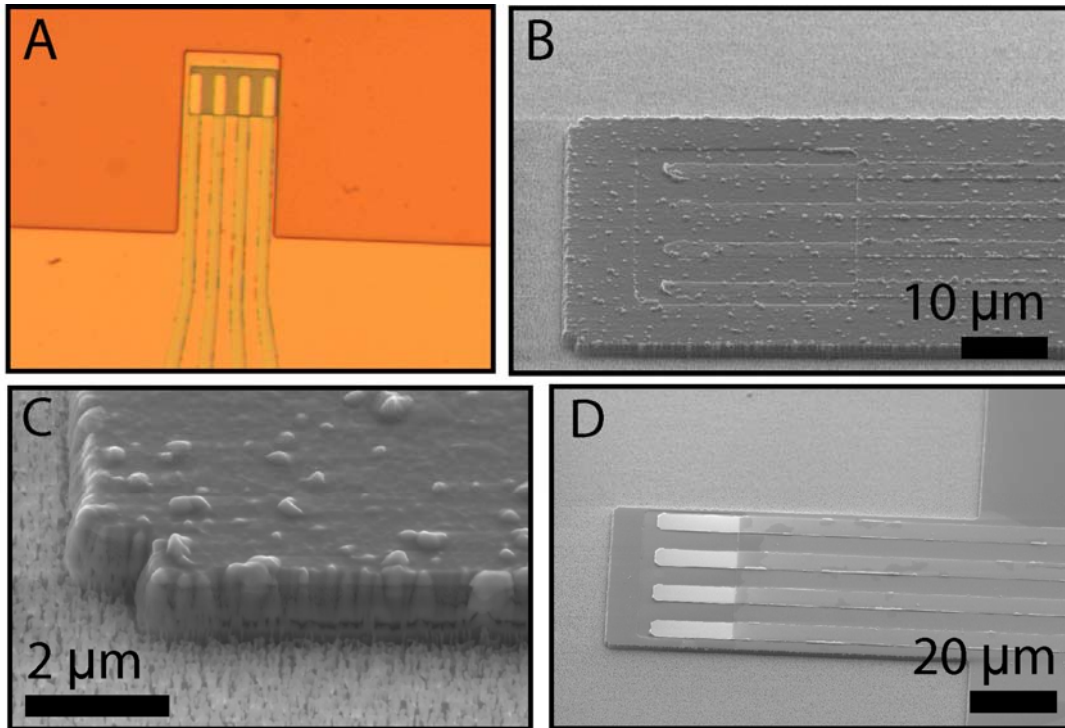


Figure 99 A) Photolithography defines the area for deposition of the aluminum etch mask. The window in the p-Si layer is clearly seen at the tip of the cantilever geometry. B) A SEM micrograph of the structure after RIE etch. C) A close up of the structure in B, shows that the sidewalls are nearly vertical. D) A SEM micrograph after removal of the aluminum etch mask.

The etch mask is removed in an aluminum etchant leaving the structures underneath undamaged as seen in Figure 99D (corresponding to Figure 98C). For microstructured surfaces (without backside processing) the ebeam resist can be spun on using the normal recipe (with vacuum). After ebeam exposure and development, 10 nm of nickel was deposited by evaporation on the wafer shown here. The timing on the lift off in KOH is important. As for the *In situ mask* method a complete lift off is accomplished in a very short time. Visual inspection shows that the lift off in 20 % KOH at 80 °C is completed in about 20 s. Results after lift off are shown in Figure 100.

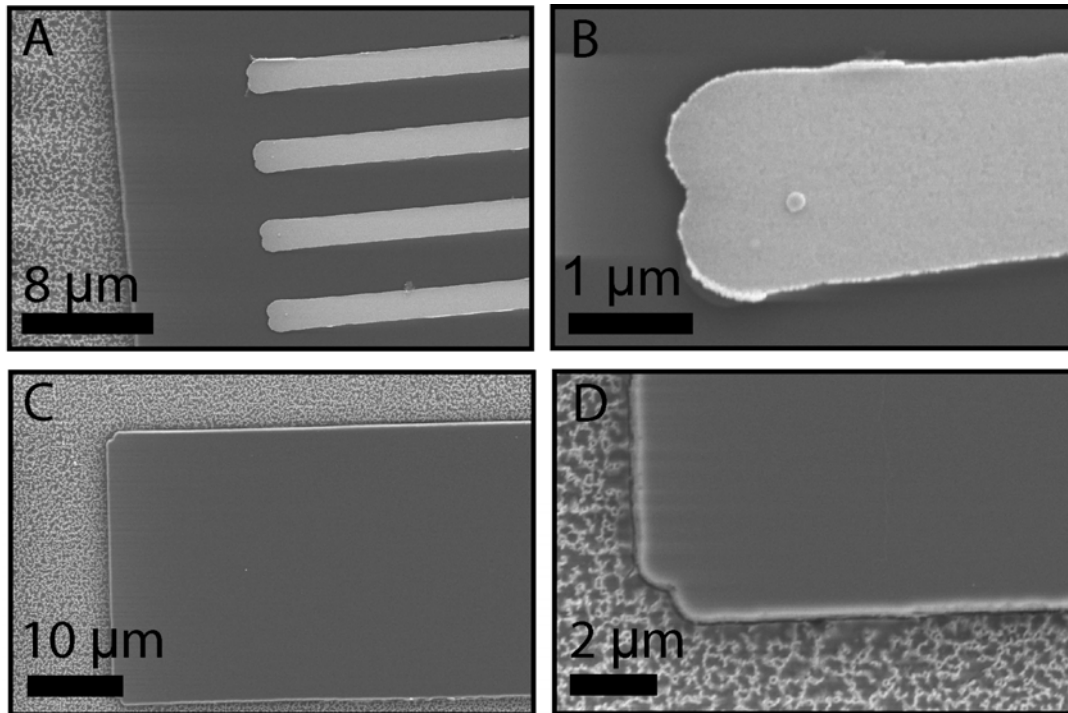


Figure 100 A) After KOH lift off, nickel dots were found on TiW leads. This structure has three out of four dots in place. B) A close up of the nickel dot on one of the TiW leads shown in A. C) On an AFM cantilever structure the nickel dot is seen in the centre. D) A close up of the cantilever corner shows that no nickel is present on the edges.

It was found that the nickel dots were left on most of the oxide cantilevers (for AFM tips), and no residual nickel could be found on the cantilever surfaces or along the edges. Apparently all nickel appears to be lifted off, leaving only the dots. However, the nickel dots seem to stick less to the TiW leads than the oxide, and more dots were missing on the TiW. Still several cantilevers with nickel dots still remaining on the TiW leads could be found as shown in Figure 100A and the close up in Figure 100B. The lift off step could possibly be optimised by either lowering the temperature of the KOH bath, or the concentration, in order to obtain better control of etching time. On the clean oxide cantilevers (without leads) most dots remained as seen in Figure 100C where a cantilever with one central catalyst dot (for AFM probe tip) is shown. The close up of the cantilever corner in Figure 100D shows that the oxide structure edges are completely clean of nickel.

CNT growth synthesis was done on samples from two different batches in the combined PECVD/CVD chamber constructed in this project. PECVD growth of CNTs was performed on some samples fabricated by Jakob Kjelstrup-Hansen according to the *Window mask* method presented here. However in this particular batch, some problems arose with the ebeam patterning step, eventually leading to a rather poor lift off. Figure 101 A shows a sequence of nickel dots, 5 nm thick, remaining on the leads. However there is also nickel film in other parts of the window area. A close up of another chip is shown in Figure 101B where only one dot is seen, as well as a large nickel film that did not get lifted off. After PECVD CNT growth it was seen that the CNTs only grew in the window area as seen in Figure 101C and D.

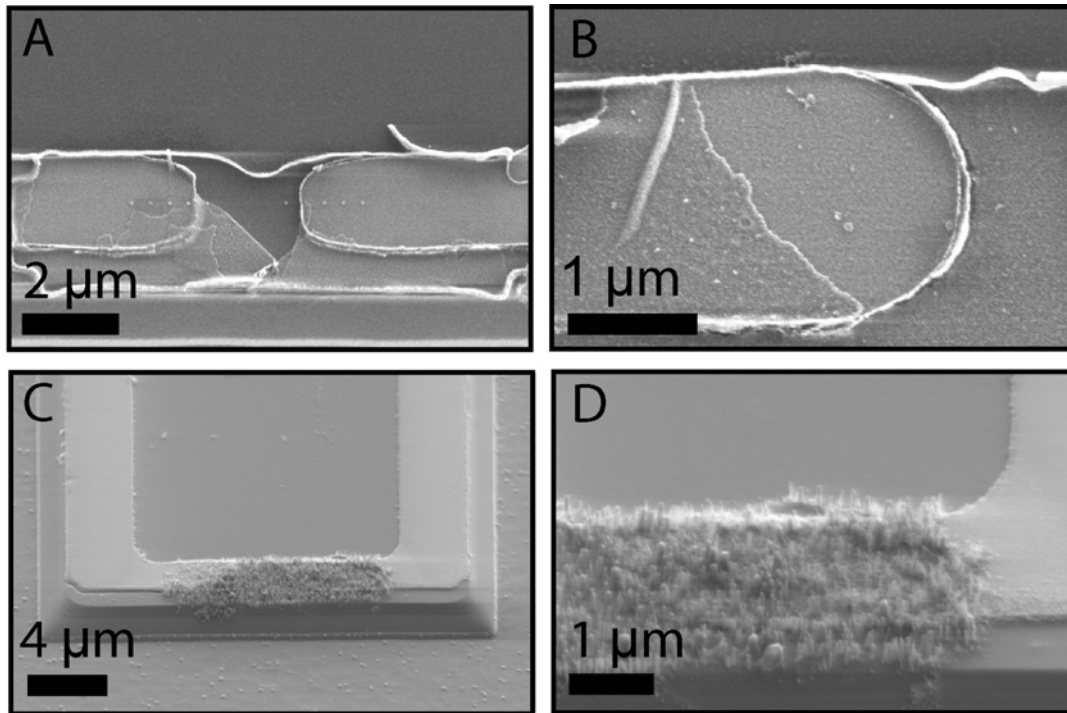


Figure 101 A) Nickel dots defined by the window mask method. Some remaining nickel film is seen in the window area. This was caused by the application of normal ebeam lift off before the KOH liftoff. B) A close up of a nickel dot. Also here the nickel film can be seen. C) PECVD growth gives growth from the entire nickel film as expected. D) A close up of the grown CNs.

CVD growth from acetylene was performed on some samples from another batch. Here it was discovered that the nickel catalyst dots had retained their catalytic activity, as seen in Figure 102. However, it was also discovered that the short dip in KOH was not enough to do a lift off in the areas outside of the oxide structures, which had no p-Si underneath. Therefore large quantities of CNTs were also synthesised in these areas. This can be avoided by making a standard ebeam lift off after the KOH lift off. Importantly, no CNT growth could be seen on the edges of the oxide structures.

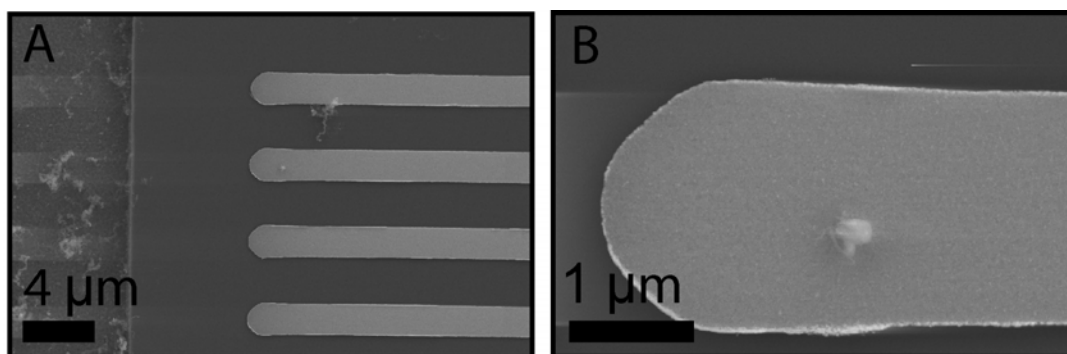


Figure 102 CVD growth with acetylene yield CN growth from the catalyst dot present on the TiW lead (inset). Also CNs are catalysed outside of the chip structure. Here there was no p-Si that lifted off the nickel during KOH lift off.

Suspended

The *window mask* method was tested on suspended structures, but before the inclusion of the in situ etch mask of aluminium. Thus nitride was deposited directly on top of the p-Si layer with the oxide layer underneath. However, due to the vertical walls of the cantilever, the nitride did not protect the p-Si good enough during KOH etching of the backside. As can be seen in Figure 103 A and B, the p-Si (pink colour) has been partly etched away on most cantilevers. The nitride attachment to the oxide walls of the cantilever is not good enough, allowing the KOH to come in between and start etching the p-Si layer.

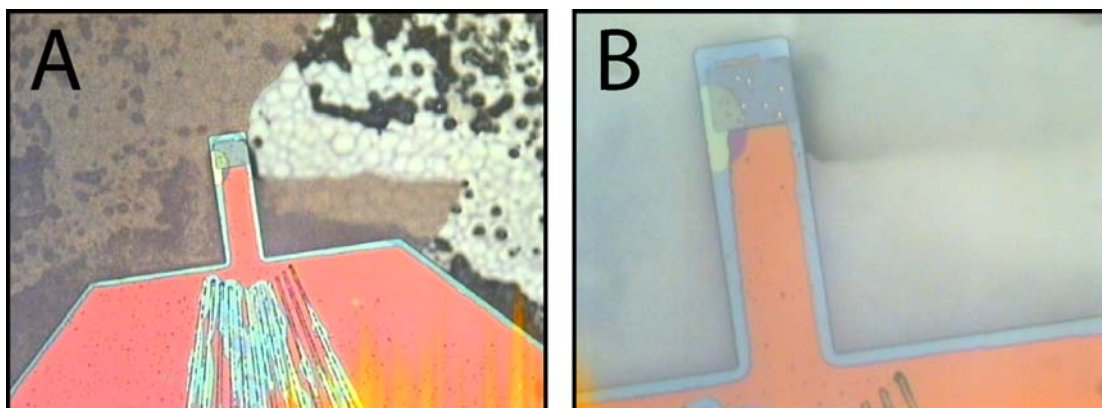


Figure 103 A) After KOH etch of the backside, it is evident that the p-Si (pink colour) has been partly etched. B) A close up of the cantilever.

It was precisely these results that lead to the development of the in situ etching mask of aluminium. That geometry, shown in Figure 98 A, survives the KOH etch of the backside, since the nitride has an oxide surface around the p-si to attach to, thus blocking the way to the p-Si.

Conclusion

It has been shown that the *Window mask* method is suitable for integrating catalyst particles on microstructured surfaces. With inclusion of the in situ etching mask for defining the final geometry of suspended structures it is highly probable that similar results will be found for suspended structures. Importantly, the method solved the problem with catalyst remains along edges of the microstructures. The yield of surviving dots is seen to be higher on plain oxide surfaces than TiW. Still many dots are seen to remain on the TiW leads. Other lead material may give higher yield, such as TiN, but this has not been tested. It was also seen that the nickel catalyst particles retained their catalytic activity after the processing.

Encapsulation

The method

The *Encapsulation* method builds on the very successful approach by Ye et al [35], where nickel particles on silicon cantilevers were encapsulated in a nitride cover, allowing subsequent microfabrication. Since nickel may contaminate the PECVD equipment used for nitride deposition, direct nitride deposition on nickel particles is not compatible with standard cleanroom processing. In this subchapter an alternative method will be investigated. The method encapsulates the nickel particles in poly silicon, before subsequent microprocessing can be done (see Figure 104). Initially, several tests were also done with aluminium as the encapsulation layer. These tests were initially promising, but it proved difficult to get nickel particles through. Further details on this are given in appendix C.

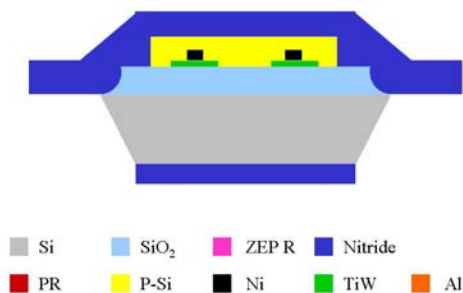


Figure 104 Illustration of the encapsulation method. The nickel particles are encapsulated, before nitride deposition.

The process sequence starts with the e-beam lithography step for defining the nickel pattern with subsequent metal deposition and lift-off. Next the encapsulating layer is deposited, and the front and back side processes for the cantilevers are done. There is a potential risk that the nickel dots may diffuse into the p-Si during hot process steps. Therefore low temperature steps should be used when possible. This is for instance implemented for the fabrication of the oxide structures which is done in BHF etch instead of RIE (see appendix B). Even the nitride removal in phosphoric etch, can be interchanged with a low power RIE etch, but this would require an additional aluminium layer on top of the p-Si. However, nickel should not diffuse into silicon for temperatures below 450 °C [125]. As can be seen in Figure 104 the p-si encapsulation leaves parts of the oxide cantilever exposed around the entire cantilever. Thus the nitride coverage can completely protect the p-Si, preventing etching by KOH during backside etch. The choice of encapsulating material is critical for several reasons. The requirements are that the nickel catalyst underneath shall survive both the deposition and later removal of the material, and the deposition of the material must be done without contaminating the cleanroom equipment. Also, the encapsulating layer must cover the particles sufficiently well to avoid contamination of any cleanroom equipment in subsequent processing. Poly silicon allows deposition, processing and removal in ways compatible with standard cleanroom processing. The deposition is

done by sputtering, and the removal is accomplished with a short etch on KOH. Refer to appendix B for the complete process recipe. It is even possible to include an extra aluminium deposition on top of the p-Si as an extra precaution to avoid contamination during processing.

Flat and nearly flat surfaces

Initial tests on large nickel patterns 5 nm thick indicated that the nickel did survive both the sputtering of the p-Si and the removal in KOH. However, to test the concept ebeam defined nickel dots 50 nm thick was placed on top of TiW leads (with the *Direct* method). 100 nm p-si was deposited on top of these patterns, and subsequently lifted off in 20 % KOH at 80 °C. The lift off occurred extremely fast, since the KOH had direct access to the p-si. Inspection with optical microscope showed that about 10 s was enough. With this very short time in KOH, the yield of remaining nickel dots was very high. A rough estimate showed that about 50% of the inspected 4 point probes had all four remaining nickel dots on the TiW leads. Moreover, the single nickel dot on the AFM design was found remaining on more than 90% of the inspected structures. Figure 105 A and B show two four point probes, both with all nickel particles intact on the TiW leads. A close up is shown in Figure 105 C. Furthermore the nickel dot shown in C is from on of the AFM designs without TiW leads.

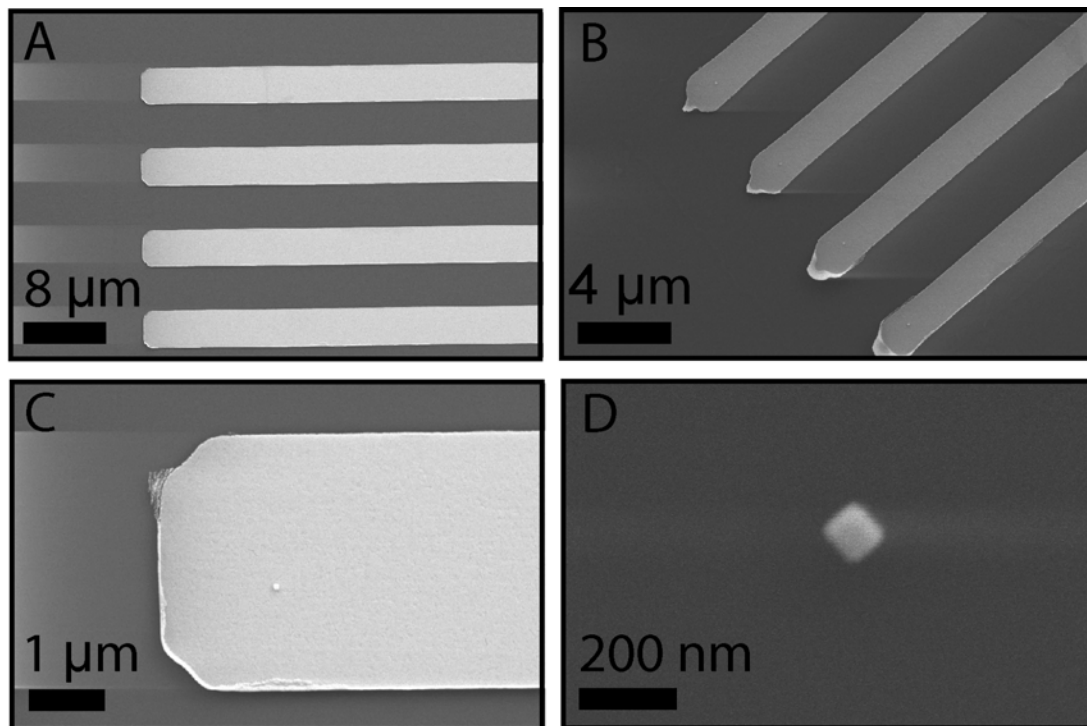


Figure 105 A) TiW leads shaped as a four point probe on top of oxide. The encapsulation method leaves nickel dots left on all leads. B) Another four point probe showing clearly defined nickel dots C) A close up picture of a nickel dot on a TiW lead. D) On the oxide cantilevers (AFM type) the nickel dots also remain. Note the that the square shape of the particle has survived the processing.

CVD synthesis with acetylene, using the combined PECVD/CVD chamber constructed in this project, was done on a sample where the p-Si had been removed

from on top of 50 nm nickel dots. The resulting CN growth from all catalyst particles showed that the catalytic activity of these dots had not been destroyed. Figure 106 shows a four point probe structure with CNs growing from each catalyst particle.

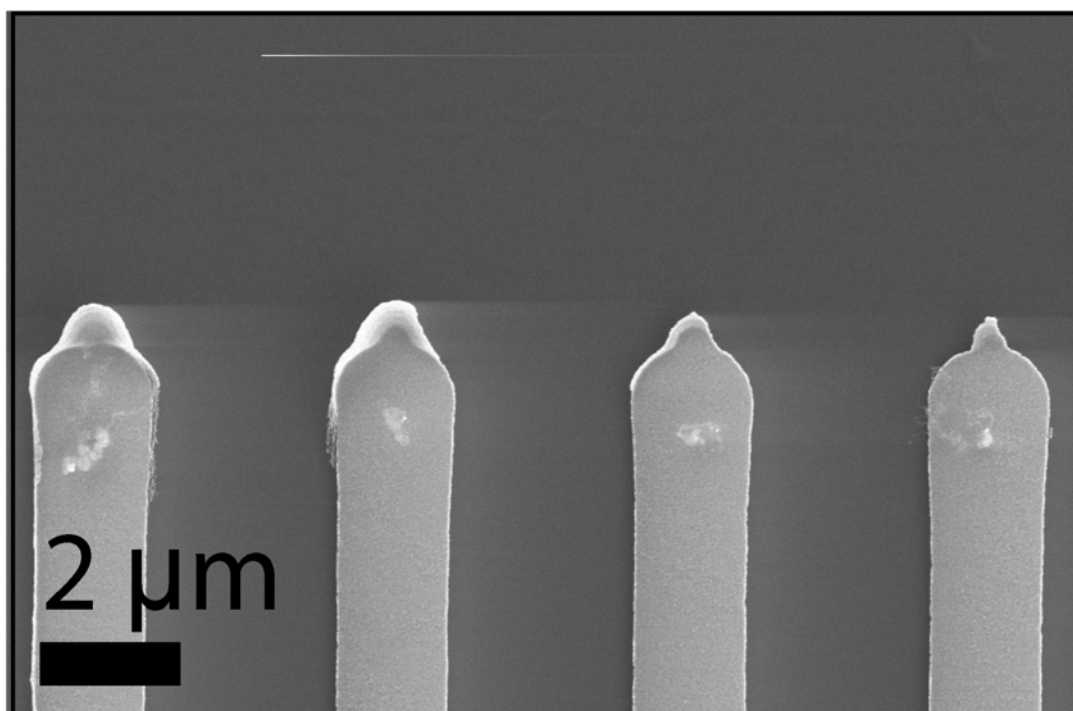


Figure 106 The catalyst particles retain their catalytic activity after removal of the p-Si encapsulation layer. The CNs are grown from acetylene using the combined PECVD/CVD chamber constructed in this project.

Conclusion

The *Encapsulation* method is very promising, unfortunately it was invented very late in this project. Therefore much optimisation remains. The yield as a function of nickel thickness is perhaps the most important study that should be done. There is a chance that the sputtering and final KOH lift off of the p-Si encapsulation layer removes a certain thickness of the nickel dots. But this can be optimised, to end up with dots of the wanted thickness. It is important that the catalytic activity of the dots remains, and that the yield appear to be high. Furthermore, the method has neither been tested on microstructured surfaces nor on suspended structures. However, the nature of the method implies that further processing should not damage the nickel particles. There is a potential risk that hot processing steps may make parts of the nickel diffuse into the p-Si. However, as suggested it is possible to avoid hot process steps, such as RIE fabrication of the cantilever structure and phosphoric etch of the nitride, in finishing suspended cantilevers.

Conclusion

The major achievement in this work has been the invention of three new methods for integrating catalyst dots in microsystems, and to show that these methods work. There

still remains further work on optimisation on all three methods, especially the *Encapsulation* method. However, the methods have been found and showed to work. Thus further optimisation and tests should be straightforward. At this stage however the methods can be compared with each other and the success criteria listed in the introduction. Table 10 summarises the results.

Table 10 Comparison of the four methods with respect to the success criteria

Criterion	Direct	In situ	Window	Encapsulation
Standard cleanroom compatible	Yes	Yes	Yes	Yes
Possible on flat surfaces	Yes	Yes	Probably	Yes
Possible on micro-structured surfaces	Poorly	Yes	Yes	Probably
Possible on suspended structures	Poorly	Yes*	Probably	Probably
Acceptable dot size precision	Yes	Yes	Yes	Yes
Acceptable yield on dots	Yes	Yes**	Yes**	Yes
Remaining catalytic activity	Yes	Yes	Yes	Yes
Range of dot diameter	As e-beam design	Slightly larger than design	As e-beam design	As e-beam design
Range of dot thickness	As deposited	Minimum thickness < 5 nm	Minimum thickness < 5 nm	Minimum thickness = ? (< 50 nm)

* Problem with catalyst remains along edges should be avoided with inclusion of the in situ etch mask

** Depends on requirement.

The four methods have each their advantages and drawbacks. Both the *Direct* method and the *Window* method have an exact definition of the dots, since the ebeam steps are done on the finished structures. The *In situ* method does not require ebeam steps on a fragile wafer structure, but the hole pattern may not be as precise as the one defined directly into the ebeam resist. The KOH lift off used for both the *In situ* and the *Window* methods provides an efficient and clean lift off not possible for the *Direct* method. This is clearly an advantage on both microstructured surfaces and suspended structures. Finally the *Encapsulation* method has a high precision on the dots, given that they are not damaged during the processing. The square structure of the catalyst dots in Figure 107 implies that this is not a major problem. However, it is still uncertain how successful this method will be for thin layers of 5 – 10 nm. If successful for thin layers it is by far the simplest method for integrating catalyst particles on suspended structures.

7 Conclusion

The main subjects of this thesis have been;

1. An investigation into the feasibility of integrating CNs into microsystems, such as microprobes with cantilevers
2. Investigations of surface properties of surfaces covered in nanotube forests
3. Construction of a CVD/PECVD setup up with the possibility of waferscale growth
4. The development of methods for fabricating microsystems with integrated catalyst dots for subsequent catalytically activated growth of CNs

Initially it was seen that the PECVD growth process was compatible with growing carbon nanotubes in situ on microprobes with suspended oxide cantilevers. Furthermore, for electrical contact to the nanotubes, choice of high melting point metals had to be made. Initially this was achieved with Wolfram, but was later changed to TiW for processing purposes. The carbon nanotubes were found to attach sufficiently well to the substrate. High control of position, diameter and size of the nanotubes is important for waferscale integration into devices. Electron beam lithography has been used to obtain control on both position and diameter of the catalyst particles. A thorough study was performed on the possibility of controlling the orientation of the nanotubes during growth. It was found that the electric field could be distorted through placing conductive graphite in special positions. The field distortion could be calculated by a finite element model, thus making it possible to predict the inclination of the tubes.

Special investigations into the surface properties of vertically aligned carbon nanotube forests showed that the surfaces behave like strong hydrophobic surfaces with inclination angles larger than 120° , initially. However, this strong hydrophobicity is more likely to be caused by strong pinning effects, rather than true hydrophobicity. The pinning simply prevents water droplets from advancing, or receding. Even if the apparent hydrophobic property of the nanotube forest could not be preserved without special coatings, it was shown that for micro and nanomanipulation purposes the surface truly behaved like a non stick surface. The surface was even less sticky than traditional non stick films such as DLC and Teflon, thus providing a work surface where manipulation of fragile organic nanostructures could be done. In this way electrical measurement could be obtained on carefully selected and positioned organic nanofibres.

The construction and performance of a combined CVD and PECVD chamber was presented. The setup allows CN growth at temperatures up to around 900°C , and pressures at least up to 50 mbar. Furthermore it allows growth from both acetylene and methane, with hydrogen as co-flow. It is important that the set up has been developed with the possibility of CN synthesis on 4 inch wafers – thus truly allowing waferscale integration of CNs. However, the present heating stage has smaller dimensions and will have to be enlarged. Growth of CNs have been accomplished both using only thermal CVD and PECVD. The best growth was found from thermal CVD using acetylene at 25 mbar and 700°C , with a gas composition of 13% acetylene and 87% hydrogen.

Three novel routes toward waferscale integration of catalyst particles for subsequent CN growth was investigated, and compared to the standard *Direct* method of EBL. The methods were developed for allowing integration of catalyst particles in complex microstructures, such as on suspended cantilevers. The new methods were; the *In situ mask*, the *Window mask*, and the *Encapsulation* method. The development and optimisation has come the furthest with the *In situ mask* method. Here high yields of 5 nm thick catalyst particles have been found, even on suspended cantilevers. Both the *In situ mask* and the *Window mask* use a p-si layer as a sacrificial lift off layer, facilitating easy and clean lift off after catalyst deposition in the end of the fabrication. Whereas the two methods have many similar aspects, their main difference is that the *Window mask* method requires EBL on fragile structures whereas the *In situ mask* finish the EBL patterning early in the process, preserving the pattern in an in situ mask of p-Si. But whereas the *Window mask* gives a precise catalyst pattern as defined by the EBL step, the *In situ mask* has some loss of precision in transferring the pattern into the p-Si layer by RIE. Finally, the *Encapsulation* method uses poly silicon to encapsulate catalyst particles made with the *Direct* method early in the processing. This method is the last developed, and needs to be tested further. However, if the results become as good as the initial results presented here indicate, this method promises to be the best method for true waferscale integration of catalyst dots in microsystems for subsequent CN growth.

The main goal of this work was to develop methods for integration of catalyst particles into microsystems, in a way compatible with standard cleanroom processing, for subsequent in situ growth of nanostructures, such as carbon nanotubes and nanofibres (CNs). It has been shown that

- PECVD synthesis of CNs is feasible on various microstructures. Both the mechanical and electrical properties are satisfactory.
- It is possible to grow inclined CNs with a high degree of control in microsystems. Furthermore, it was seen that the inclination angle could be calculated through a finite element model.
- Several methods have been developed for integrating catalyst particles into microsystems, compatible with standard cleanroom processing. Optimisation work still remains.
- A new method for nanomanipulation of fragile nanostructures was found and investigated. It was seen that surfaces covered with nanotube forests were ideal for manipulation of fragile nanostructures due to the low stiction
- A set up was developed for growing CNs. The set up is built to allow growth on 4 inch wafers, although the present heating stage is smaller.

The methods developed in this project should make integration of nanostructures into microsystems easier. They provide new routes compatible with standard cleanroom processing, and suggest that waferscale fabrication of complex 3D structures, such as four point probes, with integrated CNs may soon become a reality.

Appendix A

List of Publications

- K. Gjerde, T. Schurmann, K. B. K. Teo, W. I. Milne and P. Bøggild. Fabrication of microliquid channels with in-situ grown inclined carbon nanotubes. *Proceedings of μ TAS 2004*, Vol 1, p 327-329, (2004).
- K. Gjerde, T. Schurmann, K. B. K. Teo, M. Aono, W. I. Milne and P. Bøggild. Functionalisation of microfluidic channels with in situ grown carbon nanotubes. *Mater. Res. Soc. Symp. Proc.*, Vol 872, 371-375, (2005).
- K. Gjerde, M. F. Mora, J. Kjelstrup-Hansen, T. Schurmann, L. Gammelgaard, M. Aono, K. B. K. Teo, W. I. Milne and P. Bøggild. Integrating nanotubes into microsystems with electron beam lithography and in situ catalytically activated growth. *Phys. Stat. Sol. (a)*, Vol 203, no 6, p 1094-1099, (2006).
- K. Gjerde, T. Schurmann, I. Bu, K. B. K. Teo, W. I. Milne and P. Bøggild. Integration of carbon nanotubes with controllable inclination angle into microsystems. *Carbon*, (In press)
- K. Gjerde, J. Kjelstrup-Hansen, C. H. Clausen, K. B. K. Teo, W. I. Milne, H-G. Rubahn and P. Bøggild. Carbon nanotube forests: a non-stick workbench for nanomanipulation. *Submitted to Nanotechnology*
- K. Gjerde, L. Gammelgaard, J. Kjelstrup-Hansen, K. B. K. Teo, W. I. Milne and P. Bøggild. New Methods for wafer scale integration of catalyst particles into 3D microsystems for subsequent carbon nanotube growth. *In preparation*

List of workshop contributions

- K. Gjerde. P. Bøggild. Integrated growth of carbon nanotube using C-CVD. *Oral presentation and poster at Les Houches summer school on nanoscience*, (2003)
- K. Gjerde. Integrated growth of carbon nanotubes. *Oral presentation at the EDM group, Cambridge University*, (2003)
- K. Gjerde, T. Schurmann, K.B.K. Teo, W. Milne and P. Bøggild, Functionalisation of Microsystems With In-situ Grown Carbon Nanotubes. *Oral presentation and poster at Danish Physical Society*, (2004)
- K. Gjerde, T. Schurmann, K. B. K. Teo, W. I. Milne, P. Bøggild. Functionalisation of Microsystems with In Situ Grown Carbon Nanotubes. *Poster at Nano-Day DTU Nanosymposium* (2004)





- K. Gjerde, T. Schurmann, C. Persson, K. B. K. Teo, W. I. Milne, P. Bøggild. Multiple Contact Angles on Carbon Nanotube Forests. *Poster at Danish Physical Society*, (2005)
- K. Gjerde, K. B, K. Teo, W. I. Milne, P. Bøggild, K. Mølhave. Applied nanotechnology in space: Proposal for DTU cube-sat Payload with Carbon Nanotube and Nanowire Based Devices. *Oral presentation at DTU-Sat*, (2005)



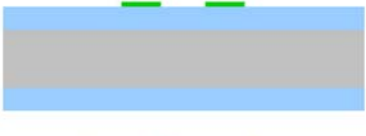


Appendix B



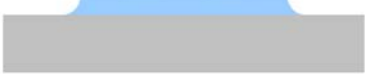
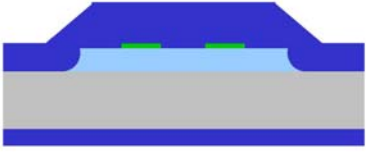
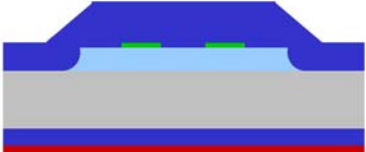
Process sequences

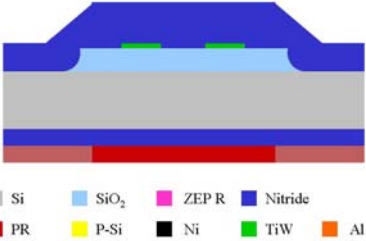
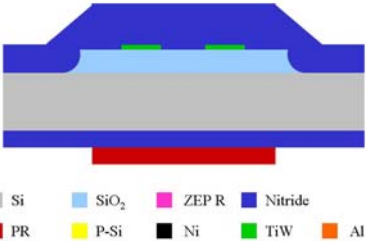
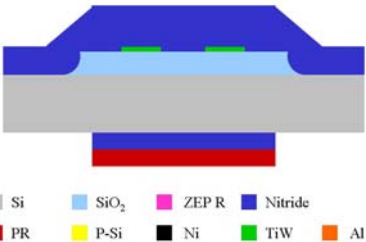
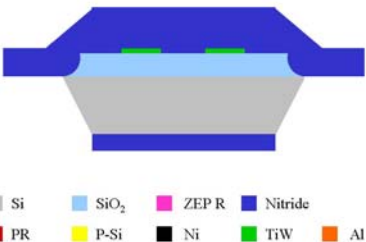
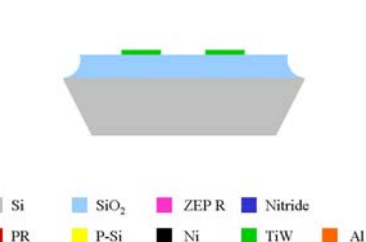
Direct method

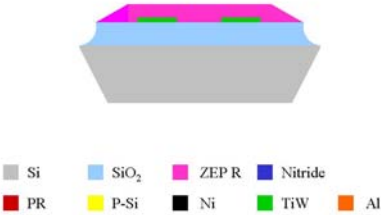
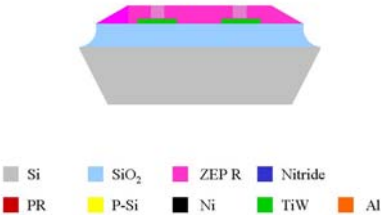
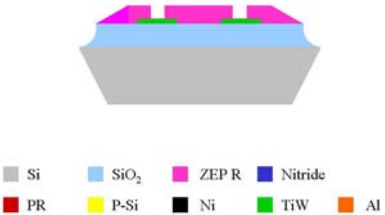
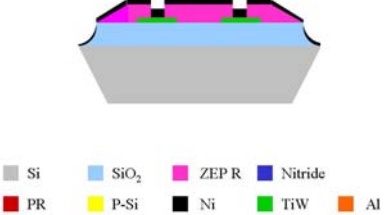
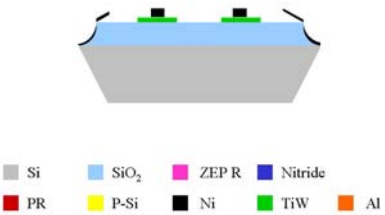
Table 11 Process sequence for Direct method with oxide structures and leads

#	Process	Description	Cross section
1	Starting wafer	Si (100), 4", double polished	 Si SiO ₂ ZEP R Nitride PR P-Si Ni TiW Al
2	Grow 1µm SiO ₂	Phosphor drive-in furnace, wet oxidation, time = 2h30min, T = 1100°C	 Si SiO ₂ ZEP R Nitride PR P-Si Ni TiW Al
3	Spin on photo resist	(Pretreatment with 30 min in HMDS) SSI spinner, thickness = 1.5 µm, prebake at 90°C for 60 s, resist: AZ 5214E	 Si SiO ₂ ZEP R Nitride PR P-Si Ni TiW Al
4	1 st photolithography step (Wires): align + expose	KS aligner, negative. exposure time = 3.5 s, at intensity 9, Hard contact, flood exposure 30 s	 Si SiO ₂ ZEP R Nitride PR P-Si Ni TiW Al

5	Develop	Time = 65s, AZ 351B	 <p>Legend:</p> <ul style="list-style-type: none"> <li style="margin-right: 10px;">■ Si <li style="margin-right: 10px;">■ SiO₂ <li style="margin-right: 10px;">■ ZEP R <li style="margin-right: 10px;">■ Nitride <li style="margin-right: 10px;">■ PR <li style="margin-right: 10px;">■ P-Si <li style="margin-right: 10px;">■ Ni <li style="margin-right: 10px;">■ TiW <li style="margin-right: 10px;">■ Al
6	Sputtering of TiW wires	Wordentech: TiW sputtering; 150W, $7 \cdot 10^{-3}$ mbar, 8 min gives 50 nm, [124]	 <p>Legend:</p> <ul style="list-style-type: none"> <li style="margin-right: 10px;">■ Si <li style="margin-right: 10px;">■ SiO₂ <li style="margin-right: 10px;">■ ZEP R <li style="margin-right: 10px;">■ Nitride <li style="margin-right: 10px;">■ PR <li style="margin-right: 10px;">■ P-Si <li style="margin-right: 10px;">■ Ni <li style="margin-right: 10px;">■ TiW <li style="margin-right: 10px;">■ Al
7	Lift off	Lift off bath (acetone) with ultrasound	 <p>Legend:</p> <ul style="list-style-type: none"> <li style="margin-right: 10px;">■ Si <li style="margin-right: 10px;">■ SiO₂ <li style="margin-right: 10px;">■ ZEP R <li style="margin-right: 10px;">■ Nitride <li style="margin-right: 10px;">■ PR <li style="margin-right: 10px;">■ P-Si <li style="margin-right: 10px;">■ Ni <li style="margin-right: 10px;">■ TiW <li style="margin-right: 10px;">■ Al
8	Spin on photo resist	(Pretreatment with 30 min in HMDS) SSI spinner, thickness = 1.5 um, prebake at 90°C for 60 s, resist: AZ 5214E	 <p>Legend:</p> <ul style="list-style-type: none"> <li style="margin-right: 10px;">■ Si <li style="margin-right: 10px;">■ SiO₂ <li style="margin-right: 10px;">■ ZEP R <li style="margin-right: 10px;">■ Nitride <li style="margin-right: 10px;">■ PR <li style="margin-right: 10px;">■ P-Si <li style="margin-right: 10px;">■ Ni <li style="margin-right: 10px;">■ TiW <li style="margin-right: 10px;">■ Al
9	2 nd photolithography step: align + expose	KS aligner, negative. exposure time = 3.5 s, at intensity 9, Hard contact, flood exposure 30 s	 <p>Legend:</p> <ul style="list-style-type: none"> <li style="margin-right: 10px;">■ Si <li style="margin-right: 10px;">■ SiO₂ <li style="margin-right: 10px;">■ ZEP R <li style="margin-right: 10px;">■ Nitride <li style="margin-right: 10px;">■ PR <li style="margin-right: 10px;">■ P-Si <li style="margin-right: 10px;">■ Ni <li style="margin-right: 10px;">■ TiW <li style="margin-right: 10px;">■ Al





10	Develop	Time = 65s, AZ 351B	 <p>Legend: Si (grey), SiO₂ (light blue), ZEP R (pink), Nitride (dark blue), PR (red), P-Si (yellow), Ni (black), TiW (green), Al (orange)</p>
11	Etch Oxide	BHF, 13min	 <p>Legend: Si (grey), SiO₂ (light blue), ZEP R (pink), Nitride (dark blue), PR (red), P-Si (yellow), Ni (black), TiW (green), Al (orange)</p>
12	Strip Resist	Strip I lift off bath, since metal is present on wafers	 <p>Legend: Si (grey), SiO₂ (light blue), ZEP R (pink), Nitride (dark blue), PR (red), P-Si (yellow), Ni (black), TiW (green), Al (orange)</p>
13	Deposit 450 nm low-stress, silicon-rich silicon nitride to protect front side by PECVD, and 300 nm on backside	PECVD 3 Recipe JKHKGNITRI 26 min backside (300 nm) 39 min frontside (450 nm)	 <p>Legend: Si (grey), SiO₂ (light blue), ZEP R (pink), Nitride (dark blue), PR (red), P-Si (yellow), Ni (black), TiW (green), Al (orange)</p>
14	Spin photo resist on back side	SSI spinner, thickness = 1.5 um, prebake at 90°C for 60 s, resist: AZ 5214E	 <p>Legend: Si (grey), SiO₂ (light blue), ZEP R (pink), Nitride (dark blue), PR (red), P-Si (yellow), Ni (black), TiW (green), Al (orange)</p>

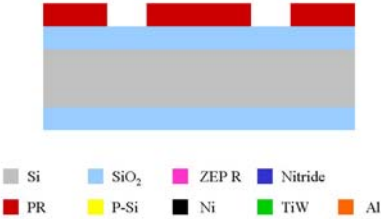
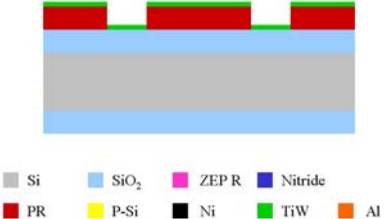
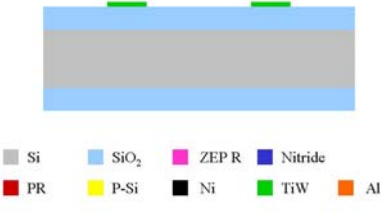
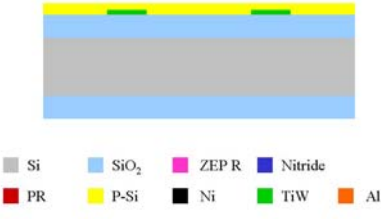
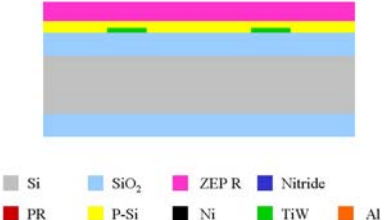
15	4 th photolithography step (back side): align + expose	KS aligner, positive, exposure time = 6 s at intensity 9	 <p>Legend: Si (grey), SiO₂ (light blue), ZEP R (pink), Nitride (dark blue) PR (red), P-Si (yellow), Ni (black), TiW (green), Al (orange)</p>
16	Develop	Time = 65 s, AZ 351B	 <p>Legend: Si (grey), SiO₂ (light blue), ZEP R (pink), Nitride (dark blue) PR (red), P-Si (yellow), Ni (black), TiW (green), Al (orange)</p>
17	Etch silicon nitride on back side by RIE	STS RIE2, (power = 30 W, time = 12 min, composition = 40 sccm SF ₆ + 8 sccm O ₂ , pressure = 80 mtorr[126])	 <p>Legend: Si (grey), SiO₂ (light blue), ZEP R (pink), Nitride (dark blue) PR (red), P-Si (yellow), Ni (black), TiW (green), Al (orange)</p>
18	KOH etch of Si	80°C, about 4h50 min, Mechanical Frontside Protection.	 <p>Legend: Si (grey), SiO₂ (light blue), ZEP R (pink), Nitride (dark blue) PR (red), P-Si (yellow), Ni (black), TiW (green), Al (orange)</p>
19	Remove Silicon nitride	Silicon nitride wet etch. 30 min at 160 °C	 <p>Legend: Si (grey), SiO₂ (light blue), ZEP R (pink), Nitride (dark blue) PR (red), P-Si (yellow), Ni (black), TiW (green), Al (orange)</p>

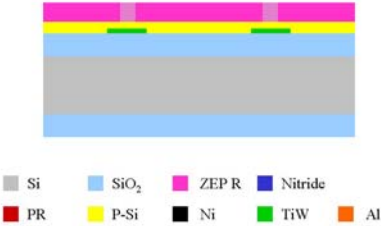
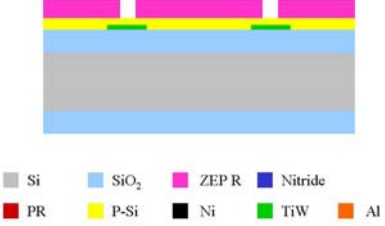
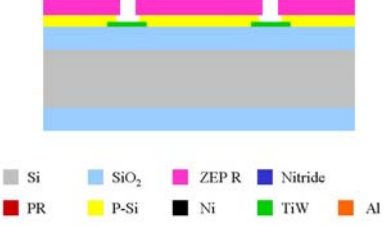
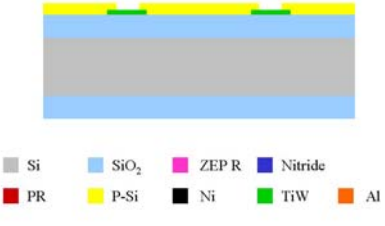
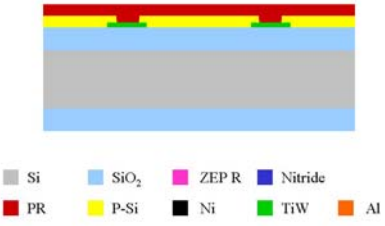
20	Spin on EBL resist	<p>KS-spinner, without vacuum, thickness = 100 nm, resist: ZEP-520A7, undiluted, prebake at 160°C for 2 min</p> <p>Use spin recipe for 300 nm resist (500 rpm 5 s, 3000 rpm 30 s) (Diluted, 1:2 in anisole gives 100 nm)</p>	
21	Define hole for Ni dot by EBL	<p>JEOL E-beam writer, acceleration voltage = 100 kV, current = 0.8 nA.</p> <p>Exposure dose 600 $\mu\text{C}/\text{cm}^2$</p>	
22	Develop	<p>Developer: N50 1min30s Then rinse in IPA</p>	
23	Deposit Ni	<p>Wordentec evaporator, thickness 5-10 nm</p>	
24	Lift off	<p>Microposit remover 1165, 12h, + ultrasound pulses towards the end</p>	

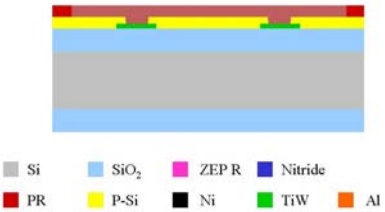
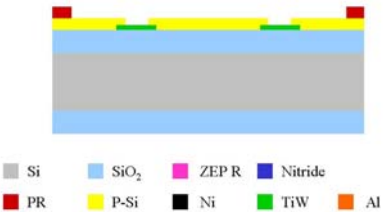
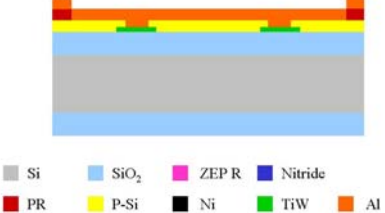
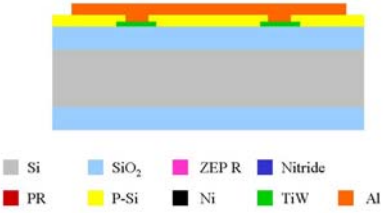
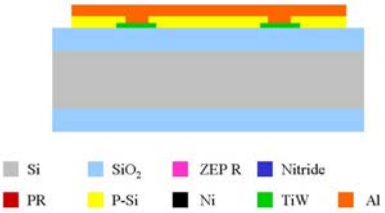
In situ mask with oxide structures and leads

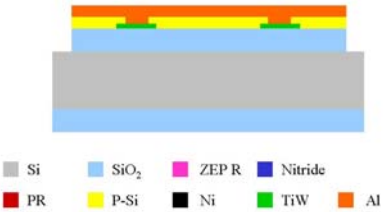
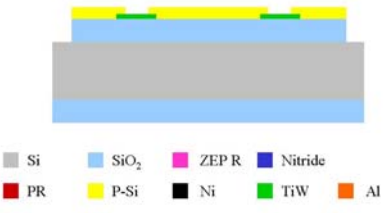
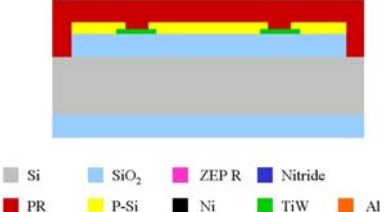
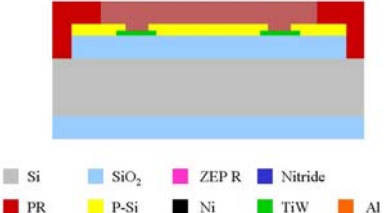
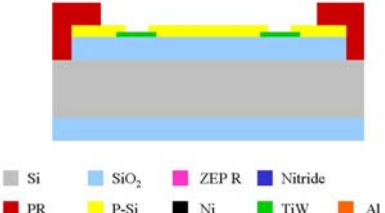
Table 12 Process sequence for In situ mask with oxide structures and leads

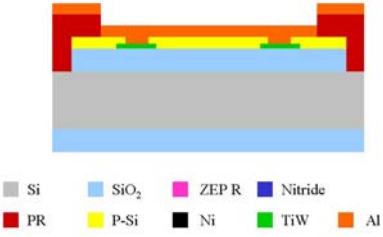
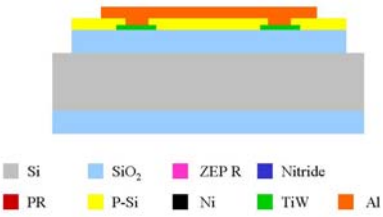
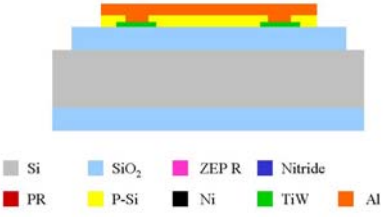
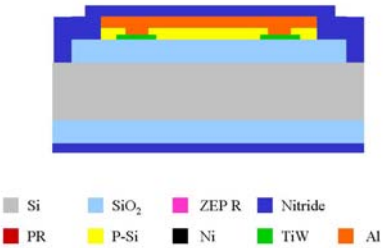
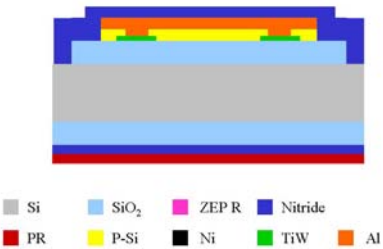
#	Process	Description	Cross section
1	Starting wafer	Si (100), 4", double polished	 ■ Si ■ SiO ₂ ■ ZEP R ■ Nitride ■ PR ■ P-Si ■ Ni ■ TiW ■ Al
2	Grow 1µm SiO ₂	Phosphor drive-in furnace, wet oxidation, time = 2h30min, T = 1100°C	 ■ Si ■ SiO ₂ ■ ZEP R ■ Nitride ■ PR ■ P-Si ■ Ni ■ TiW ■ Al
3	Spin on photo resist	(Pretreatment with 30 min in HMDS) SSI spinner, thickness = 1.5 µm, prebake at 90°C for 60 s, resist: AZ 5214E	 ■ Si ■ SiO ₂ ■ ZEP R ■ Nitride ■ PR ■ P-Si ■ Ni ■ TiW ■ Al
4	1 st photolithography step (Wires): align + expose	KS aligner, negative. exposure time = 3.5 s, at intensity 9, Hard contact, flood exposure 30 s	 ■ Si ■ SiO ₂ ■ ZEP R ■ Nitride ■ PR ■ P-Si ■ Ni ■ TiW ■ Al

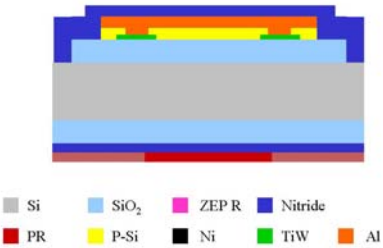
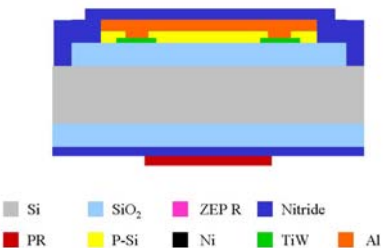
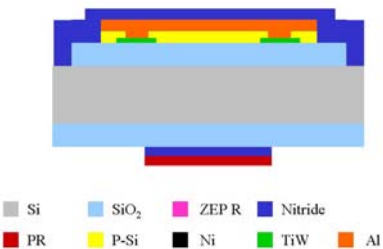
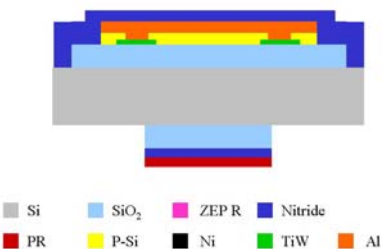
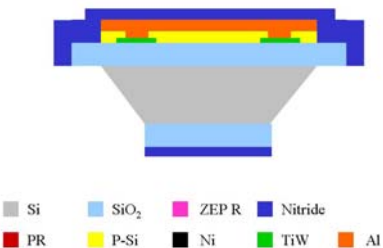
5	Develop	Time = 65s, AZ 351B	
6	Sputtering of TiW wires	Wordentech: TiW sputtering; 150W, $7 \cdot 10^{-3}$ mbar, 8 min gives 50 nm, [124]	
7	Lift off	Lift off bath (acetone) with ultrasound	
8	Sputtering of 100 nm p-Si	Alcatel 5.5 min p-si sputtering. 440 W Note; The p-Si could possibly be patterned with PL – to avoid a later etch step in RIE, and allow first cantilever etch with BHF and PR as mask	
9	Spin on EBL resist	III-IV-spinner, thickness = 100 nm, resist: ZEP-520A7, undiluted, prebake at 160°C for 2 min Use spin recipe for 300 nm resist (500 rpm 5 s, 3000 rpm 30 s) (Diluted, 1:2 in anisole gives 100 nm)	






10	Define hole for Ni dot by EBL	<p>JEOL E-beam writer, acceleration voltage = 100 kV, current = 0.8 nA.</p> <p>Exposure dose 600 $\mu\text{C}/\text{cm}^2$</p>	
11	Develop	<p>Developer: N50 1min30s Then rinse in IPA</p>	
12	Etch p-Si in RIE	<p>STS RIE2, Time : 60s, 32 sccm SF₆, 8 sccm O₂, 30 W, 80 mTorr.</p> <p>Possible to optimize shorter etch time.</p> <p>Note; this step could possibly be done in wet poly etch</p>	
13	Strip EBL Resist	<p>Nanoremoval 2 min Rinse in IPA</p>	
14	Spin on photo resist	<p>(Pretreatment with 30 min in HMDS) SSI spinner, thickness = 1.5 μm, prebake at 90°C for 60 s, resist: AZ 5214E</p>	

15	2 nd photolithography step: align + expose	KS aligner, negative. exposure time = 3.5 s, at intensity 9, Hard contact, flood exposure 30 s	
16	Develop	Time = 65s, AZ 351B	
17	Deposit Al	Alcatel 200 nm	
18	Lift off	Lift off bath (acetone), with ultrasound	
19	Etch p-Si by RIE	STS RIE2, Time : 90s, 32 sccm SF ₆ , 8 sccm O ₂ , 30 W, 80 mTorr.	

20	Etch silicon dioxide by RIE	STS RIE2, power = 150 W, time = 26 min, composition = 40 sccm CHF ₃ , + 8 sccm CF ₄ pressure = 150 mTorr [126]	
21	Remove Al	Aluminium etchant Transene D. 23 minutes at room temperature. Rinse in water	
22	Spin on photo resist	(Pretreatment with 30 min in HMDS) SSI spinner, thickness = 1.5 um, prebake at 90°C for 60 s, resist: AZ 5214E	
23	3 rd Photolithography step (Cantilever): align + expose	KS aligner, negative. exposure time = 3.5 s, at intensity 9, Hard contact, flood exposure 30 s	
24	Develop	Time = 65s, AZ 351B	





25	Deposit Al	Alcatel 200 nm	
26	Lift off	Lift off bath (acetone), with ultrasound	
27	Etch p-Si by RIE	STS RIE2, Time : 90s, 32 sccm SF ₆ , 8 sccm O ₂ , 30 W, 80 mTorr.	
28	Deposit 450 nm low-stress, silicon-rich silicon nitride to protect front side by PECVD, and 300 nm on backside	PECVD 3 Recipe JKHKGNITRI 26 min backside (300 nm) 39 min frontside (450 nm)	
29	Spin photo resist on back side	SSI spinner, thickness = 1.5 um, prebake at 90°C for 60 s, resist: AZ 5214E	



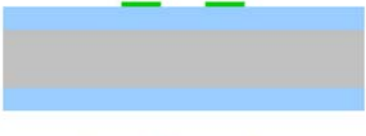


30	4 th photolithography step (back side): align + expose	KS aligner, positive, exposure time = 6 s at intensity 9	
31	Develop	Time = 65 s, AZ 351B	
32	Etch silicon nitride on back side by RIE	STS RIE2, (power = 30 W, time = 12 min, composition = 40 sccm SF ₆ + 8 sccm O ₂ , pressure = 80 mtorr[126])	
33	Etch silicon dioxide on back side by RIE	STS RIE2, power = 150 W, time = 26 min, composition = 40 sccm CHF ₃ , + 8 sccm CF ₄ pressure = 150 mTorr [126]	
34	KOH etch of Si	80°C, about 4h50 min, Mechanical Frontside Protection.	






35	Remove Nitride in RIE	STS RIE2, (power = 30 W, time = 8 min, composition = 40 sccm SF ₆ + 8 sccm O ₂ , pressure = 80 mtorr[126])	 <p>Legend: Si (grey), SiO₂ (light blue), ZEP R (pink), Nitride (dark blue), PR (red), P-Si (yellow), Ni (black), TiW (green), Al (orange)</p>
36	Etch Silicondioxide in RIE	STS RIE2, power = 150 W, time = 26 min, composition = 40 sccm CHF ₃ ,+ 8 sccm CF ₄ pressure = 150 mTorr [126] Note; To improve p-si overhang a short dip in BHF can further etch SiO ₂ . This may require thicker initial oxide	 <p>Legend: Si (grey), SiO₂ (light blue), ZEP R (pink), Nitride (dark blue), PR (red), P-Si (yellow), Ni (black), TiW (green), Al (orange)</p>
37	Remove Al	Aluminium etchant Transene D. 23 minutes at room temperature. Rinse in water	 <p>Legend: Si (grey), SiO₂ (light blue), ZEP R (pink), Nitride (dark blue), PR (red), P-Si (yellow), Ni (black), TiW (green), Al (orange)</p>
38	Deposit Ni	Wordentec evaporator, thickness 5-10 nm	 <p>Legend: Si (grey), SiO₂ (light blue), ZEP R (pink), Nitride (dark blue), PR (red), P-Si (yellow), Ni (black), TiW (green), Al (orange)</p>
39	Lift-off p-Si in KOH	Different pieces. KOH at 80 °C. Time Maximum 1 min	 <p>Legend: Si (grey), SiO₂ (light blue), ZEP R (pink), Nitride (dark blue), PR (red), P-Si (yellow), Ni (black), TiW (green), Al (orange)</p>

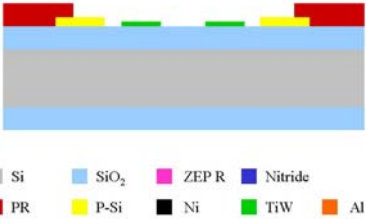
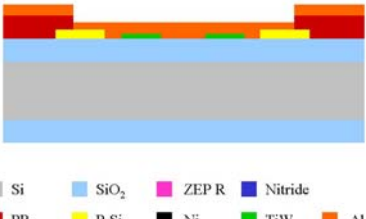
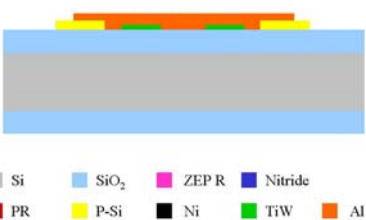
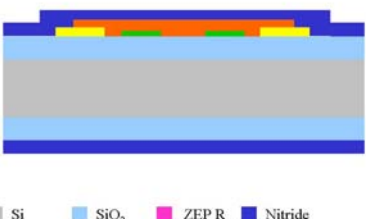
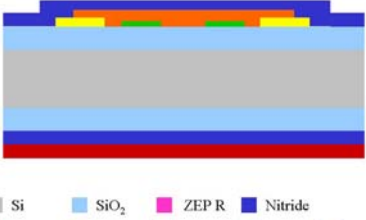
Window with oxide structures and leads

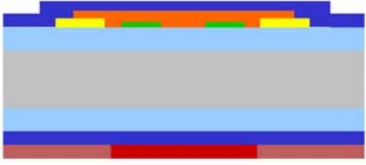




Table 13 Process sequence for Window with oxide structures and leads


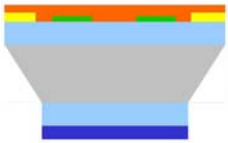
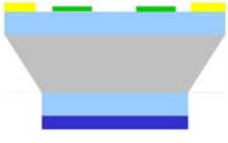


#	Process	Description	Cross section
1	Starting wafer	Si (100), 4", double polished	 ■ Si ■ SiO ₂ ■ ZEP R ■ Nitride ■ PR ■ P-Si ■ Ni ■ TiW ■ Al
2	Grow 1μm SiO ₂	Phosphor drive-in furnace, wet oxidation, time = 2h30min, T = 1100°C	 ■ Si ■ SiO ₂ ■ ZEP R ■ Nitride ■ PR ■ P-Si ■ Ni ■ TiW ■ Al
3	Spin on photo resist	(Pretreatment with 30 min in HMDS) SSI spinner, thickness = 1.5 μm, prebake at 90°C for 60 s, resist: AZ 5214E	 ■ Si ■ SiO ₂ ■ ZEP R ■ Nitride ■ PR ■ P-Si ■ Ni ■ TiW ■ Al
4	1 st photolithography step (Wires): align + expose	KS aligner, negative. exposure time = 3.5 s, at intensity 9, Hard contact, flood exposure 30 s	 ■ Si ■ SiO ₂ ■ ZEP R ■ Nitride ■ PR ■ P-Si ■ Ni ■ TiW ■ Al




5	Develop	Time = 65s, AZ 351B	 <p>Legend: Si (grey), SiO₂ (light blue), ZEP R (pink), Nitride (dark blue), PR (red), P-Si (yellow), Ni (black), TiW (green), Al (orange)</p>
6	Sputtering of TiW wires	Wordentech: TiW sputtering; 150W, $7 \cdot 10^{-3}$ mbar, 8 min gives 50 nm, [124]	 <p>Legend: Si (grey), SiO₂ (light blue), ZEP R (pink), Nitride (dark blue), PR (red), P-Si (yellow), Ni (black), TiW (green), Al (orange)</p>
7	Lift off	Lift off bath (acetone) with ultrasound	 <p>Legend: Si (grey), SiO₂ (light blue), ZEP R (pink), Nitride (dark blue), PR (red), P-Si (yellow), Ni (black), TiW (green), Al (orange)</p>
8	Spin on photo resist	(Pretreatment with 30 min in HMDS) SSI spinner, thickness = 1.5 μ m, prebake at 90°C for 60 s, resist: AZ 5214E	 <p>Legend: Si (grey), SiO₂ (light blue), ZEP R (pink), Nitride (dark blue), PR (red), P-Si (yellow), Ni (black), TiW (green), Al (orange)</p>
9	2 nd photolithography step: align + expose	KS aligner, negative. exposure time = 3.5 s, at intensity 9, Hard contact, flood exposure 30 s	 <p>Legend: Si (grey), SiO₂ (light blue), ZEP R (pink), Nitride (dark blue), PR (red), P-Si (yellow), Ni (black), TiW (green), Al (orange)</p>

10	Develop	Time = 65s, AZ 351B	 <p>Legend: Si (grey), SiO₂ (light blue), ZEP R (pink), Nitride (dark blue), PR (red), P-Si (yellow), Ni (black), TiW (green), Al (orange)</p>
11	Sputtering of 100 nm p-Si	Alcatel 5.5 min p-si sputtering. 440 W	 <p>Legend: Si (grey), SiO₂ (light blue), ZEP R (pink), Nitride (dark blue), PR (red), P-Si (yellow), Ni (black), TiW (green), Al (orange)</p>
12	Lift off	Lift off bath (acetone) with ultrasound	 <p>Legend: Si (grey), SiO₂ (light blue), ZEP R (pink), Nitride (dark blue), PR (red), P-Si (yellow), Ni (black), TiW (green), Al (orange)</p>
13	Spin on photo resist	(Pretreatment with 30 min in HMDS) SSI spinner, thickness = 1.5 um, prebake at 90°C for 60 s, resist: AZ 5214E	 <p>Legend: Si (grey), SiO₂ (light blue), ZEP R (pink), Nitride (dark blue), PR (red), P-Si (yellow), Ni (black), TiW (green), Al (orange)</p>
14	3 rd Photolithography step (Cantilever): align + expose	KS aligner, negative. exposure time = 3.5 s, at intensity 9, Hard contact, flood exposure 30 s	 <p>Legend: Si (grey), SiO₂ (light blue), ZEP R (pink), Nitride (dark blue), PR (red), P-Si (yellow), Ni (black), TiW (green), Al (orange)</p>

15	Develop	Time = 65s, AZ 351B	 <p>Legend: Si (grey), SiO₂ (light blue), ZEP R (pink), Nitride (dark blue) PR (red), P-Si (yellow), Ni (black), TiW (green), Al (orange)</p>
16	Deposit Al	Alcatel 200 nm	 <p>Legend: Si (grey), SiO₂ (light blue), ZEP R (pink), Nitride (dark blue) PR (red), P-Si (yellow), Ni (black), TiW (green), Al (orange)</p>
17	Lift off	Lift off bath (acetone), with ultrasound	 <p>Legend: Si (grey), SiO₂ (light blue), ZEP R (pink), Nitride (dark blue) PR (red), P-Si (yellow), Ni (black), TiW (green), Al (orange)</p>
18	Deposit 450 nm low-stress, silicon nitride to protect front side by PECVD, and 300 nm on backside	PECVD 3 Recipe JKHKGNITRI 26 min backside (300 nm) 39 min frontside (450 nm)	 <p>Legend: Si (grey), SiO₂ (light blue), ZEP R (pink), Nitride (dark blue) PR (red), P-Si (yellow), Ni (black), TiW (green), Al (orange)</p>
19	Spin photo resist on back side	SSI spinner, thickness = 1.5 um, prebake at 90°C for 60 s, resist: AZ 5214E	 <p>Legend: Si (grey), SiO₂ (light blue), ZEP R (pink), Nitride (dark blue) PR (red), P-Si (yellow), Ni (black), TiW (green), Al (orange)</p>


20	4 th photolithography step (back side): align + expose	KS aligner, positive, exposure time = 6 s at intensity 9	 <p>Legend: Si (grey), SiO₂ (light blue), ZEP R (pink), Nitride (dark blue), PR (red), P-Si (yellow), Ni (black), TiW (green), Al (orange)</p>
21	Develop	Time = 65 s, AZ 351B	 <p>Legend: Si (grey), SiO₂ (light blue), ZEP R (pink), Nitride (dark blue), PR (red), P-Si (yellow), Ni (black), TiW (green), Al (orange)</p>
22	Etch silicon nitride on back side by RIE	STS RIE2, (power = 30 W, time = 12 min, composition = 40 sccm SF ₆ + 8 sccm O ₂ , pressure = 80 mtorr[126])	 <p>Legend: Si (grey), SiO₂ (light blue), ZEP R (pink), Nitride (dark blue), PR (red), P-Si (yellow), Ni (black), TiW (green), Al (orange)</p>
23	Etch silicon dioxide on back side by RIE	STS RIE2, power = 150 W, time = 26 min, composition = 40 sccm CHF ₃ , + 8 sccm CF ₄ pressure = 150 mTorr [126]	 <p>Legend: Si (grey), SiO₂ (light blue), ZEP R (pink), Nitride (dark blue), PR (red), P-Si (yellow), Ni (black), TiW (green), Al (orange)</p>
24	KOH etch of Si	80°C, about 4h50 min, Mechanical Frontside Protection.	 <p>Legend: Si (grey), SiO₂ (light blue), ZEP R (pink), Nitride (dark blue), PR (red), P-Si (yellow), Ni (black), TiW (green), Al (orange)</p>






25	Remove Nitride (and etch p-Si) in RIE	STS RIE2, recipe kgnitri 8 min (power = 30 W, time = 4 min, composition = 40 sccm SF ₆ + 8 sccm O ₂ , pressure = 80 mtorr[126]) ?	 <ul style="list-style-type: none"> ■ Si ■ SiO₂ ■ ZEP R ■ Nitride ■ PR ■ P-Si ■ Ni ■ TiW ■ Al
26	Etch Silicondioxide in RIE	STS RIE2, power = 150 W, time = 26 min, composition = 40 sccm CHF ₃ ,+ 8 sccm CF ₄ pressure = 150 mTorr [126] Note; To improve p-si overhang a short dip in BHF can further etch SiO ₂ . This may require thicker initial oxide	 <ul style="list-style-type: none"> ■ Si ■ SiO₂ ■ ZEP R ■ Nitride ■ PR ■ P-Si ■ Ni ■ TiW ■ Al
27	Remove Al	Aluminium etchant Transene D. 23 minutes at room temperature. Rinse in water	 <ul style="list-style-type: none"> ■ Si ■ SiO₂ ■ ZEP R ■ Nitride ■ PR ■ P-Si ■ Ni ■ TiW ■ Al
28	Spin on EBL resist	III-IV-spinner, thickness = 100 nm, resist: ZEP-520A7, undiluted, prebake at 160°C for 2 min Use spin recipe for 300 nm resist (500 rpm 5 s, 3000 rpm 30 s) (Diluted, 1:2 in anisole gives 100 nm)	 <ul style="list-style-type: none"> ■ Si ■ SiO₂ ■ ZEP R ■ Nitride ■ PR ■ P-Si ■ Ni ■ TiW ■ Al
29	Define hole for Ni dot by EBL	JEOL E-beam writer, acceleration voltage = 100 kV, current = 0.8 nA. Exposure dose 600 μC/cm ²	 <ul style="list-style-type: none"> ■ Si ■ SiO₂ ■ ZEP R ■ Nitride ■ PR ■ P-Si ■ Ni ■ TiW ■ Al

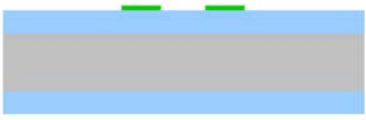
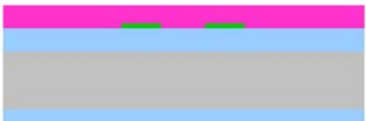



30	Develop	Developer: N50 1min30s Then rinse in IPA	 <p>Legend: Si (grey), SiO₂ (light blue), ZEP R (pink), Nitride (blue), PR (red), P-Si (yellow), Ni (black), TiW (green), Al (orange)</p>
31	Deposit Ni	Wordentec evaporator, thickness 5-10 nm	 <p>Legend: Si (grey), SiO₂ (light blue), ZEP R (pink), Nitride (blue), PR (red), P-Si (yellow), Ni (black), TiW (green), Al (orange)</p>
32	Lift-off p-Si in KOH	Different pieces. KOH at 80 °C. Time Maximum 1 min	 <p>Legend: Si (grey), SiO₂ (light blue), ZEP R (pink), Nitride (blue), PR (red), P-Si (yellow), Ni (black), TiW (green), Al (orange)</p>

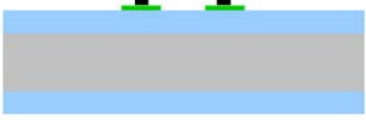




Encapsulation with oxide structures and leads






Table 14 Process sequence for Encapsulation with oxide structures and leads


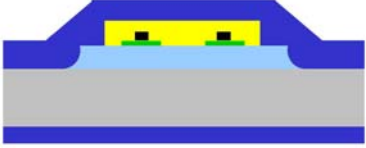



#	Process	Description	Cross section
1	Starting wafer	Si (100), 4", double polished	 <p>Legend: Si (grey), SiO₂ (light blue), ZEP R (pink), Nitride (blue), PR (red), P-Si (yellow), Ni (black), TiW (green), Al (orange)</p>

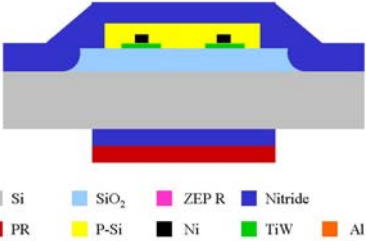
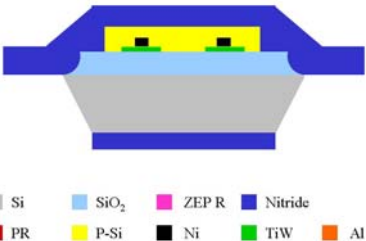
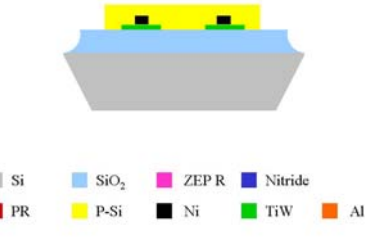
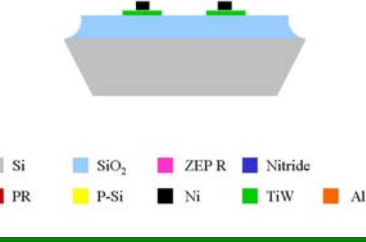
2	Grow 1 μ m SiO ₂	Phosphor drive-in furnace, wet oxidation, time = 2h30min, T = 1100°C	 <ul style="list-style-type: none"> ■ Si ■ SiO₂ ■ ZEP R ■ Nitride ■ PR ■ P-Si ■ Ni ■ TiW ■ Al
3	Spin on photo resist	(Pretreatment with 30 min in HMDS) SSI spinner, thickness = 1.5 μ m, prebake at 90°C for 60 s, resist: AZ 5214E	 <ul style="list-style-type: none"> ■ Si ■ SiO₂ ■ ZEP R ■ Nitride ■ PR ■ P-Si ■ Ni ■ TiW ■ Al
4	1 st photolithography step (Wires): align + expose	KS aligner, negative. exposure time = 3.5 s, at intensity 9, Hard contact, flood exposure 30 s	 <ul style="list-style-type: none"> ■ Si ■ SiO₂ ■ ZEP R ■ Nitride ■ PR ■ P-Si ■ Ni ■ TiW ■ Al
5	Develop	Time = 65s, AZ 351B	 <ul style="list-style-type: none"> ■ Si ■ SiO₂ ■ ZEP R ■ Nitride ■ PR ■ P-Si ■ Ni ■ TiW ■ Al
6	Sputtering of TiW wires	Wordentech: TiW sputtering; 150W, 7*10 ⁻³ mbar, 8 min gives 50 nm, [124]	 <ul style="list-style-type: none"> ■ Si ■ SiO₂ ■ ZEP R ■ Nitride ■ PR ■ P-Si ■ Ni ■ TiW ■ Al

7	Lift off	Lift off bath (acetone) with ultrasound	 <p>Legend: Si (grey), SiO₂ (light blue), ZEP R (pink), Nitride (dark blue), PR (red), P-Si (yellow), Ni (black), TiW (green), Al (orange)</p>
8	Spin on EBL resist	III-IV-spinner, thickness = 100 nm, resist: ZEP-520A7, undiluted, prebake at 160°C for 2 min Use spin recipe for 300 nm resist (500 rpm 5 s, 3000 rpm 30 s) (Diluted, 1:2 in anisole gives 100 nm)	 <p>Legend: Si (grey), SiO₂ (light blue), ZEP R (pink), Nitride (dark blue), PR (red), P-Si (yellow), Ni (black), TiW (green), Al (orange)</p>
9	Define hole for Ni dot by EBL	JEOL E-beam writer, acceleration voltage = 100 kV, current = 0.8 nA. Exposure dose 600 μC/cm ²	 <p>Legend: Si (grey), SiO₂ (light blue), ZEP R (pink), Nitride (dark blue), PR (red), P-Si (yellow), Ni (black), TiW (green), Al (orange)</p>
10	Develop	Developer: N50 1min30s Then rinse in IPA	 <p>Legend: Si (grey), SiO₂ (light blue), ZEP R (pink), Nitride (dark blue), PR (red), P-Si (yellow), Ni (black), TiW (green), Al (orange)</p>
11	Deposit Ni	Wordentec evaporator, thickness 5-10 nm	 <p>Legend: Si (grey), SiO₂ (light blue), ZEP R (pink), Nitride (dark blue), PR (red), P-Si (yellow), Ni (black), TiW (green), Al (orange)</p>

12	Lift off	Microposit remover 1165, 12h, + ultrasound pulses towards the end	 <p>Legend: Si (grey), SiO₂ (light blue), ZEP R (pink), Nitride (dark blue), PR (red), P-Si (yellow), Ni (black), TiW (green), Al (orange)</p>
13	Spin on photo resist	(Pretreatment with 30 min in HMDS) SSI spinner, thickness = 1.5 μm, prebake at 90°C for 60 s, resist: AZ 5214E	 <p>Legend: Si (grey), SiO₂ (light blue), ZEP R (pink), Nitride (dark blue), PR (red), P-Si (yellow), Ni (black), TiW (green), Al (orange)</p>
14	2 nd photolithography step: align + expose	KS aligner, negative. exposure time = 3.5 s, at intensity 9, Hard contact, flood exposure 30 s	 <p>Legend: Si (grey), SiO₂ (light blue), ZEP R (pink), Nitride (dark blue), PR (red), P-Si (yellow), Ni (black), TiW (green), Al (orange)</p>
15	Develop	Time = 65s, AZ 351B	 <p>Legend: Si (grey), SiO₂ (light blue), ZEP R (pink), Nitride (dark blue), PR (red), P-Si (yellow), Ni (black), TiW (green), Al (orange)</p>
16	Sputtering of 100 nm p-Si	Alcatel 5.5 min p-si sputtering. 440 W	 <p>Legend: Si (grey), SiO₂ (light blue), ZEP R (pink), Nitride (dark blue), PR (red), P-Si (yellow), Ni (black), TiW (green), Al (orange)</p>

17	Lift off	Lift off bath (acetone), with ultrasound	 <p>Legend: Si (grey), SiO₂ (light blue), ZEP R (yellow), Nitride (blue), PR (red), P-Si (grey), Ni (black), TiW (green), Al (orange)</p>
18	Spin on photo resist	(Pretreatment with 30 min in HMDS) SSI spinner, thickness = 1.5 μm, prebake at 90°C for 60 s, resist: AZ 5214E	 <p>Legend: Si (grey), SiO₂ (light blue), ZEP R (yellow), Nitride (blue), PR (red), P-Si (grey), Ni (black), TiW (green), Al (orange)</p>
19	3 rd Photolithography step (Cantilever): align + expose	KS aligner, negative. exposure time = 3.5 s, at intensity 9, Hard contact, flood exposure 30 s	 <p>Legend: Si (grey), SiO₂ (light blue), ZEP R (yellow), Nitride (blue), PR (red), P-Si (grey), Ni (black), TiW (green), Al (orange)</p>
20	Develop	Time = 65s, AZ 351B	 <p>Legend: Si (grey), SiO₂ (light blue), ZEP R (yellow), Nitride (blue), PR (red), P-Si (grey), Ni (black), TiW (green), Al (orange)</p>
21	Etch Oxide	BHF, 13min	 <p>Legend: Si (grey), SiO₂ (light blue), ZEP R (yellow), Nitride (blue), PR (red), P-Si (grey), Ni (black), TiW (green), Al (orange)</p>

22	Strip Resist	Strip in lift off bath, since metal is present on wafers	 <p>Legend:</p> <ul style="list-style-type: none"> Si (grey) SiO₂ (light blue) ZEP R (pink) Nitride (blue) PR (red) P-Si (yellow) Ni (black) TiW (green) Al (orange)
23	Deposit 450 nm low-stress, silicon-rich silicon nitride to protect front side by PECVD, and 300 nm on backside	PECVD 3 Recipe JKHKGNITRI 26 min backside (300 nm) 39 min frontside (450 nm)	 <p>Legend:</p> <ul style="list-style-type: none"> Si (grey) SiO₂ (light blue) ZEP R (pink) Nitride (blue) PR (red) P-Si (yellow) Ni (black) TiW (green) Al (orange)
24	Spin photo resist on back side	SSI spinner, thickness = 1.5 um, prebake at 90°C for 60 s, resist: AZ 5214E	 <p>Legend:</p> <ul style="list-style-type: none"> Si (grey) SiO₂ (light blue) ZEP R (pink) Nitride (blue) PR (red) P-Si (yellow) Ni (black) TiW (green) Al (orange)
25	4 th photolithography step (back side): align + expose	KS aligner, positive, exposure time = 6 s at intensity 9	 <p>Legend:</p> <ul style="list-style-type: none"> Si (grey) SiO₂ (light blue) ZEP R (pink) Nitride (blue) PR (red) P-Si (yellow) Ni (black) TiW (green) Al (orange)
26	Develop	Time = 65 s, AZ 351B	 <p>Legend:</p> <ul style="list-style-type: none"> Si (grey) SiO₂ (light blue) ZEP R (pink) Nitride (blue) PR (red) P-Si (yellow) Ni (black) TiW (green) Al (orange)

27	Etch silicon nitride on back side by RIE	STS RIE2, (power = 30 W, time = 12 min, composition = 40 sccm SF ₆ + 8 sccm O ₂ , pressure = 80 mtorr[126])	 <p>Legend: Si (grey), SiO₂ (light blue), ZEP R (pink), Nitride (blue), PR (red), P-Si (yellow), Ni (black), TiW (green), Al (orange)</p>
28	KOH etch of Si	80°C, about 4h50 min, Mechanical Frontside Protection.	 <p>Legend: Si (grey), SiO₂ (light blue), ZEP R (pink), Nitride (blue), PR (red), P-Si (yellow), Ni (black), TiW (green), Al (orange)</p>
29	Remove Silicon nitride	Silicon nitride wet etch. 30 min at 160 °C Note; this step can be switched with removal in RIE (at only 30 W), if 200 nm Al is deposited on top of the p-Si right after p-Si deposition	 <p>Legend: Si (grey), SiO₂ (light blue), ZEP R (pink), Nitride (blue), PR (red), P-Si (yellow), Ni (black), TiW (green), Al (orange)</p>
30	Remove p-Si	KOH dip at 80°C, 10-15 s Note; may have more control of time at 60 °C	 <p>Legend: Si (grey), SiO₂ (light blue), ZEP R (pink), Nitride (blue), PR (red), P-Si (yellow), Ni (black), TiW (green), Al (orange)</p>

Appendix C

Additional material

Gas correction factor

The formula for gas correction factor calculation is given as;

$$f = 0.3106 \frac{\sum_n a_n f_n}{\sum_n a_n d_n C_{p,n}}$$

where n sums over the different gases in the flow. a_n is the fraction of gas n, d_n is the density (g/l), $C_{p,n}$ is the specific heat (cal/gK) and f_n is the molecular structure factor for gas n.

Nitride removal in RIE with in situ etch mask

It has been shown that an Aluminium RIE etch mask which is carried through the processing –allows etches of both nitride, p-si, and oxide and produces close to vertical sidewalls on the cantilever.

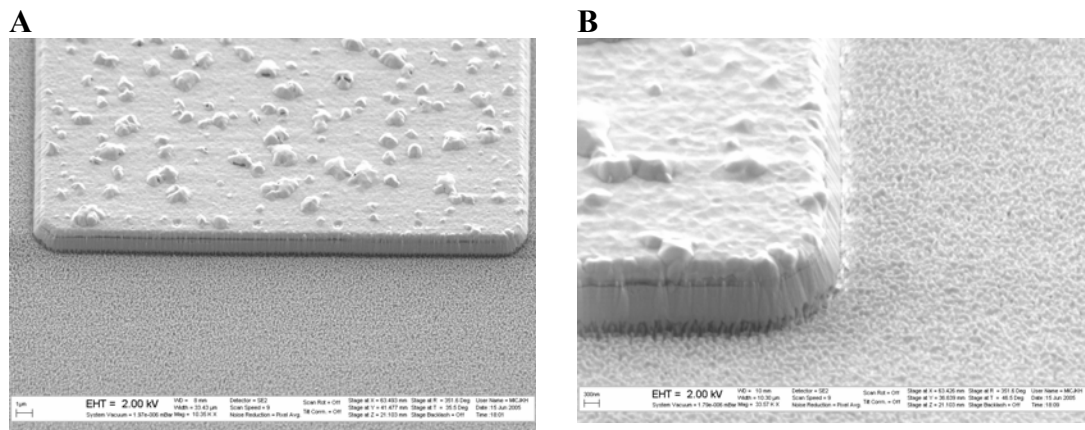


Figure 108 A) A SEM image of a cantilever and B, A close up of the cantilever structure after etch through the nitride, p-Si and Oxide layers, using aluminium as an etch mask in RIE. This clearly shows that the nitride can be etched without underetching into the p-Si layer. The etching time through the nitride and the p-si was 6 minutes (probably less could do), using the nitride etch recipe in RIE.

References

1. Feynman, R.P., *There's Plenty of Room at the Bottom*. Journal of Microelectromechanical systems, 1992. **1**(1): p. 60-66.
2. Feynman, R.P., *Infinitesimal Machinery*. Journal of Microelectromechanical Systems, 1993. **2**(1): p. 4-14.
3. Kroto, H.W., et al., *C60 Buckminsterfullerene*. Nature, 1985. **318**: p. 162-163.
4. Iijima, S., *Helical microtubules of graphitic carbon*. Nature, 1991. **354**(56-58).
5. Samuelson, L., *Self-forming nanoscale devices*. Materials Today, 2003. **6**(10): p. 22-31.
6. Lieber, C.M. *Nanowires as building blocks for nanoelectronics and nanophotonics*. in *Electron Devices Meeting, 2003. IEDM '03 Technical Digest*. 2003: IEEE International.
7. Balzer, F. and H.-G. Rubahn, *Dipole-assisted self-assembly of light-emitting p-nP needles on mica*. Appl. Phys. Lett., 2001. **79**(23): p. 3860.
8. Thelander, C., et al., *Gold nanoparticle single-electron transistor with carbon nanotube leads*. Applied Physics Letters, 2001. **79**(13): p. 2106-2108.
9. Lin, R., P. Bøggild, and O. Hansen, *Microcantilever equipped with nanowire template electrodes for multiprobe measurement on fragile nanostructures*. J. Appl. Phys., 2004. **96**(5): p. 2895-2900.
10. Avouris, P., R. Martel, and H.R. Shea, *Carbon nanotubes: nanomechanics, manipulation, and electronic devices*. Applied Surface Science, 1999. **141**(3): p. 201-209.
11. Bourlon, B., et al., *Determination of the Intershell Conductance in Multiwalled Carbon Nanotubes*. Physical Review Letters, 2004. **93**(17): p. 176806-1 - 176806-4.
12. Bourlon, B., et al., *Geometrical dependence of high-bias current in multiwalled carbon nanotubes*. Physical Review Letters, 2004. **92**(2): p. 026804/1-4.
13. Teo, K.B.K., et al., *Catalytic Synthesis of Carbon Nanotubes and Nanofibers*. Encyclopedia of Nanoscience and Nanotechnology, 2004. **1**: p. 665-686.
14. Meyyappan, M., et al., *Carbon nanotube growth by PECVD: a review*. Plasma Sources Science and Technology, 2003. **12**: p. 205-216.
15. Gangloff, L., et al., *Sel-Aligned, Gated Arrays of Individual Nanotube and Nanowire Emitters*. Nanoletters, 2004. **4**(9): p. 1575-1579.
16. Collins, P.G., M.S. Arnold, and P. Avouris, *Engineering Carbon Nanotubes and Nanotube Circuits Using Electrical Breakdown*. Science, 2001. **292**: p. 706-709.
17. Collins, P.G. and P. Avouris, *Nanotubes for Electronics*. Scientific American, 2000: p. 62-69.
18. Pirio, G., et al., *Fabrication and electrical characteristics of carbon nanotube field emission microcathodes with an integrated gate electrode*. Nanotechnology, 2002. **13**: p. 1-4.
19. Teo, K.B.K., et al., *Fabrication and electrical characteristics of carbon nanotube-based microcathodes for use in a parallel electron-beam lithography system*. J. Vac. Sci. Technol. B, 2003. **21**(2): p. 693-697.
20. Robinson, L.A.W., et al., *Fabrication of self-aligned side gates to carbon nanotubes*. Nanotechnology, 2003. **14**: p. 290-293.

21. Lee, S.B., A.S. Teh, K.B.K. Teo, M. Chhowalla, D.G. Hasko, W.I. Milne, G.A.J. Amaratunga, H. Ahmed, *Fabrication of carbon nanotube lateral field emitters*. Nanotechnology, 2003. **14**: p. 192-195.
22. Hafner, J.H., et al., *Structural and functional imaging with carbon nanotube AFM probes*. Progr. Biophys. Molec. Biol., 2001. **77**: p. 73-110.
23. Kong, J., et al., *Nanotube molecular wires as chemical sensors*. Science, 2000. **287**: p. 622-625.
24. Modi, A., et al., *Miniaturized gas ionization sensors using carbon nanotubes*. Nature, 2003. **424**: p. 171-174.
25. Collins, P.G., et al., *Extreme oxygen sensitivity of electronic properties of carbon nanotubes*. Science, 2000. **287**: p. 1801-1804.
26. Dillon, A.C., et al., *Storage of hydrogen in single-walled carbon nanotubes*. Nature, 1997. **386**: p. 377.
27. Melechko, A., et al., *Vertically aligned carbon nanofibers and related structures: Controlled synthesis and directed assembly*. J. Appl. Phys., 2005. **97**: p. 041301-1-041301-39.
28. Xia, Y., et al., *One-dimensional nanostructures: Synthesis, Characterization, and Applications*. Adv. Mater., 2003. **15**(5): p. 353-389.
29. Teo, K.B.K., et al., *Uniform patterned growth of carbon nanotubes without surface carbon*. Appl. Phys. Lett., 2001. **79**(10): p. 1534-1536.
30. Kim, D.-H., et al., *The growth of freestanding single carbon nanotube arrays*. Nanotechnology, 2003. **14**: p. 1269-1271.
31. Jang, J.E., et al., *Nanoelectromechanical switches with vertically aligned carbon nanotubes*. Appl. Phys. Lett., 2005. **87**: p. 163114.
32. Guillorn, M.A., et al., *Individually addressable vertically aligned carbon nanofiber-based electrochemical probes*. J. Appl. Phys., 2002. **91**: p. 3824.
33. McKnight, T.E., et al., *Microarrays of Vertically-Aligned Carbon Nanofiber Electrodes in an Open Fluidic Channel*. J. Phys. Chem. B, 2004. **108**: p. 7115.
34. Tseng, Y.C., et al., *Monolithic Integration of Carbon Nanotube Devices with Silicon MOS Technology*. Nanoletters, 2004. **4**(1): p. 123-127.
35. Ye, Q., et al., *Large-Scale Fabrication of Carbon nanotube Probe Tips for Atomic Force Microscopy Critical Dimension Imaging Applications*. Nanoletters, 2004. **4**(7): p. 1301-1308.
36. Petersen, C.L., *Microscopic Four-Point Probes*, in MIC. 1999, Technical University of Denmark: Kgs Lyngby.
37. Hansen, T.M., *Tools for Nanoscale Conductivity Measurements*, in Department of Micro and Nanotechnology. 2003, Technical University of Denmark: Kongens Lyngby.
38. Bøggild, P., et al., *Scanning nanoscale multiprobes for conductivity measurements*. Rev. Sci. Instruments, 2000. **71**: p. 533-537.
39. Dai, H., et al., *Nanotube as Nanoprobes in Scanning Probe Microscopy*. Nature, 1996. **384**: p. 147-151.
40. Stevens, R., et al., *Improved fabrication approach for carbon nanotube probe devices*. Appl. Phys. Lett., 2000. **77**(21): p. 3453-3455.
41. Yenilmez, E., et al., *Wafer scale production of carbon nanotube scanning probe tips for atomic force microscopy*. Appl. Phys. Lett., 2002. **80**(12): p. 2225-2227.
42. Bethune, D.S., et al., *Cobalt-catalysed growth of carbon nanotubes with single-atomic layer walls*. Nature, 1993. **363**: p. 605.

43. Iijima, S. and T. Ichihashi, *Single shell carbon nanotubes of 1 nm diameter*. Nature, 1993. **363**: p. 603.
44. Mintmire J.W., D.B.I., White C.T., *Are fullerene tubules metallic?* Phys. Rev. Lett., 1992. **68**: p. 631.
45. Hamada N., S.S., Oshiyama A., *New one-dimensional conductors - graphitic microtubules*. Phys. Rev. Lett., 1992. **68**: p. 1579.
46. Saito R., F.M., Dresselhaus G., Dresselhaus M.S., *Electronic structure of graphene tubules based on C60*. Phys. Rev. B, 1992. **46**: p. 1804.
47. Overney G., Z.W., Tomanek Z., *Structural rigidity and low frequency vibrational modes of long carbon tubules*. Phys. D, 1993. **27**: p. 93.
48. Yu, M.F., et al., *Strength and Breaking Mechanism of Multiwalled Carbon Nanotubes Under Tensile Load*. Science, 2000. **287**: p. 637.
49. Rinzler A.G., H.J.H., Nikolaev L., Lou L., Kim S.G., Tomanek D., Nordlander P., Colbert D.T., Smalley R.E., *Unravelling Nanotubes: Field emission from an atomic wire*. Science, 1995. **269**(1550).
50. Bhushan, B., ed. *Handbook of Nanotechnology*. 2004, Springer.
51. Saito, R., G. Dresselhaus, and M.S. Dresselhaus, *Physical properties of Carbon Nanotubes*. 1998, London: Imperial College Press.
52. Avouris, P., *Molecular electronics with carbon nanotubes*. Acc. Chem. Res., 2002: p. A-I.
53. Qian D., W.G.J., Liu W.K., Yu M.-F., Ruoff R.S., *Mechanics of carbon nanotubes*. Appl Mech Rev, 2002. **55**(6): p. 495-533.
54. Boskovic, B.O., et al., *Large-area synthesis of carbon nanofibres at room temperature*. Nature Mater., 2002. **1**(165): p. 165-168.
55. Meyyappan M., D.L., Cassel A., Hash D., *Carbon nanotube growth by PECVD: a review*. Plasma Sources Science and Technology, 2003. **12**: p. 205-216.
56. Wong, E.W., P.E. Sheehan, and C.M. Lieber, *Nanobeam mechanics: elasticity, strength and toughness of nanorods and nanotubes*. Science, 1997. **277**: p. 1971.
57. Forro, L. and C. Schonenberger, in *Carbon nanotubes synthesis, structure, properties and applications*, M.S. Dresselhaus, G. Dresselhaus, and P. Avouris, Editors. 2001, Springer-Verlag: New York. p. 329.
58. Thess, A., et al., *Crystalline ropes of metallic carbon nanotubes*. Science, 1996. **273**(5274): p. 483-487.
59. de Heer, W.A. and R. Martel, *Industry sizes up nanotubes*. Phys. World, 2000. **13**: p. 49.
60. Schonenberger, C., et al., *Interference and Interaction in multi-wall carbon nanotubes*. Appl. Phys. A, 1999. **69**: p. 283.
61. Lee, S.B., et al., *Fabrication of multiwalled carbon nanotube bridges by polymethylmethacrylate suspended dispersion*. J. Vac. Sci. Technol. B, 2003. **21**(3): p. 996-999.
62. Dai H., *Carbon Nanotubes: Synthesis, Integration, and Properties*. Acc. Chem. Res., 2002: p. 9.7.
63. Rinzler, A.G., et al., *Unravelling Nanotubes: Field emission from an atomic wire*. Science, 1995. **269**(1550).
64. Guo, T., et al., *Catalytic growth of single-walled nanotubes by laser vaporisation*. Chemical Physics Letters, 1995. **243**.

65. Dai H., K.J., Zhou C., Franklin N., Tomblor T., Cassel A., Fan S., Chapline M., *Controlled Chemical Routes to Nanotube Architectures, Physic and Devices*. J. Phys. Chem., 1999. **103**(51): p. 11246-11255.
66. Lee Y.-H., J.Y.-T., Choi C.-H., Kim E.-K., Ju B.-K., Kim D.-H., Lee C.-W., Yoon S.-S., *Direct nano-wiring carbon nanotube using growth barrier: A possible mechanism of selective lateral growth*. J. Appl. Phys., 2002. **91**(9): p. 6044-6050.
67. Tang S., Z.Z., Xiong Z., Sun L., Lieu L., Lin J., Shen Z.X., Tan K.L., *Controlled growth of single walled carbon nanotubes by catalytic decomposition of CH₄ over Mo/Co/MgO catalysts*. Chemical Physics Letters, 2001. **350**: p. 19-26.
68. Huang, S., L. Dai, and A. Mau, *Controlled fabrication of aligned nanotube patterns*. Physica B, 2002. **323**: p. 333-335.
69. Cassel A.M., F.N.R., Tomblor T.W., Chan E.M., Han J., Dai H., *Directed growth of free standing single-walled carbon nanotubes*. J. Am. Chem. Soc., 1999. **121**(34): p. 7975-7976.
70. Zhang Y., C.A., Cao J., Wang Q., Kim W., Li Y., Morris N., Yenilmez E., Kong J., Dai H., *Electric field directed growth of aligned single walled carbon nanotubes*. Appl. Phys. Lett., 2001. **79**(19): p. 3155-3157.
71. Ren, Z.F., et al., *Synthesis of Large Arrays of Well-Aligned Carbon Nanotubes on Glass*. Science, 1998. **282**(5391): p. 1105-1107.
72. Chhowalla, M., et al., *Growth process conditions of vertically aligned carbon nanotubes using plasma enhanced chemical vapor deposition*. Journal of Applied Physics, 2001. **90**(10): p. 5308-5317.
73. Teo, K.B.K., et al., *Characterisation of plasma enhanced chemical vapor deposited carbon nanotubes by Auger electron spectroscopy*. J. Vac. Sci. Technol. B, 2002. **20**(1): p. 116-121.
74. Teo, K.B.K., et al., *Field emission from dense, sparse, and patterned arrays of carbon nanofibers*. Appl. Phys. Lett., 2002. **80**(11): p. 2011-2013.
75. Teo, K.B.K., et al., *Plasma enhanced chemical vapour deposition carbon nanotubes/nanofibres - how uniform do they grow?* Nanotechnology, 2003. **14**: p. 204-211.
76. Ren, Z.F., Z.P. Huang, J.W. Xu, P. Bush, M.P. Siegal, P.N. Provencio, *Synthesis of large arrays of well-aligned carbon nanotubes on glass*. Science, 1998. **282**: p. 1105.
77. Teo, K.B.K., C. Singh, M. Chhowalla, W.I. Milne, *Catalytic Synthesis of Carbon Nanotubes and Nanofibers*. Encyclopedia of Nanoscience and Nanotechnology, 2003. **X**: p. 1-22.
78. AuBuchon, J.F., et al., *Multiple sharp bendings of carbon nanotubes during growth to produce zigzag morphology*. Nanoletters, 2004. **4**: p. 1781-1784.
79. Lin, C.C., et al., *Sheath-dependent orientation control of carbon nanofibres and carbon nanotubes during plasma-enhanced chemical vapour deposition*. Nanotechnology, 2004. **15**: p. 176-179.
80. Merkulov, V.I., et al., *Controlled alignment of carbon nanofibers in a large-scale synthesis process*. Appl. Phys. Lett., 2002. **80**(25): p. 4816-4818.
81. Rao, A.M., et al., *In situ-grown carbon nanotube array with excellent field emission characteristics*. Appl. Phys. Lett., 2000. **76**: p. 3813.
82. Teo, K.B.K., *Personal communication*. 2003.
83. Teo K.B.K., C.M., Amaratunga G. A. J., Milne W.I., Pirio G., Legagneux P., Olivier J., Pribat D., *Characterisation of plasma enhanced chemical vapor*

- deposited carbon nanotubes by Auger electron spectroscopy.* J. Vac. Sci. Technol. B, 2002. **20**(1): p. 116-121.
84. Wei, Y.Y., et al., *Effect of catalyst film thickness on carbon nanotube growth by selective area chemical vapor deposition.* Appl. Phys. Lett., 2001. **78**: p. 1394.
 85. Molhave, K., et al., *Towards Pick-and-Place assembly of Nanostructures.* Journal of Nanoscience and Nanotechnology, 2004. **4**(3): p. 279-282.
 86. Saito R., F.M., Dresselhaus G., Dresselhaus M.S., *Electronic structure of graphene tubules based on C60.* Phys. Rev. B, 1992. **46**: p. 1804.
 87. Ekvall, I., et al., *Preparation and characterization of electrochemically etched W tips for STM.* Meas. Sci. Technol., 1999. **10**: p. 11-18.
 88. Teo K.B.K., C.M., Amaratunga G. A. J., Milne W.I., Pirio G., Legagneux P., Wyczisk F., Pribat D., Hasko D.G., *Field emission from dense, sparse, and patterned arrays of carbon nanofibers.* Appl. Phys. Lett., 2002. **80**(11): p. 2011-2013.
 89. Dohn, S., K. Molhave, and P. Boggild, *Direct measurement of resistance of multiwalled carbon nanotubes using micro four-point probes.* Sensor Letters, 2005. **3**(4): p. 300-303.
 90. Milne, W.I., et al., *Carbon nanotubes as field emission sources.* J. Mater. Chem, 2004. **14**: p. 1-12.
 91. Chhowalla, M., et al., *Field emission from short and stubby vertically aligned carbon nanotubes.* Appl. Phys. Lett., 2001. **79**(13): p. 2079-2081.
 92. Zhang, Y., et al., *Electric field directed growth of aligned single walled carbon nanotubes.* Appl. Phys. Lett., 2001. **79**(19): p. 3155-3157.
 93. Avigal, Y. and R. Kalish, *Growth of aligned carbon nanotubes by biasing during growth.* Appl. Phys. Lett., 2001. **78**: p. 2291.
 94. Merkulov, V.I., et al., *Alignment mechanism of carbon nanofibers produced by plasma-enhanced chemical-vapor deposition.* Appl. Phys. Lett., 2001. **79**: p. 2970.
 95. Dai, H., et al., *Controlled Chemical Routes to Nanotube Architectures, Physics and Devices.* J. Phys. Chem., 1999. **103**(51): p. 11246-11255.
 96. Balzer, F. and H.-G. Rubahn, *Growth control and optics of organic nanoaggregates.* Adv. Funct. Mater., 2005. **15**: p. 17.
 97. Lau, K.K.S., et al., *Superhydrophobic Carbon Nanotube Forests.* Nanoletters, 2003. **3**(12): p. 1701-1705.
 98. Alberti, G. and A. DeSimone, *Wetting of rough surfaces: a homogenization approach.* Proc. Roy. Soc. London A, 2005. **461**: p. 79-97.
 99. Wenzel, R.N., *Resistance of solid surfaces to wetting by water.* Ind. Eng. Chem., 1936. **28**: p. 988-994.
 100. Cassie, A.B. and S. Baxter, *Wettability of porous surfaces.* Trans. Faraday Soc., 1944. **40**: p. 546-551.
 101. Bico, J., U. Thiele, and D. Quere, *Wetting of textured surfaces.* Colloids and Surfaces A, 2002. **206**: p. 41-46.
 102. Patankar, N.A., *On the modelling of hydrophobic contact angles on rough surfaces.* Langmuir, 2003. **19**: p. 1249-1253.
 103. Klier, J., et al., *Wetting behaviour of liquid 4He on rough Cs films: Pinning, memory effect, and micropuddles.* Physical Review B, 2005. **72**: p. 245410.
 104. Li, H., et al., *Super-"amphiphobic" Aligned Carbon Nanotube Films.* Angew. Chem. Int. Ed., 2001. **40**(9): p. 1743-1745.

105. Cheng, Y.-T. and D.E. Rodak, *Is the lotus leaf superhydrophobic?* Appl. Phys. Lett., 2005. **86**: p. 144101.
106. Cheng, Y.T., et al., *Effects of micro- and nano-structures on the self-cleaning behaviour of lotus leaves.* Nanotechnology, 2006. **17**: p. 1359-1362.
107. Bico, J., C. Tordeux, and D. Quere, *Rough Wetting.* Europhys. Lett., 2001. **55**(2): p. 214-220.
108. Fan, J.G., et al., *Nanocarpets Effect: Pattern Formation during the Wetting of Vertically Aligned Nanorod Arrays.* Nanoletters, 2004. **4**(11): p. 2133-2138.
109. Journet, C., et al., *Contact angle measurements on superhydrophobic Carbon Nanotube Forests : effect of fluid pressure.* Europhysics Letters.
110. Falvo, M.R., et al., *Nanometre-scale rolling and sliding of carbon nanotubes.* Nature, 1999. **397**(6716): p. 236-238.
111. Kjelstrup-Hansen, J., et al., *Mechanical properties of organic nanofibers.* Small, 2006. **2**: p. 660.
112. Senturia, S.D., *Microsystem Design.* 2001, Boston, MA: Kluwer Academic Publishers.
113. Pedersen, D.H., *High aspect ratio silicon beam fabrication and large scale nanowire integration,* in *MIC - Department of Micro and Nanotechnology.* 2006, Technical University of Denmark: Kgs Lyngby.
114. Nilson, D., *Polyme based miniaturized dye lasers for Lab-on-a-chip systems,* in *MIC - Department of Micro and Nanotechnology.* 2005, Technical University of Denmark: Kgs Lyngby.
115. Clay, K.J., et al., *Material properties and tribological performance of rf-PECVD deposited DLC coatings.* Diamond Relat. Mater., 1998. **7**: p. 1100.
116. Serway, R.A., *Physics for Scientists and Engineers.* Third ed. 1992: Saunders College Publishing.
117. Kjelstrup-Hansen, J., et al., *Versatile Method for Manipulating and Contacting Nanowires.* J. Nanosci. Nanotechnol., 2006. **6**(7): p. 1995-1999.
118. Kjelstrup-Hansen, J., et al., *Electrical properties of a single p-hexaphenylene nanofibre.* Thin Solid Films, 2006. **in press**.
119. MKS, *Gas Correction Factors for Thermal Based Flow.* 2006.
120. Terrones, H. and M. Terrones, *Curved nanostructured materials.* New Journal of Physics, 2003. **5**(1): p. 126.
121. Plummer, J.D., M.D. Deal, and P.B. Griffin, *Silicon VLSI Technology.* 2000: Prentice Hall.
122. Madou, M., *Fundamentals of Microfabrication.* 1997: CRC Press.
123. Williams, K.R., K. Gupta, and M. Wasilik, *Etch Rates for Micromachining Processing - Part II.* Journal of Microelectromechanical systems, 2003. **12**(6): p. 761-778.
124. Gammelgaard, L., *Personal communication.* 2006.
125. Sze, S.M., *VLSI Technology.* 1988, New York: McGraw-Hill.
126. Hansen, T.M., *Tools for Nanoscale Conductivity Measurements,* in *MIC.* 2003, Technical University of Denmark.